CIVIL ENGINEERING JOURNAL

číslo 1/2025

Obsah:

Article no. 1

THE CIVIL ENGINEERING JOURNAL 1-2025

CHANCE CONSTRAINED STOCHASTIC PROGRAMMING IN DESIGN OF A FRAME STRUCTURE

Eva Mrázková

Brno University of Technology, Faculty of Mechanical Engineering, Institute of Mathematics, Technická 2, Brno 616 69, Czech Republic; zampachova@fme.vutbr.cz

Received: *14.05.2024*

Received in revised form: *17.12.2024*

Accepted: *19.03.2025*

ABSTRACT

A civil engineering problem concerning the optimal design of a loaded frame structure with a random Young's modulus is discussed. The developed multi-criteria optimization model involves ODE-type constraints and also one chance constraint related to the structure's reliability. A computational scheme for this type of problem is proposed using the finite difference method for the approximation of the ODE constraint and the scenario-based approach for random variable approximation. The chance constraint is handled by two approaches – the analytical approach and penalty reformulation. A posteriori check of satisfying the chance constraint is made, and the upper bounds of the obtainable reliability are computed.

KEYWORDS

Optimal engineering design, Stochastic programming, Chance constrained optimization, Ordinary differential equations

INTRODUCTION

It is often important in engineering to find the best possible design of a studied structure. To ensure the best solution, it is necessary to use a suitable optimization method. Furthermore, it is useful to consider several optimization criteria, e.g. minimizing the cost (which corresponds to the weight of the designed structure) and maximizing its rigidity. Optimal design problems in all engineering areas often lead to multicriteria optimization models constrained by ordinary (ODE) or partial (PDE) differential equations. At first, deterministic approaches have been used to solve such problems where all parameters are considered to be deterministic. However, uncertainty plays an important role due to variations in the material, variations in the external loads, etc. Therefore, the probabilistic nature of these problems should be considered to provide a more realistic description of real-world problems.

This paper focuses on the optimal design of a loaded frame structure with a random Young's modulus. The reliability of the design is also an important issue here. Various approaches can be used to solve such a problem. Deterministic and reliability-based structural optimization of concrete cross sections has been compared, e. g. in [1], probability-based methods have been used, e.g. to optimize the spun concrete pole in [2] and heuristic algorithms have been tested, e.g. in [3]. A stochastic programming approach has been applied to a problem concerning the optimal design of beam cross section dimensions, e.g. in [4], [5], [6]. The reliability of the design has been addressed, e.g. in [7] and [8] by using chance constrained stochastic programming. This method is also utilized in this paper, and the chance constraint is handled by two approaches. Moreover, a posteriori check of satisfying the chance constraint is made, and the upper bounds of the obtainable reliability are computed.

PROBLEM FORMULATION

The problem of designing a frame structure has been chosen (see Figure 1). The task is to obtain an optimal design of rectangular cross section dimensions while the frame's weight is minimized and its rigidity is maximized. The weighted sum method is used to solve the multi-criteria problem (see [9]). A random Young's modulus related to different material characteristics is assumed. The problem can be formulated as the following ODE constrained stochastic optimization program:

$$\min_{a,b_1,b_2,b_3,v_1,v_2,v_3} \left(-\alpha \mathbb{E}\left(\frac{E(\omega)ab_1^3 + E(\omega)ab_2^3 + E(\omega)ab_3^3}{12c_{rigidity}}\right) + \beta\frac{\rho ab_1 l_1 + \rho ab_2 l_2 + \rho ab_3 l_2}{c_{weight}}\right) \tag{1}$$

$$\text{s.t.} \quad E(\omega)\frac{ab_1^3}{12}\frac{\mathrm{d}^4 v_1}{\mathrm{d}x^4}(\omega,x) = f(x), x \in \langle 0, l_1\rangle, \omega \in \Omega, \tag{2}$$

$$E(\omega)\frac{ab_2^3}{12}\frac{\mathrm{d}^4 v_2}{\mathrm{d}y^4}(\omega,y) = 0, y \in \langle 0, l_2\rangle, \omega \in \Omega, \tag{3}$$

$$E(\omega)\frac{ab_3^3}{12}\frac{\mathrm{d}^4 v_3}{\mathrm{d}y^4}(\omega,y) = 0, y \in \langle 0, l_2\rangle, \omega \in \Omega, \tag{4}$$

$$v_1(\omega,0) = 0, v_1(\omega,l_1) = 0, \omega \in \Omega, \tag{5}$$

$$v_2(\omega,0) = 0, \frac{\mathrm{d}v_2}{\mathrm{d}y}(\omega,0) = 0, v_2(\omega,l_2) = 0, \omega \in \Omega, \tag{6}$$

$$v_3(\omega,0) = 0, \frac{\mathrm{d}v_3}{\mathrm{d}y}(\omega,0) = 0, v_3(\omega,l_2) = 0, \omega \in \Omega, \tag{7}$$

$$-\frac{\mathrm{d}v_1}{\mathrm{d}x}(\omega,0) = \frac{\mathrm{d}v_2}{\mathrm{d}y}(\omega,l_2), \omega \in \Omega, \tag{8}$$

$$\frac{\mathrm{d}v_1}{\mathrm{d}x}(\omega,l_1) = -\frac{\mathrm{d}v_3}{\mathrm{d}y}(\omega,l_2), \omega \in \Omega, \tag{9}$$

$$E(\omega)\frac{ab_1^3}{12}\frac{\mathrm{d}^2 v_1}{\mathrm{d}x^2}(\omega,0) = -E(\omega)\frac{ab_2^3}{12}\frac{\mathrm{d}^2 v_2}{\mathrm{d}y^2}(\omega,l_2), \omega \in \Omega, \tag{10}$$

$$E(\omega)\frac{ab_1^3}{12}\frac{\mathrm{d}^2 v_1}{\mathrm{d}x^2}(\omega,l_1) = E(\omega)\frac{ab_3^3}{12}\frac{\mathrm{d}^2 v_3}{\mathrm{d}y^2}(\omega,l_2), \omega \in \Omega \tag{11}$$

$$\left|E(\omega)\frac{\mathrm{d}^2 v_1}{\mathrm{d}x^2}(\omega,x)\frac{b_1}{2}\right| \le \sigma_{limit}, x \in \langle 0, l_1\rangle, \omega \in \Omega, \tag{12}$$

$$\left|E(\omega)\frac{\mathrm{d}^2 v_2}{\mathrm{d}y^2}(\omega,y)\frac{b_2}{2} + \frac{\int_0^{\frac{l_1}{2}} |f(x)|\mathrm{d}x}{ab_2}\right| \le \sigma_{limit}, y \in \langle 0, l_2\rangle, \omega \in \Omega, \tag{13}$$

$$\left|E(\omega)\frac{\mathrm{d}^2 v_3}{\mathrm{d}y^2}(\omega,y)\frac{b_3}{2} - \frac{\int_{\frac{l_1}{2}}^{l_1} |f(x)|\mathrm{d}x}{ab_3}\right| \le \sigma_{limit}, y \in \langle 0, l_2\rangle, \omega \in \Omega, \tag{14}$$

$$\int_0^{\frac{l_1}{2}} |f(x)|\mathrm{d}x \le \frac{\pi^2 E(\omega) a b_2^3}{12(\gamma l_2)^2}, \int_{\frac{l_1}{2}}^{l_1} |f(x)|\mathrm{d}x \le \frac{\pi^2 E(\omega) a b_3^3}{12(\gamma l_2)^2}, \omega \in \Omega, \tag{15}$$

$$a_{min} \le a \le a_{max}, \tag{16}$$

$$b_{min} \le b_1, b_2, b_3 \le b_{max}, \tag{17}$$

where $\alpha, \beta > 0$ are the weighting coefficients, $\alpha + \beta = 1$, $\mathbb{E}(\cdot)$ denotes the expected value, $E(\omega)$ is a random Young's modulus, ω is a random outcome, Ω is a sample space, $c_{rigidity}, c_{weight}$ are typical values of rigidity and weight of the frame (normalizing constants), ρ is the beam density, l_1, l_2 are the beam lengths, x, y are the related space coordinates, $f(x)$ is a deterministic symmetric static load, a, b_1, b_2, b_3 are the first-stage decision variables (dimensions of the rectangular cross sections) and $v_1(\omega, x), v_2(\omega, y), v_3(\omega, y)$ are the second-stage decision variables (deflections). More precisely, the deflections depend on a, b_1, b_2, b_3, i.e. $v_1(\omega, a, b_1, b_2, b_3, x)$, $v_2(\omega, a, b_1, b_2, b_3, y)$, $v_3(\omega, a, b_1, b_2, b_3, y)$, but this notation is not used for the clarity of the text.

Transverse deflections of the beams in the structure are described by the ODEs (2)-(4). The boundary conditions for clamped end points given by (6) and (7) mean that there are zero transverse deflections and their slopes. Because only small deformations with respect to the dimensions of the beams are assumed, the theory of linear elasticity is used and, therefore, there are zero transverse deflections in the beam connections, see the constraints (5)-(7). The beam connections are solid, i.e. the right angles must be preserved during the deflection, see the constraints (8)-(9). Furthermore, the bending moments given as $M(x) = -EJ\frac{\mathrm{d}^2 v}{\mathrm{d}x^2}(x)$, $M(y) = -EJ\frac{\mathrm{d}^2 v}{\mathrm{d}y^2}(y)$ ($J = \frac{ab^3}{12}$ is the second moment of the rectangular cross section) must be the same in the beam connections, see the constraints (10)-(11). The maximum value of the stress must be bounded for safety reasons. The horizontal beam is influenced only by bending moment, see the constraint (12), but the vertical beams are pressure and bending loaded, see the constraints (13)-(14). The limiting value σ_{limit} relates to the proportional limit which marks the end of the area of elastic behaviour described by Hooke's law [10]. Also, the buckling stability conditions must be added for the vertical beams, see (15), where γ is the effective length factor and γl_2 is the effective length of the vertical beams. Finally, the dimensions of the beam cross section must be bounded, see (16) and (17).

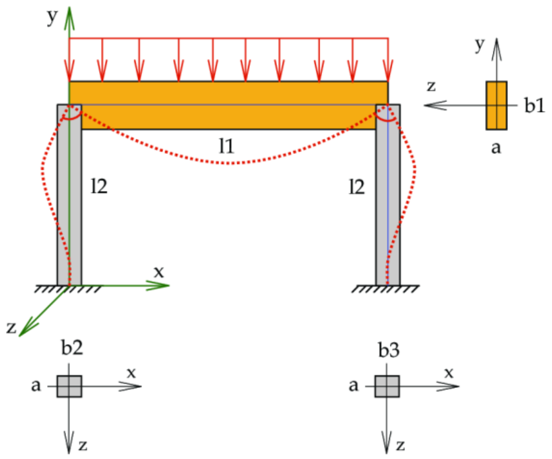

Fig. 1 – Scheme of the loaded frame structure and its cross sections with dimensions to optimize

Approximation

The approximation of the above-mentioned continuous stochastic program is made in two steps. First, a scenario-based approach for a random variable approximation is used, see e.g. [11], [12]. It is assumed that the random Young's modulus $E(\omega)$ has a discrete probability distribution with a finite number R of equiprobable scenarios $E(\omega_s)$ with the corresponding probabilities $p_s = P(\{\omega_s\}) = \frac{1}{R},\ s = 1, \dots, R$.

The second step consists of discretizing the space coordinates x and y in the constraints. A simple finite difference method (see e.g. [13]) with a uniform grid spacing is used: $x_i = id, i = 0, \dots, N$,
$y_j = jh, j = 0, \dots, M, d = \frac{l_1}{N}, h = \frac{l_2}{M}$. Derivatives are replaced by the central difference formulas and difference equations are obtained. The following notation is used: $v_1(\omega, x_i) = v_{1,s,i}$, $V_{1,s,i} \approx v_{1,s,i}$, ...

CHANCE CONSTRAINT

A very important issue regarding the engineering design is its reliability. Therefore, the so-called individual chance constraint (or probabilistic constraint) [11] is included in the model to ensure higher reliability. In the context of this paper, the reliability of the design will mean that the constraint limiting the maximum deflection of the horizontal beam should hold with high probability:

$$P(\max_{x} v_1(\omega, x) \le A) \ge 1 - \varepsilon, \tag{18}$$

where A is the given limiting value for the maximum deflection of the horizontal beam.

Analytical approach

For the given deterministic load $f(x) = -f_0$, the following formula for the maximum deflection of the horizontal beam can be derived:

$$v_{1,max}(\omega) = \frac{C}{E(\omega)}, C = \frac{f_0 l_1^4 (15 l_2^2 b_1^6 + 8 l_1 l_2 b_1^3 b_2^3 + 8 l_1 l_2 b_1^3 b_3^3 + 4 l_1^2 b_2^3 b_3^3)}{32 a b_1^3 (3 l_2^2 b_1^6 + 4 l_1 l_2 b_1^3 b_2^3 + 4 l_1 l_2 b_1^3 b_3^3 + 4 l_1^2 b_2^3 b_3^3)}. \tag{19}$$

It means that the maximum deflection $v_{1,max}(\omega)$ is the transformed random variable. The uniformly distributed Young's modulus is assumed, i.e. $E \sim U(E_{min}, E_{max})$, and the distribution function of the random variable $v_{1,max}(\omega)$ can be obtained:

$$F_{v_{1,max}}(z) = \begin{cases} 0, z \le \dfrac{C}{E_{max}}, \\ \dfrac{1}{E_{max} - E_{min}} \left(E_{max} - \dfrac{C}{z} \right), \dfrac{C}{E_{max}} \le z \le \dfrac{C}{E_{min}}, \\ 1, z \ge \dfrac{C}{E_{min}}. \end{cases} \tag{20}$$

The left-hand side of the chance constraint (18) can be written as $P\left(\max_{x} v_1(\omega, x) \le A\right) = F_{v_{1,max}}(A)$, and therefore, the chance constraint (18) in the analytical form is the following:

$$\frac{1}{E_{max} - E_{min}} \left(E_{max} - \frac{C}{A} \right) \ge 1 - \varepsilon. \tag{21}$$

This analytical approach can usually be used only for simple problems when it is possible to derive the corresponding distribution function. For more complex cases, another approach must be used to solve chance constrained problems.

Penalty reformulation

An appropriate penalty function ν [14] is used to reformulate the chance constrained problem (1)-(18):

$$\min_{a,b_1,b_2,b_3,v_1,v_2,v_3} \begin{array}{l} -\alpha\mathbb{E}\left(\frac{E(\omega)ab_1^3+E(\omega)ab_2^3+E(\omega)ab_3^3}{12c_{rigidity}}\right)+\beta\frac{\rho ab_1l_1+\rho ab_2l_2+\rho ab_3l_2}{c_{weight}} \\ +M_{pen}\mathbb{E}\left(\nu\left(\max_x v_1(\omega,x)-A\right)\right), \end{array} \tag{22}$$

where $\nu:\mathbb{R}\to\mathbb{R}_0^+$ is a continuous nondecreasing function equal to 0 on $\mathbb{R}_0^-$ and positive otherwise, M_{pen} is a penalty coefficient. Frequently used penalty function [15] is $\nu(s)=(\max(0,s))^2$ (see Equation (23)).

Hence, the approximation of the nonlinear continuous two-stage chance constrained stochastic program is given by the following nonlinear deterministic program:

$$\min_{\substack{a,b_1,b_2,b_3,\\ \mathbf{V}_{1,s},\mathbf{V}_{2,s},\mathbf{V}_{3,s}}} \begin{pmatrix} -\alpha\sum_{s=1}^{R}p_s\frac{E_sab_1^3+E_sab_2^3+E_sab_3^3}{12c_{rigidity}}+\beta\frac{\rho ab_1l_1+\rho ab_2l_2+\rho ab_3l_2}{c_{weight}} \\ +M_{pen}\sum_{s=1}^{R}p_s(\max(0,\max_i V_{1,s,i}-A))^2 \end{pmatrix} \tag{23}$$

s. t.

$$ab_1^3E_s(\mathbb{K}\mathbf{V}_{1,s}+2d\boldsymbol{\varphi}_{1,s})=\mathbf{f}, s=1,\dots,R, \tag{24}$$

$$ab_2^3E_s(\mathbb{K}\mathbf{V}_{2,s}+2h\boldsymbol{\varphi}_{2,s})=\mathbf{0}, s=1,\dots,R, \tag{25}$$

$$ab_3^3E_s(\mathbb{K}\mathbf{V}_{3,s}-2h\boldsymbol{\varphi}_{2,s})=\mathbf{0}, s=1,\dots,R, \tag{26}$$

$$V_{1,s,0}=0, V_{1,s,N}=0, V_{2,s,0}=0, V_{2,s,M}=0, V_{3,s,0}=0, V_{3,s,M}=0, s=1,\dots,R, \tag{27}$$

$$\varphi_{1,s}=\varphi_{2,s}, s=1,\dots,R, \tag{28}$$

$$\frac{ab_1^3E_s(2V_{1,s,1}+2d\varphi_{1,s})}{12d^2}=-\frac{ab_2^3E_s(2V_{2,s,M-1}+2h\varphi_{2,s})}{12h^2}, s=1,\dots,R, \tag{29}$$

$$\frac{ab_1^3E_s(2V_{1,s,N-1}+2d\varphi_{1,s})}{12d^2}=\frac{ab_2^3E_s(2V_{3,s,M-1}-2h\varphi_{2,s})}{12h^2}, s=1,\dots,R, \tag{30}$$

$$|b_1E_s(\mathbb{C}\mathbf{V}_{1,s}+d\boldsymbol{\varphi}_{1,s}^*)|\le d^2\sigma_{limit}\mathbf{g}, s=1,\dots,R, \tag{31}$$

$$\left|\frac{b_2E_s}{2h^2}(\mathbb{C}\mathbf{V}_{2,s}+h\boldsymbol{\varphi}_{2,s}^*)+\frac{f_0l_1}{2ab_2}\mathbf{1}\right|\le\sigma_{limit}\mathbf{1}, s=1,\dots,R, \tag{32}$$

$$\left|\frac{b_3E_s}{2h^2}(\mathbb{C}\mathbf{V}_{3,s}-h\boldsymbol{\varphi}_{2,s}^*)+\frac{f_0l_1}{2ab_2}\mathbf{1}\right|\le\sigma_{limit}\mathbf{1}, s=1,\dots,R, \tag{33}$$

$$\frac{f_0l_1}{2}\le\frac{\pi^2E_sab_2^3}{12(\gamma l_2)^2}, \frac{f_0l_1}{2}\le\frac{\pi^2E_sab_3^3}{12(\gamma l_2)^2}, s=1,\dots,R, \tag{34}$$

$$a_{min}\le a\le a_{max}, b_{min}\le b_1,b_2,b_3\le b_{max}, \tag{35}$$

where $\mathbf{V}_{1,s} = (V_{1,s,1}, \dots, V_{1,s,N-1})^{\mathrm{T}}$, $\mathbf{V}_{2,s} = (V_{2,s,1}, \dots, V_{2,s,M-1})^{\mathrm{T}}$, $\mathbf{V}_{3,s} = (V_{3,s,1}, \dots, V_{3,s,M-1})^{\mathrm{T}}$ are the approximations of $v_1(\omega, x)$, $v_2(\omega, y)$, $v_3(\omega, y)$, $\mathbb{K} = \begin{pmatrix} 7 & -4 & 1 & 0 & 0 & \dots & 0 \\ -4 & 6 & -4 & 1 & 0 & \dots & 0 \\ 1 & -4 & 6 & -4 & 1 & \dots & 0 \\ & & & \vdots & & & \\ 0 & \dots & 1 & -4 & 6 & -4 & 1 \\ 0 & \dots & 0 & 1 & -4 & 6 & -4 \\ 0 & \dots & 0 & 0 & 1 & -4 & 7 \end{pmatrix}$ is a square matrix of order $N-1$, $\mathbb{C} = \begin{pmatrix} 1 & 0 & 0 & \dots & 0 \\ -2 & 1 & 0 & \dots & 0 \\ 1 & -2 & 1 & \dots & 0 \\ & & \vdots & & \\ 0 & \dots & 1 & -2 & 1 \\ 0 & \dots & 0 & 1 & -2 \\ 0 & \dots & 0 & 0 & 1 \end{pmatrix}$ is a matrix of order $(M+1) \times (M-1)$, $\mathbf{f} = (12d^4 f_1, \dots, 12d^4 f_{N-1})^{\mathrm{T}}$, $\boldsymbol{\varphi}_{1,s} = (\varphi_{1,s}, 0, \dots, 0, \varphi_{1,s})^{\mathrm{T}}$ is a $(N-1)$ dimensional vector, $\boldsymbol{\varphi}_{2,s} = (0,0,\dots,0,\varphi_{2,s})^{\mathrm{T}}$ is a $(M-1)$ dimensional vector, $\boldsymbol{\varphi}^*_{1,s} = (\varphi_{1,s}, 0, \dots, 0, \varphi_{1,s})^{\mathrm{T}}$, $\mathbf{g} = (1,2,2,\dots,2,2,1)^{\mathrm{T}}$ are $(N+1)$ dimensional vectors, $\boldsymbol{\varphi}^*_{2,s} = (0,0,\dots,0,\varphi_{2,s})^{\mathrm{T}}$, $\mathbf{1} = (1,\dots,1)^{\mathrm{T}}$ are $(M+1)$ dimensional vectors.

For the analytical approach, the resulting model differs in the objective function (penalty term is removed from Equation (23)) and Equation (21) is added to model the chance constraint (18).

NUMERICAL STUDY

The results are presented for the following input data. The number of grid points are $N = 50$, $M = 50$, the number of scenarios is $R = 25, 100, 200$. The load is constant: $f(x) = -f_0$, $f_0 = 10$ Nmm^{-1}. The lengths of the steel beams are $l_1 = l_2 = 1000$ mm, their density is $\rho = 7.85 \cdot 10^{-9}$ tmm^{-3}. The stress limit is $\sigma_{limit} = 100$ MPa. The limiting values of the beam dimensions are $a_{min} = b_{min} = 10$ mm, $a_{max} = b_{max} = 100$ mm. The random Young's modulus is uniformly distributed: $E_s \sim U(200 \cdot 10^3, 230 \cdot 10^3)$ MPa. The weighting coefficients are $\alpha = 0.5$, $\beta = 0.5$ and the normalizing constants are $c_{rigidity} = 5.25 \cdot 10^{12}$ Nmm^2, $c_{weight} = 0.009$ t. The limiting value is $A = 0.9$ mm.

Both programs (using analytical approach and penalty reformulation) are implemented in GAMS with solver CONOPT and ran on a PC with Intel Core i7 CPU 860 2.8GHz and 8GB RAM.

Tab. 1 - Summary of the analytical approach results

Reliability	**R=25** Opt.solution [mm]			**Obj.**	**R=100** Opt.solution [mm]			**Obj.**	**R=200** Opt.solution [mm]			**Obj.**
$1-\varepsilon$	a	b_1	$b_2 = b_3$	**value**	a	b_1	$b_2 = b_3$	**value**	a	b_1	$b_2 = b_3$	**value**
0.2	10	91.72	12.82	0.4987	10	91.72	12.86	0.4991	10	91.72	12.86	0.4991
0.4	10	92.56	12.82	0.5020	10	92.56	12.86	0.5023	10	92.56	12.86	0.5024
0.6	10	93.43	12.82	0.5054	10	93.43	12.86	0.5058	10	93.43	12.86	0.5058
0.8	10	94.33	12.82	0.5089	10	94.33	12.86	0.5093	10	94.33	12.86	0.5093
0.9	10	94.80	12.82	0.5107	10	94.80	12.86	0.5111	10	94.80	12.86	0.5111
0.99	10	95.22	12.82	0.5124	10	95.22	12.86	0.5128	10	95.22	12.86	0.5128
0.9999	10	95.27	12.82	0.5126	10	95.27	12.86	0.5129	10	95.27	12.86	0.5130
1	10	95.27	12.82	0.5126	10	95.27	12.86	0.5130	10	95.27	12.86	0.5130

Table 1 shows the summary of the analytical approach results. More precisely, the influence of the right-hand side $1-\varepsilon$ of the chance constraint (18) on the optimal dimensions for three different number of scenarios R is shown. There is a little difference only in dimensions b_2 and b_3 for different R.

The point estimate of probability (P.E. of probability.) in Table 2 is computed as the relative frequency of the event $\max_x v_1(\omega, x) \leq A$. The summary of the penalty reformulation results is presented in Table 2 shows the influence of the penalty coefficient value M_{pen} on the optimal dimensions and also on the probability of satisfying $\max_x v_1(\omega, x) \leq A$ for three different number of scenarios R. With an increasing penalty coefficient, the dimension b_1 and also the rigidity of the beam increase, and its deflection decreases. Therefore, the probability of satisfying $\max_x v_1(\omega, x) \leq A$ must also increase, as can be seen in Figure 2.

Tab. 2 - Summary of the penalty reformulation results

Penalty coeff.	**R=25**				**R=100**				**R=200**			
	Opt.solution [mm]			**P.E. of**	**Opt.solution [mm]**			**P.E. of**	**Opt.solution [mm]**			**P.E. of**
M_{pen}	a	b_1	$b_2 = b_3$	**probab.**	a	b_1	$b_2 = b_3$	**prob.**	a	b_1	$b_2 = b_3$	**probab.**
0.5	10	89.56	12.82	0.00	10	89.65	12.86	0.00	10	89.67	12.86	0.000
0.7	10	90.47	12.82	0.00	10	90.56	12.86	0.00	10	90.58	12.86	0.000
0.9	10	91.02	12.82	0.08	10	91.11	12.86	0.04	10	91.13	12.86	0.045
1	10	91.24	12.82	0.08	10	91.32	12.86	0.06	10	91.35	12.86	0.070
5	10	93.36	12.82	0.48	10	93.45	12.86	0.45	10	93.48	12.86	0.490
10	10	93.82	12.82	0.60	10	93.93	12.86	0.64	10	93.99	12.86	0.635
50	10	94.44	12.82	0.76	10	94.60	12.86	0.83	10	94.65	12.86	0.830
100	10	94.57	12.82	0.84	10	94.77	12.86	0.90	10	94.83	12.86	0.895
1000	10	94.90	12.82	0.96	10	95.09	12.86	0.97	10	95.13	12.86	0.965
10000	10	94.95	12.82	0.96	10	95.23	12.86	0.99	10	95.23	12.86	0.985
50000	10	94.96	12.82	0.96	10	95.25	12.86	0.99	10	95.25	12.86	0.990
10^7	10	94.96	12.82	0.96	10	95.25	12.86	0.99	10	95.25	12.86	0.995

The comparison of the analytical approach and the penalty reformulation is made for $R = 200$ scenarios. Several values of the penalty coefficients corresponding to the selected reliabilities are determined using the graph in Figure 3. The solutions for both approaches are quite comparable (see Table 3). Also, the computational times are similar (~ 8 min). The penalty reformulation is useful for more complex problems when the analytical approach cannot be used.

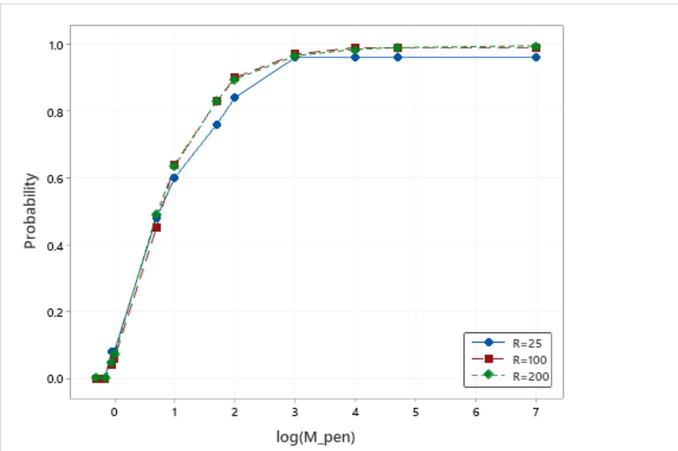

Fig. 2 – Probability of satisfying the constraint $\max_x v_1(\omega, x) \leq A$

DOI 10.14311/CEJ.2025.01.0001

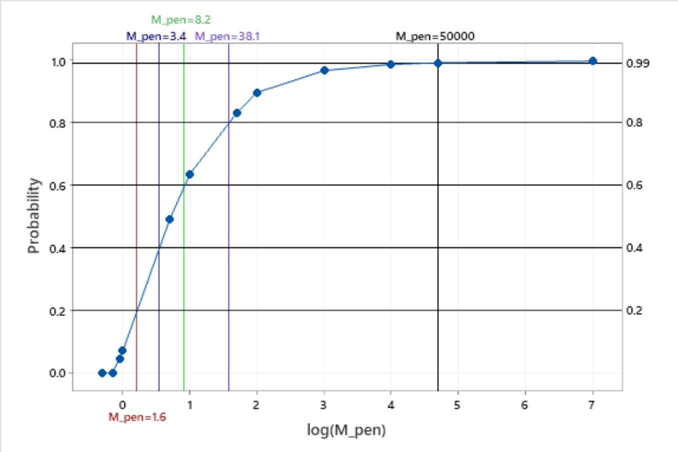

Fig. 3 – Determining the penalty coefficients for $R = 200$

Tab. 3 - Comparison of the analytical approach and penalty reformulation for $R = 200$

Reliability	Analytical approach				Penalty reformulation				***Penalty***
	Optimal solution [mm]			Objective	Optimal solution [mm]			Objective	***coeff.***
$1-\varepsilon$	a	b_1	$b_2 = b_3$	value	a	b_1	$b_2 = b_3$	value	M_{pen}
0.2	10	91.72	12.86	0.4991	10	92.15	12.86	0.5047	1.6
0.4	10	92.56	12.86	0.5024	10	93.12	12.86	0.5073	3.4
0.6	10	93.43	12.86	0.5058	10	93.86	12.86	0.5092	8.2
0.8	10	94.33	12.86	0.5093	10	94.56	12.86	0.5111	38.1
0.99	10	95.22	12.86	0.5128	10	95.24	12.86	0.5129	50000

RELIABILITY CHECK

A disadvantage of the penalty reformulation is that the reliability $1-\varepsilon$ from the chance constraint (18) is not involved in the model. Therefore, it would be useful to make an a posteriori check of satisfying this constraint.

First, the penalty reformulated problem with a smaller sample to yield a candidate first-stage solution $\hat{a}, \hat{b}_1, \hat{b}_2, \hat{b}_3$ is solved. Then, this solution is fixed and an a posteriori check is conducted (see [16], [17]) to see if $P\left(\max_x v_1(\omega, x) \leq A\right) \geq 1-\varepsilon$. Very large Monte Carlo sample $E(\omega_1), \ldots, E(\omega_{R'})$ is taken, and it is calculated how many times the maximum deflection is smaller than the given limit, i.e. $\sum_{s=1}^{R'} \mathbb{I}\,(\max_i V_{1,s,i} \leq A)$. This number is denoted as r. The random variable $Y \sim Bi(R', p)$ expresses the number of experiment realizations when the random event $\max_x v_1(\omega, x) \leq A$ occurs, i.e. $p = P(\max_x v_1(\omega, x) \leq A)$. And now, the lower bound of the risk level ε, for which the chance constraint (18) is still satisfied with the given confidence level $1-\delta$, can be determined.

The following statistical hypotheses must be tested: null hypothesis $H_0\!: p < 1-\varepsilon$ and alternative hypothesis $H_1\!: p \geq 1-\varepsilon$. The observed value of the test statistic is $z = \frac{\frac{r}{R'} - (1-\varepsilon)}{\sqrt{\frac{(1-\varepsilon)(1-(1-\varepsilon))}{R'}}}$. The critical region is $C = \langle u_{1-\delta}, \infty)$ where $u_{1-\delta}$ is the $(1-\delta)$-quantile of the standard normal distribution. If $z \in C$, H_0 is rejected and H_1 is not rejected at the significance level δ, i.e. the solution is accepted as feasible. To obtain the lower bound of the risk level ε, the following equation must be solved:

$$\frac{\frac{r}{R'} - (1-\varepsilon)}{\sqrt{\frac{(1-\varepsilon)(1-(1-\varepsilon))}{R'}}} = u_{1-\delta}. \tag{36}$$

The lower bound of the risk level ε, for which the chance constraint is still satisfied, i.e. the solution is accepted as feasible, with confidence $1-\delta$ is $\bar{\varepsilon}$:

$$\bar{\varepsilon} = \frac{2(R'-r) + u_{1-\delta}^2 + \sqrt{4ru_{1-\delta}^2 + u_{1-\delta}^4 - \frac{4r^2u_{1-\delta}^2}{R'}}}{2(R' + u_{1-\delta}^2)}. \tag{37}$$

The upper bound of the obtainable reliability $1-\varepsilon$ with confidence $1-\delta$ is $1-\bar{\varepsilon}$.

If R' is a very large number ($R' = 50000$ is used in this case), it is impossible to solve the optimization problem directly. However, the objective function (23) is separable for fixed a, b_1, b_2, b_3:

$$\beta \frac{\rho a(b_1 l_1 + b_2 l_2 + b_3 l_2)}{c_{weight}} + \\ + \sum_{s=1}^{R} \min_{\mathbf{V}_s} \left[-\alpha p_s \frac{E_s a(b_1^3 + b_2^3 + b_3^3)}{12 c_{rigid}} + M_{pen} p_s (\max(0, \max_i V_{1,s,i} - A))^2 \right]. \tag{38}$$

It is advantageous for a multi-core processor to compute the problem in parallel because the speed-up of the computations. The upper bounds of the obtainable reliability $1-\varepsilon$ for different penalty coefficients M_{pen} are presented in Table 4 and Figure 4. The confidence level is $1-\delta = 0.999$.

Tab. 4 - Summary of the reliability check

Penalty coeff.	**R=25** Opt.solution [mm]			**Upp.b.**	**R=100** Opt.solution [mm]			**Upp.b.**	**R=200** Opt.solution [mm]			**Upp.b.**
M_{pen}	a	b_1	$b_2 = b_3$	**of** $1-\varepsilon$	a	b_1	$b_2 = b_3$	**of** $1-\varepsilon$	a	b_1	$b_2 = b_3$	**of** $1-\varepsilon$
0.5	10	89.56	12.82	0.0000	10	89.65	12.86	0.0000	10	89.67	12.86	0.0000
0.7	10	90.47	12.80	0.0000	10	90.56	12.86	0.0000	10	90.58	12.86	0.0000
0.9	10	91.02	12.82	0.0223	10	91.11	12.86	0.0452	10	91.13	12.86	0.0429
1	10	91.24	12.82	0.0753	10	91.32	12.86	0.0958	10	91.35	12.86	0.1144
5	10	93.36	12.82	0.5746	10	93.45	12.86	0.5954	10	93.48	12.86	0.6067
10	10	93.82	12.82	0.6766	10	93.93	12.86	0.7017	10	93.99	12.86	0.7171
50	10	94.44	12.82	0.8147	10	94.60	12.86	0.8499	10	94.65	12.86	0.8720
100	10	94.57	12.82	0.8432	10	94.77	12.86	0.8871	10	94.83	12.86	0.8935
1000	10	94.90	12.82	0.8971	10	95.09	12.86	0.9565	10	95.13	12.86	0.9589
10000	10	94.95	12.82	0.8971	10	95.23	12.86	0.9888	10	95.23	12.86	0.9814
50000	10	94.96	12.82	0.8971	10	95.25	12.86	0.9935	10	95.25	12.86	0.9935
10^7	10	94.96	12.82	0.8971	10	95.25	12.86	0.9941	10	95.25	12.86	0.9941

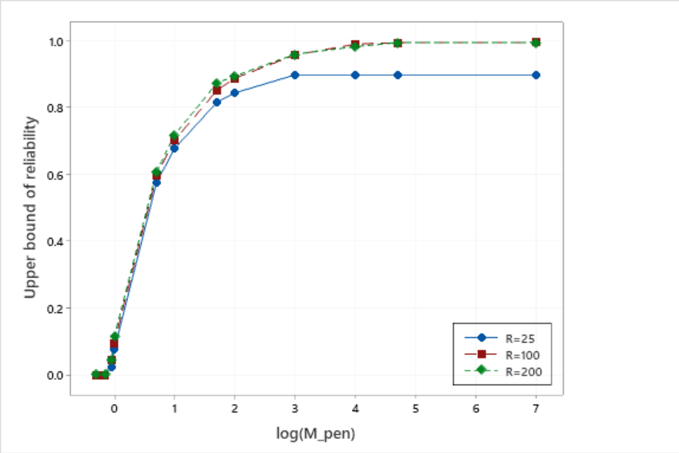

Fig. 4 – Upper bound of the obtainable reliability $1-\varepsilon$

CONCLUSION

The applicability of the chance constrained stochastic programming approach to the civil engineering problem (a frame structure design) with a random parameter (Young's modulus) has been discussed. It has been shown that the chance constraint relates to the reliability of the structure. Two possible approaches have been used – the analytical approach and penalty reformulation. Both approaches have provided comparable solutions. Unlike the analytical approach, the penalty reformulation is applicable also for more complex problems. An a posteriori check of satisfying the chance constraint has been made, and the upper bounds of the obtainable reliability have been computed for different number of scenarios and penalty coefficients. Further research should focus on reaching higher reliability and also on problems with more random variables and joint chance constraints.

ACKNOWLEDGEMENTS

The paper was supported by the project of specific research FSI-S-23-8161.

REFERENCES

[1] Plšek J., Štěpánek P., Popela P., 2007. Deterministic and reliability based structural optimization of concrete cross-section. Jornal of Advanced Concrete Technology, vol. 5: 63–74. DOI:10.3151/jact.5.63
[2] Laníková I., Štěpánek P., Šimůnek P., 2014. Optimized design of concrete structures considering environmental aspects. Advances in Structural Engineering, vol. 17, no. 4: 495-511. DOI:10.1260/1369-4332.17.4.495
[3] Venclovský J., Štěpánek P., Laníková I., 2018. Stochastic optimization of reinforces concrete elements using heuristic algorithm. In: Proceedings of the 24th Concrete Days 2017. Solid State Phenomena, vol. 272: 262-269. DOI:10.4028/www.scientific.net/SSP.272.262
[4] Žampachová E., 2010. Approximations in stochastic optimization and their applications. Ph.D. thesis (Brno University of Technology) 95 pp.
[5] Žampachová E., Popela P., Mrázek M., 2010. Optimum beam design via stochastic programming. Kybernetika, vol. 46, no. 3: 571–582
[6] Žampachová E., Popela P., 2012. Two approaches to multi-criteria stochastic programming in beam design problem. In: Proceedings of the 18th International Conference of Soft Computing MENDEL 2012. Mendel Journal series: 393-397
[7] Žampachová E., Mrázek M., 2010. Stochastic optimization in beam design and its reliability check. In: Proceedings of the 16th International Conference of Soft Computing MENDEL 2010. Mendel Journal series: 405-410

[8] Kůdela J., Popela P., 2018. Chance constrained optimal beam design: Convex reformulation and probabilistic robust design. Kybernetika, vol. 54, no. 6: 1201-1217. DOI:10.14736/kyb-2018-6-1201

[9] Steuer R.E., 1986. Multiple Criteria Optimization: Theory, Computation and Application (New York: John Wiley) 546 pp. DOI:10.1002/oca.4660100109

[10] Oberg E., Jones F.D., Horton H., Ryffel H., McCauley C., 2020. Machinery's Handbook (Industrial Press). 2996 pp.

[11] Ruszczynski A., Shapiro, A. (eds.), 2003. Handbooks in Operations Research and Management Science, vol.10: Stochastic Programming (Amsterdam: Elsevier) 682 pp.

[12] Birge J., Louveaux F., 1997. Introduction to Stochastic Programming (New York: Springer) 485 pp. DOI:10.1007/978-1-4614-0237-4

[13] Mathews J.H., Fink K.D., 2004. Numerical Methods using Matlab (New Jersey: Pearson Prentice Hall) 696 pp.

[14] Branda M., Dupačová J., 2012. Approximations and contamination bounds for probabilistic programs. Annals of Operations Research, vol. 193, no.1: 3-19. DOI: 10.1007/s10479-010-0811-1

[15] Bazaraa M.S., Sherali H.D., Shetty C.M., 2005. Nonlinear programming: Theory and Algorithms. (New York: Wiley and Sons) 853 pp. DOI:10.1002/0471787779

[16] Luedtke J., Ahmed S., 2008. A sample approximation approach for optimization with probabilistic constraints. SIAM Journal on Optimization, vol. 19, no. 2: 674-699. DOI:10.1137/070702928

[17] Pagnoncelli B.K., Ahmed S., Shapiro A., 2009. Sample average approximation method for chance constrained programming: Theory and applications. Journal of Optimization Theory and Applications, vol. 142: 399-416. DOI:10.1007/s10957-009-9523-6

AN ANALYTICAL INVESTIGATION ON NONLINEAR FREE VIBRATIONS OF BEAM WITH A FATIGUE-CRACK

Qiang Li [1,2] and Qingze Tian [1,2]

1. *School of Intelligent Manufacturing, Taizhou University, Taizhou 318000, China; liqiang1988@tzc.edu.cn*
2. *Institute of Robotics and Intelligent Systems, Taizhou University, Taizhou 318000, China; tianqingze92@gmail.com*

Received: *22.06.2024*
Received in revised form: *09.01.2025*
Accepted: *11.03.2025*

ABSTRACT

This study examines the nonlinear free vibration behavior of beams affected by a fatigue crack. Initially, transverse vibrations of a cantilevered beam are demonstrated as a single-degree-of-freedom system with equivalent mass and stiffness in the first mode. Subsequently, a novel bilinear stiffness model for beams with breathing cracks is introduced. Utilizing this model, the governing differential formula is formulated analytically using the Lindest-Poincaré perturbation method. The results indicate that the response derived through the perturbation method comprises 2 distinct components. With stiffness equal to the mean of the crack's completely open and fully closed states, the first component depicts the system's reaction. The additional correction terms, supplementing the initial response, account for variations in stiffness resulting from crack opening and closing dynamics. These corrections elucidate the impact of changing equivalent stiffness on the system's response due to crack dynamics. Indeed, the correction terms encompass higher harmonic components that emerge in the response, stemming from the nonlinear behavior of the structure. These additional terms capture the intricate interplay between crack dynamics and system response, providing a comprehensive understanding of the system's nonlinear characteristics.

KEYWORDS

Nonlinear vibration, Fatigue-crack, Bilinear stiffness, Natural frequency, Analytical method

INTRODUCTION

Fatigue cracks frequently manifest in structural components subjected to repetitive loads, posing a risk of failure if left undetected. Studies indicate distinguishable dynamic responses between defective and healthy structures, offering a potential avenue for detecting defects such as crack depth and location by quantifying these differences based on a model of the defective structure [1-3]. The majority of research in this area relies on linear models, where structural cracks are typically represented as continuously open grooves. In these models, alterations in natural frequencies and vibration mode shapes serve as primary indicators for detecting defects within the structure [4-7].

Dynamic analysis of cracked configurations holds promise as a valuable indicator for diagnosing faults. By examining the nonlinear behavior of vibrations, such as changes in frequency, amplitude, or mode shapes, engineers can detect and characterize structural defects, including cracks [8-10]. Vibration analysis offers advantages over traditional linear approaches, as it can reveal subtle changes in structural behavior that may indicate the presence of defects even in their early stages [11-13]. Therefore, leveraging vibration analysis can enhance the accuracy and effectiveness of defect diagnosis in structures. In the context of crack modeling, numerous researchers have explored various models. For example, Rezaee and Maleki [14] examined the nonlinear behavior of a beam containing both open and closed cracks within its primary vibration mode. To this end, by some realistic presumptions, novel functions for displacement and stress fields are recommended. Peng et al. [15] performed an exploration focusing on the nonlinear characteristics of cracks through employing nonlinear output frequency response functions. Their analysis discerned that these graphs, elicited by system stimulation at optimal frequencies, exhibit pronounced sensitivity towards the detection of fatigue-induced cracks. Kharazan et al. [16] explore the nonlinear dynamics behavior of a cantilever beam affected by multiple breathing cracks. Their approach involves calculating the stiffness of a multi-cracked beam by introducing the concept of effective length to accommodate local stiffness reduction near cracks. Their research reveals that beams with a greater number of cracks or deeper cracks demonstrate significant softening behavior. Consequently, this softening behavior results in more prominent jumps in the system's response. Ma et al. [17] introduced a loose coupling analysis tactic for conducting vibration fatigue analysis on a simply supported beam subjected to typical harmonic excitation. The method assumes that the crack does not propagate during each vibration cycle but rather grows at the end of each cycle. This approach allows for a detailed investigation of the fatigue behavior of the structure under cyclic loading conditions, considering the dynamic effects of crack propagation on the overall system response. Zao et al. [18] conducted a nonlinear forced vibration analysis of an Euler-Bernoulli beam with multi-cracked while incorporating damping effects. Their study aimed to investigate the dynamics of a curved beam afflicted with multiple cracks under external excitation, considering nonlinearities and damping influences. Gaderi et al. [19] explored the dynamic and stability characteristics of cracked columns under axial load. Their study investigated the dynamic response and buckling of cracked columns under axial load. They researched the vibration and stability characteristics of columns with cracks to offer information on the behavior that may be exhibited by such columns, including possible modes of failure, which is vital in ensuring safety and reliability in structural systems for engineering applications. Long et al. [20] were motivated by the necessity for condition monitoring and fault diagnostics of beams employed in vibrating screens within the mining industry. In response to this challenge, they sought to establish a dependable model-based approach. Their focus centered on devising a novel stiffness matrix for a finite element to accurately simulate a beam affected by a breathing crack. Aggumus et al. [21] investigated the effects of cracks in the columns of a single-degree-of-freedom steel structure scheme on system responses, focusing on the reduction in the equivalent spring coefficient. Hai and Nam [22] presented a simplified pattern of a cracked beam using a single-degree-of-freedom system. The equivalence between the beam and SDOF models ensures that they share the same fundamental natural frequency and exhibit similar frequency response functions. Kharazan et al. [16] explored the nonlinear vibration behavior of a cantilever beam with multiple breathing cracks. To achieve this, they calculated the stiffness of the multi-cracked beam by introducing an effective length that accounts for the local stiffness reduction near the cracks. Additionally, Liu et al. [23] proposed a tactic for determining breathing fatigue cracks in compressor blades by leveraging the nonlinear characteristics induced by the cracks.

Although many works recognize the presence of harmonic components in the dynamic response of faulty structures and their sensitivity to crack parameters, the time evolution of system parameters and the analytical explanation of such behavior is a challenging task. Therefore, most of the studies in this field are performed with the help of numerical or finite element methods. Yet their inherent numerical nature and computationally lengthy procedures make such approaches practically inapplicable for definition of dynamic fault indicators within the frames of vibration-based troubleshooting techniques. Recent research has indeed been conducted into the nonlinear dynamics of cracked structures through various methods of modeling. SDOF models have widely been used to simplify the system, while a bilinear stiffness model effectively realizes the dynamic behavior of the crack opening and closing. Perturbation methods, among which the Lindest-Poincaré method is very outstanding, have emerged as powerful tools for studying nonlinear characteristics. However, substantial challenges arise. Most of the existing models fall short of providing an accurate description of the detailed impact of crack dynamics on the harmonic response of the system. Moreover, comprehensive studies that establish analytical relations between crack parameters depth and position-with the ensuing nonlinear behavior are scant. These lacunae indicate the need for more robust models and analytical approaches to enhance the understanding of cracked beam dynamics.

This work seeks to relate the harmonic components present in the frequency spectrum of vibration responses of a cracked beam to both crack parameters and system characteristics analytically, with the help of the Lindest-Poincaré perturbation method. The transverse vibrations of a single-crack beam with open and closed fatigue cracks are modeled as a single-degree-of-freedom oscillator with bilinear stiffness. Accordingly, a new model for bilinear stiffness is presented, and by performing the mathematical operations and using the Lindest-Poincaré method, the governing differential formula is brought to a standard analyzable form. Then, employing the Lindest-Poincaré method, the system response is obtained, and the results are verified using numerical methods. This novelty develops the representative modeling of structural beams with cracks better and allows for better condition monitoring and fault diagnosis of vibrating screens in mining operations.

SDOF MODEL OF A CRACKED BEAM

In this study, an equivalent mass and stiffness SDOF system represents the free vibrations of a cantilever beam displaying a transverse fatigue fracture in its initial vibration mode (Figure 1). This modeling approach is grounded in equating the kinetic and potential energies of the cracked beam with those of the equivalent degree of freedom framework.

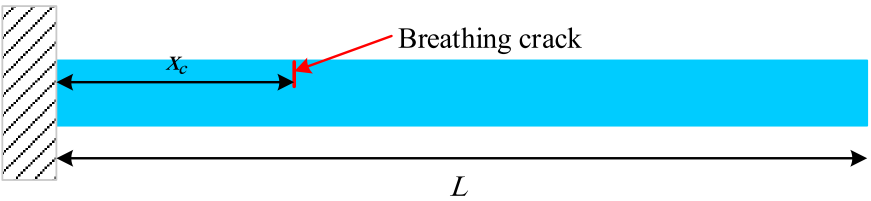

(a)

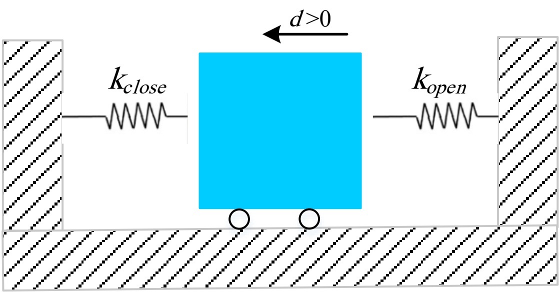

(b)

Fig. 1 - (a) Cantilever beam crack in and (b) the corresponding SDOF model

The studies conducted on fatigue crack behavior display that the non-linear load-displacement relationship of the cracked structure can be considered almost as a bilinear relationship [24] (Figure 2). As a result, when the beam vibrates, by changing the state of the crack between completely open and completely closed states, the equivalent stiffness changes between the equivalent stiffness values corresponding to these states.

DOI 10.14311/CEJ.2025.01.0002

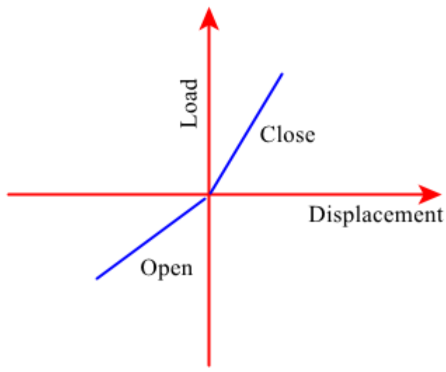

Fig. 2 - Fatigue crack in the fractured beam's bilinear load-displacement diagram.

The bilinear stiffness model, which consists of the combination of 2 lines with different slopes, is a function of the oscillation amplitude and is expressed as follows:

$$k(d) = \begin{cases} k_{close} & d > 0 \\ k_{open} & d < 0 \end{cases} \tag{1}$$

Where the comparable stiffnesses in the completely open and fully closed crack states are represented, respectively, by the variables k_{open} and k_{close}. The equivalent stiffness of an intact beam is derived according to:

$$k_c = \frac{1}{C_c} = \int_0^L EI\varphi''^2(x)dx \tag{2}$$

In this equation, C_c stands for the flexibility of a healthy structure, E is elastic modulus, I stands for the cross-section moment and L is the length. It is supposed that by applying suitable initial conditions, the beam vibrates in the first mode, so the mode shape of the first vibration of the beam is monotonous. Mukhopadhyay [25] has proposed the following approximate relationship to calculate the form of the first vibration mode of a cantilever beam:

$$\psi(x) = 1 - cos\left(\frac{\pi}{2}\frac{x}{L}\right) \tag{3}$$

In most of the research in this field, the above relationship has been used to derive the equivalent mass and stiffness of the system. In this research, to increase the accuracy, the shape of vibration modes of the Euler-Bernoulli beam, which are obtained from the analytical solution of the equations of motion below, have been used:

$$\varphi(x) = cos\,\beta\,x - cosh\,\beta\,x - \frac{(sin\,\beta\,x - sinh\,\beta\,x)(cos\,\beta\,L + cosh\,\beta\,L)}{(sin\,\beta\,L + sinh\,\beta\,L)} \tag{4}$$

In the above equation, the shape of the first vibration mode is obtained $\lambda L = 1.875$. Figure 3 shows the disparity between the analytical mode shape used in the current research and the approximate mode shape proposed in Ref. [25].

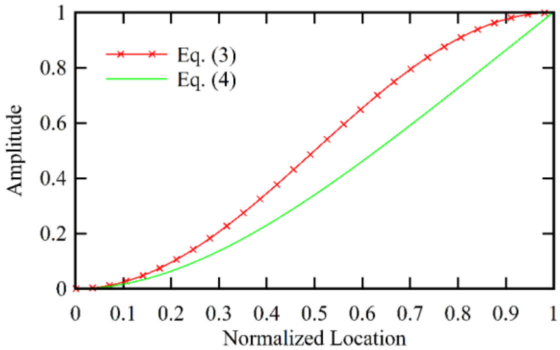

Fig. 3 - The initial mode form of a clamped-free beam, derived from the approximation function suggested in Ref. [19] *and the analytical resolution of the Euler-Bernoulli beam motion equations*

The equivalent stiffness with a completely open crack is obtained from the following relationship:

$$k_{\circ} = \frac{1}{C_{\circ}} \tag{5}$$

When the existence of fractures causes a change in the beam's flexibility (ΔC), expressed as $C_{\circ} = \Delta C + C$. Dimarogonas et al. [26] have presented the following relationship to determine the change in the flexibility of a cantilever beam owing to the presence of cracks deep and at a distance from the free end of the beam:

$$\Delta C = w\frac{\partial^2}{\partial {P_i}^2}\int_0^a J da = \frac{72 l_c^2 \pi (1-\nu^2)}{E w b^4}\phi \tag{6}$$

In which, *b* and *w* denote the height and width, *J* remains the strain energy release rate and *v* is Poisson's ratio, and ϕ is obtained from the following relationship:

$$\begin{gathered}\phi = \ 19.70\frac{a^{10}}{b^8} - 40.64\frac{a^9}{b^7} + 47.45\frac{a^8}{b^6} - 32.78\frac{a^7}{b^5} + 20.89\frac{a^6}{b^4} - 9.68\frac{a^5}{b^3} \\ +4.45\frac{a^4}{b^2} - 1.06\frac{a^3}{b} + 0.67a^2\end{gathered} \tag{7}$$

The equivalent mass of the beam is obtained as:

$$m = \int_0^L \varphi^2(x) m(x) dx \tag{8}$$

In which *m*(*x*) stands the unit mass. According to the above assumptions, the governing differential equation of the equivalent system is obtained below:

$$m\ddot{x} + k(x)x = 0 \tag{9}$$

Where *x* displays the displacement of the beam and relates to the displacement of the beam's free end.

PRESENTING A NEW MODEL FOR BILINEAR STIFFNESS OF THE CRACKED BEAM

It has been shown that if the differential equation governing a nonlinear dynamic system can be expressed in the form of Eq. (10), its answer can be obtained using the Lindest-Poincaré method, which is one of the perturbation methods [27].

DOI 10.14311/CEJ.2025.01.0002

$$\ddot{x} + \omega_o^2 x = \varepsilon f(x,t) \tag{10}$$

Where ε is regarded as a tiny dimensionless factor and ω_0 remains the associated linear beam's inherent frequency.

Equation 1 displays that the equivalent stiffness is a function of the oscillation amplitude. By considering the bilinear function provided for $k(d)$, the bilinear stiffness of the cracked beam is stated below:

$$\begin{cases} k_{close} = k(1+\varepsilon) \\ k_{open} = k(1-\varepsilon) \end{cases} \tag{11}$$

k displays the comparable average stiffness in the crack's completely open and fully closed states:

$$k = \frac{1}{2}\left(k_{open} + k_{close}\right) \tag{12}$$

And ε is a dimensionless and small parameter defined as follows:

$$\varepsilon = -\frac{k_{open} - k_{close}}{k_{open} + k_{close}} \tag{13}$$

Drawing from Equations 11 to 13 the subsequent novel model for the bilinear stiffness of the fractured beam is introduced:

$$k(x) = kx + \varepsilon k|x| \tag{14}$$

By substituting Equation 14 into Equation 9, the following is obtained:

$$m\ddot{x} + kx = -\varepsilon k|x| \tag{15}$$

By dividing both sides of Equation 15 on *m*, the governing differential equation is expressed in the following final form:

$$\ddot{x} + \omega_0^2 x = -\varepsilon\omega_0^2|x| \tag{16}$$

Where:

$$\omega_0 = \sqrt{\frac{k}{m}} \tag{17}$$

By comparing Equations 10 and 16, it can be seen that by presenting a new model for bilinear stiffness of the cracked beam model, the governing differential equation can be written in an analyzable form by the perturbation method. In addition, in this model, unlike time-varying stiffness models, the equivalent stiffness is a function of the oscillation amplitude, which has led to the formation of a non-linear differential equation. Certainly, such a model leads to a better understanding of the non-linear behavior of fatigue cracks compared to time-varying stiffness models.

APPLICATION OF THE LINDEST-POINCARÉ METHOD

In the current research, the Lindest-Poincaré method was used to obtain the system response [27]. Based on this, the response of the system and its frequency are considered as the following series:

$$x = x_0 + \varepsilon x_1 + \varepsilon^2 x_2 + .. \tag{18}$$

$$\omega = \omega_0 + \varepsilon\omega_1 + \varepsilon^2\omega_2 + ... \tag{19}$$

According to $\tau = \omega t$, the derivatives of *x* in terms of time can be expressed in terms of the new variable as:

$$\frac{dx}{dt} = \omega\frac{dx}{d\tau} = (\omega_0 + \varepsilon\omega_1 + \varepsilon^2\omega_2 + ...)\frac{d}{d\tau}(x_0 + \varepsilon x_1 + \varepsilon^2 x_2 + ...) \tag{20}$$

$$\frac{d^2x}{dt^2} = \omega^2 \frac{d^2x}{d\tau^2} = (\omega_0 + \varepsilon\omega_1 + \varepsilon^2\omega_2 + \ldots)^2 \frac{d^2}{d\tau^2}(x_0 + \varepsilon x_1 + \varepsilon^2 x_2 + ..) \tag{21}$$

By substituting Equations 18 to 21 in Equation 16, the following is obtained:

$$\begin{gathered}(\omega_0 + \varepsilon\omega_1 + \varepsilon^2\omega_2 + \ldots)^2 \frac{d^2}{d\tau^2}(x_0 + \varepsilon x_1 + \varepsilon^2 x_2 + \ldots) \\ +\omega_0^2(x_0 + \varepsilon x_1 + \varepsilon^2 x_2 + \ldots) + \varepsilon\omega_0^2|x_0 + \varepsilon x_1 + \varepsilon^2 x_2 + \ldots| = 0\end{gathered} \tag{22}$$

By arranging the above relationship in terms of increasing powers of ε, 3 differential equations are obtained as follows:

$$\varepsilon^0: \quad \omega_0^2\left(\frac{d^2x_0}{d\tau^2} + x_0\right) = 0 \tag{23}$$

$$\varepsilon^1: \quad \omega_0^2\left(\frac{d^2x_1}{d\tau^2} + x_1\right) = -2\omega_0\omega_1\frac{d^2x_0}{d\tau^2} - \omega_0^2|x_0| \tag{24}$$

$$\begin{gathered}\varepsilon^2: \quad \omega_0^2\left(\frac{d^2x_2}{d\tau^2} + x_2\right) = \\ -2\omega_0\omega_1\frac{d^2x_1}{d\tau^2} - (\omega_1^2 + 2\omega_0\omega_2)\frac{d^2x_0}{d\tau^2} - \omega_0^2\frac{|x_0 + \varepsilon x_1|}{x_0 + \varepsilon x_1}x_1\end{gathered} \tag{25}$$

Equation 23 is a homogeneous differential equation whose solution yields the answer of the beam with the average equivalent stiffness in both the completely closed and open states of the fracture. This system, which is called the corresponding linear system, includes the main part of the answer. Equations 24 and 25 may be solved to determine the consequences of the crack's opening and closure on the system's reaction, which is produced by a change in equivalent stiffness. In this research, the second method is used. Thus, assuming the initial conditions of net displacement, the main part of the answer is obtained from the solution of the differential Equation 23 as follows:

$$x_0 = A\cos\tau \tag{26}$$

Where in:

$$A = A_0 + \varepsilon A_1 + \varepsilon^2 A_2 \tag{27}$$

In which, A_0 is the initial displacement of the beam and A_1 and A_2 are determined in such a way that the initial conditions of the first and second-order correction sentences become zero. To remove only the secular term of Eq. (24), the following is obtained:

$$-2\omega_0\omega_1\frac{d^2x_0}{d\tau^2} = 0 \tag{28}$$

In which $\omega_1 = 0$. By removing the secular term from Equation 24 and inserting the result obtained in Eq. (26) into it, this equation is expressed as:

$$\frac{d^2x_1}{d\tau^2} + x_1 = -A|\cos\tau| \tag{29}$$

$|\cos\tau|$ is an even periodic function whose Fourier expansion is obtained as follows:

$$g(\tau) = \frac{2}{\pi} + \sum_{n=1}^{\infty}\frac{4}{\pi}\left\{\frac{1}{(1-4n^2)}(-1)^n\right\}\cos 2n\tau \tag{30}$$

Substituting Equation 30 in Equation 29, the following is obtained:

DOI 10.14311/CEJ.2025.01.0002

$$\frac{d^2x_1}{d\tau^2}+x_1=-Ag(\tau)=-A\left\{\frac{2}{\pi}+\sum_{n=1}^{\infty\Sigma}\frac{4}{\pi}\left\{\frac{1}{(1-4n^2)}(-1)^n\right\}\cos 2\,n\tau\right\} \tag{31}$$

As can be seen, the right side of Equation 31 consists of a constant value and a set of harmonic terms. By solving the differential equation, the private answer is obtained as follows:

$$x_1=-A\left\{\frac{2}{\pi}+\sum_{n=1}^{\infty}\frac{4}{\pi}\left\{\frac{1}{(1-4n^2)^2}(-1)^n\right\}\cos 2\,n\tau\right\} \tag{32}$$

In Equation 25, the expression $\left(\frac{|x_0+\varepsilon x_1|}{x_0+\varepsilon x_1}\right)x_1$can be written as follows using Fourier expansion:

$$f(\tau)=b_0+\sum_{m=1}^{\infty}b_m\cos m\,\tau \tag{33}$$

Where the Fourier expansion coefficients are obtained as follows:

$$b_0=\frac{1}{\pi}\left\{\int_0^z\bar{x}_1d\tau-\int_z^\pi\bar{x}_1d\tau\right\} \tag{34}$$

$$b_m=\frac{2}{\pi}\left\{\int_0^z\bar{x}_1\cos m\,\tau\;d\tau-\int_z^\pi\bar{x}_1\cos m\,\tau\;d\tau\right\}\;,\;m=1,2,.. \tag{35}$$

In which *z* is the place where the sign of the function $(x_0+\varepsilon\;x_1)$ changes and the average value of $\bar{x}_1$obtained in Equation 32. By calculating the above integrals, the Fourier expansion coefficients of Equation 33 are obtained as follows:

$$b_0=\left(\frac{\bar{b}_1}{\pi}\right)(2z-\pi) \tag{36}$$

And:

$$b_m=\left(\frac{4\bar{b}_1}{m\pi}\right)\sin m\,z\;,\quad m=1,2,\ldots \tag{37}$$

By placing the Fourier expansion provided for the expression $\left(\frac{|x_0+\varepsilon x_1|}{x_0+\varepsilon x_1}\right)x_1$ in Equation 25, it can be seen that the first term of this expansion is a secular term, which requires the following relationship to be removed:

$$-2\omega_0\omega_2(-A\cos\tau)-\omega_0^2(b_m\cos m\,\tau)|_{m=1}=0 \tag{38}$$

So

$$\omega_2=\frac{\omega_0 b_1}{2\;A} \tag{39}$$

By removing the secular term from Equation 25 and solving this differential equation, the private answer is obtained as follows:

$$x_2=b_0+\sum_{m=2}^{\infty}\left(\frac{b_m}{1-m^2}\right)\cos m\,\tau \tag{40}$$

in which b_0 is b_m obtained from Equations 36 and 37 respectively. Finally, the response of the beam is achieved as follows:

$$x(\tau)=x_0(\tau)+\varepsilon x_1(\tau)+\varepsilon^2x_2(\tau) \tag{41}$$

where:

$$\tau = \omega\ t \quad (42)$$
$$\omega = \omega_0 + \varepsilon^2 \omega_2 \quad (43)$$

Case Study Analysis and Discussion

The geometric dimensions and mechanical characteristics of the steel beam with a crack are investigated as follows: beam length L=500 mm, beam cross section A=4×6.5 mm^2, elastic modulus E=206 GPa, and density is ρ=7850 kg/m^3. Moreover, the relative position of the fracture is indicated by $\beta = x_c/L$, and its relative depth is shown by $\alpha = a/h$, which is the ratio of the crack's depth to the beam's thickness. The initial conditions are the same in all the cases that will be examined.

To verify the proposed model, the results from Ref. [28] are utilized. Specifically, a single beam with a length of 500 units and a cross-sectional area of 29×20 units is considered. The elastic modulus and density are assumed to be the same as previously described. Table 1 presents a comparison of the first natural frequency for varying crack depths. The results demonstrate a strong agreement between the findings of the present study and those of Ref. [28], with errors ranging from 1.06% to 3.25%. However, the natural frequencies predicted by the present study are consistently higher than those in Ref. [28], attributed to the increased equivalent stiffness in the opening-and-closing crack model.

Tab. 1 - Natural frequencies (Hz) of the cracked beam

Method	Crack depth (mm)				
	4	8	12	16	20
Present work	593.7	585.8	586.8	581.9	569.1
Ref. [28]	587.5	578.3	572.3	566.8	551.2
Error (%)	1.06	1.30	2.53	2.66	3.25

Figure 4 illustrates the comparison between the numerical solution of the bilinear crack model and the open crack model. The results demonstrate consistency in the upper cycles, where the crack remains open. In contrast, during the lower cycles, the closing of the crack results in reduced equivalent stiffness, leading to discrepancies between the two models. In Figure 4a and 4c, the upper and lower peaks of the response for both the corresponding linear system (fully open crack model) and the final response obtained using the Runge-Kutta numerical method are presented. The results indicate that while the highest peaks of the two graphs coincide, discrepancies are observed in the lower peaks. These differences arise due to the closing of cracks during the lower peaks, which reduces the system's equivalent stiffness. To address this discrepancy, a first-order correction term is introduced, as illustrated in Figure 4b. It is noteworthy that in the upper peaks, where the two graphs overlap, the correction term approaches zero. Figure 5 compares the analytical solution derived using the Lindest-Poincaré perturbation method with the numerical solution for the bilinear crack model. The close alignment between the two responses validates the accuracy of the analytical method in capturing the nonlinear dynamics of the cracked beam.

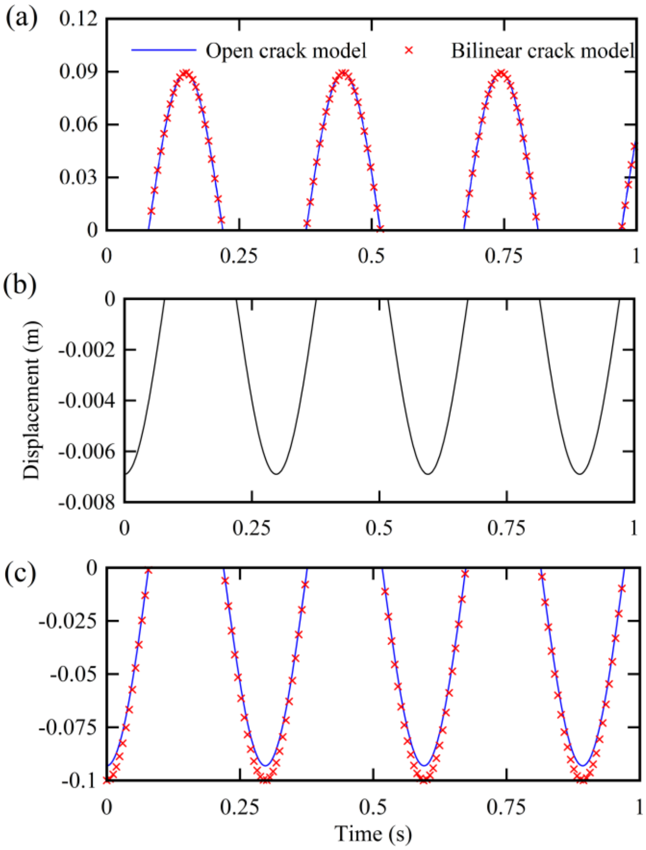

Fig. 4 - (a) Upper peaks of the response from the corresponding linear system (b) First-order correction term and (c) Lower peaks of the response from the corresponding linear system compared with the response obtained via the Runge-Kutta numerical method, for $\alpha = 0.4$ *and* $\beta = 0.4$*.*

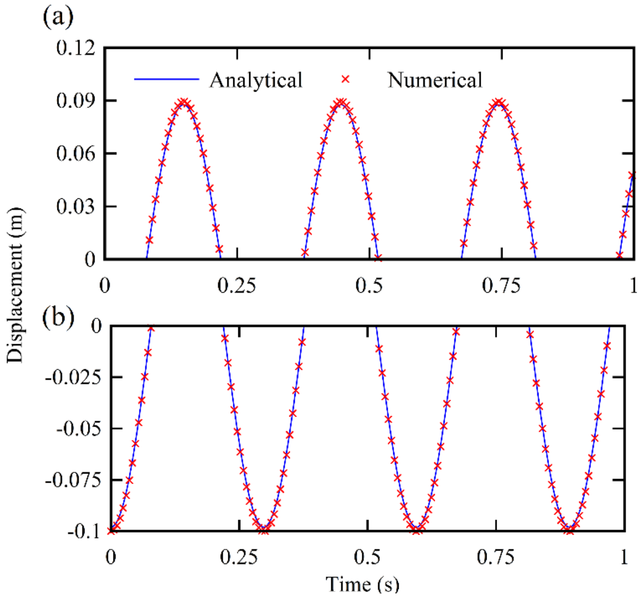

Fig. 5 - (a) Upper peaks and (b) Lower peaks of the response obtained via the Lindest-Poincaré method following the application of the first-order correction, alongside the response from the Runge-Kutta numerical method, for $\alpha = 0.4$*and* $\beta = 0.4$*.*

As the relative depth of a crack at a fixed position increases, its effect on the system's dynamic response is analyzed and presented in Figure 6. The results indicate a clear trend: the degree of reduction in the system's equivalent stiffness grows proportionally with the increase in crack depth. This reduction in stiffness introduces significant nonlinearities into the system's behavior, which, in turn, exacerbates the disparity between the response predicted by the numerical method and that of the corresponding linear system. A closer examination reveals that these discrepancies become particularly evident during the lower half-cycles of the system vibration. In this phase, the crack undergoes opening dynamics, resulting in a notable drop in the equivalent stiffness of the system. Consequently, the system exhibits larger deviations in the lower peaks of its response, as shown in Fig. 6. The lower peaks of the two graphs—representing the numerical method's reaction and the linear system's response—clearly illustrate this divergence. Furthermore, the increased crack depth not only magnifies the stiffness reduction but also intensifies the nonlinearity in the system's vibration behavior. This behavior underscores the critical role of crack parameters, such as depth, in influencing the system's dynamic characteristics. By comparing the lower peaks in Fig. 6, it becomes evident that the numerical method accurately captures the effects of crack dynamics, including the substantial impact of the crack opening and closing on the equivalent stiffness. These findings highlight the limitations of the linear system model in addressing such nonlinear effects and reinforce the necessity of incorporating nonlinear modeling approaches to achieve accurate predictions of the system's behavior under varying crack conditions.

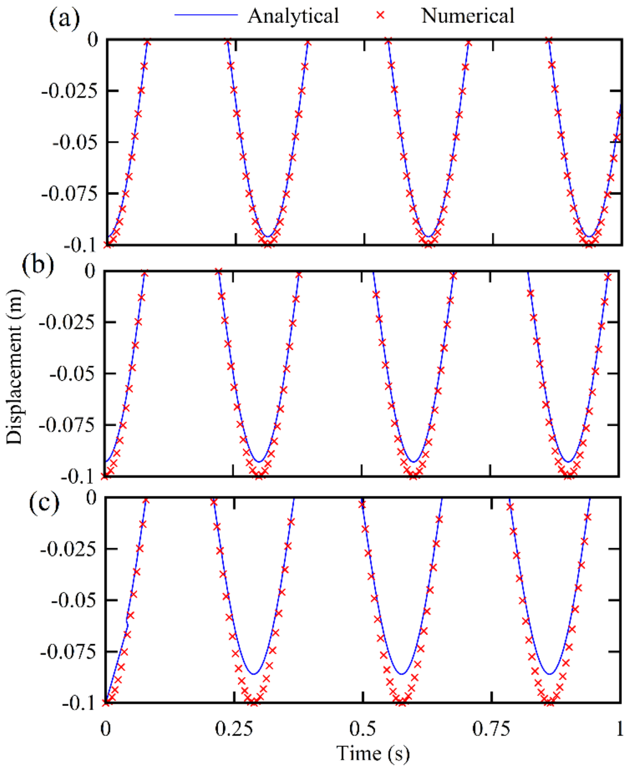

Fig. 6 - Comparison of the lower peaks of the response of the corresponding linear system and the final response obtained by the Rang-Kuta numerical method, for $\beta = 0.4$ and relative depths of the crack (a) $\alpha = 0.2$, (b) $\alpha = 0.4$, and (c) $\alpha = 0.6$.

As the relative crack depth increases while maintaining a fixed relative position, a noticeable augmentation in the discrepancies between the response of the corresponding linear system and that acquired through numerical methods occurs. This discrepancy expansion consequently leads to an increase in the range of fluctuations observed in the first-order correction term. This noteworthy phenomenon is vividly depicted in Figure 7.

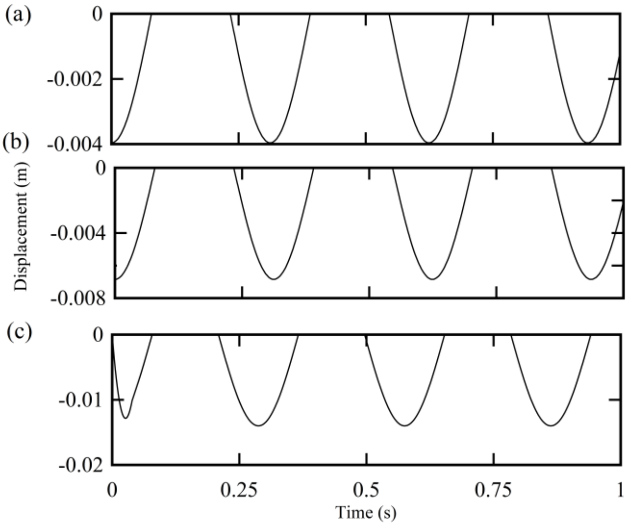

Fig. 7 - First-order correction term of the response obtained using the Lindest-Poincaré method for varying relative positions $\beta = 0.4$ and depths of the crack (a) $\alpha = 0.2$, (b) $\alpha = 0.4$, and (c) $\alpha = 0.6$.

The relative position of the crack, akin to the relative depth, exerts a notable effect on the vibration response of the cracked structure. In Figure 8, the impact of altering the crack's relative position while maintaining a constant relative depth on the range of fluctuations in the first-order correction term is explored. The first-order correction term's amplitude of fluctuations increases as the crack's location gets closer to the beam's cantilever end. This escalation signifies an intensified effect of crack opening and closing on the system's vibration response, consequently accentuating the system's nonlinear behavior. It is evident that the response of the system, with the application of the first-order correction, closely mirrors the final response obtained through numerical methods. The impact of the second-order correction term on the response is substantially lesser than that of the first-order correction term. However, it remains sensitive to crack parameters, exhibiting alterations in its shape during open and closed half-cycles.

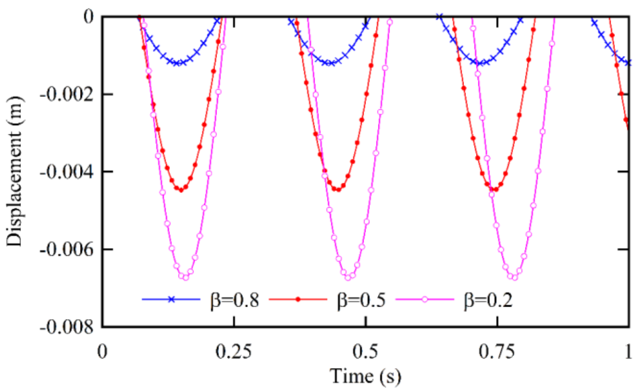

Fig. 8 - Correction term of the response obtained using the Lindest-Poincaré method for varying relative crack depths of $\alpha = 0.5$and positions (a) $\beta = 0.2$, (b) $\beta = 0.5$, and (c) $\beta = 0.8$.

Figure 9 illustrates the effect of increasing the relative depth of the crack while maintaining a fixed relative position, on the amplitude of fluctuations in the second-order correction term. The second-order correction term's range of variations grows in tandem with an increase in the relative fracture depth.

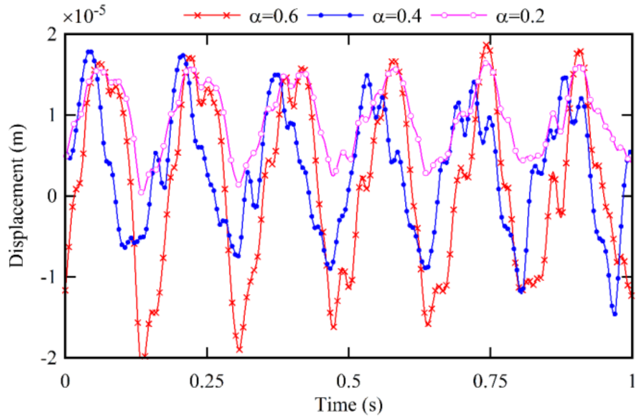

Fig. 9 - Second-order correction term of the response obtained using the Lindest-Poincaré method for relative positions $\beta = 0.4$ and for $\alpha = 0.2$, $\alpha = 0.4$ and $\alpha = 0.6$.

Furthermore, Figure 10 demonstrates how changes in the relative crack position affect the amplitude of fluctuations in the second-order correction term. As the crack's position approaches the end of the gripper with a fixed relative depth, the amplitude of fluctuations in the second-order correction term increases.

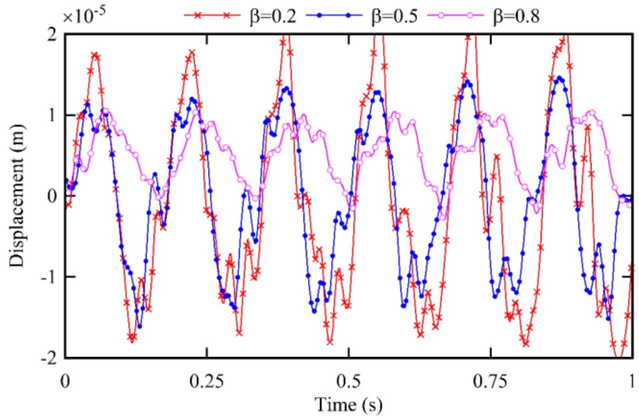

Fig. 10 - Second-order correction term of the response obtained using the perturbation method for relative crack depths of$\alpha = 0.5$and for $\beta = 0.2$, $\beta = 0.5$, and $\beta = 0.8$.

One of the primary features of the nonlinear behavior exhibited by the vibration response of a cracked structure, whether it possesses an open or closed crack, is the emergence of harmonic components in its response. In fact, the correction part of the answer obtained by the Lindest-Poincaré method, which is added to the first term of the answer in order to apply the crack opening and closing effects is presented in Eqs. (31) and (39), include harmonic components. Is. In Figure 11, the frequency response diagram obtained using the fast Fourier transform of the time trace obtained by the method presented in this research after adding the first-order correction term to the response of the corresponding linear system for the relative crack depth of $\alpha = 0.5$ and relative crack position of $\beta = 0.2$ is drawn. It is clear that the first-order correction term includes harmonics in even multiples of the system's natural frequency, in which the harmonic component of 2X has the greatest effect on the system's response. Figure 12 shows the frequency spectrum of the response after adding the first and second-order correction sentences to the response of the corresponding linear system in the case of relative crack depth of $\alpha = 0.5$ and relative crack position of=β 0.2 It becomes evident that upon incorporating the second-order correction term into the system response, odd-order harmonics emerge in the frequency spectrum of the response. This divergence arises from the fact that while the first-order correction term solely encompasses harmonic components in even

DOI 10.14311/CEJ.2025.01.0002

multiples of the system's natural frequency, the second-order correction term encompasses harmonic components in all integer multiples of the system's natural frequency. Given that even harmonics correspond to order (*2n*) and odd harmonics correspond to order (2*n*+1), the range of even harmonics notably surpasses that of odd harmonics. Experimental and analytical findings from reference [29] also corroborate this observation.

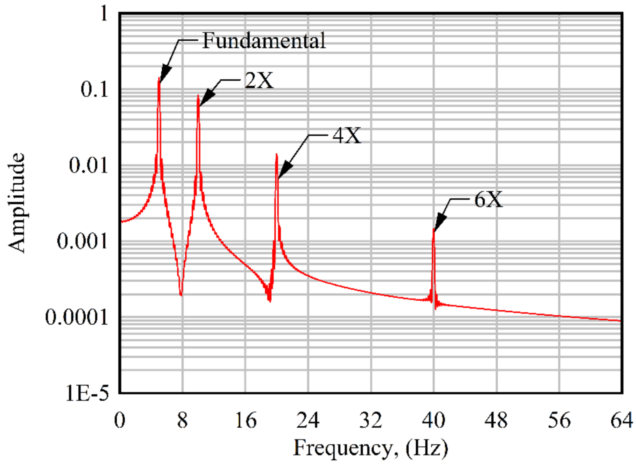

Fig. 11 - The frequency spectrum of the response, after the first-order correction term is applied, to changes in the relative location and depth of the fracture

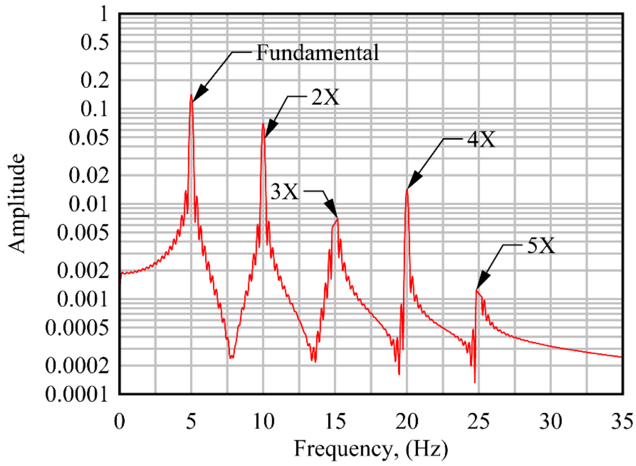

Fig. 12 - When the relative depth and relative location of the crack are disturbed, the frequency spectrum of the reaction following the application of the first and second-order corrective phrases

Figure 13 illustrates the variation in the natural frequency of the system under 2 conditions: assuming an open crack and assuming both open and closing crack states, as a function of the relative depth of the crack at a relatively fixed position. It is apparent that in both scenarios—assuming an open crack and assuming both open and closing crack states—the increase in crack parameters results in a reduction in natural frequencies. However, the decrease in natural frequencies when assuming both open and closing crack states is less pronounced than when assuming the crack is solely open.

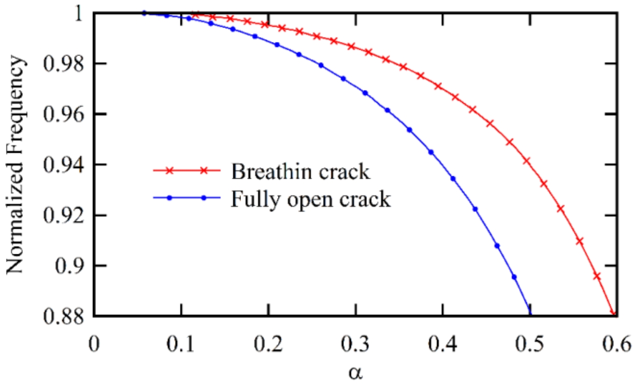

Fig. 13 - Dependent on the relative depth of the fracture in $\beta = 0.1$, variation in the natural frequency with the assumptions of a fully open crack and an open and closing crack

CONCLUSIONS

This study looked at the nonlinear behavior of free vibrations in a single-span beam with a transverse fatigue fracture. There was a proposal for a new model for the bilinear stiffness of the beam with a fatigue fracture. Using this model, the bilinear differential equation governing the behavior of the cracked beam was derived in an analyzable form through the Lindest-Poincaré method.

These findings reveal that the response obtained through the Lindest-Poincaré method comprises the aggregate response of the corresponding linear system and a series of correction terms. These correction terms account for the variations in the equivalent stiffness of the system during vibration induced by crack opening and closing, thereby incorporating harmonic components with correct coefficients of the system's natural frequency. This analysis elucidates the relationship between the nonlinear characteristics of the beam's behavior with fatigue cracks, as well as the harmonic components in the response, with the crack parameters and system characteristics. Notably, the correction terms encapsulate harmonic components in the response, with the governing rules expressing the analytical relationship between these components and the crack parameters and system characteristics. Furthermore, it is observed that the first-order correction term, which includes harmonic components in even multiples of the system's natural frequency, exerts a greater influence on the response compared to higher-order correction terms.

Comparison between the behavior derived from this analytical solution and numerical solutions demonstrates a high degree of concordance across a broad spectrum of crack parameters. Additionally, graphs depicting frequency changes with crack parameters in both the open and closed crack models utilized in this research highlight a lesser reduction in natural frequency caused by real fatigue cracks exhibiting open and closed behavior compared to cracks solely in an open state. This observation is further corroborated by experimental results reported in the technical literature.

REFERENCES

[1] Lee, Y.F. and Y. Lu (2022) Identification of fatigue crack under vibration by nonlinear guided waves. *Mechanical Systems and Signal Processing*, 163, 108138.

[2] Haiyan, Z., L. Shengrong, J. Mingze, W. Yi, S. Yang, L. Qiaodan, T. Zeyu, and X. Qian (2023) Review of research on the influence of vibration and thermal fatigue crack of brake disc on rail vehicles. *Engineering Failure Analysis*, 107603.

[3] Li, L., Z. Zhang, P. Zhang, and Z. Zhang (2023) A review on the fatigue cracking of twin boundaries: Crystallographic orientation and stacking fault energy. *Progress in Materials Science*, 131, 101011.

[4] Rezaee, M., H. Javadian, and V.A. Maleki (2015) Vibration behavior and crack detection of a cracked short beam under a axial load. *Mechanical Engineering*, 47(2).

[5] Eslami, G., V.A. Maleki, and M. Rezaee (2016) Effect of open crack on vibration behavior of a fluid-conveying pipe embedded in a visco-elastic medium. *Latin American Journal of Solids and Structures*, 13, 136-154.

[6] Xu, W., Z. Su, M. Radzieński, M. Cao, and W. Ostachowicz (2021) Nonlinear pseudo-force in a breathing crack to generate harmonics. *Journal of Sound and Vibration*, 492, 115734.

[7] Kushwaha, N. and V. Patel (2020) Modelling and analysis of a cracked rotor: a review of the literature and its implications. *Archive of Applied Mechanics*, 90(6), 1215-1245.

[8] Khosravi, S., S. Amirsardari, and M.A. Goudarzi (2024) Dynamic Behavior of Rectangular Tanks with Limited Freeboard Under Seismic Loads: Experimental, Analytical and Machine Learning Investigations. *Journal of Pressure Vessel Technology*, 1-34.

[9] Khosravi, S. and M.A. Goudarzi (2023) Seismic risk assessment of on-ground concrete cylindrical water tanks. *Innovative Infrastructure Solutions*, 8(1), 68.

[10] Khosravi, S., M.M. Yousefi, and M. Goudarzi (2021) Development of seismic fragility curves of cylindrical concrete tanks using nonlinear analysis. *Amirkabir Journal of Civil Engineering*, 53(1), 71-88.

[11] Spagnol, J., H. Wu, and C. Yang (2020) Application of non-symmetric bending principles on modelling fatigue crack behaviour and vibration of a cracked rotor. *Applied Sciences*, 10(2), 717.

[12] Wang, T., M. Noori, and W.A. Altabey (2021) Identification of cracks in an Euler–Bernoulli beam using Bayesian inference and closed-form solution of vibration modes. *Proceedings of the Institution of Mechanical Engineers, Part L: Journal of Materials: Design and Applications*, 235(2), 421-438.

[13] Li, H., T. Wang, and G. Wu (2023) Nonlinear vibration analysis of beam-like bridges with multiple breathing cracks under moving vehicle load. *Mechanical Systems and Signal Processing*, 186, 109866.

[14] Rezaee, M. and V. Maleki (2011) A New Nonlinear Model for Flexural Vibration Analysis of a Cracked Beam with a Fatigue Crack. *Journal of Applied and Computational Sciences in Mechanics*, 22(2), 35-52.

[15] Peng, Z., Z. Lang, and S. Billings (2007) Crack detection using nonlinear output frequency response functions. *Journal of Sound and Vibration*, 301(3-5), 777-788.

[16] Kharazan, M., S. Irani, M.A. Noorian, and M.R. Salimi (2021) Nonlinear vibration analysis of a cantilever beam with multiple breathing edge cracks. *International Journal of Non-Linear Mechanics*, 136, 103774.

[17] Dezfuli, M.A., M. Zeinoddini, and R.M. Harati (2020) An analytical model for the coupled-field dynamic fatigue crack growth in a metallic beam under chaotic excitations. *Theoretical and Applied Fracture Mechanics*, 109, 102726.

[18] Zhao, X., S. Li, W. Zhu, and Y. Li (2022) Nonlinear forced vibration analysis of a multi-cracked Euler-Bernoulli curved beam with inclusion of damping. *Mechanical Systems and Signal Processing*, 180, 109147.

[19] Ghaderi, M., H. Ghaffarzadeh, and V.A. Maleki (2015) Investigation of vibration and stability of cracked columns under axial load. *Earthquakes and Structures*, 9(6), 1181-1192.

[20] Long, H., Y. Liu, and K. Liu (2023) Vibration analysis of a cracked beam using the finite element method. *Transactions of the Canadian Society for Mechanical Engineering*.

[21] Aggumus, H., M. Daskin, M. Haskul, and A. Turan (2024) The Effect of the Crack-Stiffness Relationship on the System Response in Columns of an SDOF Steel Structure Model under Harmonic and Earthquake Excitations. *Shock and Vibration*, 2024(1), 9278849.

[22] Hai, T.T. and D. Nam (2023) A single degree of freedom model for cracked beam. *Vietnam Journal of Mechanics*, 45(2), 183-196.

[23] Liu, Y., W. Long, Y. Chen, and H. Hu (2024) Nonlinear vibration characteristics and damage detection method of blade with breathing fatigue crack. *Aerospace Science and Technology*, 155, 109715.

[24] Alshammrei, S., B. Lin, and J. Tong (2020) Full-field experimental and numerical characterisation of a growing fatigue crack in a stainless steel. *International Journal of Fatigue*, 133, 105449.

[25] Mukhopadhyay, M., *Structural Dynamics*. 2021: Springer.

[26] Dimarogonas, A.D., S.A. Paipetis, and T.G. Chondros, *Analytical methods in rotor dynamics*. 2013: Springer Science & Business Media.
[27] Nayfeh, A.H. and D.T. Mook, *Nonlinear oscillations*. 2008: John Wiley & Sons.
[28] Orhan, S. (2007) Analysis of free and forced vibration of a cracked cantilever beam. *Ndt & E International*, 40(6), 443-450.
[29] Saavedra, P. and L. Cuitino (2001) Crack detection and vibration behavior of cracked beams. *Computers & Structures*, 79(16), 1451-1459.

CIVIL ENGINEERING JOURNAL

Article no. 3

THE CIVIL ENGINEERING JOURNAL 1-2025

AUGMENTED REALITY AS A 3D LAND COVER VISUALISATION TECHNIQUE

František Mužík

Czech Technical University in Prague, Faculty of Civil Engineering, Department of Geomatics, Prague, Thákurova 2077/7, Czech Republic; frantisek.muzik@fsv.cvut.cz

Received: *26.06.2024*

Received in revised form: *13.12.2024*

Accepted: *13.02.2025*

ABSTRACT

Augmented Reality (AR) is an established technique for both 2D and 3D visualisations in several fields such as sports, entertainment or culture (museums). However, in cartography or in GIS, it is still considered as a minor niche visualisation technique. Therefore, the aim of this paper is to present AR as a 3D visualisation method for land cover development. The presented output is a part of a mobile application for Android. Land cover GIS data obtained from historical and contemporary large-scale maps are processed using City Engine, resulting in the creation of several 3D models viewed via augmented reality. Procedural modelling in City Engine is used to visualise 3D land cover data such as buildings or forests (including coniferous, deciduous and mixed). Other land cover types (e.g. arable land, grassland or roads) are displayed as 2D textures. In this way, the user can experience an innovative perspective of land cover changes over time in a study area of Chudenice (a village in the southwest of Czechia). The 3D land cover maps are presented in two time periods (1837 and 2023). The 3D models are accompanied by a map legend, scale, north arrow and title, so that the user can keep track of the current model without the need for additional essential map information.

KEYWORDS

Augmented reality, AR, Land cover, Visualisation, Old maps, City engine, Unity

INTRODUCTION

The development of land use/cover is a topic that is covered from many science perspectives, such as ecology, history, geography or GIS and cartography. Almost every outcome in this specific research sector involves tables, charts or 2D maps [1, 2, 3, 4]. The focus of this paper is to visualise a land cover development in an innovative way and it is redundant to provide the reader (or a mobile application user) a new perspective on this topic. The presented visualisation consists of several 3D terrain models viewed via augmented reality (AR). These 3D models show the development of the study area in two different time periods (Table 1). With AR, user can view the virtual 3D terrain models using a mobile device (a phone or tablet).

The use of augmented reality is rapidly increasing due to the technological evolution, so it is being used not only in cartography, but also in many other domains. The main area of use is still entertainment, such as sports [5], video games [6, 7] or books [8]. Nevertheless, AR is being present in many more serious domains, being culture (e.g. cultural heritage [9, 10, 11], arts [12], museums [13]), medicine [14], education [15], interior design [16] or industry [17, 18].

Land cover/use changes are typically presented mostly as 2D maps (as mentioned above). However, a 3D visualisation of this phenomenon not only gives the reader a new perspective, but can also visualise the terrain more effectively by using the third dimension [19]. The terrain could undergo a massive change during the presented time, therefore it is important to correctly depict its changes in a certain scale. This is quite well possible in a presentation of a contemporary changes or those that have happened in the near past due to the airborne laser scanning and its outputs being very precise digital terrain models (DTM). The older mappings have to rely on a less accurate elevation that had been obtained with older surveying techniques, which often results in a less reliable comparison between two selected time periods [20]. Because of the very minor terrain changes in the study area and the scale of final visualisations, the DMR5G elevation model (data from 2023) provided by the Czech State Administration of Land Surveying and Cadastre (ČÚZK) [21] was used as a basis for both presented 3D models.

Tab. 1 - Time periods of tracked land cover changes with map sources for data comparison

Period	Map basis
1837	Imperial Obligatory Imprints of the Stable Cadastre 1:2,880
2023	Basic Topographic Map of the Czech Republic 1:5,000

Augmented reality

Augmented reality (AR) is defined as a real-time view of a physical world that has been enhanced by virtual information [22] and is a part of extended reality (XR). Other defined branches of extended reality are virtual reality (VR) and mixed reality (MR) as seen bellow in Figure 1. The difference between the types of XR lies in the degree of user immersion in the virtual world based on Milgram's real-virtual continuum (upper part of Figure 2) [23]. Virtual reality offers the most immersive experience for the user as it is presented through a headset that places the user directly in the virtual world. Mixed reality connects the real and virtual worlds, with the use of a headset or goggles, while a greater degree of immersion is still determined by the presence of the user as part of the virtual world. Augmented reality offers the lowest level of user immersion, as it 'only' enhances the real world with virtual elements. In some cases, there is almost no clear distinction between these types of XR, and the borderline cases can therefore sometimes be named, for example, both AR and MR. This claim is also supported by the evolution of technology, which makes the update and re-evaluation of the definitions on which Milgram's scheme is based necessary (lower part of Figure 2) [24].

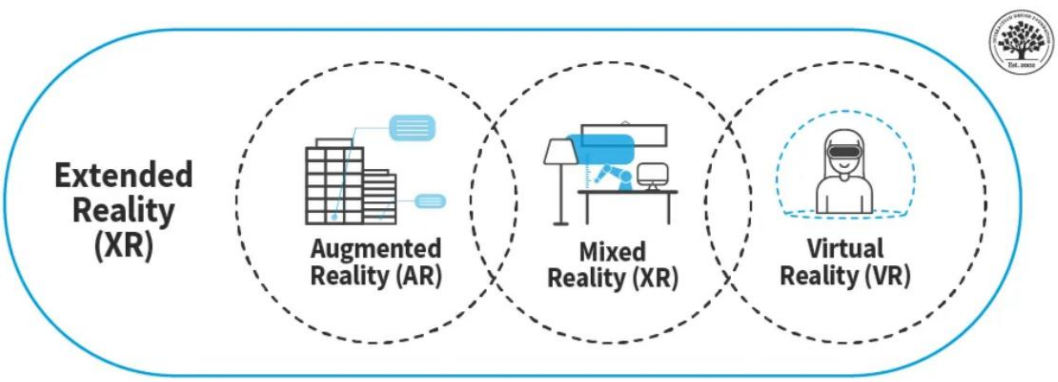

Fig. 1 – Extended Reality scheme [25]

DOI 10.14311/CEJ.2025.01.0003

Augmented reality can be divided into several types according to different parameters [26, 27] (e.g. according to display technology or orientation in real space), while the terminology is not clearly established and thus it is possible to encounter different names for the same type of augmented reality (e.g. location-based AR = geospatial AR = GPS AR [28]). To simplify the terminology, this paper only works with a certain subset of augmented reality types. These are the types of AR classifications based on the orientation in real space (markerless AR, marker AR and location-based AR).

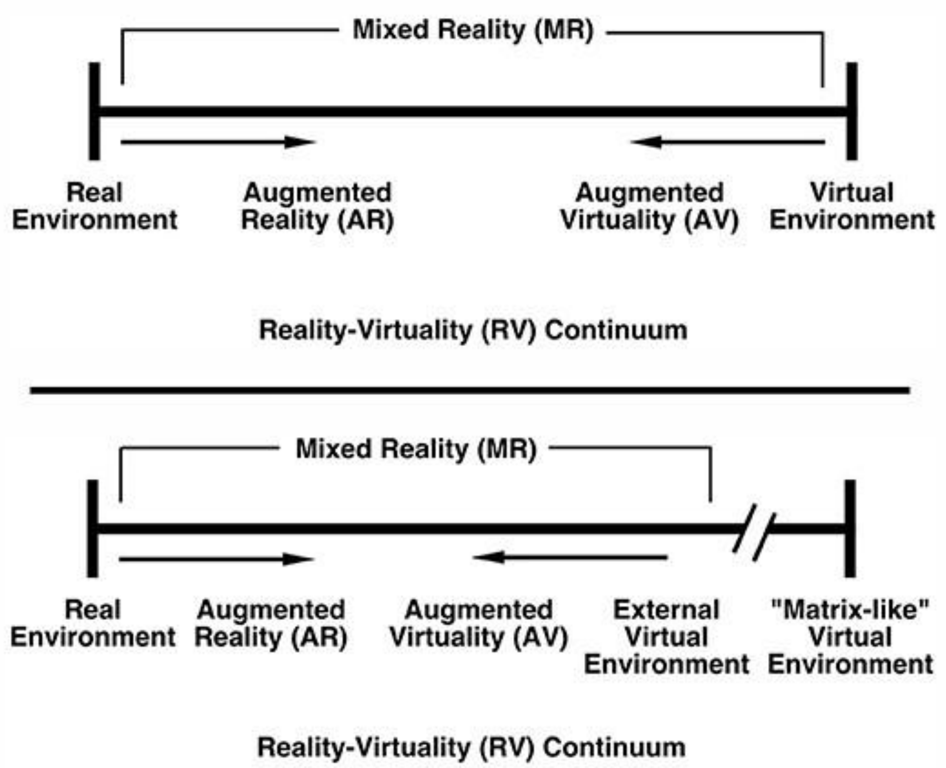

Fig. 2 – Milgram original reality-virtuality continuum (upper part) [23], Milgram revised reality-virtuality continuum (lower part) [24]

The most basic visualisation method for augmented reality is markerless AR, which displays the virtual model based on the user's scan of an environment (e.g. a table or floor). Once the environment has been scanned, the virtual element can be placed in space and can be therefore moved (on scanned horizontal or vertical planes), rotated or resized.

Marker AR places the virtual object based on the recognition of a specific marker [29]. The object is directly tied to this marker. The applications are then divided into those that allow the user to move, rotate and resize the object - as in the previous case. The second type of applications uses the marker as an anchoring element that directly defines the size, rotation and position of the virtual model. In this case, the displayed virtual model is directly tied to the marker.

Location-based AR visualises the virtual model in a predefined location in the environment (e.g. city street or field) [30, 31]. Therefore, the model cannot be displayed at a different location using this method, as it is tied to a specific location.

Study Area

The study area of a Chudenice is located in the south-western of Czechia on the border of the Domažlice and Klatovy district (Figure 3). The municipality consists of four cadastral communities Chudenice, Lučice, Bezpravovice and Slatina and its area is approximately 25 square kilometres. According to the latest census from 2021 [32], the population of the village was 733 inhabitants. The figures in the text (Figures 5-7) are depicting AR models visualising the cadastral community Chudenice.

The first mention of Chudenice dates back to 1291 [33]. Until the end of the Second World War, the area was under administration of the Czernin family from Chudenice [34]. During this period, several cultural buildings were built here, making Chudenice a popular regional tourist destination. The most important buildings are the Old Czernin Castle, the Museum of Josef Dobrovský, the Church of St. John the Baptist, the Castle of St. Wolfgang and the Bolfánek observation tower (built on the ruins of the Church of St. Wolfgang) [35].

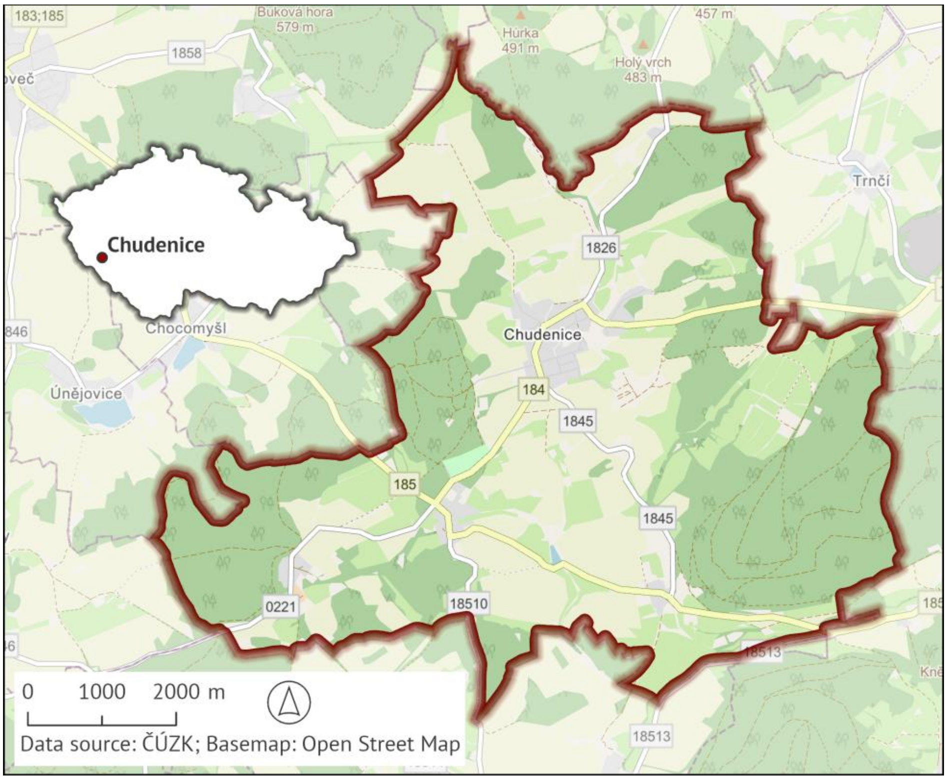

Fig. 3 – Map of the study area

METHODS AND RELATED WORKS

Land cover changes are observed in two time periods, as shown in Table 1. The monitored types of land cover and its specification are described in Table 2 below. These are the land cover types that can be distinguished on both of the used map basis, historical (1837) and contemporary (2023). Some of the land cover types are visually merged for achieving a better interpretation and comparison at a given map scale. For example, used historical map distinguish three types of grassland (meadow, pasture and garden). Contemporary map uses only two of them (meadow and garden). Therefore, some way of adjusting the distribution and merging certain land cover types into larger groups was needed for a clearer overview on the area of interest, as visualised in Table 1.

This paper is concerned with the use of markerless AR for 3D cartographic visualisations, which is a method that is also described in a paper by Halik and Wielebski [36].They have developed a web AR application showing peaks of Polish mountains based on a digital terrain model (DTM) with an orthophoto map as a texture. The 3D models are supplemented with a scale, cardinal direction arrows and map labels making the map fully readable and informative with no need for any additional description. The presented models can be visualised both in a web browser and in augmented reality (if viewed on a mobile device). This approach allows the user to choose their way of viewing 3D scenes, which makes the application flexible in its visualisation methods, so it can be examined by a larger amount of users and not only by those who want to use the AR experience. However, the aim of this paper is to visualise 3D landscape in augmented reality only, so the web application is not being developed at the moment.

Tab. 2 - Monitored land cover types derived from maps at a given time period

Type	Stable Cadastre (1837)	Basic Topographic Map of the Czech Republic (2023)
Arable land	Arable land	Arable land
Grassland	Meadow Pasture Garden	Meadow Garden
Forest	Coniferous, deciduous and mixed forest Park	Forest Park
Water body	Water body River	Water body River
Built-up	Built-up space	Built-up space
Other	Path and road Yard Barren land Graveyard	Path and road Yard Barren land Graveyard Farm area

Another approach in a 3D landscape visualisation was presented by Lázna [37]. He used both marker and markerless AR for showing 3D scenes. Firstly, the markerless AR method works in a standard way of placing the 3D model after a plane detection is completed. Similarly, to the previous example, the models are created on a base of DTM with a texture from aerial imagery. Lázna is presenting several different cartographic models but most of them lack any additional map information such as a scale or labels. The result is presented as a mobile application developed in Unity, which is an approach that is carried with Chudenice AR presentation as well. His second presented method, the use of marker AR, is utilized for showing virtual models placed on a 3D printed relief after recognising a QR code. This method seems to be exciting because it connects the real physical model with virtual elements, which is an approach that should be more studied in the future due to its possible implementation in museums or education [38, 39].

Visualisation of the virtual model on a 3D printed terrain model is also described by Zhang et al. [40]. Their work is concerned with the use of AR as a 3D flood visualisation method and it presents the developed method as an innovative way of displaying the threat of natural disasters in AR, which can be helpful in avoiding the threat or lessening the consequences of flood. Another great example of 3D cartographic visualisation in AR is a connection between AR and printed school atlases, which is described by Schnürer et al. [41]. Their work presents 2D and 3D visualisations of thematic cartography maps that are enhancing printed school atlas with virtual elements such as charts or maps. Similarly to most of other mentioned works, this one is developed using Vuforia engine and Unity. Schnürer et al. had to solve a problem with an AR visualisation on a curved double-sided atlas map, which they resolved by anchoring a virtual object to the page with the biggest recognized part of the map.

3D Cartographic scenes in AR should always follow the rules of cartographic visualisations. In this case, a 3D cartographic scene is understood as a large scale cartographic visualisation of a landscape scenery complemented with schematic vegetation and buildings procedurally or manually modelled. As was mentioned before, not all works handle this topic correctly. Therefore, it is very important to make sure that the presented model is well recognisable, so the user does not lose track of its details or the position of viewed area in map. This can be done in several ways, but the most straightforward approach is to label the model well, as described by Halik [36, 42]. The labels can be minimalistic and user can toggle their visibility, so the labels could be turned on only if necessary. As the user moves the mobile device around the presented object, the labels should be always facing the camera, so they are well readable from every angle.

Processing of GIS data

The GIS data were obtained from historical and contemporary large scale maps (Table 1). The historical maps were manually vectorized and the contemporary map was already obtained in a vector format. Firstly, the historical maps had to be georeferenced. The Imperial Obligatory Imprints of the Stable Cadastre 1:2,880 were georeferenced on identical points with the use of affine transformation resulting in residuals around 3 meters. The State Map 1:5,000-derived was georeferenced with the use of projective transformation based on four corner points of the map sheets with residuals around 4 meters. The used methods of georeferencing are described by Cajthaml [43, 44], Janata [45] or Balletti [46]. As for the contemporary map, the Basic Topographic Map of the Czech Republic 1:5,000 in vector format was used for obtaining large scale land cover data. The forest composition data (coniferous, deciduous and mixed) were derived from CORINE Land Cover 2018 [47].

The 3D terrain is based on a DMR5G elevation model, which is a very precise elevation model provided by the Czech State Administration of Land Surveying and Cadastre. This model is measured by the technique of airborne laser scanning with a mean elevation error between 0.18 m (exposed ground) and 0.30 m (forested ground) [21]. The terrain was converted into TIN and simplified relatively to the scale and visualisation use of the final virtual 3D models. All GIS work was done in ArcGIS Pro 3.2.

RESULTS

3D Land use models

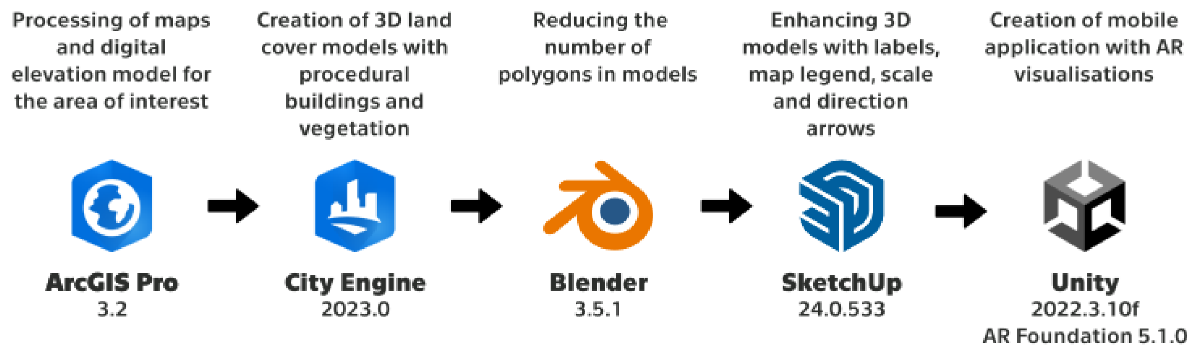

Fig. 4 – Workflow chart including used software versions

When the process of vectorization was completed, the vector data in shapefile (.shp) format were imported to City Engine (version 2023.0), where the data were used as a basis for procedural modelling. The schematic workflow chart of the data processing is shown in Figure 4. Procedural modelling generates 3D models based on rule files (.cga). These rules automatically apply a set of predefined rules for each 3D object (etc. house, tree, road) and use these rules randomly on the dataset at a set ratio. For example, user can define that 25% of the modelled houses will have hip roof, 35% will have pyramid roof and the rest will have gable roof. However, this set of rules is applied randomly or based on certain attributes of the geodata. Using .cga rules, procedurally modelled were simplified houses, forest areas and avenues based on methods described by Janovský et al. [48], Watson et al. [49] and Kitsakis et al. [50]. For a more immersive visualisation the height of a terrain was multiplied by the ratio of 1.5. Different models were generated for both tracked time periods depending on the vector land cover shapefiles.

Fig. 5 – Details of land cover 3D model

The generated 3D land cover model was then exported to Blender (version 3.5.1), where the terrain mesh had to be compressed [51] due to its visualisation on mobile platforms, which require a lower number of polygons (in 3D models) for a smoother presentation. This was done by Decimate modifier in Blender resulting in a significant decrease in a number of used polygons. Due to optimalisation of the 3D model for mobile platforms, the models of procedurally generated trees had to be also simplified, as seen in Figure 5. The coniferous trees were simplified more easily thanks to their pyramid shape. However, the deciduous trees are harder to generalise due to their rounded crown, which can be triangulated much trickier when compared to the coniferous trees.

In CAD software SketchUp (version 24.0.533), additional map information was added, such as the map scale, labels, legend and cardinal directions. The labels show the name of a viewed area and a reference year. The map legend describes the types of land cover with schematic 3D overlays (trees or buildings). Under the map legend the map scale and data sources are situated (Figure 6). Both 3D models are labelled in Czech language because they are prepared to be viewed mostly by the Czech users. Also, some of the more important or interesting buildings, such as Bolfánek observation tower (Figure 5), were modelled manually using CAD. At this point, both models were ready for visualisation in augmented reality.

Visualisation in a mobile application

From CAD software, the models were imported to Unity game engine (version 2022.3.10f) in .fbx format, which is considered as the most convenient because of its good compatibility with Unity. This step was followed by application testing, which resulted in a several repeated steps of optimalisation of the visualised models due to the limits of mobile device performance. As the test device, Samsung A14 5G (2023) was chosen, which is a lower-class device, therefore if the application runs well on this device, it is considered to be working fine on most of the current mobile phones or tablets. The AR Foundation library (version 5.1.0) with plane detection was used for the AR visualisation and it was supplemented by additional C# scripting.

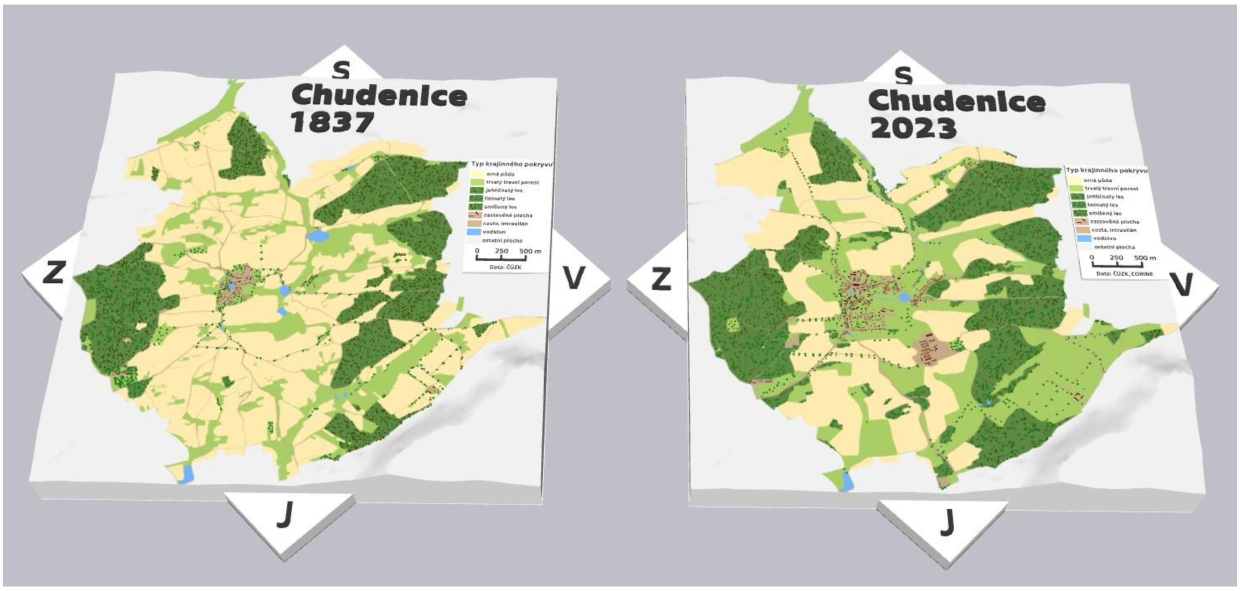

Fig. 6 – Comparison of final 3D models with land cover in 1837 (left) and 2023 (right)

The final application firstly scans the surroundings and detects any horizontal planes (e.g. table, floor) using the AR Plane Manager (AR Foundation component). In the second step, the user can visualise the 3D cartographic land cover model by tapping on the detected plane, after which the model appears (as seen in Figure 7 - left side). Now, the user can rotate, move and scale the model using finger gestures (pinch or swipe). Using the button on the top left side of the screen, all scanned horizontal planes can be hidden making the model glued to its current position. However, it can be still rotated and scaled with finger gestures (Figure 7 - right side). By locking the position of the model, the user can interact with the model without accidentally moving it, so the details or the map legend can be viewed in a larger scale.

Fig. 7 – 3D land cover visualisation in AR

DISCUSSION

The aim of this papers is to present the possibilities of visualising the development of land cover on a 3D terrain in augmented reality using native mobile application. As mentioned before, there are lot of different approaches for 3D cartographic visualisations in AR but all of them have to share two essential characteristics, which are key for the user experience and proper visualisation. The first one is a visual legibility of the model, which plays a huge role in understanding the map depicted on the 3D model (e.g. well readable text, recognizable colours or symbols). The second important characteristic is the preservation of cartographic principles, meaning that even the AR 3D model should be full-featured map with map scale, labels, legend and north orientation (if necessary).

When compared to work of Halik and Wielebski [36], the models presented in this paper share the same method of geographic orientation described by four triangles with symbols of a given cardinal direction. This seems to be the easiest way of describing the orientation of a 3D AR map. Additionally, the map legend and the map scale can be presented directly on the model regarding the shape of the Chudenice cadastral community. Also the scale of presented models is quite similar in this paper compared to their work. Both papers refer about large-scale 3D maps, which means that some details can be still preserved at this level of detail (forest composition, smaller land units, narrow pathways or types of buildings). Halik and Wielebski use orthophoto as the model texture, which could make the 3D model more visually appealing and realistic. On the other hand, the use of vectorised land cover used in this paper can give the user better awareness of the real use of certain land units throughout the whole area. Halik and Wielebski utilize the map labels very well because labels on their model aways follow the user's camera which makes the map very well readable from different angles. This feature should be incorporated to Chudenice AR map in the future.

Very important decision to consider in the future work is whether to use native mobile application built in Unity or to visualise AR models using web browser (using WebXR) as mentioned by Halik and Wielebski [36]. WebXR is easy to use for the user as they do not have to download a standalone mobile application. All they need is a standard web browser capable of visualising AR (e.g. Google Chrome or Safari), which is very convenient. On the other hand, this kind of visualisation only allows less complex models to be shown because everything is rendered via web browser. This also means that users need to have a good (and stable) internet connection, otherwise the application will not function. Although the native mobile applications require to be downloaded from Google Play or App Store, they can be viewed offline and can handle much more complex visualisations. With the use of native applications, the augmented reality can be more stable as well, which minimizes the model drifting in AR. More complex stable AR tracking methods are also (at the moment) only available through a native mobile application.

As Halik and Wielebski [36] mention, the combination of real world and virtual model create an immersive experience for the user. This experience can be enhanced by connecting the visualised models with printed maps (or map atlases) as described by Schnürer et al. [41]. The possibility of viewing 3D land cover models in AR on top of a 2D printed map (or a 3D printed model [37, 40]) will be the aim of author's future research because it is an interesting way of adding more map information that enhances the 2D/3D printed map with both static and animated cartographic data visualisations. The immersion and connection between physical and virtual environments is something that only augmented reality is capable of. Therefore, it is essential to explore its possibilities within thematic cartography and geovisualisation more deeply. AR can not only stand as another method of digital maps visualisation, but it can also visualise elements that could not be added (for different reasons) to printed 2D map. These can be interactive charts, infographics or audiovisual materials complementing and enhancing the physical printed 2D static map.

None of the above-mentioned works utilize procedural modelling for generating buildings or vegetation in AR, which is a feature that adds details to the whole 3D model, although the generated outputs are mostly schematic copies of real world. Most of the houses are procedurally generated, only few important models are created using CAD as seen in Figure 5. Although procedural modelling can be used widely in web based or VR applications rendered on a regular computer or laptop (as seen in works of Janovský et al. [48], Watson et al. [49] and Kitsakis et al. [50]), its implementation in AR can be problematic mostly due to large number of generated polygons. This can lead to problems with stability and with lagging of the AR visualisation viewed through a mobile device, which is not (in most cases) comparable in its performance to computers or laptops. Procedural modelling combined with land cover map is the core part of this paper because there can be found only little information in visualising this kind of 3D map in AR among other studies. In the future, this approach can be enhanced by adding more levels of detail for every procedurally generated object. This will lead the way to optimize this visualisation so it can be available also through using a web browser. Another way to improve and enhance the visualisation is to make it more immersive using interactive information about the map such as attributes for a selected polygon or building.

CONCLUSION

This paper is concerned with the use of augmented reality as a visualisation technique for 3D land cover cartographic models. Because the AR visualisation has its specifics, mostly as it is directly tied to a mobile device, the use case of this method may differ and certain data visualisations are more suitable than other. The land cover data are well suited for being viewed via AR because the data is well visually recognised. However, the biggest issue of the presented technique is the scale of the viewed area. It is fundamental to select smaller area, otherwise the schematic landscape elements or buildings would not be clearly visible until the model is properly scaled. However, if the model would be scaled too much, it can lose track of the scanned horizontal plane, resulting in its drifting, which can make the user experience displeasing. The larger the area is, the sparser the schematic 3D landscape (mostly trees or other landscape elements) need to be due to hardware limitations of the mobile devices. The best example for this kind of visualisation is a mountainous area (because the plasticity and the depth of the model is then depicted better without no need to manually adjust the "Z factor" - scale of vertical axis). By following this, the model depth is increased while the visual proportions remain similar. Nevertheless, the topic will be studied further, and its results will undergo user feedback to help validate the best approach of a 3D land cover visualisation in AR. The emphasis will be mostly on adjusting the level of detail, number of polygons, used colours and a size of area of interest. The advantages and disadvantages of using web or native applications for this sort of AR visualisation should also be part of future research.

ACKNOWLEDGEMENTS

This work was supported by the Grant Agency of the Czech Technical University in Prague, grant No. SGS24/049/OHK1/1T/11.

REFERENCES

[1] SHALABY, A. A., R.R. ALI a A. GAD. Urban sprawl impact assessment on the agricultural land in Egypt using remote sensing and GIS: a case study, Qalubiya Governorate. Journal of Land Use Science [online]. 2012, 7(3), 261-273 [cit. 2024-05-15]. ISSN 1747-423X. doi:10.1080/1747423X.2011.562928

[2] TORTORA, A., D. STATUTO a P. PICUNO. Rural landscape planning through spatial modelling and image processing of historical maps. Land Use Policy [online]. 2015, 42, 71-82 [cit. 2024-05-15]. ISSN 02648377. doi: 10.1016/j.landusepol.2014.06.027

[3] ALBRIGHT, M. G., C. VICKERY, R. BOWER a J. E. QUINN. Patterns of land use change, land governance, and the supply of ecosystem services in a multifunctional landscape: A case study from Upstate SC, USA. Journal of Land Use Science [online]. 2023, 2023-12-31, 18(1), 284-295 [cit. 2024-05-15]. ISSN 1747-423X. doi:10.1080/1747423X.2023.2234903

[4] SKOKANOVÁ, H., M. HAVLÍČEK, R. BOROVEC, et al. Development of land use and main land use change processes in the period 1836–2006: case study in the Czech Republic. Journal of Maps [online]. 2012, 8(1), 88-96 [cit. 2024-05-15]. ISSN 1744-5647. doi:10.1080/17445647.2012.668768

[5] SOLTANI, P. a A. H. P. MORICE. Augmented reality tools for sports education and training [online]. 2020, 155 [cit. 2024-05-31]. ISSN 03601315. doi: 10.1016/j.compedu.2020.103923

[6] LI, J., E. D. VAN DER SPEK, L. FEIJS, F. WANG a J. HU. Augmented Reality Games for Learning: A Literature Review. In: Distributed, Ambient and Pervasive Interactions. Cham: Springer International Publishing, 2017, 2017-05-18, s. 612-626. Lecture Notes in Computer Science. ISBN 978-3-319-58696-0. doi:10.1007/978-3-319-58697-7_46

[7] RAUSCHNABEL, P. A., A. ROSSMANN a M. C. TOM DIECK. An adoption framework for mobile augmented reality games: The case of Pokémon Go. Computers in Human Behavior [online]. 2017, 76, 276-286 [cit. 2024-05-31]. ISSN 07475632. doi: 10.1016/j.chb.2017.07.030

[8] MAGNENAT, S., M. GROSS, R. W. SUMNER, et al. Live Texturing of Augmented Reality Characters from Colored Drawings. IEEE Transactions on Visualization and Computer Graphics [online]. 2015, 2015-11-15, 21(11), 1201-1210 [cit. 2024-05-31]. ISSN 1077-2626. doi:10.1109/TVCG.2015.2459871

[9] CHALVATZARAS, D., N. YIANNOUTSOU, C. SINTORIS a N. AVOURIS. Do you remember that building? Exploring old Zakynthos through an augmented reality mobile game. In: 2014 International Conference on Interactive Mobile Communication Technologies and Learning (IMCL2014). IEEE, 2014, s. 222-225. ISBN 978-1-4799-4742-3. doi:10.1109/IMCTL.2014.7011136

[10] NOH, Z., M. S. SUNAR a Z. PAN. A Review on Augmented Reality for Virtual Heritage System. In: Learning by Playing. Game-based Education System Design and Development. Berlin, Heidelberg: Springer Berlin Heidelberg, 2009, s. 50-61. Lecture Notes in Computer Science. ISBN 978-3-642-03363-6. doi:10.1007/978-3-642-03364-3_7

[11] PAVELKA JR., K. a J. PACINA. Using of modern technologies for visualization of cultural heritage. Stavební obzor - Civil Engineering Journal [online]. 2023, 2023-12-31, 32(4), 549-563 [cit. 2024-05-31]. ISSN 1805-2576. doi:10.14311/CEJ.2023.04.0041

[12] BINTI MAT SAH, S. B., N. TECK CHYAN a S. BINTI HISHAM. Interactive augmented reality art book to promote Malaysia traditional game. In: 2014 International Conference on Computer, Communications, and Control Technology (I4CT). IEEE, 2014, s. 203-208. ISBN 978-1-4799-4555-9. doi:10.1109/I4CT.2014.6914175

[13] WÜEST, R. a S. NEBIKER. Geospatial Augmented Reality for the interactive exploitation of large-scale walkable orthoimage maps in museums. In: Proceedings of the ICA. 2018, s. 1-6. ISSN 2570-2092. doi:10.5194/ica-proc-1-124-2018

[14] ECKERT, M., J. S. VOLMERG a C. M. FRIEDRICH. Augmented Reality in Medicine: Systematic and Bibliographic Review. JMIR mHealth and uHealth [online]. 2019, 7(4) [cit. 2024-05-31]. ISSN 2291-5222. doi:10.2196/10967

[15] SAIDIN, N. F., N. D. ABD HALIM a N. YAHAYA. A Review of Research on Augmented Reality in Education: Advantages and Applications. International Education Studies [online]. 2015, 2015-06-25, 8(13) [cit. 2024-05-31]. ISSN 1913-9039. doi:10.5539/ies.v8n13p1

[16] TANG, J. K.T., W. LAU, K. CHAN a K. TO. AR interior designer: Automatic furniture arrangement using spatial and functional relationships. In: IEEE, 2014, s. 345-352. ISBN 978-1-4799-7227-2. doi:10.1109/VSMM.2014.7136652

[17] DE PACE, F., F. MANURI a A. SANNA. Augmented Reality in Industry 4.0. American Journal of Computer Science and Information Technology [online]. 2018, 06(01) [cit. 2024-05-31]. ISSN 23493917. doi:10.21767/2349-3917.100017

[18] BOTTANI, E. a G. VIGNALI. Augmented reality technology in the manufacturing industry: A review of the last decade. IISE Transactions [online]. 2019, 2019-03-04, 51(3), 284-310 [cit. 2024-05-31]. ISSN 2472-5854. doi:10.1080/24725854.2018.1493244

[19] DĚDKOVÁ, P. a S. POPELKA. VIRTUAL 3D RESTORATION OF AN EXTINCT VILLAGE AND ITS EYE-TRACKING ASSESSMENT. Journal of Mobile Multimedia [online]. 2015, 11(3), 181–192 [cit. 2024-05-28]. https://journals.riverpublishers.com/index.php/JMM/article/view/4497

[20] PACINA, J., J. CAJTHAML, D. KRATOCHVÍLOVÁ, J. POPELKA, V. DVOŘÁK a T. JANATA. Pre - dam valley reconstruction based on archival spatial data sources: Methods, accuracy, and 3D printing possibilities. Transactions in GIS [online]. 2022, 26(1), 385-420 [cit. 2024-05-28]. ISSN 1361-1682. doi:10.1111/tgis.12854

[21] STATE ADMINISTRATION OF LAND SURVEYING AND CADASTRE. Digital Terrain Model of the Czech Republic of the 5th generation (DMR 5G) [online]. 2023 [cit. 2024-12-12]. https://cuzk.cz/en

[22] CARMIGNIANI, J., B. FURHT, M. ANISETTI, P. CERAVOLO, E. DAMIANI a M. IVKOVIC. Augmented reality technologies, systems and applications. Multimedia Tools and Applications [online]. 2011, 51(1), 341-377 [cit. 2024-05-31]. ISSN 1380-7501. doi:10.1007/s11042-010-0660-6

[23] MILGRAM, P. a F. KISHINO. A Taxonomy of Mixed Reality Visual Displays. IEICE TRANSACTIONS on Information and Systems. 1994, E77-D(12), 1321–1329. ISSN 0916-8532.

[24] SKARBEZ, R., M. SMITH a M. C. WHITTON. Revisiting Milgram and Kishino's Reality-Virtuality Continuum. Frontiers in Virtual Reality [online]. 2021, 2021-3-24, 2 [cit. 2024-05-22]. ISSN 2673-4192. doi:10.3389/frvir.2021.647997

[25] TREMOSA, L. Beyond AR vs. VR: What is the Difference between AR vs. MR vs. VR vs. XR? Interaction Design Foundation [online]. [cit. 2024-05-15]. https://www.interaction-design.org/literature/article/beyond-ar-vs-vr-what-is-the-difference-between-ar-vs-mr-vs-vr-vs-xr

[26] PEDDIE, J. Types of Augmented Reality. In: Augmented Reality [online]. Springer Cham, 2017, s. 29–46 [cit. 2024-05-22]. ISBN 978-3-319-54502-8. https://link.springer.com/chapter/10.1007/978-3-319-54502-8_2

[27] SYED, T. A., M. S. SIDDIQUI, H. B. ABDULLAH, S. JAN, A. NAMOUN, A. ALZAHRANI, A. NADEEM a A. B. ALKHODRE. In-Depth Review of Augmented Reality: Tracking Technologies, Development Tools, AR Displays, Collaborative AR, and Security Concerns. Sensors [online]. 2023, 23(1) [cit. 2024-05-22]. ISSN 1424-8220. doi:10.3390/s23010146

[28] DARGAN, S., S. BANSAL, M. KUMAR, A. MITTAL a K. KUMAR. Augmented Reality: A Comprehensive Review. Archives of Computational Methods in Engineering [online]. 2023, 30(2), 1057-1080 [cit. 2024-05-31]. ISSN 1134-3060. doi:10.1007/s11831-022-09831-7

[29] ROHS, M., J. SCHÖNING, M. RAUBAL, G. ESSL a A. KRÜGER. Map navigation with mobile devices. Proceedings of the 9th international conference on Multimodal interfaces [online]. New York, NY, USA: ACM, 2007, 2007-11-12, 146-153 [cit. 2024-05-31]. ISBN 9781595938176. doi:10.1145/1322192.1322219

[30] GILL, L. a E. LANGE. Getting virtual 3D landscapes out of the lab. Computers, Environment and Urban Systems [online]. 2015, 54, 356-362 [cit. 2024-05-31]. ISSN 01989715. doi: 10.1016/j.compenvurbsys.2015.09.012

[31] BREJCHA, J., M. LUKÁČ, Y. HOLD-GEOFFROY, O. WANG a M. ČADÍK. LandscapeAR: Large Scale Outdoor Augmented Reality by Matching Photographs with Terrain Models Using Learned Descriptors. In: Computer Vision – ECCV 2020. Cham: Springer International Publishing, 2020, 2020-10-07, s. 295-312. Lecture Notes in Computer Science. ISBN 978-3-030-58525-9. doi:10.1007/978-3-030-58526-6_18

[32] Census 2021. Czech Statistical Office [online]. 2021 [cit. 2024-05-28]. https://scitani.gov.cz/

[33] KUČA, K. Krajinná památková zóna Chudenicko. In: Krajinné památkové zóny České republiky. Praha: Národní památkový ústav, 2015, s. 188–193. ISBN 978-80-7480-045-0.

[34] ŠANTRŮČKOVÁ, M. Krajinářská tvorba Jana Rudolfa Černína: Vznik a vývoj parků v Krásném Dvoře, Jemčině, Petrohradě a Chudenicích. Praha: Karolinum, 2014, 316 s. ISBN 978-80-246-2397-9.

[35] DRNEK, J., O. BRACHTEL a J. KUBEC. Chudenice – městečko pod sv. Wolfgangem – I. díl. Netoliko, 2022. ISBN 978-80-907142-1-2.

[36] HALIK, Ł. a Ł. WIELEBSKI. Usefulness of Plane-Based Augmented Geovisualization—Case of “The Crown of Polish Mountains 3D.” ISPRS International Journal of Geo-Information [online]. 2023, 12(2) [cit. 2024-05-23]. ISSN 2220-9964. doi:10.3390/ijgi12020038

[37] LÁZNA, R. Geovizualizace založené na integraci 3D fyzických modelů terénu a rozšířené reality [online]. Olomouc, 2023 [cit. 2024-05-20]. https://theses.cz/id/teqjtl/. Diplomová práce. Univerzita Palackého v Olomouci, Přírodovědecká fakulta, Katedra geoinformatiky.

[38] ADEDOKUN-SHITTU, N. A., A. H. AJANI, K. M. NUHU a A. K. SHITTU. Augmented reality instructional tool in enhancing geography learners academic performance and retention in Osun state Nigeria. Education and Information Technologies [online]. 2020, 25(4), 3021-3033 [cit. 2024-05-31]. ISSN 1360-2357. doi:10.1007/s10639-020-10099-2

[39] ELMQADDEM, N. Augmented Reality and Virtual Reality in Education. Myth or Reality? International Journal of Emerging Technologies in Learning (iJET) [online]. 2019, 2019-02-14, 14(03), 234-242 [cit. 2024-05-31]. ISSN 1863-0383. doi:10.3991/ijet.v14i03.9289

[40] ZHANG, G., J. GONG, Y. LI, et al. An efficient flood dynamic visualization approach based on 3D printing and augmented reality. International Journal of Digital Earth [online]. 2020, 2020-11-01, 13(11), 1302-1320 [cit. 2024-05-31]. ISSN 1753-8947. doi:10.1080/17538947.2019.1711210

[41] SCHNÜRER, R., C. DIND, S. SCHALCHER, P. TSCHUDI a L. HURNI. Augmenting Printed School Atlases with Thematic 3D Maps. Multimodal Technologies and Interaction [online]. 2020, 4(2) [cit. 2024-05-23]. ISSN 2414-4088. doi:10.3390/mti4020023

[42] HALIK, Ł. The analysis of visual variables for use in the cartographic design of point symbols for mobile Augmented Reality applications. Geodesy and Cartography. 2012, 61(1), 19–30.

[43] CAJTHAML, J. METHODS OF GEOREFERENCING OLD MAPS ON THE EXAMPLE OF CZECH EARLY MAPS. In: Proceedings of the 25th International Cartographic Conference. 2011. ISBN 978-1-907075-05-6.

[44] CAJTHAML, J. POLYNOMIAL GEOREFERENCING METHOD FOR OLD MAP SERIES. In: 13th International Multidisciplinary Scientific GeoConference SGEM 2013. 2013, s. 859–866. ISBN 978-1-62993-275-0. ISSN 1314-2704.

[45] JANATA, T. a J. CAJTHAML. Georeferencing of Multi-Sheet Maps Based on Least Squares with Constraints—First Military Mapping Survey Maps in the Area of Czechia. Applied Sciences [online]. 2021, 11(1) [cit. 2024-06-05]. ISSN 2076-3417. doi:10.3390/app11010299

[46] BALLETTI, C. Georeference in the analysis of the geometric content of early maps. E-Perimetron [online]. 2006, 1(1), 32–39 [cit. 2024-06-05].

[47] COPERNICUS. CORINE Land Cover 2018 (vector/raster 100 m), Europe, 6-yearly [online]. 2019 [cit. 2024-06-14]. https://land.copernicus.eu/en/products/corine-land-cover/clc2018

[48] JANOVSKÝ, M, P TOBIÁŠ a V CEHÁK. 3D Visualisation of the Historic Pre-Dam Vltava River Valley—Procedural and CAD Modelling, Online Publishing and Virtual Reality. ISPRS International Journal of Geo-Information [online]. 2022, 11(7) [cit. 2024-06-05]. ISSN 2220-9964. doi:10.3390/ijgi11070376

[49] WATSON, B., P. M, O. VERYOVKA, A. FULLER, P. WONKA a C. SEXTON. Procedural Urban Modeling in Practice. IEEE Computer Graphics and Applications [online]. 2008, 28(3), 18-26 [cit. 2024-06-05]. ISSN 0272-1716. doi:10.1109/MCG.2008.58

[50] KITSAKIS, D., E. TSILIAKOU, T. LABROPOULOS a E. DIMOPOULOU. PROCEDURAL 3D MODELLING FOR TRADITIONAL SETTLEMENTS. THE CASE STUDY OF CENTRAL ZAGORI. The International Archives of the Photogrammetry, Remote Sensing and Spatial Information Sciences [online]. 2017, XLII-2/W3, 369-376 [cit. 2024-06-05]. ISSN 2194-9034. doi:10.5194/isprs-archives-XLII-2-W3-369-2017

[51] JANEČKA, K. a L. VÁŠA. Compression of 3D Geographical Objects at Various Level of Detail. In: The Rise of Big Spatial Data. Cham: Springer International Publishing, 2017, 2017-10-15, s. 359-372. Lecture Notes in Geoinformation and Cartography. ISBN 978-3-319-45122-0. doi:10.1007/978-3-319-45123-7_26

Article no. 4

THE CIVIL ENGINEERING JOURNAL 1-2025

EFFECT OF FIBERS ON SELF-HEALING PROPERTIES OF MICROBIAL MINERALIZED CEMENT MORTARS

Shijie Wang[1,2], Buyuan Zhang[3], Yunpeng Zhao[3], Minggang Sun[1], Xinzhi Wang[1] and Hexiang Wu[3]

1. *Longjian Road & Bridge Company Limited, Harbin, 150096, China*
2. *College of Civil and Architectural Engineering, Heilongjiang Institute of Technology, Harbin, 150050, China*
3. *School of Civil Engineering and Transportation, Northeast Forestry University, Harbin, 150040, China*

Received: *10.09.2024*
Received in revised form: *30.12.2024*
Accepted: *12.03.2025*

ABSTRACT

In this study, we selected cement mortar as the research object, used the expanded perlite (EP) which adsorbed bacteria as the self-healing agent, and mixed basalt fibers to improve the properties. The effects of different dosages and sizes of self-healing agent and basalt fibers on the mechanical properties and self-healing properties of cement mortar were investigated by compressive strength, SEM, EDS, XRD, and optical microscopy tests. The results of the study showed that under the perfect conditions for ideal bacterial activity, the bacteria were able to survive in cement mortar using expanded perlite as a carrier and induced the generation of calcium carbonate precipitates to fill the cracks. The healing agent can significantly improve the self-healing property of mortar, and the fibers can adsorb metabolic precipitates to improve the self-healing rate of mortar. The simultaneous addition of healing agent and basalt fibers can realize the complementary advantages. By adding a small amount of healing agent and a moderate amount of fibers, we achieve 100% self-healing performance, and at the same time improve the compressive strength of mortar. In this study, the addition of 10% self-healing agent and 0.1% volume fraction of 6mm long basalt fibers can not only achieve 100% self-healing performance, but also increase the compressive strength of the mortar by 7.96% when the curing age is 28 days.

KEYWORDS

Cement mortars, Bacteria; Basalt fibre, Self-healing, Mechanical property

INTRODUCTION

Concrete is one of the most widely used construction materials in the world, with applications ranging from infrastructure construction to high-rise buildings [1]. Despite its excellent compressive strength and durability, the brittle nature of concrete makes it susceptible to cracks when subjected to tensile stresses [2]. These cracks not only affect the overall strength of the concrete structure, but also lead to the infiltration of water, chloride ions, and other corrosive substances, which accelerates the corrosion of the rebar and shortens the service life of the structure [3-5].

How to effectively repair concrete cracks and extend the service life of the structure has been an important research topic in the field of civil engineering. The traditional concrete crack repair methods mainly include physical and chemical methods, such as grouting and daubing repair materials [6,7]. However, these methods often have limitations such as high repair cost, unsustainable effect, and polluting the environment. In order to overcome these limitations, in recent years, academic circles and engineering circles have begun to explore the use of biotechnological means to repair concrete cracks, wherein, Microbially Induced Calcium Carbonate Precipitation (MICP) has become a hotspot of the research due to its unique advantages. The main principle of Microbially Induced Calcium Carbonate Precipitation (MICIC) is a bioremediation technique that utilizes microbial metabolic activities to precipitate calcium carbonate at cracks [8-12]. Compared with traditional repair methods, MICP technology has the following significant advantages: economy and environmental friendliness.

For MICP technology to repair cracks, the survival rate of microorganisms in cement mortar directly affects the level of repair rate of cracks. The hydration reaction of cement during the mixing process leads to a very high alkalinity within the concrete, with a pH value of approximately 11-13 [12]. At the same time, the continuous hardening of the concrete during the curing process also squeezes the living space of the internal bacteria and thus causes bacterial death. Therefore, the bacteria incorporated into the mortar must be able to adapt to the highly alkaline environment. Bacillus is an alkalophilic solitary anaerobic spore-producing bacterium that can produce spores and survive in highly alkaline environment, and it is the most widely used microorganism in related research at present [13]. However, some studies have also shown that placing bacteria in concrete for a long period of time leads to a decrease in the survival rate of spores [14-16]. This is due to the high alkalinity of the internal environment of the concrete, and the products of the hydration reaction compress the internal environmental space, resulting in the death of some bacteria. Therefore, the problem of bacterial survival should be considered when incorporating bacteria into geopolymer mortar. Fixing the bacterial spores in the protective carrier can significantly increase the survival rate of bacteria and enhance the self-healing ability of concrete. Expanded perlite (EP), limestone powder (LSP), ceramsite and their modified materials are common bacterial carriers that can increase the survival rate of bacteria, increase the ultimate self-healing width of cracks in concrete, and improve the self-healing efficiency of concrete [17-20]. Among them, fibers, as a common additive material in concrete, can also be used as a carrier for bacteria. The fibers were modified with high temperature or alkali solution, and the bacteria was adsorbed on the fiber surface and incorporated into the concrete [21]. This can not only effectively weaken deformation localization, reduce damage degree, enhance fracture bridging, and improve the mechanical properties and durability of concrete through prolonging plastic deformation and preventing breakage by fibers, but also be beneficial to the early repair of microcracks, and significantly improve the self-healing performance of concrete [21-25].

In this study, we selected the cement mortar as the research object, used the expanded perlite (EP) which adsorbed bacteria as the self-healing agent, and replaced the standard sand by equal volume. Meanwhile, we considered mix basalt fibers (BF) to improve the performance of the mortar. We tested the mechanical properties of cement mortar based on microbial mineralization by experiments, observed the self-healing properties of macroscopic cracks, and revealed the coupling mechanism of incorporated microorganism and fibers to improve the properties of geopolymer mortars.

MATHERIALS AND METHODS

Materials

Cement

The cement used in the test is P.042.5R ordinary Portland Cement produced by Ningguo Cement Factory of Anhui Conch Cement Co., Ltd. Its chemical composition is shown in Table 1.

Tab. 1 - Chemical Composition of the Cement

Chemical Composition	CaO	SiO_2	Al_2O_3	Fe_2O_3	Na_2O	K_2O	SO_3	MgO
Content (%)	64.84	20.14	4.94	3.83	0.25	0.88	3.02	1.34

Expanded perlite

The inorganic porous material used in the test is expanded perlite, which was purchased through Shanhe New Material Co., Ltd, Xinyang City, Henan Province. The basic parameters of expanded perlite are shown in Table 2. The diameter of the expanded perlite used in the test is in the range of 2~4mm, as shown in Figure 1, which is the morphological characteristics of the expanded perlite and its microscopic characterization under the electron scanning microscope. The adsorption rate of expanded perlite is low, but the open part of the pores absorbs solution faster than other aggregates, it is often used as a protective carrier for bacteria, and can protect the bacteria from the influence of cement hydration reaction in the mortar to ensure the survival capacity of the bacteria.

Tab. 2 - Basic Parameters of the Expanded Perlite

Chemical Composition	SiO_2	Al_2O_3	Na_2O	K_2O	Fe_2O_3	CaO	MgO	Others	Loss on Ignition
Content (%)	73.72	14.25	4.24	3.95	0.86	0.76	0.32	0.44	1.46

(a) Macroscopic Appearance *(b) Scanning Electron Microscopy Features*

Fig. 1 - Expanded Perlite

The basalt fibers used in the test were produced by Changsha Ningxiang Building Materials Co., Ltd, with lengths of 6 mm and 12 mm respectively, diameters of 17 μm, specific gravities of 2.8~3.3 g/cm3, and elastic modulus of 100 GPa. The morphology of the basalt fibers is shown in Figure 2. In the concrete, basalt fibers tend to create agglomerates. In order to avoid such problems, basalt fibers should be fully separated before mixing.

(a) 6mm *(b) 12mm* *(c) Comparison*

Fig. 2 - Basalt Fibers Morphology

Culture of Bacteria and Preparation of Self-healing Agents

The bacteria used in this study is Bacillus Pseudofirmus (CICC 10722), which was purchased from China Center of Industrial Culture Collection (CICC). It has the characteristics of high temperature resistance, strong ability of secreting enzymes, and high efficiency of spore transformation into bacteria. The reaction mechanism for the conversion of calcium lactate to calcium carbonate by Bacillus Pseudofirmus is as follows [26-28]:

$$CaC_6H_{10}O_6+6O_2 \rightarrow CaCO_3\downarrow+5H_2O+5CO_2 \quad (1)$$

The process of bacterial culture is as follows: Firstly, we prepared a solid medium for bacterial solution, and the main material was nutrient gravy agar. In addition, when cultivating Bacillus, it was also necessary to add an additional 5mg of $MnSO_4 \cdot H_2O$ to promote the growth of Bacillus. Then, we sterilized the culture medium and adjusted the pH value of the culture medium to 9.7 using a sterile solution of 1mol/L sodium sesquicarbonate. Finally, we poured the adjusted medium and bacterial mixture into a conical flask and placed it on a constant temperature shaker to culture for 24 hours at a temperature of 30℃ and an oscillation frequency of 120r/min. After the culture was completed, we centrifuged it at 8000rpm for 5 minutes, and collected bacterial spores and diluted them with distilled water to obtain the required bacterial concentration.

Expanded perlite cannot be used directly to adsorb bacteria. Firstly, we took out enough expanded perlite into a large beaker and poured enough water to fill the beaker to clean the expanded perlite. The low-density expanded perlite would float on the water surface and the impurities would be deposited to the bottom of the water. Then, we placed the cleaned expanded perlite on a filter screen to filter the water, evenly spread the expanded perlite in the rectangular tray after the water was filtered, and weighed and recorded the common weight of the tray and expanded perlite. Finally, we placed the expanded perlite in the drying box and adjusted the temperature for drying. In the process of drying, we took out and weighed a portion of the expanded perlite at regular intervals until the weight of the expanded perlite remained constant. At this point, the dried expanded perlite could be used as a carrier for the solidified bacteria.

After preparing the expanded perlite, we took out the pre-configured bacterial solution and shaked it well to ensure that the bacterial solution could be evenly distributed in the culture solution. We measured the required distilled water according to the demand of bacterial concentration, and mixed the distilled water with the bacterial solution to prepare the bacterial solution of specific concentration, and the bacterial solution could be evenly distributed in the water by continuing to stir. After completing the dilution of the bacterial solution, we poured the above-mentioned spare expanded perlite into the bacterial solution container to absorb the bacterial solution. There was a problem of the expanded perlite floating on the upper surface of the liquid due to its low density. Therefore, it was necessary to use a plastic film to cover the upper surface of the liquid and apply downward pressure with a heavy object so that all the expanded perlites could be suspended in the liquid to fully absorb the bacterial solution. After standing at room temperature for 24 hours, we removed the plastic film on the upper surface of the container, and poured the mixture of the expanded perlite and bacterial solution in the container into a funnel net to separate the outflow liquid. We evenly spread the expanded perlite adsorbed with bacterial solution on the tray for weighing, after adjusting the oven to 40°C, we placed the tray into the oven for drying. We removed and weighed the tray at regular intervals until the weight of the tray remained constant, indicating that the expanded perlite was completely dry. Compared with the weighing results of the expanded perlite before absorbing the bacteria, it could be seen that the weight of the expanded perlite increased by 8 grams per 100 grams, which indicated that the bacteria had been adsorbed to the interior of the expanded perlite. This result is consistent with the research result of Tziviloglou[29] et al.

Specimen Preparation

Cement mortar specimens were prepared using ISO standard sand, ordinary Portland cement, tap water and expanded perlite loaded with bacteria. According to the test purpose, the mix ratio was designed, and ten groups of cement mortar specimens with different mix ratios of admixtures were determined, as shown in Table 3. Among them, the expanded perlite (EP) specimens mixed with immobilized bacteria only were used as the control group, with the dosage of 10% and 30% equal volume instead of standard sand, respectively, and the codes were labeled as groups P1 and P6. The cement mortar with 10% expanded perlite was further added with 0.1% volume fraction of 6mm fibers and 12mm fibers, and 0.5% volume fraction of 6mm fibers and 12mm fibers, respectively, and the codes were labeled as P2, P3, P4, and P5. The cement mortar with 30% expanded perlite was further added with 0.1% volume fraction of 6mm fibers and 12mm fibers, and 0.5% volume fraction of 6mm fibers and 12mm fibers, respectively, and the codes were labeled as P7, P8, P9 and P10.

Tab. 3 - Mix Ratio of Cement Mortar Specimens

Group	Code	Water (g)	Cement (g)	Sand (g)	Expanded Perlite (g)	Basalt Fibers (g)
EP10	P1	175	350	630	4.7	—
EP6F10-0.1	P2	175	350	630	4.7	0.5
EP12F10-0.1	P3	175	350	630	4.7	0.5
EP6F10-0.5	P4	175	350	630	4.7	2.5
EP12F10-0.5	P5	175	350	630	4.7	2.5
EP30	P6	175	350	490	14.1	—
EP6F30-0.1	P7	175	350	490	14.1	0.5
EP12F30-0.1	P8	175	350	490	14.1	0.5
EP6F30-0.5	P9	175	350	490	14.1	2.5
EP12F30-0.5	P10	175	350	490	14.1	2.5

The preparation process of the cement mortar specimens is as follows:

(1) We poured the weighed cement, standard sand, expanded perlite with solid bacteria, and fibers into the mixer, and the mixture was dried stir at low speed for 30 seconds to fully mix the raw materials.

(2) We added water, and the mixture was continued to be stirred at low speed for 60 seconds, and then we used a shovel to treat the mortar bonded to the inner wall and the bottom layer of the mixing pot, and fully mixed the raw materials.

(3) We stirred the mixture at high speed for 90 seconds, then stopped stirring.

(4) We poured the mortar into the mold and vibrated it thoroughly. Then we used polyethylene film to wrap the surface of the mold to prevent the loss of water in the mortar, demolded after 24 hours of curing, and put it into 20±1℃ water to continue curing.

Preparation and healing methods of cracks

In the process of studying the effect of bacteria-adsorbed expanded perlite and fibers on the self-healing ability of mortar, it was necessary to preform cracks on the specimens that have completed the curing. The preparation process of cracks is shown in Figure 3. Among them, the cement mortar specimens were maintained for 28 days. Firstly, we put the cube specimen with a side length of 40mm into the compressive test area of YAW-300H universal material testing machine, and placed a needle with a diameter of 1.5mm and a length of 1cm at the bottom of the specimen. Then, we turned on the pressure tester to apply pressure, and set the compression speed of the press to 2.4 kN/s. When the applied pressure reached about 7 kN, the specimen would crack. At this point, we stopped the continued application of pressure and the specimen formed a crack on both sides that was wider at the bottom and thinner at the top. To prevent the pre-cracked specimen from fracturing as a whole, we could wrap the specimen with black insulating waterproof tape to maintain the integrity of the specimen.

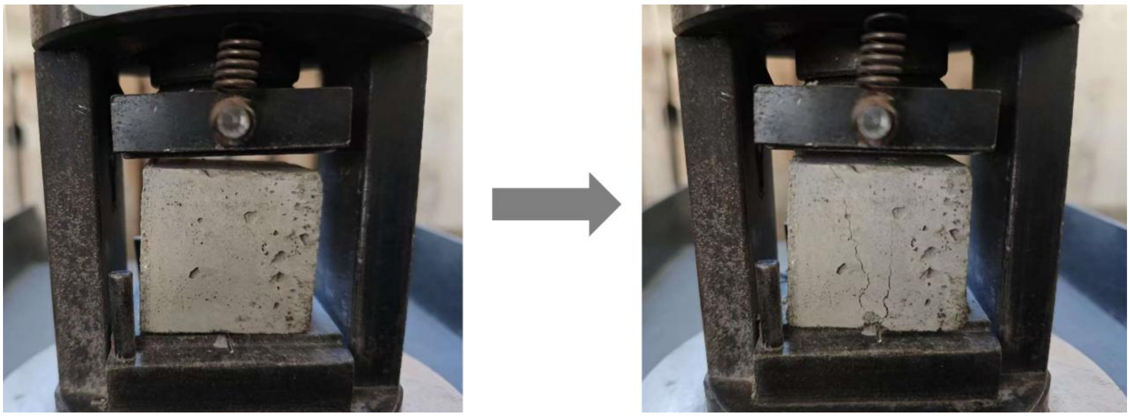

Fig. 3 - Preparation of Cracks

During the self-repairing process of mortar, bacteria required water and a calcium source. Therefore, during the self-repairing period, we placed the specimen in water, and added an appropriate amount of calcium lactate to the water, and stirred until uniform. According to the research report of Ryparová [31], the spores of Bacillus pseudostrongylus were able to survive in the temperature range from -20°C to 140°C and showed optimal reproductive and metabolic efficiency at 30°C. Therefore, in the process of self-healing curing of the specimen, we placed a constant temperature heater to keep the water temperature constant at 30℃. Since the mineralization process of Bacillus pseudotoughii required the involvement of oxygen, we used a small oxygenating pump to aerate the water to keep Bacillus pseudotoughii at its most metabolically active state. The results of this study were obtained based on the activity of bacteria under the above ideal perfect conditions.

Testing Process

Compression Experiment

We used YAW-300H universal material testing machine to carry out the compressive test, as shown in Figure 4. We put the maintained cube mortar specimen into the compressive test area of the testing machine. During the test, the compression speed was controlled to be 2.4kN/s. When the specimen reached the limit state and broke, we stopped the test and recorded the load value P at the time of failure. Formula (2) was used to calculate the compressive strength of the specimen.

$$\sigma = \frac{P}{b^2} \tag{2}$$

where P is the failure load, b is the side length of the cube specimen.

DOI 10.14311/CEJ.2025.01.0004

Fig. 4 - YAW-300H Universal Material Testing Machine

Crack Observation

(1) Pictorial representation

After the specimen completed pre-cracking, we marked both sides of the crack using a red waterproof neutral pen to facilitate observation of the healing progress of the crack. On day 0, 3, 7 and 28 of the healing of the specimen, we observed the crack using a GAOPIN GP-660V microscope, and measured the crack-marked areas using the software VPAPlatform, which is matched with the microscope, and took photos to record the results of the width of the cracks, as shown in Figure 5. We calculated the crack repair rate according to the crack widths measured at different repair ages. The calculation formula is shown in formula (3).

$$R_w = \frac{W_0 - W_t}{W_0} \times 100\% \tag{3}$$

where R_w is the crack repair rRate, W0 is average width of the initial crack, Wt is Average width of the crack at healing time t.

Fig. 5 - GAOPIN GP-660V Microscope

(2) Healing rate of the crack area

After using VPAPlatform software to photograph the specimen with crack, we imported the image into ImageJ software and set the scale, then selected the crack area and used the analyze function to calculate the crack area. We calculated the healing rate of the crack area according to the area measured before pre-cracking and after 28 days of curing, and the calculation formula was shown in Formula (4).

$$\omega = \frac{S_0 - S_t}{S_0} \times 100\% \tag{4}$$

where ω is the healing rate of the crack area, S_0 is crack area at pre-cracking, S_t is crack area at repair age of t days.

Microscopic Analysis of Healing Products

After the pre-cracked mortar specimen was maintained in water for 28 days, we took out the specimen and wiped the surface moisture, put it into an oven at 50 ° C, took out and weighed at regular intervals until constant weight. Then, we collected the product at the crack of the specimen, and observed and analyzed the microstructure of the product by SEM, EDS and XRD tests.

RESULTS

Compressive Strength

Compressive strength is one of the basic mechanical properties of concrete, and it is also a common evaluation index of concrete properties. The cement mortar specimen with the size of 40mm×40mm×40mm was prepared for compressive strength test experiments. Figure 6 gives the results of compressive strength test of specimens at day 3, 7 and 28 with different mix proportions of admixtures in cement mortar. As shown in the figure, the cement particles continuously underwent hydration reaction during the curing process and the compressive strength of the cement mortar specimens increased with the increase of curing age. By comparing the test results in Figure 6 (a) and (b), it could be found that the compressive strength of the cement mortar specimens decreased with the increase of the expanded perlite dosage. This was due to the large amount of internal pores of expanded perlite and lower strength. Adding expanded perlite to the cement mortar specimens increased the porosity of the cement mortar and decreased the average strength of the cement mortar [32]. In addition, it could be seen from the figure that the effect of fibers on the compressive strength of cement mortar was not the same when expanding perlite with different dosages of solid-loaded bacteria was added to the cement mortar.

As shown in Figure 6 (a), when 10% bacteria-adsorbing expanded perlite was added to the cement specimens, with the increase of the dosage of basalt fibers, the compressive strength of the cement mortar specimens showed a trend of first increasing and then decreasing. This indicated that the moderate addition of fibers could improve the compressive strength of cement mortar, and excessive addition of fibers would reduce the compressive strength of cement mortar. This was because the fibers played a bridging role in the cement mortar, which could limit the formation and expansion of cracks and improve the compressive strength of the cement mortar. With the increasing dosage of basalt fibers, the fibers would agglomerate inside the cement mortar. The fibers were not only not embedded into the cement mortar to form a tight whole, but also formed pores in the cement mortar, which reduced the strength of the cement mortar [33]. Under the condition of low fibers dosage, with the increase of the length of the basalt fibers, the compressive strength of the cement mortar specimens also showed the trend of first increasing and then decreasing; under the condition of high fibers dosage, with the increase of the length of the basalt fibers, the change of compressive strength of the cement mortar specimens was not obvious. This was because under the condition of low fibers dosage, short fibers were more easily embedded in the cement mortar to play a bridging role, improve the compressive strength of the cement mortar, while long fibers were easy to agglomerate in the cement mortar and reduce the compressive strength of the cement mortar. Under the condition of high fibers dosage, both short fibers and long fibers agglomerated inside the cement mortar, which reduced the compressive strength of the cement mortar.

As shown in Figure 6 (b), when 30% bacteria-adsorbing expanded perlite was added to the cement specimen, with the increase of the dosage of bacteria-adsorbing expanded perlite, the effect of basalt fibers dosage showed differences. With the increase of the dosage of basalt fibers, the compressive strength of the cement mortar specimens showed an increasing trend within a certain range. Compared with the control group (P6), the compressive strength of all the specimens showed increase to varying degrees. This was because the increase of expanded perlite dosage led to more pores in the specimens, and the bridging effect of basalt fibers was more obvious. By connecting the pores, the loss of compressive strength of the specimens was reduced, and the optimal dosage of basalt fibers was therefore increased. In addition, with the increase of the dosage of bacteria-adsorbing expanded perlite, the effect of the adding length of basalt fibers also showed differences. Under the condition of different fibers dosage, with the increase of the length of basalt fibers, the compressive strength of the cement mortar specimens all showed a tendency of increasing first and then decreasing. This was because short fibers were more easily embedded in cement mortar and played a bridging role to improve the compressive strength of cement mortar, while long fibers were more likely to agglomerate in cement mortar and reduce the compressive strength of cement mortar. Moreover, even under the condition of high fibers dosage, there were a large number of pore dispersed short fibers in the expanded perlite with high dosage, and short fibers would not agglomerate inside the cement mortar.

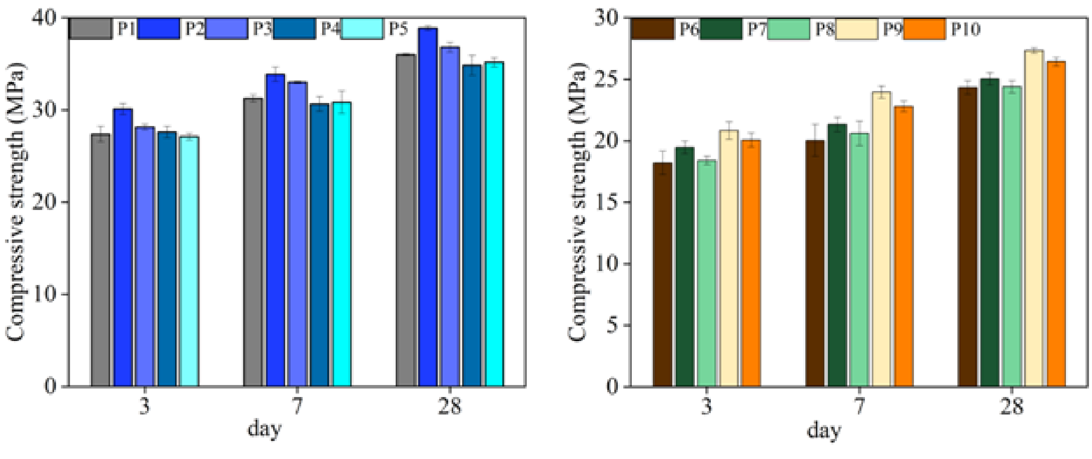

(a) 10% Expanded Perlite Specimens *(b) 30% Expanded Perlite Specimens*

Fig. 6 - Column Charts of Compressive Strength Tests

Figure 7 gives the variation relationship between the compressive strength and the length of basalt fibers of specimens with 10% expanded perlite added at different curing ages. As shown in the figure, when the volume fraction of basalt fibers was 0.1%, the compressive strength of the

DOI 10.14311/CEJ.2025.01.0004

mortar specimens added with 6 mm (P2) and 12 mm (P3) long fibers improved to different degrees compared with the control mortar specimens (P1) without fibers. Among them, the mortar specimens added with 6mm long basalt fibers had the most significant compressive strength improvement effect, and the growth rate could reach 7.96% when the curing age was 28 days. When the volume fraction of basalt fibers was 0.5%, the change of compressive strength of the mortar specimens with 6mm (P4) and 12mm (P5) long fibers was not obvious. When the curing age was 28 days, the compressive strength of the mortar specimens even decreased, with a decrease rate of 3.24% and 2.31% respectively.

Figure 8 gives the variation relationship between the compressive strength and the length of basalt fibers of specimens with 30% expanded perlite added at different curing ages. As shown in the figure, when the volume fraction of basalt fibers was 0.1%, the compressive strength of the mortar specimens (P7) added with 6mm long fibers increased by about 2.87% in the curing age of 28 days compared with the mortar specimens (P6) of the control group. The compressive strength of the mortar specimens (P8) added with 12mm long fibers improved to some extent in the early curing period, but the compressive strength was basically the same as that of the control group at the curing age of 28 days. When the volume fraction of basalt fibers was increased to 0.5%, the compressive strength of mortar specimens added with 6mm (P9) and 12mm (P10) long fibers increased to different degrees. Among them, the mortar specimens added with 6mm long basalt fibers had the most significant compressive strength improvement effect, and the growth rate could reach 12.02% when the curing age was 28 days.

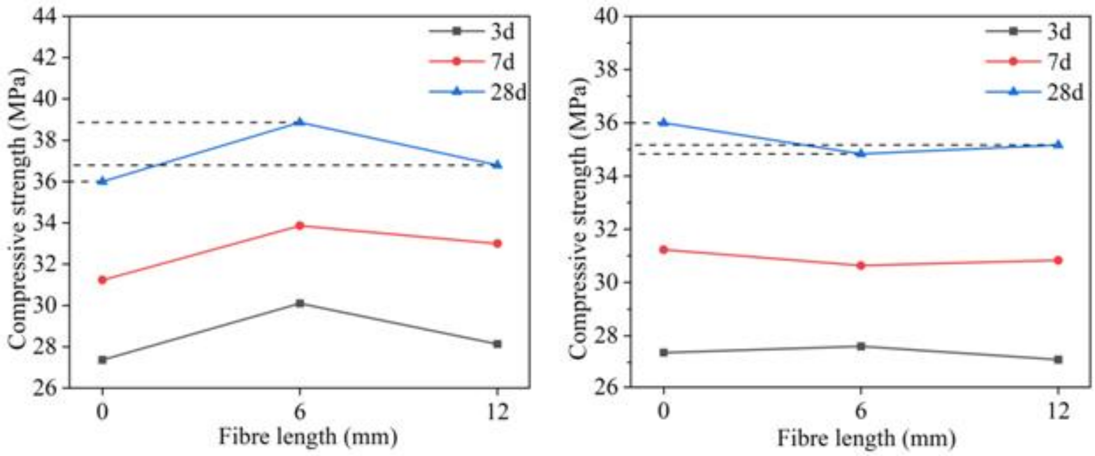

(a) The volume fraction is 0.1% *(b) The volume fraction is 0.5%*

Fig. 7 - The relation between compressive strength and basalt fibers length of specimens added with 10% expanded perlite

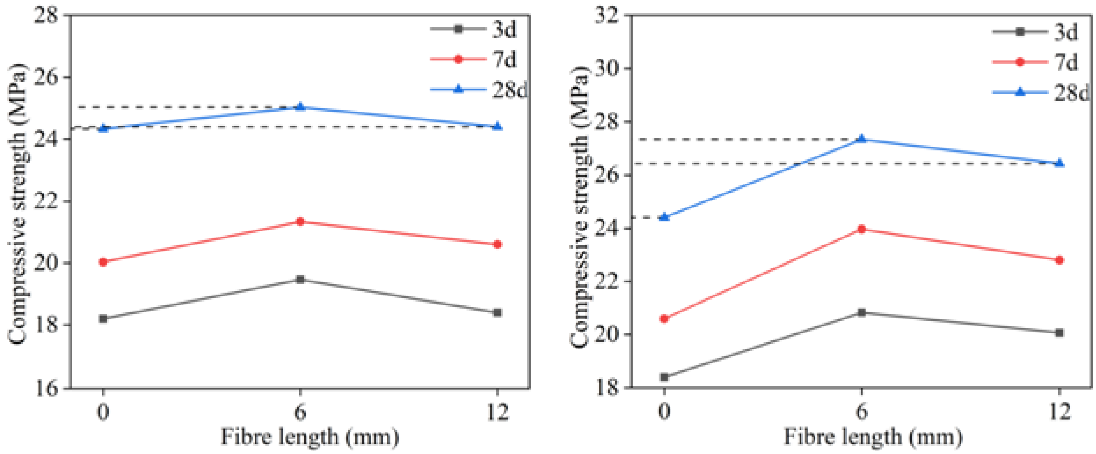

(a) The volume fraction is 0.1% *(b) The volume fraction is 0.5%*

Fig. 8 - The relation between compressive strength and basalt fibers length of specimens added with 30% expanded perlite

Figure 9 and figure 10 respectively give the variation relationship between the compressive strength and the volume fraction of basalt fibers of the specimens with different dosages of expanded perlite at different curing ages. As shown in the figure, for the mortar specimens added with 10% expanded perlite, when 6mm and 12mm fibers were added, the compressive strength of the specimens showed an increase at low fibers dosage (0.1%) and a decrease at high fibers dosage (0.5%). For the mortar specimens added with 30% expanded perlite, the compressive strength of the specimens showed an increase with the increase of fibers dosages when 6mm and 12mm fibers are added.

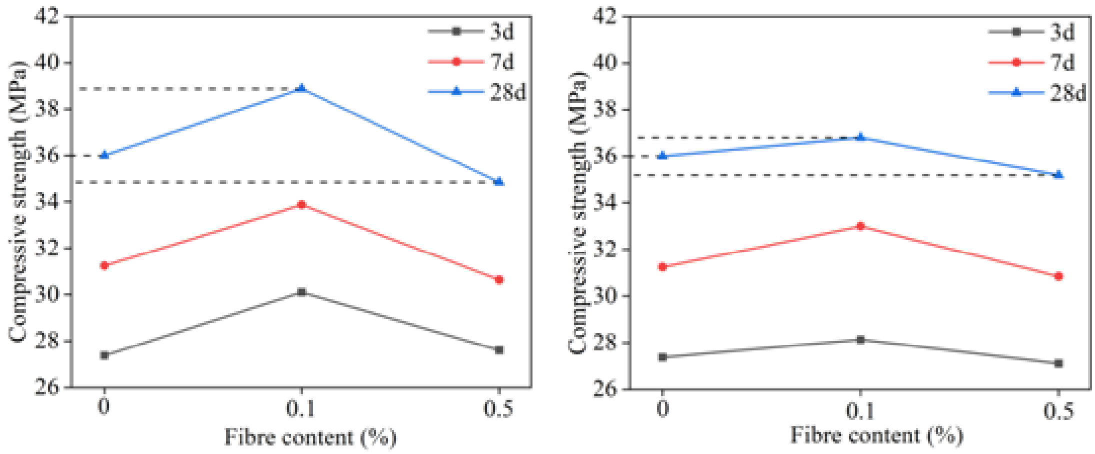

(a) The basalt fibers length is 6mm *(b) The basalt fibers length is 12mm*

Fig. 9 - The relation between compressive strength and basalt fibers fraction of specimens added with 10% expanded perlite

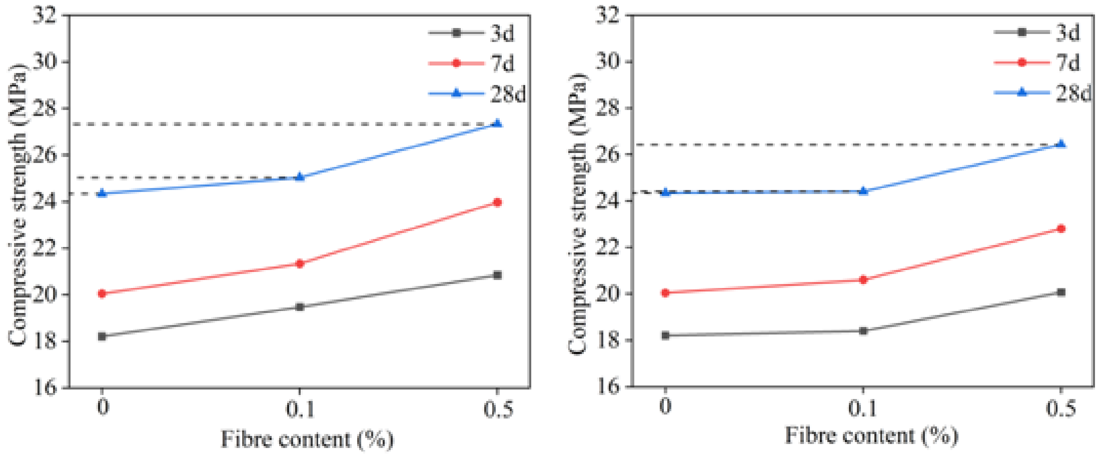

(a) The basalt fibers length is 6mm *(b) The basalt fibers length is 12mm*

Fig. 10 - The relation between compressive strength and basalt fibers fraction of specimens added with 30% expanded perlite

In summary, different dosages of expanded perlite had different effects on the internal pores of mortar specimens. With the increase of the expanded perlite dosage, the pores in the mortar specimens increased, the optimal dosage of basalt fibers increased, and the bridging effect of fibers became more obvious. Under the condition that the size of the mortar specimens was 40mm×40mm×40mm, the spacing between the internal pores of the specimens was very small, and the fibers with a length of 6mm could always play a role without negatively affecting on the compressive strength of the mortar specimens to the maximum extent, while the fibers with a length of 12mm were easy to agglomerate, which reduced the compressive strength of the mortar specimens.

Self-healing Performance

The crack self-healing property of cement mortar has an important influence on the overall property of the material, and the healing rate and healing degree determine the influence degree to which the internal material is affected by the external environment. The crack self-healing property of cement mortar can be evaluated by observing the healing conditions of cracks on the surface of specimens under different curing age conditions. Figure 11 gives the self-healing results of the cement mortar specimens added with 10% expanded perlite at 0, 3, 7 and 28 days after pre-cracking. As shown in the figure, with the increase of curing days, the width of the cracks gradually decreased, and the healing rate of each group could reach 100% at 28 days of self-healing curing. This was due to the fact that after cracks appeared in the mortar specimens, the spores in the cracks germinated, generated white precipitate through their own metabolism, and could completely fill the crack.

The self-healing efficiency of cracks could be effectively improved by adding fibers to cement mortar, and the self-healing efficiency of cracks increased gradually with the increase of fibers dosage. Figure 12 shows the self-healing results of cement mortar specimens added with self-healing agent and fibers at day 0, 3, 7 and 28 after pre-cracking. For the cement mortar specimens added with 0.5% fibers, the healing rate of the cracks could reach nearly 100% at 7 days of curing after pre-cracking. This was because the basalt fibers bridged on both sides of the cracks, providing

DOI 10.14311/CEJ.2025.01.0004

landing points for the white precipitate generated by bacterial metabolism, which improved the efficiency of crack healing. Compared with the cement mortar specimens added with 12 mm fibers, the cement mortar specimens added with 6 mm fibers had a higher self-healing efficiency, but the advantage was not obvious.

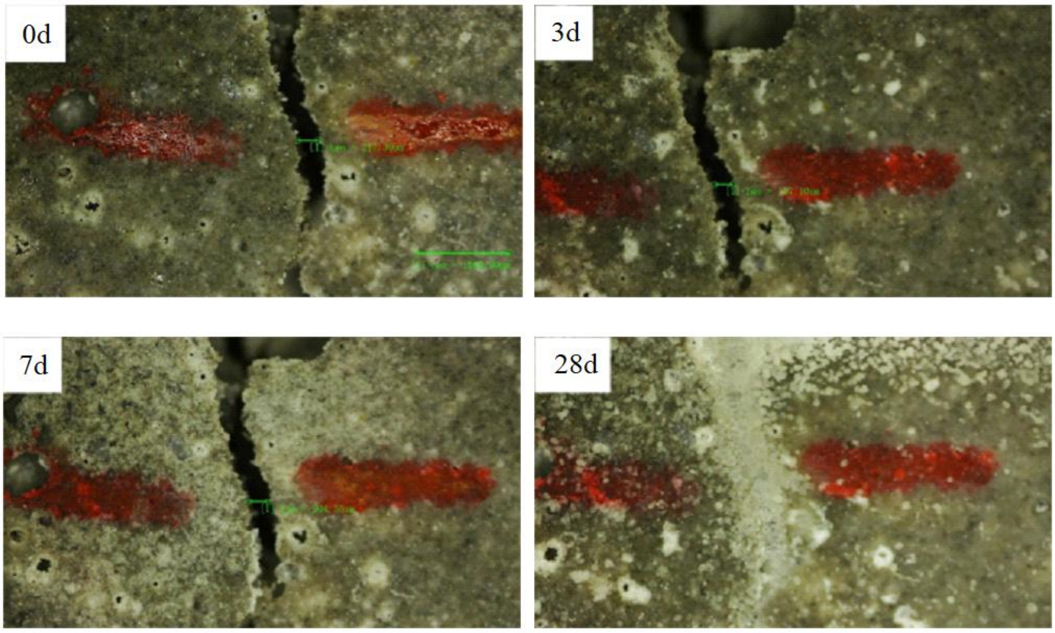

Fig. 11 - Self-healing results of cracks at days 0, 3, 7 and 28 in specimens doped with 10% expanded perlite under microscope

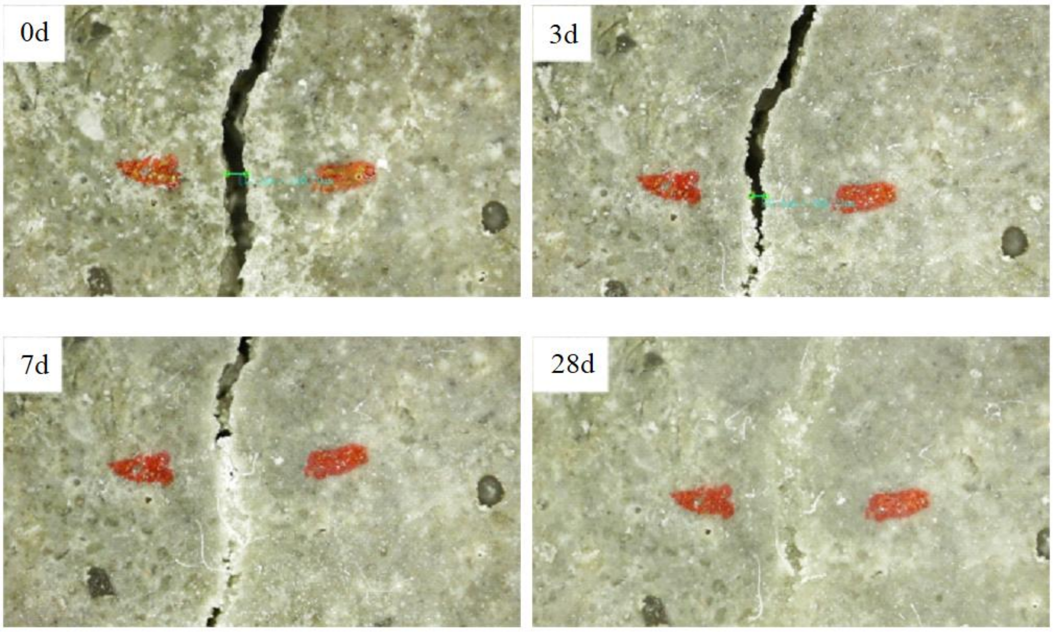

(a) Specimens containing 0.1% 6mm fibers and 10% expanded perlite

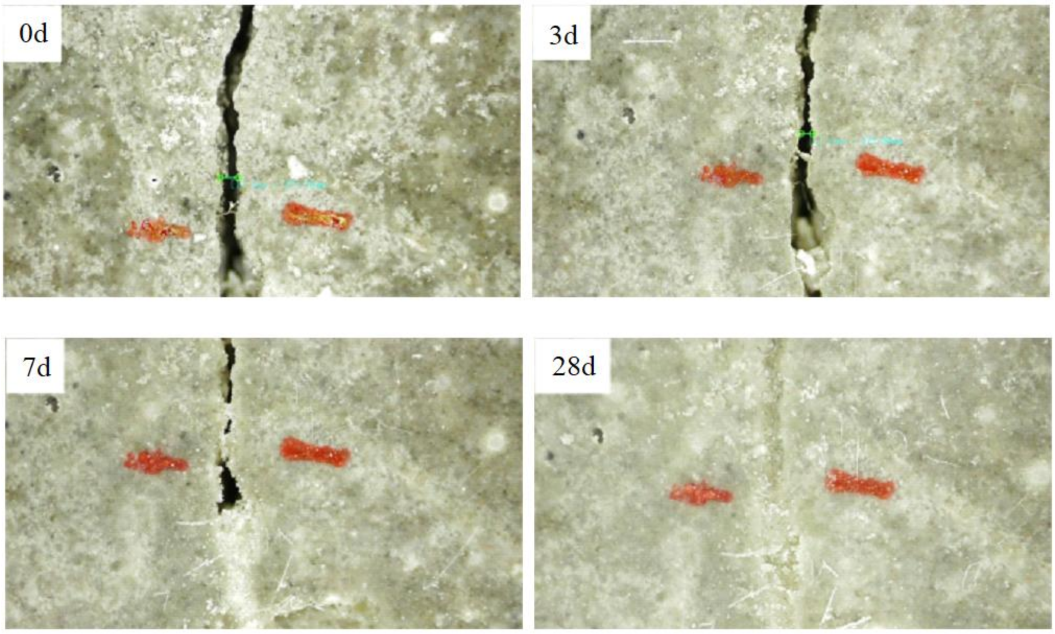

(b) Specimens containing 0.1% 12mm fibers and 10% expanded perlite

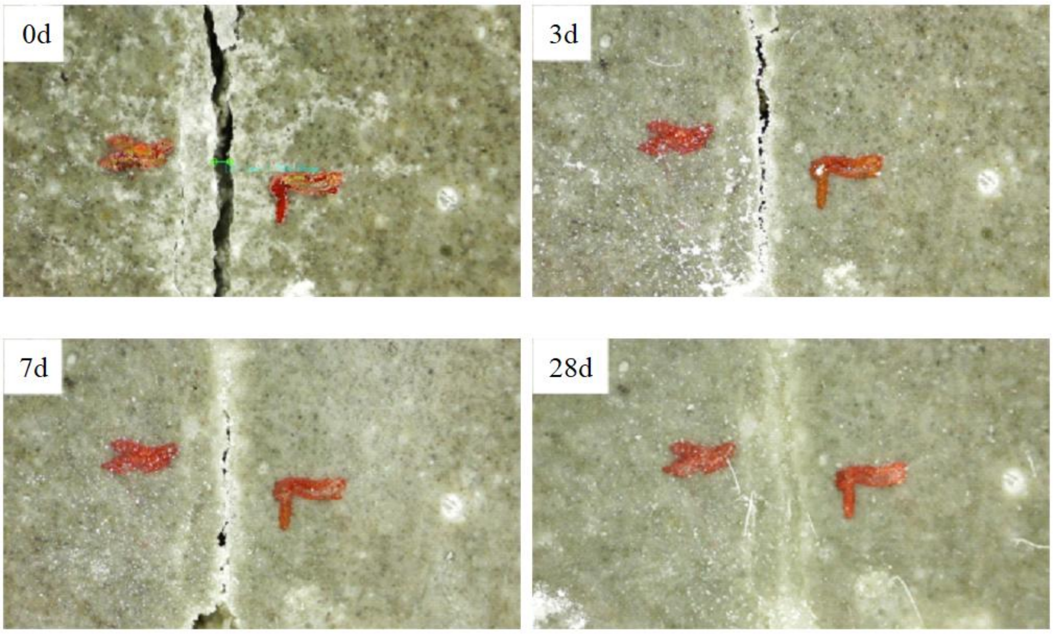

(c) Specimens containing 0.5% 6mm fibers and 10% expanded perlite

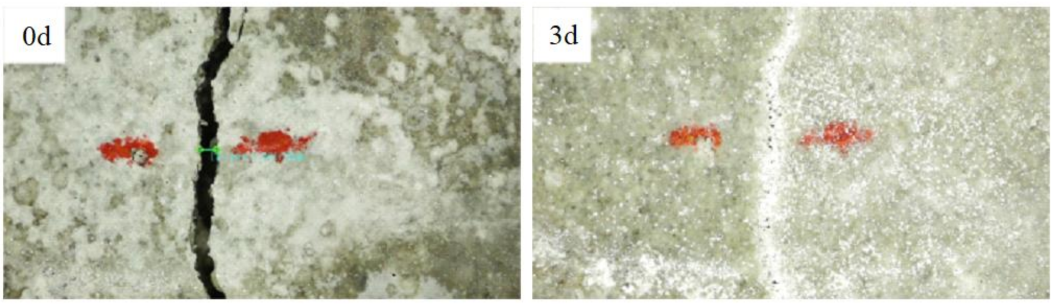

DOI 10.14311/CEJ.2025.01.0004

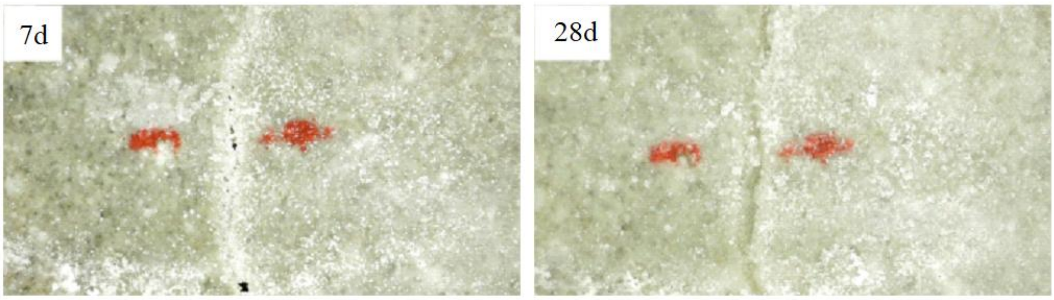

(d) Specimens containing 0.5% 12mm fibers and 10% expanded perlite

Fig. 12 - Self-healing results of cracks at day 0, 3, 7 and 28 under the microscope

Figure 13 shows the self-healing results of the cement mortar specimens added with 30% expanded perlite at 0 and 3 days after pre-cracking. As shown in the figure, the self-healing efficiency of the cement mortar specimens added with 30% self-healing agent was significantly improved compared to the cement mortar specimens added with 10% expanded perlite. For the specimens without basalt fibers, the healing rate of the cracks could also reach 20% at the curing age of 3 days.

Figure 14 shows the self-healing results of cement mortar specimens added with self-healing agent and fibers at day 0, 3, 7 and 28 after pre-cracking. As is shown in the figure, for the specimens added with fibers, the healing rate of the cracks could all reached 100% at the curing age of 3 days. This indicated that the basalt fibers in the mortar specimens could control the width of the cracks and play a bridging role at the cracks, providing a adsorption space for the comfortable landing points of the precipitate of bacterial metabolic reaction, which was conducive to improving the self-healing efficiency of the crack, as shown in Figure 15. However, under the condition of a large number of self-healing agents were added, the effect of the dosage and length of basalt fibers on the self-healing performance of cement mortar specimens was not very obvious.

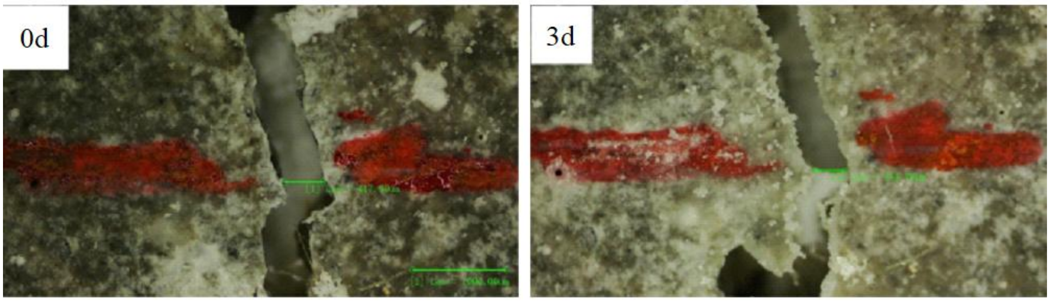

Fig. 13 - Self-healing results of cracks at day 0 and 3 in specimens doped with 30% expanded perlite under microscope

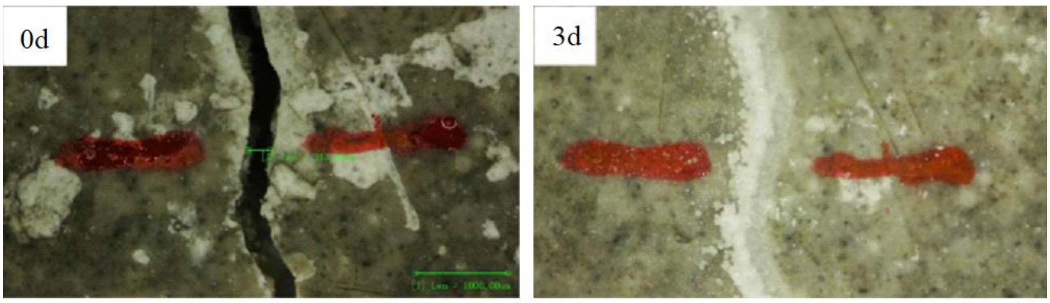

DOI 10.14311/CEJ.2025.01.0004

(a) Specimens containing 0.1% 6mm fibers and 30% expanded perlite

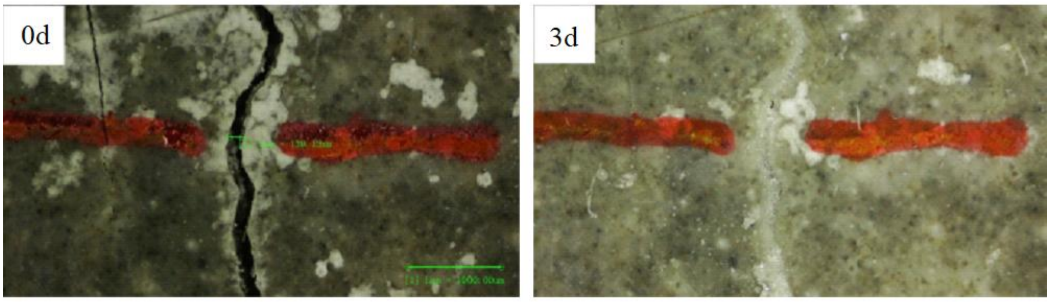

(b) Specimens containing 0.1% 12mm fibers and 30% expanded perlite

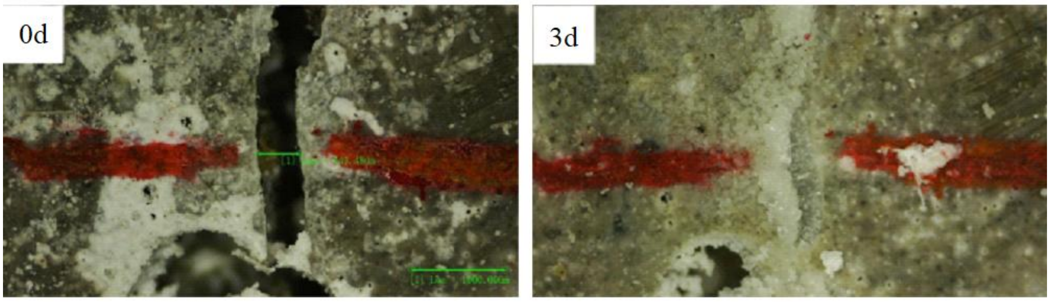

(c) Specimens containing 0.5% 6mm fibers and 30% expanded perlite

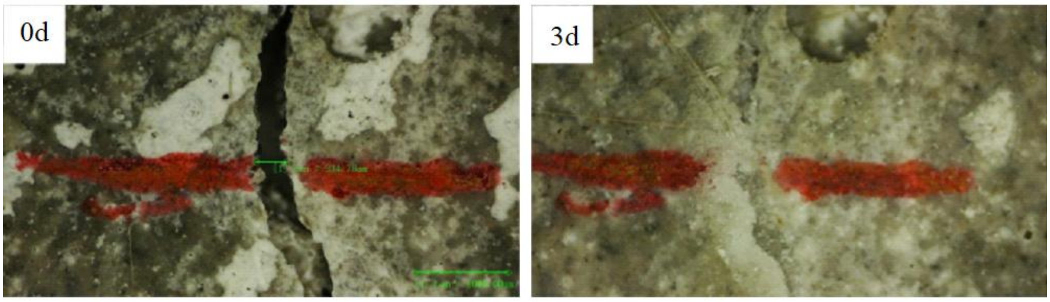

(d) Specimens containing 0.5% 12mm fibers and 30% expanded perlite

Fig. 14 - Self-healing results of cracks at day 0 and 3 under the microscope

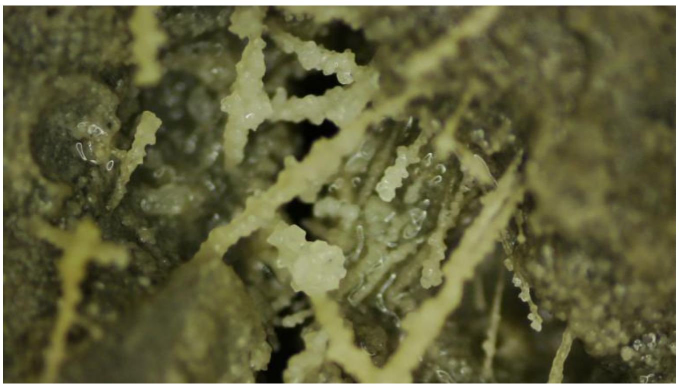

Fig. 15 - Calcium carbonate attaches to the surface of fibers

In order to further study the effects of self-healing agents with different dosages and different sizes and dosages of fibers on the self-healing performance of mortar specimens, the maximum

DOI 10.14311/CEJ.2025.01.0004

healing efficiency diagram of cracks with different widths was drawn. As shown in Figure 16, the crack width was divided into five intervals for statistics.

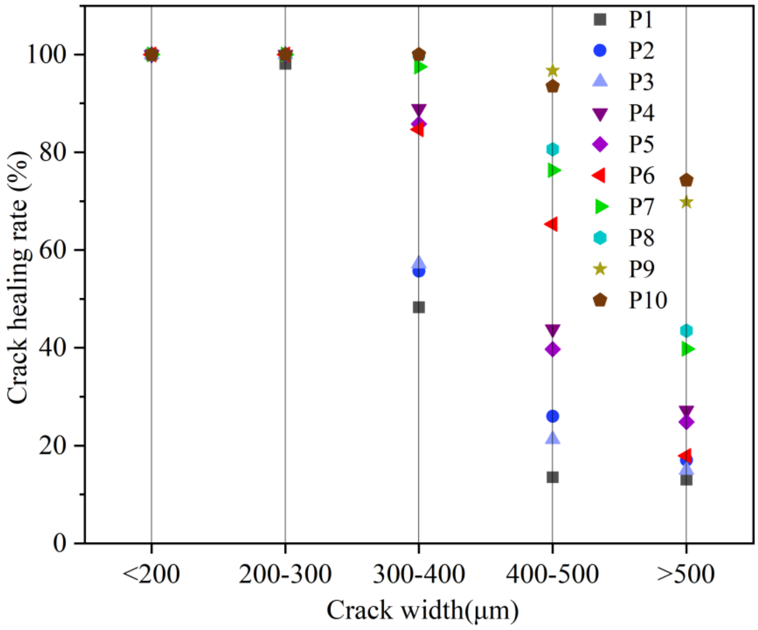

Fig. 16 - The healing rates of different crack widths at 28 days of self-healing

It can be seen from Figure 16 that when the crack width was less than 300μm, the mortar specimens could basically heal completely, and the healing rate of specimens of each group was all above 95%. However, when the crack width increased to 300-400μm, the self-healing efficiency of the specimens with 10% self-healing agent dosage began to decline, among which P1, P2 and P3 decreased the most, which was due to the fact that when the crack width was too large, the precipitate produced by the bacterial mineralization could not connect the two sides of the cracks, resulting in the poor final repair effect. Although the self-healing agent dosage of P4 and P5 specimens was 10%, the internal fibers dosage was enough to provide a large number of precipitation anchor points at the cracks, which could improve the self-healing efficiency.

For cracks larger than 500μm, only P9 and P10 could maintain a healing rate of more than 50%, which was because the crack width was too large, exceeding the self-healing limit of the remaining groups. Only P9 and P10 showed better healing rates under the coupling of self-healing agents and fibers.

Microscopic and Phase Analysis

SEM Microscopic Analysis

In order to further clarify the self-healing mechanism of the cracks, this paper observes the morphology of the healing products in the cracks by SEM test. More healing products could be obtained by choosing to extract healing products from P10 specimens. Figure 17 shows the microscopic morphology of the expanded perlite at the cracks. As can be seen in Figure 17(a), calcium carbonate precipitate was generated around the holes on the surface of expanded perlite. This indicated that bacteria could survive in expanded perlite and fill the cracks by germinating and generating calcium carbonate precipitate when cracks appeared in the cement mortar specimens. As can be seen in Figure 17(b), the bacterial spores were fixed in the pores inside the expanded perlite, but the distribution was not uniform. This also indicated that the repair efficiency at different locations of the same crack was not the same.

Figure 18 gives the microstructure of the product at the crack healing site. As can be seen in Figure 18 (a), a large amount of cube-shaped calcite was generated at the crack, indicating that the metabolic product of bacteria at the crack was calcium carbonate [34]. From Figure 18(b), it could be seen that a large amount of calcium carbonate was attached to the surface of basalt fibers, which indicated that the contact area of bacterial mineralization deposition could be increased by mixing basalt fibers, and the deposited calcium carbonate filling the pores inside the cement mortar improved the mechanical properties and impermeability of the mortar. The fibers at the cracks both bridged and anchored the deposits, controlling the crack width and providing deposition anchor points for calcium carbonate precipitation.

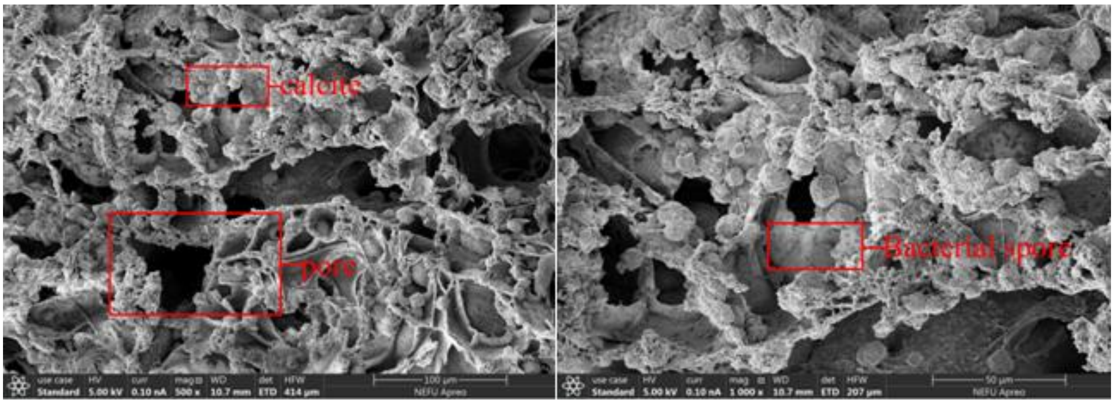

(a) Calcium carbonate on expanded perlite *(b) Bacterial spores on expanded perlite*

Fig. 17 - The surface microstructure of expanded perlite under SEM

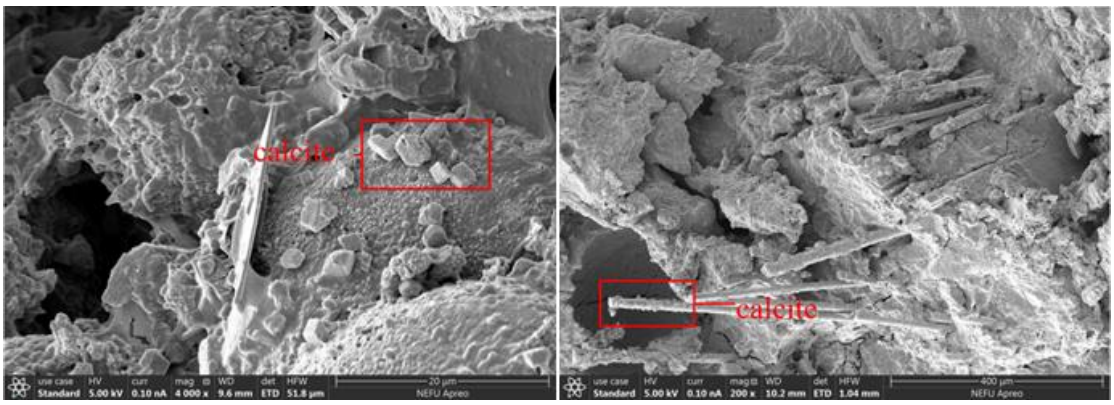

(a) Cubic calcite *(b) Calcium carbonate on fibers*

Fig. 18 - The microstructure of CaCO3 produced by cracks under SEM

XRD Phase Analysis

Figure 19 gives the XRD results of healing products at cracks in the cement mortar specimens added with 30% expanded perlite. As shown in the figure, $CaCO_3$, SiO_2 and other substances were detected in the XRD spectra of specimens of all the 5 groups. Among them, calcite peaks were found at 29.4 and 39.4. This indicated that the bacteria could survive in cement mortar using expanded perlite as the carrier and generate calcium carbonate through metabolism [35]. From the figure, we could also find that the more fibers dosage, the higher the calcite peak. This indicated that the addition of fibers was beneficial to adsorbing the calcium carbonate precipitation generated by bacterial metabolism, and the dense bonding could improve the self-healing performance of cement mortar.

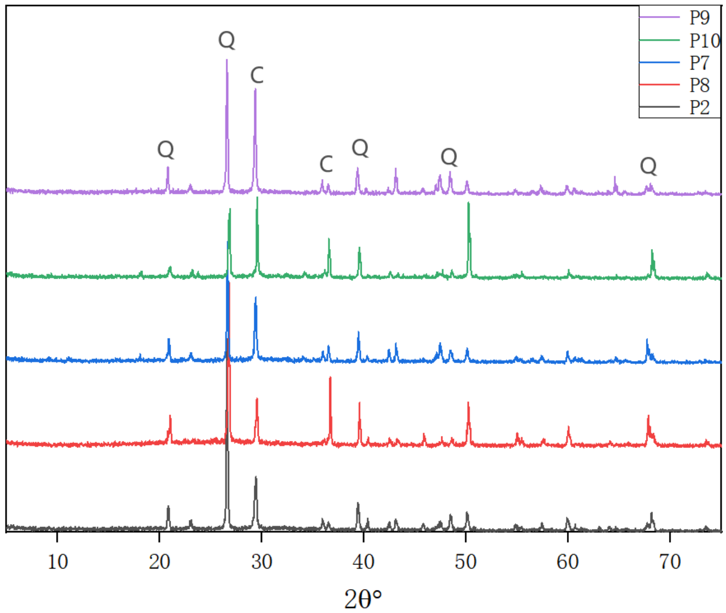

Fig. 19 - XRD results, Q-quartz, C-calcite of self-healing products of the specimens at 28 days of healing

CONCLUSION

(1) Adding an appropriate number of basalt fibers has no negative effect on the compressive strength of cement mortar. For the cement mortar specimens added with 10% expanded perlite, basalt fibers added with 6mm and 0.1% volume fraction had the highest compressive strength. For the cement mortar specimens added with 30% expanded perlite, basalt fibers added with 6mm and 0.5% volume fraction had the highest compressive strength.

(2) The number of self-healing agents added to cement mortar was proportional to the number of healing products generated after mortar cracking. Under the perfect conditions for ideal bacterial activity, increasing the dosage of self-healing agents could significantly improve the self-healing property of cracks in cement mortar, but at the same time, it also reduced the compressive strength of cement mortar. By adding basalt fibers to cement mortar at the same time, the mechanical properties of the material could be improved, and the complementary advantages with the effect of self-healing agents could be achieved. By adding a small number of healing agents and a moderate number of fibers at the same time, not only could achieve 100% self-healing performance, but also benefit to the compressive strength of cement mortar.

(3) Through XRD analysis, it was found that the healing product at the cracks was calcium carbonate. Through SEM observation tests, it was found that bacteria could survive in cement mortar

with expanded perlite as carriers, and further determined that the healing products were cubes and amorphous calcite.

DECLARATION OF COMPETING INTEREST

The authors declare that they have no known competing financial interests or personal relationships that could have influenced the work reported in this paper.

ACKNOWLEDGEMENTS

This work is supported by the Fundamental Research Funds for the Central Universities (No. 2572022DX07).

REFERENCES

[1] S. Mindess, J.F. ve Young, Concrete, Prentice-Hall, New Jersey, 1981.
[2] Luo, M.; Qian, C.X.; Li, R.Y. Factors affecting crack repairing capacity of bacteria-based self-healing concrete. Constr. Build. Mater. 2015, 87, 1–7.
[3] W. De Muynck, K. Cox, N.D. Belie, W. Verstraete, Bacterial carbonate precipitation as an alternative surface treatment for concrete, Construction and Building Materials 22(5) (2008) 875-885.
[4] Z. Yang, J. Hollar, X. He, X. Shi, A self-healing cementitious composite using oil core/silica gel shell microcapsules, Cement and Concrete Composites 33(4) (2011) 506-512.
[5] V.C. Li, E. Herbert, Robust Self-Healing Concrete for Sustainable Infrastructure, Journal of Advanced Concrete Technology 10(6) (2012) 207-218.
[6] W. Khaliq, M.B. Ehsan, Crack healing in concrete using various bio influenced self-healing techniques, Construction and Building Materials 102 (2016) 349-357.
[7] M. Seifan, A.K. Samani, A. Berenjian, Bioconcrete: next generation of self-healing concrete, Applied Microbiology and Biotechnology 100(6) (2016) 2591-2602.
[8] S.S.P. Reddy, M.V.S. Rao, P. Aparna, C. Sasikala, Performance of standard grade bacteria (Bacillus Subtilis) concrete, cafetinnova org (2010).
[9] M. Jamnu, A Study of Performance of Bacillus Lentus on Concrete Cracks, (2013).
[10] U.K. Gollapudi, C.L. Knutson, S.S. Bang, M.R. Islam, A new method for controlling leaching through permeable channels, Chemosphere 30(4) (1995) 695-705.
[11] H.M. Jonkers, Self Healing Concrete: A Biological Approach, in: S. van der Zwaag (Ed.), Self Healing Materials: An Alternative Approach to 20 Centuries of Materials Science, Springer Netherlands, Dordrecht, 2007, pp. 195-204.
[12] H.M. Jonkers, A. Thijssen, G. Muyzer, O. Copuroglu, E. Schlangen, Application of bacteria as self-healing agent for the development of sustainable concrete, Ecol. Eng. 36 (2) (2010) 230–235.
[13] Nguyen T H, Ghorbel E, Fares H, et al. Bacterial self-healing of concrete and durability assessment[J]. Cement and Concrete Composites, 2019, 104: 103340.
[14] Jonkers H M, Thijssen A, Muyzer G, et al. Application of bacteria as self-healing agent for the development of sustainable concrete[J]. Ecological engineering, 2010, 36(2): 230-235.
[15] Sharma T K, Alazhari M, Heath A, et al. Alkaliphilic Bacillus species show potential application in concrete crack repair by virtue of rapid spore production and germination then extracellular calcite formation[J]. Journal of applied microbiology, 2017, 122(5): 1233-1244.
[16] Achal V, Pan X, Özyurt N. Improved strength and durability of fly ash-amended concrete by microbial calcite precipitation[J]. Ecological Engineering, 2011, 37(4): 554-559.
[17] Zhang J, Liu Y, Feng T, et al. Immobilizing bacteria in expanded perlite for the crack self-healing in concrete[J]. Construction and Building Materials, 2017, 148: 610-617.
[18] Xu J, Wang X, Zuo J, et al. Self-healing of concrete cracks by ceramsite-loaded microorganisms[J]. Advances in Materials Science and Engineering, 2018, 2018.
[19] Su Y, Li F, He Z, et al. Artificial aggregates could be a potential way to realize microbial self-healing concrete: An example based on modified ceramsite[J]. Journal of Building Engineering, 2021, 35: 102082.

[20] Shaheen N, Khushnood R A. Bioimmobilized limestone powder for autonomous healing of cementitious systems: A feasibility study[J]. Advances in Materials Science and Engineering, 2018, 2018.
[21] Singh, H., & Gupta, R. (2020). Cellulose fiber as bacteria-carrier in mortar: Self-healing quantification using UPV. Journal of Building Engineering, 28, 101090.
[22] Lin Z, Li V C. Crack bridging in fiber reinforced cementitious composites with slip-hardening interfaces[J]. Journal of the Mechanics and Physics of Solids, 1997, 45(5): 763-787.
[23] Zeng Y, Tang A. Comparison of effects of basalt and polyacrylonitrile fibers on toughness behaviors of lightweight aggregate concrete[J]. Construction and Building Materials, 2021, 282: 122572.
[24] Yang L, Xie H, Zhang D, et al. Acoustic emission characteristics and crack resistance of basalt fiber reinforced concrete under tensile load[J]. Construction and Building Materials, 2021, 312: 125442.
[25] Khan M, Cao M, Chu S H, et al. Properties of hybrid steel-basalt fiber reinforced concrete exposed to different surrounding conditions[J]. Construction and Building Materials, 2022, 322: 126340.
[26] Jonkers H M, Schlangen H. Crack repair by concrete immobilized bacteria[C]//Proceedings of the first international conference on self healing materials. Springer, 2007: 1-7.
[27] Tziviloglou E, Wiktor V, Jonkers H M, et al. Selection of nutrient used in biogenic healing agent for cementitious materials[J]. Frontiers in Materials, 2017, 4: 15.
[28] Tan L, Xu J, Wei Y, et al. Aerobic non-ureolytic bacteria-based self-healing cementitious composites: a novel approach without added calcium precursor[J]. Engineering Research Express, 2023, 5(3): 035006.
[29] Tziviloglou E, Wiktor V, Jonkers H M, et al. Bacteria-based self-healing concrete to increase liquid tightness of cracks[J]. Construction and Building Materials, 2016, 122: 118-125.
[30] Ryparová P, Tesárek P, Schreiberová H, et al. The effect of temperature on bacterial self-healing processes in building materials[C]//IOP conference series: materials science and engineering. IOP Publishing, 2020, 726(1): 012012.
[31] Ryparová P, Tesárek P, Schreiberová H, et al. The Effect of Temperature on Bacterial Self-Healing Processes in Building Materials[C]. IOP conference series: materials science and engineering. IOP Publishing, 2020, 726(1): 012012
[32] Sengul O, Azizi S, Karaosmanoglu F, et al. Effect of Expanded Perlite on The Mechanical Properties and Thermal Conductivity of Lightweight Concrete[J]. Energy and Buildings, 2011, 43(2-3): 671-676.
[33] Fu D, Fu Y and Guo C M. Effect of basalt fiber dosage on mechanical properties of silicate concrete [J]. Bonding, 2023, 50(02): 65-68. (in Chinese)
[34] Braissant O, Cailleau G, Dupraz C, et al. Bacterially Induced Mineralization of Calcium Carbonate in Terrestrial Environments: The Role of Exopolysaccharides And amino Acids[J]. Journal of Sedimentary Research, 2003, 73(3): 485-490.
[35] Gupta S, Kua H W, Dai P S. Healing Cement Mortar by Immobilization of Bacteria in Biochar: An Integrated Approach of Self-Healing And Carbon Sequestration[J]. Cement and Concrete Composites, 2018, 86: 238-254.

CIVIL ENGINEERING JOURNAL

Article no. 5

THE CIVIL ENGINEERING JOURNAL 1-2025

POINT CLOUD LOCAL NEIGHBORHOOD FEATURES USED FOR CLASSIFICATION - A REVIEW

Martin Boušek, Jakub Kučera and Hana Váchová

Czech Technical University in Prague, Faculty of Civil Engineering, Department of Special Geodesy, Prague, Thákurova 7, 166 29 Prague 6, Czech Republic; martin.bousek@fsv.cvut.cz

Received: *2.12.2024*

Received in revised form: *20.01.2025*

Accepted: *14.02.2025*

ABSTRACT

Point clouds are essential for 3D spatial analysis and widely used in geodesy, photogrammetry, and remote sensing. While modern technologies simplify their collection, processing remains challenging due to data size, irregularity, and noise. Classification is critical for object identification and noise removal.

This paper explores geometric features of points derived from their local 3D neighbourhoods. It examines neighbourhood definitions, feature computation via principal component analysis (PCA), and their impact on real dataset classification. Using a test point cloud with natural and anthropogenic features, we analyze feature dependencies, identify redundancies, and highlight key metrics. Additionally, we propose new approaches for noise filtering, contributing to more efficient point cloud processing and practical applications.

KEYWORDS

Classification, Filtering, Geometric features, Neighbourhood, Point cloud

INTRODUCTION

Nowadays, non-selective spatial data collection methods are increasingly used to obtain spatial information. The resulting products of these methods are so-called point clouds, which serve as a fundamental representation of 3D space and have a wide range of applications [1]. They are utilized in various fields such as geodesy, remote sensing, photogrammetry, robotics, computer vision, and others [2, 3]. Point clouds are a key source of information in modern applications, making their accurate interpretation essential.

Although modern measurement methods and advanced technologies enable fast and convenient data collection, they also introduce new challenges in post-processing. The size, complexity, and irregularity of the collected data require advanced methods for analysis and information extraction.

To extract meaningful information from a point cloud containing diverse objects, classification is often necessary. This involves assigning a specific value (label) to each point. For example, to separate vegetation from other categories, we can assign a label (e.g., a value of 1) to vegetation points and a different label to other classes. This classification can then be extended into a filtering process, where points with specific labels are removed to clean the point cloud. Significant progress in point cloud classification methods, particularly those using machine learning, has been made in the last decade.

Each point of the point cloud carries with it some information either directly measured or obtained from the data measured by the sensor (XYZ coordinates, RGB color, intensity, echo). We classify this information as a basic measured feature that gives us information about the point itself. Furthermore, from the neighbouring points of each point, it is possible to infer geometric features of the nearby neighbourhood, which can be interpreted as a description of the scanned object.

The paper by Qi et al. [4] proposes a neural network model working exclusively with the basic spatial coordinates of the XYZ point cloud, using which the network segments the cloud into semantic objects. In [5], Štroner et al. use the RGB point cloud information to derive various vegetation indices, using which they filter vegetation from the point cloud. Atik and Duran [6] use RGB information both alone and together with derived geometric information from neighbouring points to classify different types of objects - terrain, buildings, high and low vegetation. Authors Liu et al. [7] classify vegetation and ground points in lidar aerial point cloud using intensity, elevation, scan angle and distance from scanner. They also use features calculated from the point's neighbourhood - eigenvalues, normal vector and geometric features calculated from eigenvalues such as planarity, linearity and eigenentropy. Chehata et al. in [8] also add to these features information about the order of reflection (echo) of the lidar beam.

Other studies such as in Weinmann et al. [9, 10] use only the features of the local 3D neighbourhood computed from eigenvalues to classify and segment the point cloud. They also discuss the relevance of the individual features and the importance of the correct selection of the 3D local neighbourhood. In this approach, the type of data collection does not matter, as it does not use sensor-specific information - RGB color in the case of photogrammetry or reflection intensity and echo in the case of laser scanning - and is thus generally applicable. Therefore, in this paper we will focus exclusively on features computed from the 3D neighbourhood of a point.

However, many of these methods have been proposed and tested on idealized datasets that do not reflect real-world conditions. Real-world data often contains noise, exhibit non-uniform point densities, and are influenced by measurement conditions or technical limitations of the instruments. To ensure correct interpretation and efficient processing, these aspects must be considered, and individual points carefully analyzed based on their local neighbourhood. Therefore, this paper addresses two key questions: 1) what features can be computed for each 3D point in the point cloud, and 2) what object properties in the point cloud are represented by these features. We further analyze feature correlations and propose potential new approaches for their computation.

MATERIALS AND METHODS

Test point cloud

In the point cloud selected for testing (Figure 1), a portion of a railway bridge over a forested valley is captured. The scene was chosen for its diversity, as it contains both anthropogenic features such as straight walls, arches and small engineering features, as well as a variety of natural terrain including trees and slopes. The cloud contains approximately 830,000 points and covers an area of approximately 1,180 m2. The cloud was created by combining data acquired with a Leica P40 laser scanner and data acquired by aerial photogrammetry using a DJI Phantom 4 RTK UAV.

Inconsistencies in the distribution of points in the point cloud may arise due to the combination of the two data collection methods. In order to homogenize the data, the point cloud was subsampled to 7 cm and since we used a sufficiently large neighborhood when calculating the characteristics, the differences in methods will not be apparent. The two methods we used are compared in terms of accuracy in the papers [11, 12], where the authors determined a difference in accuracy of the methods in the order of centimeters. For the purposes of our testing, such accuracy between point clouds from different methods is sufficient.

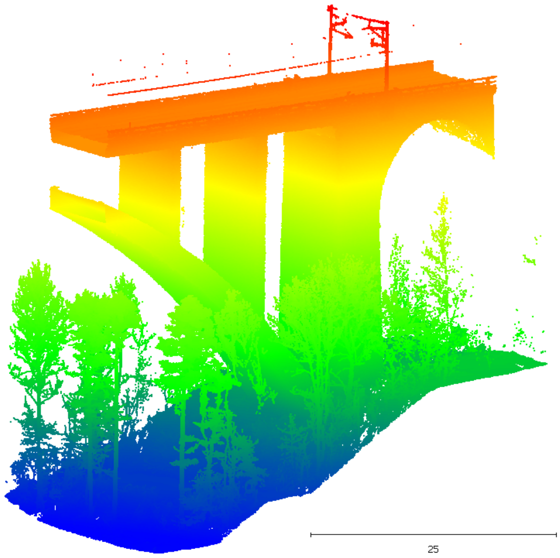

Fig. 1 – Test point cloud colored based on elevation

GEOMETRIC FEATURES

3D neighbourhood

Geometric features are used to describe the relationships between neighbouring points in a point cloud. Therefore, in order to analyze the local 3D structure around a point X using geometric features, it is important to first define the relevant neighbourhood correctly. There are several strategies to define this neighbourhood of a point X: based on a fixed number of nearest neighbours, using a spherical neighbourhood or a cylindrical neighbourhood [8]. The actual neighbourhood is then the set of points falling within this region, i.e. the "neighbours" of point X, which is shown in Figure 2.

The choice of the neighbourhood and the extraction of the features interact because the distinction of the geometric features depends on the relevant neighbourhood into which the 3D points used for feature extraction fall. Some features may be more pronounced in a wider neighbourhood, while others will be more evident in a smaller neighbourhood. The choice of neighbourhood size also depends on the density of the point cloud and its local variations [13].

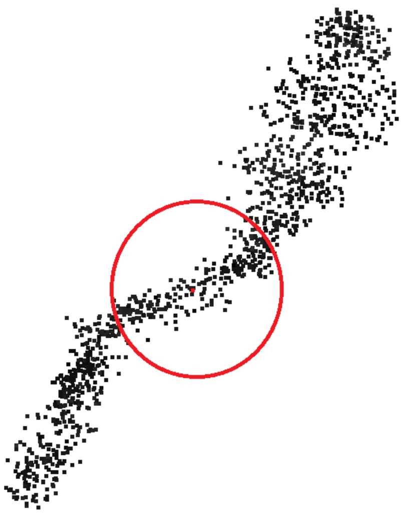

Fig. 2 – 2D representation of a spherical neighbourhood of a point in a point cloud

DOI 10.14311/CEJ.2025.01.0005

Calculation of local neighbourhood features

Principal component analysis (PCA) is used to calculate the local features of neighbours of a point in the point cloud. This is a set of unit vectors that give the direction of the lines that best represent a collection of points. Each i-th vector must be perpendicular to all previous vectors. The first one is in the direction of the highest variance of the collection. After the influence of the first vector is removed, the next vector is again found as the direction of greatest variance. The set of such vectors is orthonormal and points to the directions of the axes of the largest variances of the collection, which are linearly uncorrelated with each other. The resulting PCA vectors of the data set are identical to the eigenvectors of its covariance matrix. Its eigenvalues $\lambda_1, \lambda_2, \lambda_3$ then indicate the variance in the direction of these vectors (Figure 3) [14, 15]. For these eigenvalues, it is always the case that $\lambda_1 > \lambda_2 > \lambda_3$. In practice, singular value decomposition (SVD) is used to compute the eigenvalues from the covariance matrix [14].

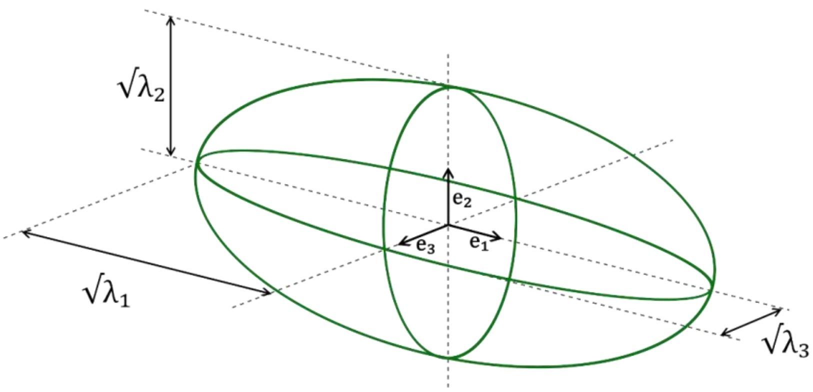

Fig. 3 – A general ellipsoid characterizing the shape of the point's neighbourhood with a representation of the eigenvalues and eigenvectors

Features based on eigenvalues and eigenvectors

Based on this description of a point's neighbourhood, also known as the 3D structure tensor, the derived neighbourhood features can be calculated.

The program for loading point clouds and calculating characteristics was developed in Python using the CloudComPy library. For the calculations, a neighbourhood of 0.5 m was chosen. The examined features are as follows:

Planarity

The value of planarity in the local neighbourhood can be calculated using the Equation 1:

$$P = \frac{\lambda_2 - \lambda_3}{\lambda_1}. \tag{1}$$

This feature describes how closely the distribution of points in the local neighbourhood approximates a plane, as shown in Figure 4 a). Red indicates the highest planarity values (e.g., bridge structure walls), while blue and green shades represent lower values (e.g., vegetation). This visual distinction makes it possible to differentiate planar surfaces from more complex, less planar structures.

Linearity

The linearity in the chosen neighbourhood of the point can be calculated according to Equation 2:

DOI 10.14311/CEJ.2025.01.0005

$$L = \frac{\lambda_1 - \lambda_2}{\lambda_1}. \quad (2)$$

This feature determines how much the surrounding points are aligned along a straight line. When λ_2 and λ_3 are small, it indicates that the points are stretched significantly in one direction. Elements with high linearity are highlighted in red in Figure 4 b). This is the most noticeable on the tree trunks and the technical equipment at the top of the bridge.

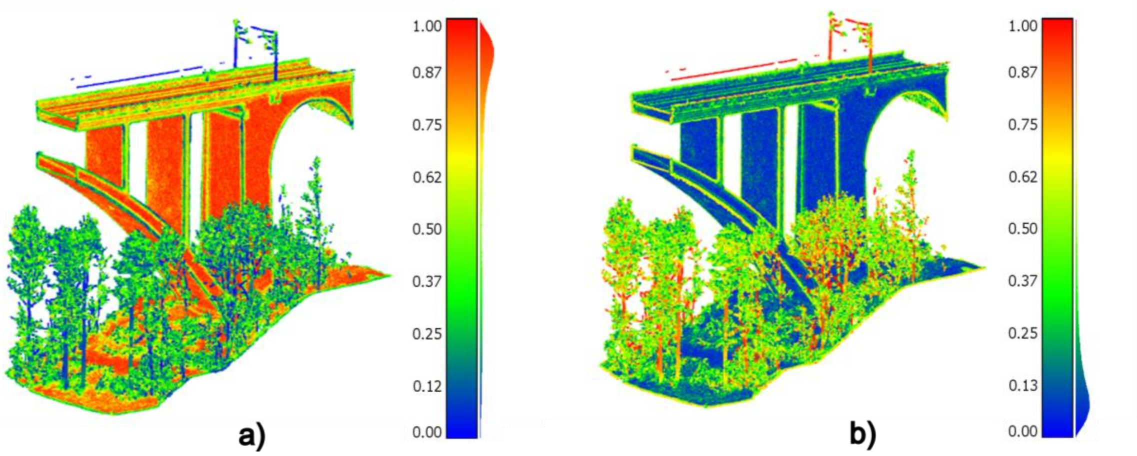

Fig. 4 – Test point cloud colored based on: a) Planarity, b) Linearity

Sphericity

The formula for calculating the sphericity in the local neighbourhood of a point is Equation 3:

$$S = \frac{\lambda_3}{\lambda_1}. \quad (3)$$

Sphericity describes the degree to which the points in the neighbourhood are distributed in all directions. In Figure 5 a), blue represents areas with lower sphericity, while green indicates higher values. The bridge structure appears mostly in dark blue, as expected, because it consists of linear and planar surfaces where the points are not uniformly distributed in all directions but are concentrated in certain directions. In contrast, trees and vegetation show more directionally dispersed points, as the leaves and branches create an irregular, three-dimensional structure. However, the boundary between these two types of features is not entirely clear.

Anisotropy

The value of anisotropy in the local neighbourhood can be calculated using Equation 4:

$$A = \frac{\lambda_1 - \lambda_3}{\lambda_1}. \quad (4)$$

This feature indicates how much the points are arranged along a dominant direction (high anisotropy) compared to a uniform distribution in all directions (low anisotropy). High anisotropy values are present where the points are more linearly distributed (e.g., along one direction). In Figure 5 b), high anisotropy values are visualized in red, highlighting regions with a distinct directional arrangement of points, which typically correspond to engineering structures. In contrast, vegetation exhibits variable anisotropy, reflecting its more complex geometry.

DOI 10.14311/CEJ.2025.01.0005

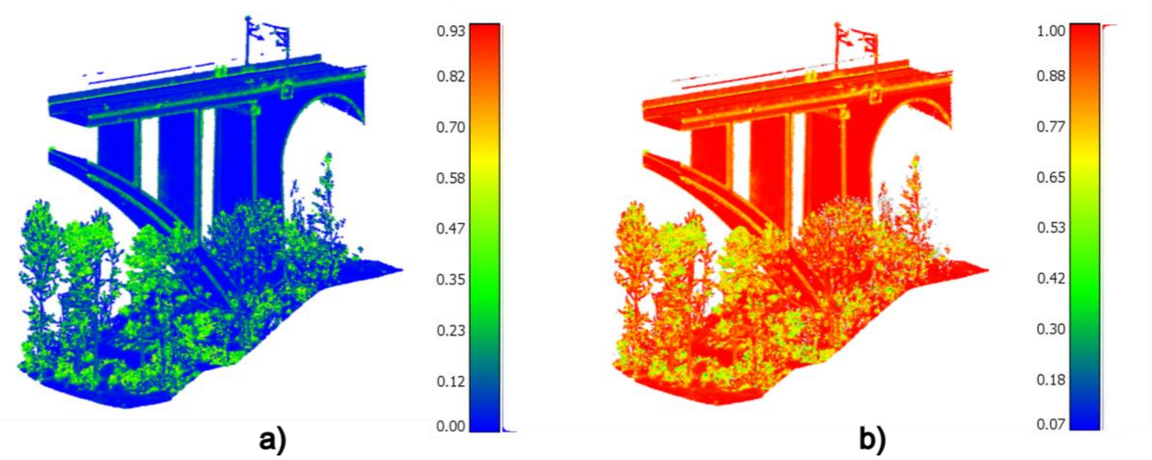

Fig. 5 – Test point cloud colored based on: a) Sphericity, b) Anisotropy

Omnivariance

We can calculate the omnivariance using Equation 5:

$$O = \sqrt[3]{\lambda_1 \lambda_2 \lambda_3}. \tag{5}$$

This feature shows the distribution of points in different directions and is shown in Figure 6 a). When λ_1, λ_2, and λ_3 are similarly large, the omnivariance is higher, indicating a uniform distribution of points. Omnivariance captures the size and scale of the point distribution, relying solely on the magnitude of the eigenvalues.

Eigenentropy

The formula for calculating eigenentropy in a local neighbourhood of a point is Equation 6:

$$E = -\Sigma_{i=1}^{3} \lambda_i \, \ln \lambda_i. \tag{6}$$

Eigenentropy indicates the degree of "chaos" or uncertainty in the distribution of points. A higher value suggests a more uniform distribution (Figure 6 b)). Unlike omnivariance, eigenentropy is scale-independent and focuses on the relative relationships between the eigenvalues, rather than their absolute magnitudes.

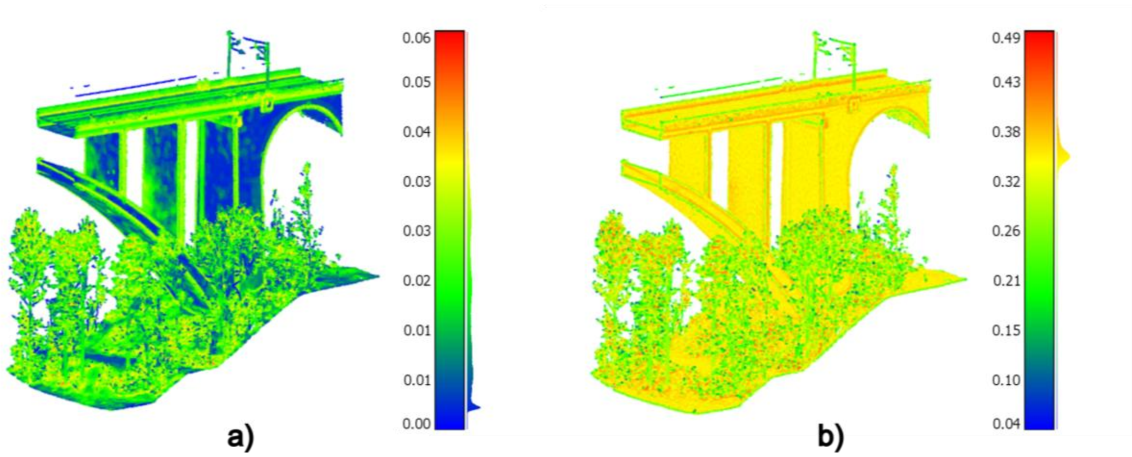

Fig. 6 – Test point cloud colored based on: a) Omnivariance, b) Eigenentropy

Surface variation

Surface variation can be calculated according to Equation 7:

$$Sv = \frac{\lambda_3}{\lambda_1 + \lambda_2 + \lambda_3}. \quad (7)$$

Surface variation describes the deviation of neighbouring points from the plane in a given local neighbourhood, indicating how smooth or rough a surface is. Values close to zero mean the points lie nearly in a plane, while higher values indicate a rough or irregular surface. In Figure 7 a), the main structure of the bridge is predominantly blue, suggesting that the bridge surface is relatively flat, which aligns with expectations for an engineering structure. The figure also implies a potential correlation between this feature and sphericity or anisotropy.

Verticality

The verticality value is calculated by subtracting the absolute value of the scalar product of the unit vector in the direction of the vertical axis and the third eigenvalue λ_3 from one (Equation 8):

$$V = 1 - |\langle[0 \;\; 0 \;\; 1], \lambda_3\rangle|. \quad (8)$$

Verticality ranges from 0 to 1, with a perfect vertical orientation corresponding to a value of 1. In Figure 7 b), high values are predominantly seen in the vertically oriented bridge walls and the trunks of larger trees. Conversely, low values are found mainly in points located on the horizontal surface beneath the bridge and in points forming the bridge deck.

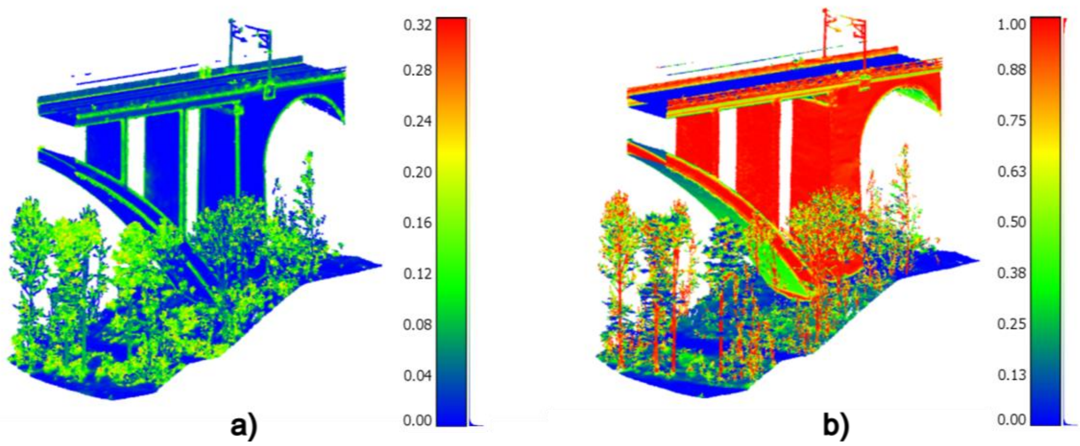

Fig. 7 – Test point cloud colored based on: a) Surface variation, b) Verticality

PCA1

PCA1 equals to a division of the first eigenvalue λ_1 and sum of all eigenvalues (Equation 9):

$$PCA1 = \frac{\lambda_1}{\lambda_1 + \lambda_2 + \lambda_3}. \quad (9)$$

A high value (max. 1) indicates that the surrounding points are concentrated in one direction, corresponding to linear structures (e.g., trunks, wires). In this case, the wires above the bridge deck and some tree branches are particularly noticeable in the point cloud. Conversely, low values suggest that the surrounding points are not primarily aligned in one direction, which can be seen in Figure 8 a).

PCA2

This feature is very similar to PCA1, the difference being that the dividend in the equation is λ_2 (Equation 10):

$$PCA2 = \frac{\lambda_2}{\lambda_1 + \lambda_2 + \lambda_3}. \quad (10)$$

Values close to 0.5 (the maximum value) indicate a planar distribution of points in the selected neighbourhood. As with PCA1, low values suggest the opposite of high values, meaning either a non-planar or omnidirectional distribution of points (Figure 8 b)).

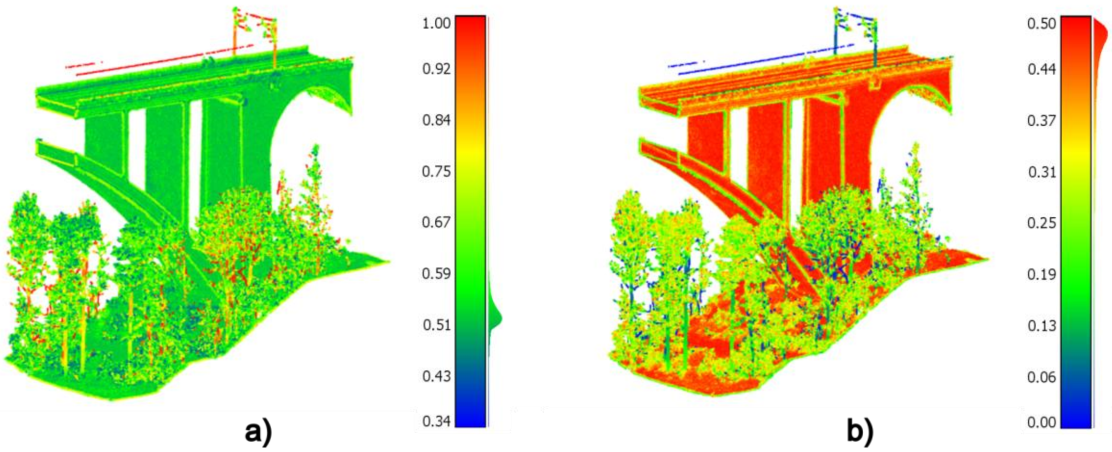

Fig. 8 – Test point cloud colored based on: a) PCA1, b) PCA2

Sum of eigenvalues

The sum of eigenvalues in the selected local neighbourhood can be calculated using Equation 11:

$$\Sigma\lambda_i = \lambda_1 + \lambda_2 + \lambda_3. \tag{11}$$

This feature reflects 3D variance of the neighbouring points. It is the quadratic sum of the standard deviations in the local 3D neighbourhood. The distinct color boundary between object types is not clearly defined in Figure 9, where all features are represented in yellow and green.

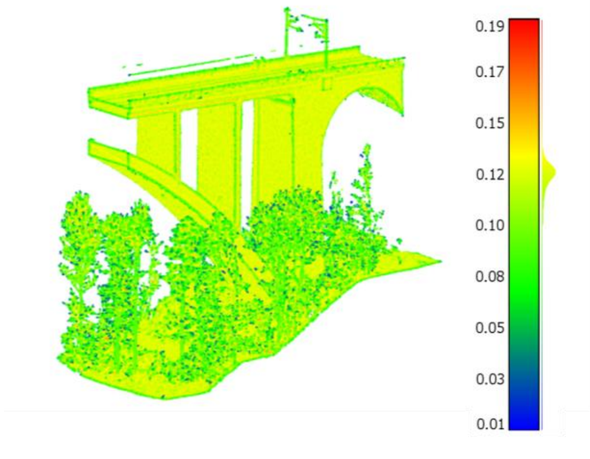

Fig. 9 – Test point cloud colored based on Sum of eigenvalues

Other features

Number of neighbours

The number of neighbours specifies the total number of points, n, in the selected neighbourhood of a given point (Figure 10 a)). As mentioned earlier in the chapter, the choice of neighbourhood size and type is crucial for the eigenvalue calculation. In this case, a spherical neighbourhood with a radius of 0.5 meters was selected to calculate all the presented features, including the number of neighbours.

DOI 10.14311/CEJ.2025.01.0005

Distance to plane

Distance to plane expresses distance of point X from plane p and can be calculated using Equation 12:

$$\vartheta(X, p) = \frac{|ax_i + by_i + cz_i + d|}{\sqrt{a^2 + b^2 + c^2}}, \tag{12}$$

where a, b, c, d are the parameters of the point-normal equation of the plane, and x_i, y_i, z_i represent the coordinates of the neighbouring points. The parameters a, b and c correspond to the values of the normal vector calculated through Singular Value Decomposition (SVD), and the parameter d is computed using a, b and c along with the coordinates of the center of gravity through which the plane passes. This feature can be helpful, for example, in identifying noise or low vegetation in point clouds (Figure 10 b)).

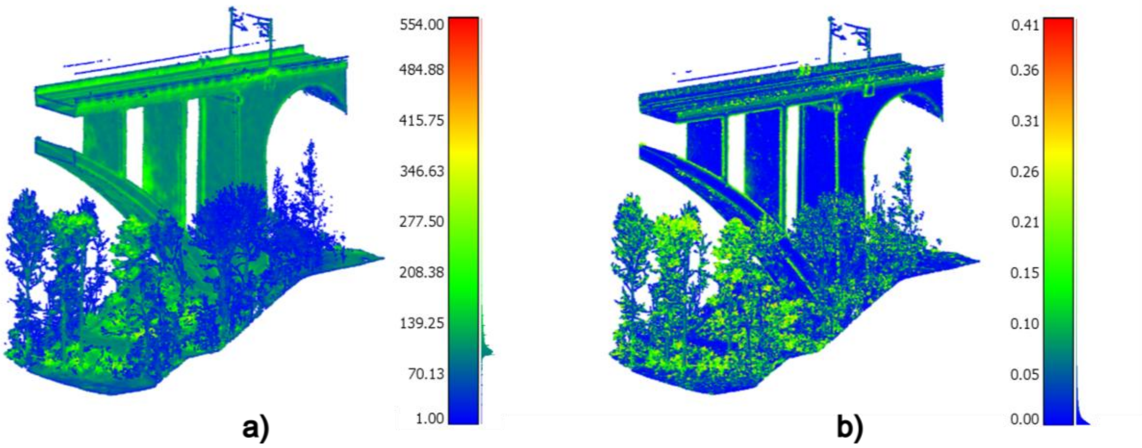

Fig. 10 – Test point cloud colored based on: a) Number of neighbours, b) Distance to plane

Surface density

Surface density expresses the density of points in the surface of a circle of the selected radius. It can be used to infer the density of points per unit area. In a relative color scale, the feature appears to be strongly similar to number of neighbours, as can be seen in Figure 11 a). The value of this feature can be calculated according to Equation 13:

$$Sd = \frac{n}{\pi r^2}, \tag{13}$$

where r is the radius of the local neihbourhood and n is the number of points in the neighbourhood.

Volume density

Volume density expresses the point density within the volume of the selected neighbourhood's sphere. It can be used to infer the number of points per unit volume. In a relative color scale, this feature appears similar to the number of neighbours and surface density features (Figure 11 b)). The value of this feature can be calculated using Equation 14:

$$Vd = \frac{n}{\frac{4}{3}\pi r^3}, \tag{14}$$

where r is the radius of the local neihbourhood and n is the number of points in the neighbourhood.

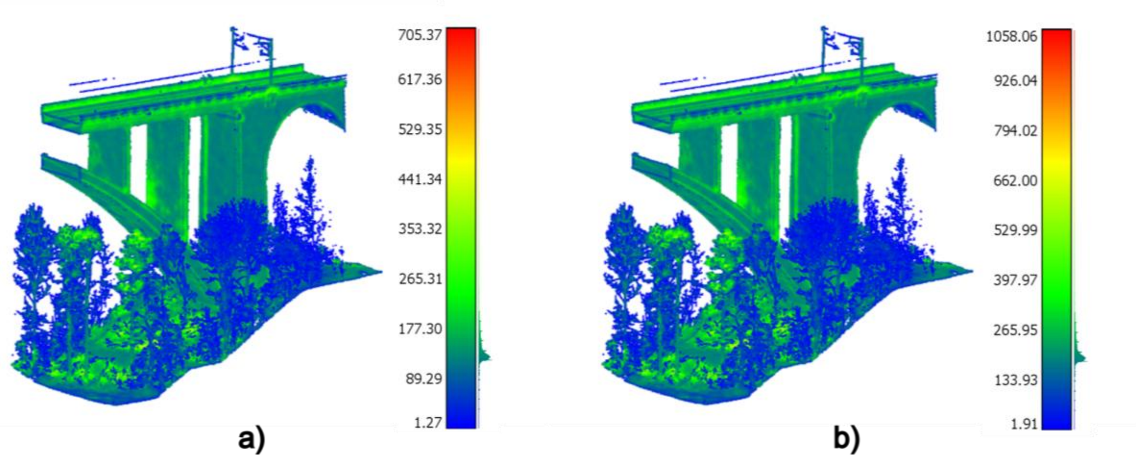

Fig. 11 – Test point cloud colored based on: a) Surface density, b) Volume density

Height standard deviation

This feature shows the standard deviation of the heights of all points in the local neighbourhood. As seen in the Figure 12 a), it can be used to distinguish between horizontal, vertical, and inclined surfaces. The formula for the calculation is described in the Equation 15:

$$s_Z = \sqrt{\frac{\sum_{i=1}^{n}(\bar{Z} - Z_i)^2}{n}}, \tag{15}$$

where n is the number of points in the neighbourhood, Z_i is height of a point of the neighbourhood and $\bar{Z}$ is the mean of the heights of all the points in the neighbourhood.

Max height difference

The feature is calculated as the difference between the height of the highest and lowest point of the neighbourhood. The result is similar to the Height standard deviation and can be used to detect horizontal surfaces (Figure 12 b)).

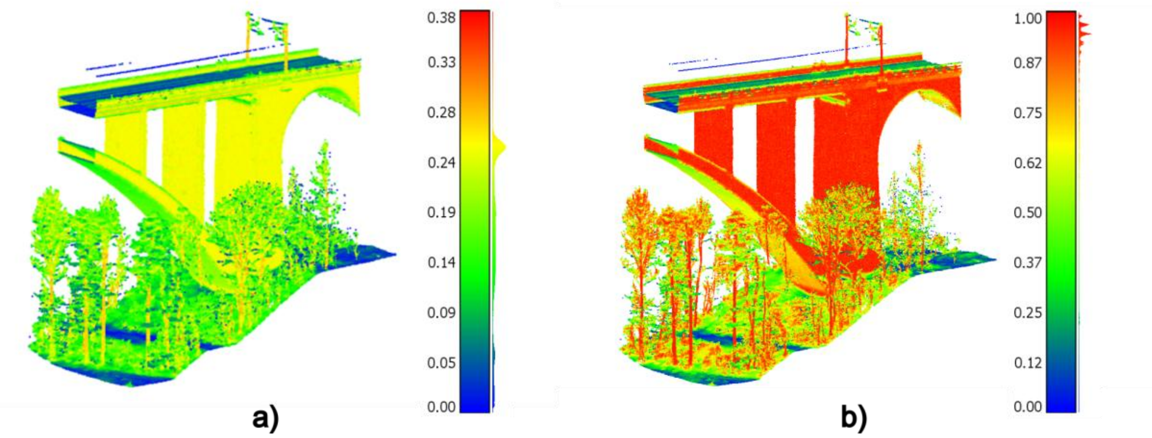

Fig. 12 – Test point cloud colored based on: a) Height standard deviation, b) Max height difference

FEATURE ANALYSIS

The relationships between the individual features describing the geometric and spatial properties of the points in the point cloud were analyzed based on the coefficient of determination. This reflects how well the values of one feature can be explained by the other. The results show the presence of strong, medium and weak dependencies, see Figure 13.

r = 0.5 m	PLA	LIN	SPHE	NON	SOE	OMNI	ENTR	ANI	SV	VD	SD	MHD	DTP	HSD	VERT	PCA1	PCA2
planarity (PLA)																	
linearity (LIN)	0.75																
sphericity (SPHE)	0.51	0.07															
number of neigh-bours (NON)	0.00	0.07	0.23														
sum of eigen-values (SOE)	0.28	0.41	0.02	0.15													
omnivariance (OMNI)	0.38	0.07	0.67	0.31	0.00												
eigenetropy (ENTR)	0.06	0.27	0.06	0.35	0.82	0.18											
anisotropy (ANI)	0.51	0.07	1.00	0.23	0.02	0.67	0.06										
surface variation (SV)	0.62	0.14	0.97	0.18	0.04	0.70	0.04	0.97									
volume density (VD)	0.00	0.07	0.23	1.00	0.15	0.31	0.35	0.23	0.18								
surface density (SD)	0.00	0.07	0.23	1.00	0.15	0.31	0.35	0.23	0.18	1.00							
max height difference	0.04	0.01	0.07	0.04	0.01	0.06	0.03	0.07	0.08	0.04	0.04						
distance to plane (DTP)	0.00	0.00	0.01	0.01	0.05	0.01	0.05	0.01	0.00	0.01	0.01	0.01					
height standard deviation (HSD)	0.02	0.01	0.02	0.01	0.00	0.02	0.01	0.02	0.03	0.01	0.01	0.94	0.00				
verticatlity (VERT)	0.00	0.01	0.00	0.01	0.00	0.01	0.00	0.00	0.00	0.01	0.01	0.66	0.00	0.77			
PCA1	0.19	0.66	0.09	0.26	0.30	0.06	0.46	0.09	0.04	0.26	0.26	0.01	0.01	0.00	0.01		
PCA2	0.91	0.92	0.24	0.01	0.37	0.19	0.18	0.24	0.34	0.01	0.01	0.02	0.00	0.02	0.00	0.46	

degree of determination
0.00-0.69
0.70-0.80
0.81-0.90
0.91-1.00

Fig. 13 – Coefficients of determination of the examined features

The analysis revealed a complete dependence between anisotropy and sphericity. This result suggests that both features share common geometric properties of the point cloud, and their calculation is strongly linked. One hundred percent dependence was also found between the features number of neighbours, volume density and surface density.

DOI 10.14311/CEJ.2025.01.0005

Strong coefficient of determination was found between anisotropy and surface variation (0.97), sphericity and surface variation (0.97) or between maximum height difference and height standard deviation (0.94).

From looking at the point cloud and the distribution of features in it, it was concluded that some of them do not have significant predictive value for filtering and classifying point clouds. For example, we have identified omnivariance, sum of eigenvalues, eigenentropy and PCA1 as such. The features planarity, surface variation, PCA2 and distance to plane may be suitable for classification and filtering. Some features, which work for example with the height distribution of points in the neighbourhood, are mainly suitable for creating digital terrain models and for finding horizontal surfaces. These features include verticality, height standard deviation, max height difference.

This analysis suggests that some features of the point neighbourhood are redundant, while others may be of great importance for describing the point cloud.

CHALLENGES AND FUTURE DIRECTIONS

Currently used features calculated from the local 3D neighbourhood of a point work well in the case of resolution of e.g. flat surfaces and complex objects (vegetation), where the classification is reliable. The description of a set of points by eigenvectors is in fact a fitting of the points of the neighbourhood with a plane. However, in the real world, flat surfaces do not often occur and when we change the scale (the size of the local 3D neighbourhood of a point) we can get more complex surfaces. Because of this, the difference between the features of each object can then be unclear and indistinguishable to an automated program. Therefore, when using large neighborhoods, we suggest fitting the neighbourhood points with a higher order surface and determine the deviations of individual points from this surface in the direction of the 3rd eigenvector. Such a surface can better represent the studied object, and for example, noise removal can then be more effective. A possible limitation of this approach in dense point clouds may be the high demand on computer power when calculating the surface using the least squares method. It is used for adjustment of the second order surface parameters according to Equation 16:

$$z_{r,i} = a_0 + a_1 x_{r,i} + a_2 y_{r,i} + a_3 {x_{r,i}}^2 + a_4 {y_{r,i}}^2 + a_5 x_{r,i} y_{r,i}, \tag{16}$$

where $a_0 - a_5$ are the second order surface parameters and $x_{r,i}, y_{r,i}, z_{r,i}$ are the coordinates of the i-th point in the local neighbourhood, which are rotated for calculation purposes so that their third eigenvector is identical to the direction of the Z-axis. After alignment, the deviations of the points from the surface in the direction of the third eigenvector v are calculated and the standard deviation (Equation 17) is determined from them:

$$s_s = \sqrt{\frac{\sum_{i=1}^{n} {v_i}^2}{n-6}}, \tag{17}$$

where n is the number of points in the local neighbourhood of the selected point.

Figure 14 shows a scan of a terrain with variable curvature, showing the difference between a plane and a second order surface representation of the terrain shape. The point cloud is colored based on standard deviation of deviation of each point from the surface in the direction of the third eigenvector. It can be seen that rounded shapes stand out when the terrain is fitted with the plane, but this representation is unsuitable for noise filtering. Because the second order surface adheres better to the terrain, noise can be removed even in areas with variable curvature.

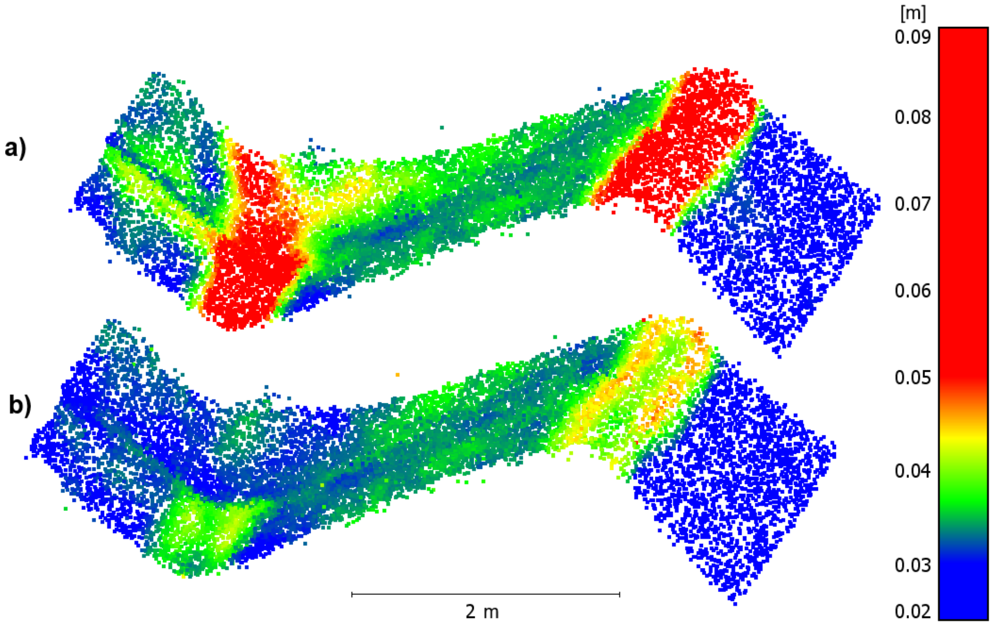

Fig. 14 – A point cloud of a terrain with variable curvature colored based on standard deviation of deviations from: a) a plane, b) a surface of the second order, both fitted to the points of the neighbourhood with radius of 0.5 m

Another limitation of the calculation of features from the local 3D neighbourhood of a point is the calculation method used, for example, in the CloudCompare software (paper [16] cited in their documentation [17]). The coordinates of the points falling within the 3D neighbourhood of the point of interest are reduced to the center of gravity of the neighbourhood points for computation purposes, and the eigenvalues and eigenvectors are then related to this center of gravity. This approach is suitable to describe the point cloud, or parts of it, as a whole. The reduction of a neighbourhood point to a center of gravity is done according to Equation 18:

$$X_{i,red} = X_i - \bar{X};\ \bar{X} = \frac{1}{n}\sum\nolimits_{i=1}^{n} X_i, \tag{18}$$

where X_i is a point of the neighbourhood, n is the number of points in the neighbourhood.

However, if the purpose of the feature is to determine the probability that a given point is noise, a different approach must be taken. If the point under study is part of the noise, it is often far from the center of gravity of the neighbourhood, which is likely to be located on the denser object we want to preserve. In order to characterize this point more accurately, it is possible to reduce the coordinates of the neighbourhood to the surveyed point to obtain information related directly to it. The reduction to the surveyed point is performed according to Equation 19:

$$X_{i,red} = X_i - X_P, \tag{19}$$

where X_P is the surveyed point.

Figure 15 shows the difference between the standard deviation (square root of the 3rd eigenvalue) to the center of gravity and to the surveyed point. The second approach is preferable for noise filtering.

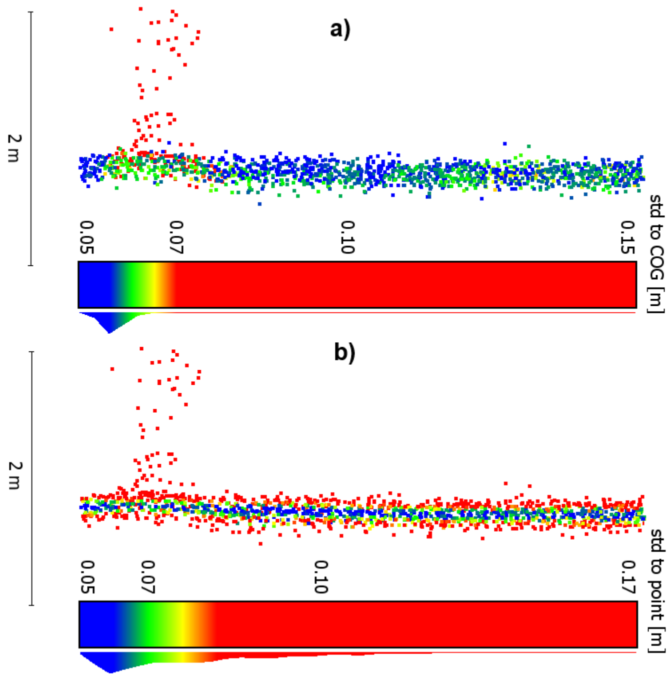

Fig. 15 – A point cloud of terrain with vegetation colored based on standard deviation of neighbourhood points in the direction of 3rd eigenvalue calculated from: a) the centre of gravity, b) the surveyed point

These two approaches can be further explored in the future and could increase the efficiency of automated filtering and classification of point clouds using neural networks and other types of machine learning.

CONCLUSION

This paper has provided a comprehensive review of the various features of the local 3D neighbourhood of a point in a point cloud that are used for data classification and analysis purposes. Furthermore, the suitability of using each feature to identify different types of objects including noise in the point cloud was evaluated.

Analysis of the dependencies between these features showed that some of them exhibit strong correlations with each other, suggesting the possibility of simplifying their use for data classification and filtering. For example, the strong correlation between anisotropy and sphericity indicates their interdependence. The use of only one of them can lead to an optimization of the selection of the most appropriate point cloud classification parameters.

Even though in the description of characteristics we reference several connections between the characteristics and the artificial or natural objects, we do not believe that these connections can be universally applied. The results of classification are always influenced by factors such as the nature of the data, the chosen scale or the level of noise.

New approaches proposed in this article could lead to more efficient classification and filtering of point clouds in the future. One of them is the use of a higher order surface for determining outliers in the neighbourhood. This approach could help remove noise in complex objects. Another new approach is to reduce the coordinates of the neighbouring points to the surveyed point rather than to the center of gravity of the neighbourhood. This makes it possible to obtain a characterization of the surveyed point with respect to its neighbourhood, not of the neighbourhood as a whole. These two new approaches should be the subject of further research.

ACKNOWLEDGMENTS

This work was supported by the Grant Agency of the Czech Technical University in Prague, grant No. SGS24/048/OHK1/1T/11 "Data filtering and classification using machine learning methods".

LIST OF SYMBOLS

3D – three-dimensional
X, Y, Z – point coordinates
RGB – red-green-blue color
PCA – principal component analysis
SVD – singular value decomposition
λ_i – i-th eigenvalue
COG – center of gravity
STD – standard deviation

REFERENCES

[1] PAVELKA JR., Karel; PACINA, Jan. Using of modern technologies for visualization of cultural heritage. Online. Stavební obzor - Civil Engineering Journal. 2023, vol. 32, No. 4, p. 549-563. ISSN 1805-2576. Available from: https://doi.org/10.14311/CEJ.2023.04.0041.

[2] MATOUŠKOVÁ, Eva; PAVELKA, Karel; SMOLÍK, Tobiáš and PAVELKA, Karel. Earthen Jewish Architecture of Southern Morocco: Documentation of Unfired Brick Synagogues and Mellahs in the Drâa-Tafilalet Region. Online. Applied Sciences. 2021, vol. 11, No. 4. ISSN 2076-3417. Available from: https://doi.org/10.3390/app11041712.

[3] KOVANIČ, Ľudovít; PEŤOVSKÝ, Patrik; TOPITZER, Branislav and BLIŠŤAN, Peter. Complex Methodology for Spatial Documentation of Geomorphological Changes and Geohazards in the Alpine Environment. Online. Land. 2024, vol. 13, No. 1. ISSN 2073-445X. Available from: https://doi.org/10.3390/land13010112.

[4] QI, Charles R.; SU, Hao; MO, Kaichun and GUIBAS, Leonidas J. PointNet: Deep Learning on Point Sets for 3D Classification and Segmentation. Online. 2017. Available from: https://doi.org/10.48550/arXiv.1612.00593.

[5] ŠTRONER, Martin; URBAN, Rudolf and SUK, Tomáš. Filtering Green Vegetation Out from Colored Point Clouds of Rocky Terrains Based on Various Vegetation Indices: Comparison of Simple Statistical Methods, Support Vector Machine, and Neural Network. Online. Remote Sensing. 2023, vol. 15, No. 13. ISSN 2072-4292. Available from: https://doi.org/10.3390/rs15133254.

[6] ATIK, Muhammed Enesq and DURAN, Zaide. Classification of aerial photogrammetric point cloud using recurrent neural networks. Online. Fresenius environmental bulletin. 2021, vol. 30, No. 04A/2021, p. 4270-4275. ISSN 1018-4619. Available from: https://www.prt-parlar.de/download_list/?c=FEB_2021#.

[7] LIU, Kunbo; LIU, Shuai; TAN, Kai; YIN, Mingbo and TAO, Pengjie. ANN-Based Filtering of Drone LiDAR in Coastal Salt Marshes Using Spatial–Spectral Features. Online. Remote Sensing. 2024, vol. 16, No. 18. ISSN 2072-4292. Available from: https://doi.org/10.3390/rs16183373.

[8] CHEHATA, Nesrine; GUO, Li and MALLET, Clément. Airborne LIDAR feature selection for urban classification using random forests. Online. Laser scanning, IAPRS. 2009, Vol. XXXVIII. Available from: https://www.researchgate.net/publication/242731335_Airborne_LIDAR_feature_selection_for_urban_classification_using_random_forests.

[9] WEINMANN, M.; JUTZI, B. and MALLET, C. Feature relevance assessment for the semantic interpretation of 3D point cloud data. Online. ISPRS Annals of the Photogrammetry, Remote Sensing and Spatial Information Sciences. 2013, vol. II-5/W2, p. 313-318. ISSN 2194-9050. Available from: https://doi.org/10.5194/isprsannals-II-5-W2-313-2013.

[10] WEINMANN, M.; JUTZI, B.; MALLET, C. and WEINMANN, M. GEOMETRIC FEATURES AND THEIR RELEVANCE FOR 3D POINT CLOUD CLASSIFICATION. Online. ISPRS Annals of the Photogrammetry, Remote Sensing and Spatial Information Sciences. 2017, vol. IV-1/W1, p. 157-164. ISSN 2194-9050. Available from: https://doi.org/10.5194/isprs-annals-IV-1-W1-157-2017. [cit. 2024-11-23].

[11] KOVANIČ, Ľudovít; PEŤOVSKÝ, Patrik; TOPITZER, Branislav and BLIŠŤAN, Peter. Spatial Analysis of Point Clouds Obtained by SfM Photogrammetry and the TLS Method—Study in Quarry Environment. Online. Land. 2024, vol. 13, No. 5. ISSN 2073-445X. Available from: https://doi.org/10.3390/land13050614.
[12] RAPUCA, Almedina; MATOUŠKOVÁ, Eva. Testing of close-range photogrammetry and laser scanning for easy documentation of historical objects and buildings parts. Online. Stavební obzor - Civil Engineering Journal. 2023, vol. 32, No. 4, p. 504-518. ISSN 1805-2576. Available from: https://doi.org/10.14311/CEJ.2023.04.0038.
[13] WEINMANN, Martin; JUTZI, Boris; HINZ, Stefan and MALLET, Clément. Semantic point cloud interpretation based on optimal neighborhoods, relevant features and efficient classifiers. Online. ISPRS Journal of Photogrammetry and Remote Sensing. 2015, vol. 105, p. 286-304. ISSN 09242716. Available from: https://doi.org/10.1016/j.isprsjprs.2015.01.016.
[14] JOLLIFFE, Ian T. and CADIMA, Jorge. Principal component analysis: a review and recent developments. Online. Philosophical Transactions of the Royal Society A: Mathematical, Physical and Engineering Sciences. 2016, vol. 374, No. 2065. ISSN 1364-503X. Available from: https://doi.org/10.1098/rsta.2015.0202.
[15] BARNETT, T. P. and PREISENDORFER, R. Origins and Levels of Monthly and Seasonal Forecast Skill for United States Surface Air Temperatures Determined by Canonical Correlation Analysis. Monthly Weather Review. 1987, vol. 115, no. 9, p. 1825-1850. ISSN 0027-0644. Available from: https://doi.org/10.1175/1520-0493(1987)115<1825:OALOMA>2.0.CO;2.
[16] HACKEL, Timo; WEGNER, Jan D. and SCHINDLER, Konrad. Contour Detection in Unstructured 3D Point Clouds. Online. 2016 IEEE Conference on Computer Vision and Pattern Recognition (CVPR). 2016, p. 1610-1618. ISBN 978-1-4673-8851-1. Available from: https://doi.org/10.1109/CVPR.2016.178.
[17] Compute geometric features. Online. CLOUDCOMPARE. CloudCompare Wiki. 2024, 7. January 2024. Available from: https://www.cloudcompare.org/doc/wiki/index.php?title=Compute_geometric_features.

CIVIL ENGINEERING JOURNAL

Article no. 6

THE CIVIL ENGINEERING JOURNAL 1-2025

SIMULATION OF RC-T BEAM REINFORCED BY STEEL WIRE MESH AND POLYURETHANE CEMENT COMPOSITE (SWM-PUC)

Shiyu Chen, Kenxin Zhang, Dianye Cao, Yi Wang and Longsheng Bao

Shenyang Jianzhu University, School of Transportation and Geomatics Engineering, Shenyang, No.25 Hunnan Zhong Road, China; jt_zkx@sjzu.edu.cn

Received: *01.10.2024*

Received in revised form: *05.12.2024*

Accepted: *27.01.2025*

ABSTRACT

In this paper, the flexural performance of seven steel wire mesh and polyurethane cement (SWM-PUC) composite-strengthened beams was investigated experimentally. The variation law of flexural performance of reinforced beams is clarified. Based on the experimental research, the deflection and stress analysis of SWM-PUC composite strengthened reinforced concrete beams was conducted using finite element analysis software ABAQUS. The Bending properties of reinforced beams with different steel wire mesh (SWM) reinforcement rates and different polyurethane cement (PUC) thickness parameters were researched.The finite element analysis shows that as the reinforcement ratio of the SWM increases, the yield and ultimate loads gradually increase and the deflection then gradually decreases. When the reinforcement ratio reaches a certain level, the increase in yield load decreases with the increase of the reinforcement ratio. As the thickness of the PUC increases, the yield limit and ultimate load gradually increase, and the deflection value decreases continuously. The optimum configuration of the SWM -PUC composite reinforcement layer was given through the finite element analysis.

KEYWORDS

Finite Element Analysis, Steel Wire Mesh, Polyurethane Cement, Reinforcement

INTRODUCTION

Nowadays, bridge deck pavement is prone to cracking, potholes and other problems under vehicle loads, temperature and environmental factors[1,2]. However, demolition and reconstruction of bridges is time-consuming and costly[3]. Therefore, to ensure that the existing bridge structure based on the bridge reinforcement can have considerable economic benefits at the same time can also produce good social benefits[4,5].

Stranded wire mesh (SWM) has good tensile strength, toughness and durability, often with polymer mortar as its bonding with concrete anchoring materials[6]. Polymer mortar has good film-forming properties and can adapt to the uneven surface of the reinforced concrete structure[7,8]. However, due to the relatively low strength of the polymer mortar, the composite reinforcement layer is prone to premature cracking, which negatively affects the durability of the SWM at the cracks[9-11]. And compared to polymer mortars, Polyurethane Cement (PUC) can make bridge reinforcement more efficient and easier at a lower cost. In this way, the PUC material not only solves the problem of bonding to concrete but also provides additional reinforcement[12]. Shengran Zhang conducted an experimental study on PUC steel wire ropes in strengthening reinforced concrete structures. Findings show that PUC steel wire ropes can significantly improve the bearing capacity of reinforced concrete beams. The bearing capacity increases with the increase of the reinforcement ratio of the wire rope. The maximum increase in load-bearing capacity after reinforcement was 75.3%.

Although reinforcement methods such as steel wire mesh and polyurethane cement(SWM-PUC) composite reinforcement are costly, require professional skills and are highly affected by weather factors, they provide high strength and stiffness, good durability and corrosion resistance, convenient and fast construction, and are suitable for various structural forms[13-16]. The effects of various reinforcement techniques on reinforced elements can be obtained utilizing experimental methods[17,18]. However, to draw accurate conclusions, a large number of experiments would have to be carried out, which would be quite labor-intensive and costly. Therefore, it is necessary to simulate and analyze the reinforcement tests with the help of finite element software[19-21].

In this paper, an experimental study was conducted on seven reinforced concrete T-beams using SWM-PUC to improve the bending resistance of strengthened concrete beams. Based on the model, numerical analysis was conducted on SWM-PUC composite reinforced reinforced concrete beams using finite element analysis software ABAQUS. The effect of steel wire mesh (SWM) reinforcement rate and thickness of PUC on ultimate load was comparatively analyzed.

EXPERIMENTAL STUDY OF SWM AND PUC COMPOSITE REINFORCEMENT OF RC-T BEAMS FOR FLEXURAL RESISTANCE

Flexural Test Overview

A total of 7 Reinforced Concrete (RC) beams were designed in the experiment, of which 6 were composite reinforced beams and 1 was a beam that was not reinforced with SWM-PUC or Polymer mortar. The length of the beam is 3800 mm, the width of the upper flange is 360 mm and the height of the beam is 320 mm. The concrete strength grade is C30, the thickness of the protective layer is 25 mm, the longitudinal tensile reinforcement and the erection steel bars are HRB400 steel bars, and the distance of the loading point from the support is 1500 mm. The SWM used for reinforcement is a domestic galvanized strand type with a diameter of 2.4 mm. The main parameters of the test, besides the type of bonded anchorage material in the reinforcement layer, other reinforcement parameters such as SWM reinforcement ratio, PUC thickness, anchorage method and loading method were also considered. The design parameters of the specimens are presented in Table 1. The elevation details of the test beam are presented in Figure 1.

Tab.1 - Specimens design parameters

Beam	Bonded anchoring materials	Bonded anchoring materials thickness(mm)	Number of longitudinal steel wires	End anchoring method	Loading method
CB	-	-	-	-	-
B1	Polymer mortar	20	8	-	-
B2	Polymer mortar	20	8	End U-shaped anchorage	-
B3	PUC	20	5	-	-
B4	PUC	20	8	-	-
B5	PUC	30	5	-	-
B6	PUC	20	8	-	Preload

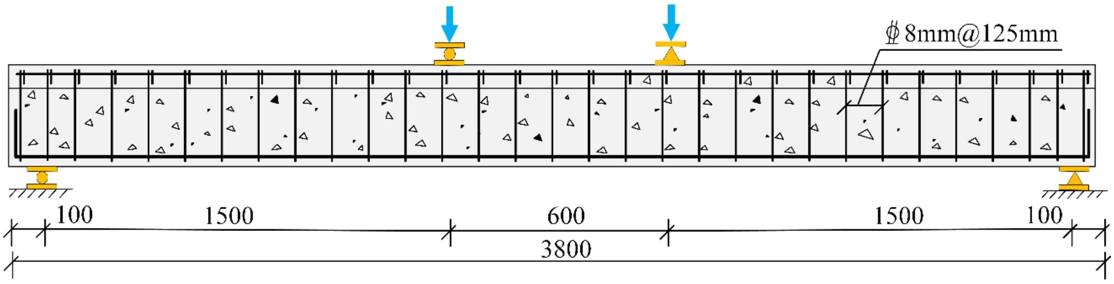

Fig. 2 – Elevation detail of test beam (unit: mm)

Test Measurement

The test used bow strain sensors to measure concrete strain and PUC strain, and resistance strain gauges to measure rebar strain and strand strain. Pre-load the test beam before testing formal loading, and check whether all test instruments and meters work normally. Before the beams cracked, they were loaded in 1 grade of 2kN. After cracks appeared in the concrete at the bottom of the beams, 1 loading level of 5kN was applied with a waiting time of 3 minutes to observe and record the test phenomena. All measurements are automatically recorded by the collection box. Once the bars were tied, an electrical resistance streak meter was installed at the center of each tensile bar. After the SWM has been stretched, one resistance strain gauge is arranged at the center of each longitudinal strand. The arrangement of the strain measurement points for reinforcement and strand in the elevation is shown in Figure 2. For the reinforced test beams, six strain measurement points were arranged along the length of the profile. The strain arrangement of the cross-section measurement points is shown in Figure 3.

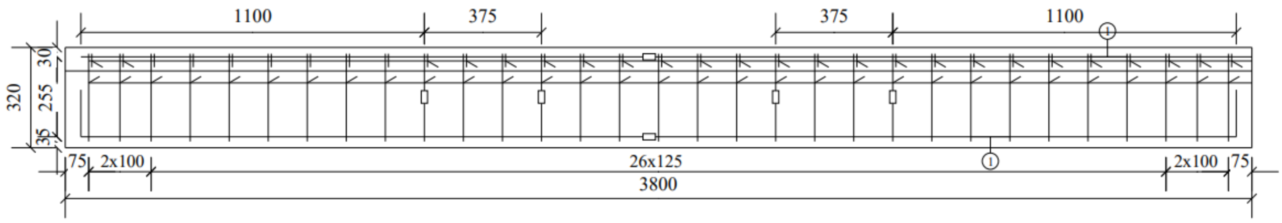

Fig. 2 – Reinforcing steel strand strain measurement point arrangement diagram

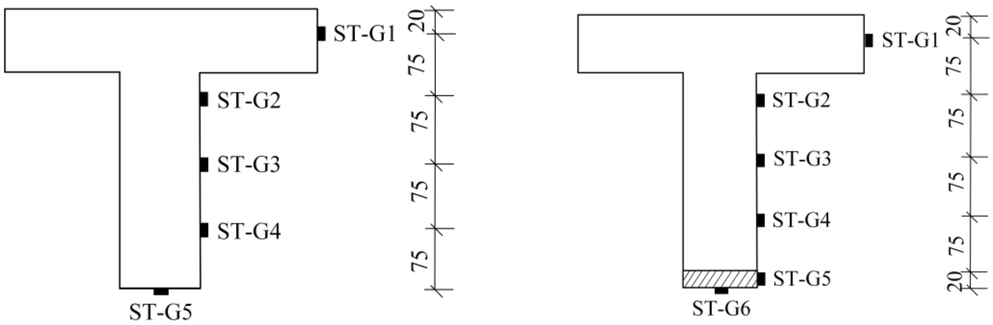

(a) – Unreinforced beam *(b) – Reinforced beam*

Fig. 3 – Concrete strain measurement point arrangement (unit: mm)

Test Results and Analysis

Load-Displacement Curve Analysis

The load-displacement curves of the specimens are presented in Figure 4. Reinforced beams are in an elastic working stage before cracking. Load is linearly related to displacement. The slopes

DOI 10.14311/CEJ.2025.01.0006

of the load-displacement curves were the same as those of the unreinforced comparison beams. After the cracks appear, the slope of the curve decreases, the stiffness of the section decreases and the deflection grows faster. The deflection increases more slowly in reinforced members than in unreinforced members. As the load increases, the reinforcement begins to yield. The slopes of the load-displacement curves of the unreinforced beams decrease sharply and the slopes of the load-displacement curves are almost horizontal. Due to the presence of the reinforcement layer, the load-displacement curve of the SWM and PUC composite reinforced members still has a large slope and the bearing capacity continues to grow. As the load continued to improve, the PUC material fractured with the SWM and the deflection of the members improved significantly.

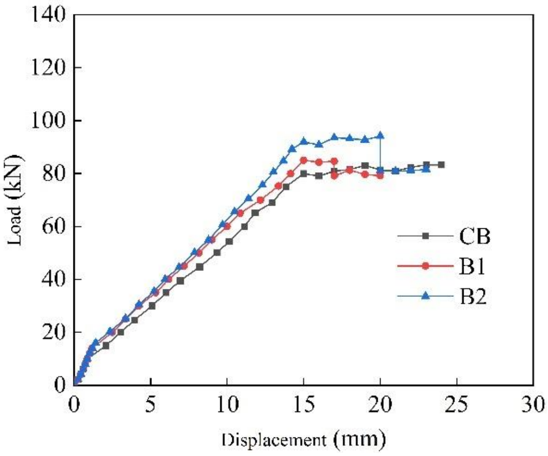

(a) – SWM-polymer mortar reinforcement specimens

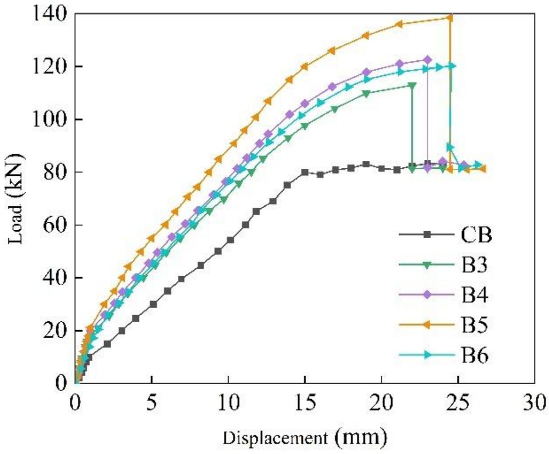

(b) – SWM-PUC reinforcement specimens

Fig. 4 – Load-displacement curve

(1) Cracking load

The cracking load, yield load and ultimate load values for each test beam are presented in Table 2. The cracking load for the unreinforced beam CB is 10 kN. The cracking loads of beams B3, B4 and B5 were 18 kN, 20 kN and 22 kN, respectively, which were 80%, 100% and 120% higher than those of the unreinforced beams. The cracking load of the reinforced beams increases with the increase in the reinforcement ratio of the SWM. When the longitudinal strands were increased from 5 to 8, the cracking load of beam B4 increased by 2 kN compared to beam B3. Cracking loads increased with increasing thickness of PUC. When the thickness of the reinforcement layer was increased from 20 mm to 30 mm, the cracking load of beam B5 increased by 4 kN compared to beam B3. Therefore, SWM-PUC reinforcement can enhance the cracking load of beams. This is mainly because PUC and SWM together provide some reinforcement. The cracking load of beam B1 is 14 kN. The cracking load was reduced by 30% compared to beam B4 with the same SWM reinforcement ratio. The cracking load of beam B2 with end U-shaped anchorage was 16 kN. The cracking load was also reduced by 20% compared to beam B4 having the same SWM reinforcement ratio. It is shown that PUC materials are significantly better than polymer mortar materials for increasing the cracking loads of the test beams.

(2) Yield load

The output of the sensors is monitored in real-time by a data acquisition system to obtain the strain changes in the beam. On the stress-strain curve, find the point where the stress no longer increases linearly with strain, the yield point. Compared with unreinforced beams, the yield loads of beams B1 and B2 were improved by 16.6% and 25% respectively, and the yield loads of beams B3, B4, B5 and B6 were increased by 31.6%, 43%, 63.3% and 40% respectively. PUC has a greater increase in yield load than polymer mortar. It shows that PUC is more effective and significant in enhancing the yield load of reinforced beams. The yield load values of beams B3 and B4 were

DOI 10.14311/CEJ.2025.01.0006

increased by 31.6% and 43%, respectively, compared to the reinforced beams. It is shown that the magnitude of yield load enhancement increases with increasing reinforcement ratio of the SWM for the same reinforcement thickness. Compared to the reinforced beams, the yield load increase is 40% for the preloaded beam B6 and 43% for the unloaded beam B4. Both have almost the same lift for yield loads. It is shown that secondary stressed beams with initial damage also have better reinforcement.

(3) Ultimate load

From Table 2, it is shown that the ultimate load of the reinforced beams can be increased by up to 75% compared to the unreinforced beams. For beams B3, B4, B5 and B6 strengthened with SWM-PUC, the ultimate load increases were 41%, 53.3%, 75% and 50%, respectively. The ultimate load enhancement of B1 and B2 beams strengthened with SWM-polymer mortar increased by 6.3% and 17.5%, respectively. The former is more effective in increasing the ultimate load of the intensification beam. In addition, there is a 47 % difference in the lifting of the ultimate loads of beams B1 and B4. It is shown that PUC with strand reinforcement is more effective than polymer mortar with SWM reinforcement in enhancing the load-carrying capacity of the specimens. Beam B4 and Beam B6 have almost the same magnitude of lift for the ultimate load. It shows that the mode of loading has essentially no effect on the bearing capacity.

Tab.2 - Characteristic load test value

Beam	Cracking load/kN	Increase relative /%	Yield load/kN	Increase relative/%	Ultimate load/kN	Increase relative/%
CB	10	-	60	-	80	-
B1	14	40	70	16.6	85	6.3
B2	16	60	75	25	94	17.5
B3	18	80	79	31.6	112.8	41
B4	20	100	85.8	43	122.6	53.3
B5	22	120	98	63.3	140	75
B6	-	-	84	40	120	50

Load-Strain Curve Analysis

(1) Longitudinal reinforcement strain

The effect of reinforced concrete beams with SWM and two different materials was investigated by applying strain gauges to the reinforcement to measure the strain. It is shown in Figure 5 that the longitudinal reinforcement strain is linearly related to the load before cracking of the specimen. When the load reaches 40 kN, the strain of the unreinforced beam is 1585 με, and the strains of the SWM-polymer mortar beams B1 and B2 are 1288 με and 1127 με, respectively. The strains in beams B3, B4, B5 and B6 reinforced with SWM-PUC at this time were 853 με, 750 με, 697 με and 632 με, respectively. The SWM-PUC reinforcement specimens should be changed to a smaller size under the same load. The reason for this is that the SWM shares part of the load during loading, resulting in a smaller load increment in the reinforced beam for the same longitudinal strain. As the load increases, the reinforcement yields and the constraint of the SWM on the concrete become more pronounced. Continuing to increase the load, the strand mesh-polymer mortar reinforcement layer peeled away from the concrete, and the slope of its load-strain curve for the SWM was greatly reduced. However, the PUC remained well bonded to the concrete with a slow decrease in the slope of the load-reinforcement strain curve.

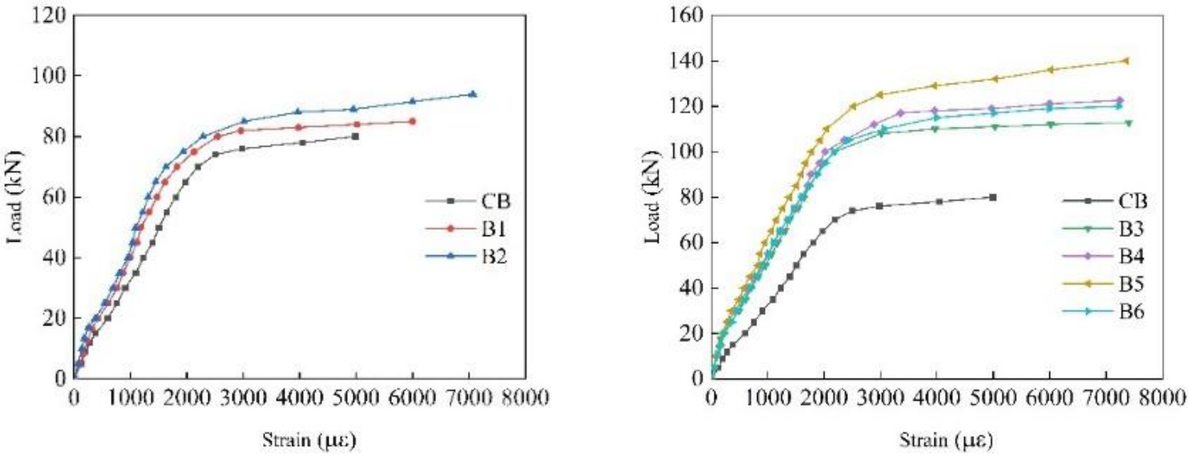

(a) – SWM-polymer mortar reinforcement specimens *(b) – SWM-PUC reinforcement specimens*

Fig. 5 – Load-strain in reinforcement curves

(2) SWM strain

The load-strand strain curve is shown in Figure 6. From the figure, it is shown that the SWM is involved in the force throughout the loading process. Before the beam cracked, the load was linearly related to the strand strain. As the load increases, the crack develops and expands gradually, the neutralization axis moves upwards and the strain in the SWM increases gradually. When the reinforcement yields, the strain in the SWM increases rapidly. This is because the SWM exits the force and part of the load increment is carried by the SWM and the other part of the load increment is carried by the PUC. Until the composite reinforcement breaks. Among them, beams B1 and B2 were reinforced by SWM-polymer mortar, the SWM was not pulled off due to the stripping damage of the reinforcement layer from the concrete, and the strength of the SWM was not fully utilized.

(3) PUC strain

Based on the test data, the load-PUC strain curves for beams B3, B4, B5 and B6 were plotted as shown in Figure 7. As can be seen in Figure 7, the trend of load-PUC strains is the same for the test beams for the four different conditions. During the plastic working stage, the PUC strains of beams B3, B4, and B5 gradually decrease under the same loads. It shows that the stiffness of the test beam increases as the thickness of polyurethane increases. In this case, the load-PUC strain curves of beams B4 and B6 almost coincide, indicating that they have the same stiffness. It was further shown that the beams that were preloaded to produce cracks and then strengthened still had good stiffness. The same ultimate load capacity as the test beam that had not been pre-loaded. The ultimate damage loads of the test beams for the four different working conditions were 122.8 kN, 122 kN, 120 kN and 140 kN, at which time the corresponding PUC strains were 7000 με, 7140 με, 7071 με and 7336 με, respectively. PUC is known to have an ultimate tensile strain of 7000 με and a tensile strength of 35.6 MPa. The tensile stresses of beam B3, beam B4, beam B5 and beam B6 are 31.4 MPa, 32 MPa, 31.6 MPa and 32.2 MPa, respectively, which have reached the ultimate tensile strength of PUC. The damage to beam B3, beam B4, beam B5 and beam B6 were all composite reinforcement fractures. PUC has better bonding and tensile strength than polymer mortar and is more effective in increasing the load-carrying capacity of beams when reinforced with SWM.

DOI 10.14311/CEJ.2025.01.0006

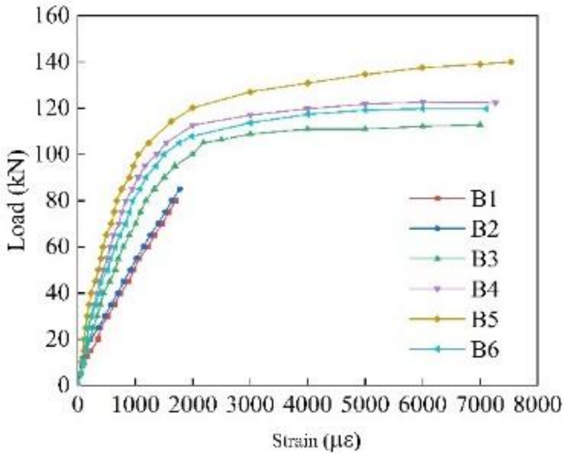

Fig.6 – Load-strand strain curve

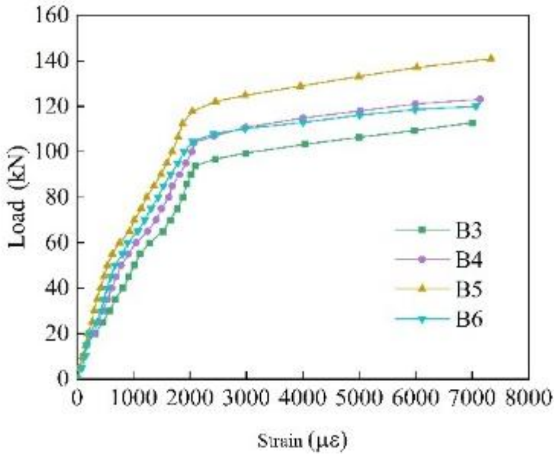

Fig.7 – Load-PUC strain curve

FINITE ELEMENT ANALYSIS OF SWM-PUC COMPOSITE REINFORCED RC-T BEAMS

Parameterisation of Materials

Concrete Unit and Parameter Setting

In this paper, a concrete plastic damage model is used, which can simulate the mechanical properties of concrete materials such as cracking and crushing. In this paper, the plasticity-based ontological relationship of concrete is used, as shown in Figure 8. The strain in the stress-strain curve of compressed concrete increases with increasing stress up to the maximum compressive strength, and eventually damage occurs when the ultimate strain is reached. The stress-strain curve of tensile concrete is linear until the maximum tensile strength is reached. After this, the concrete cracks and gradually decreases in strength. Poisson's ratio is 0.2. The modulus of elasticity is 30GPa.

$$\sigma_{c} = (1-d_{c})E_{c}\varepsilon \tag{3.1}$$

$$d_{c} = \begin{cases} 1-\dfrac{p_{c}n}{n-1+x^{n}} & x \le 1 \\ 1-\dfrac{p_{c}}{a_{c}(x-1)^{2}+x} & x > 1 \end{cases}$$

$$p_{c} = \frac{f_{c}}{E_{c}\varepsilon_{c,r}}$$

$$n = \frac{E_{c}\varepsilon_{c,r}}{E_{c}\varepsilon_{c,r}-f_{c}}$$

$$x = \frac{\varepsilon}{\varepsilon_{c,r}}$$

$$\varepsilon_{c,r} = (700+172\sqrt{f_{c}})\times 10^{-6}$$

$$a_{c} = 0.157 f_{c}^{0.785} - 0.905$$

where d_c is the concrete uniaxial compression damage evolution parameters, E_c is the modulus of elasticity of concrete, a_c is the concrete uniaxial compression stress-strain curve descending section parameter section, f_c is the Concrete axial compressive strength, $\varepsilon_{c,r}$ is the Concrete axial compressive strength fc Corresponding peak compressive strain of concrete.

$$\sigma_{\mathrm{t}} = (1-d_{\mathrm{t}})E_{\mathrm{c}}\varepsilon \tag{3.2}$$

$$d_{\mathrm{t}} = \begin{cases} 1-p_{\mathrm{t}}(1.2-0.2x^5) & x \le 1 \\ 1-\dfrac{p_{\mathrm{t}}}{a_{\mathrm{t}}(x-1)^{1.7}+x} & x > 1 \end{cases}$$

$$p_{\mathrm{t}} = \frac{f_{\mathrm{t}}}{E_{\mathrm{c}}\varepsilon_{\mathrm{t,r}}}$$

$$x = \frac{\varepsilon}{\varepsilon_{\mathrm{t,r}}}$$

$$\varepsilon_{\mathrm{t,r}} = f_{\mathrm{t}}^{0.54} \times 65 \times 10^{-6}$$

$$a_{\mathrm{t}} = 0.312 f_{\mathrm{t}}^2$$

where i_t is the concrete uniaxial tensile damage evolution parameters, a_t is the concrete uniaxial tensile stress-strain curve falling section parameter section, f_t is the concrete axial tensile strength, $\varepsilon_{t,r}$ is the concrete axial tensile strength ft corresponding concrete peak tensile strain.

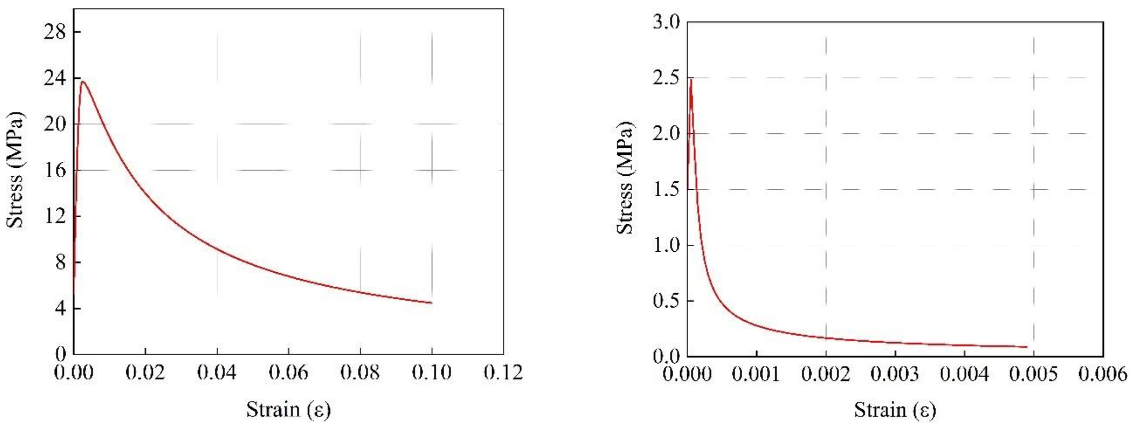

(a) – Axial compression *(b) – Axial tensile*

Fig. 8 – Constitutive relation of concrete

Rebar Unit and Strand Parameterisation

The common reinforcement required for this paper includes longitudinal bars, hoop bars, and erection bars. The intrinsic relationship adopted is a triple-fold model containing elastic, yield and strengthening phases. The strength of the bar continues to increase even after it reaches yield strength and enters the plastic phase. Es and Es* are the modulus of elasticity of the reinforcement in the elastic and strengthening phases, respectively. The simplified stress-strain curves of the steel bars are shown in Figure 9.

In this paper, measured strand stress-strain curves are used, as shown in Figure 10. SWM is hard and rigid in material, with almost no obvious plasticity section, its stress-strain curve pre-approximate a straight line. When the applied load reaches the yield load of the SWM, the SWM enters the plastic phase and subsequently reaches the ultimate load. The SWM has a modulus of elasticity of 140GPa, an ultimate tensile strain of 0.0187 and a tensile strength of 1520 MPa.

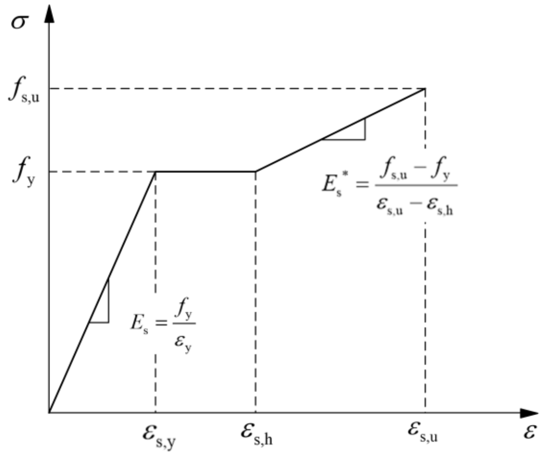

Fig. 9 – Reinforcement stress-strain simplified curve

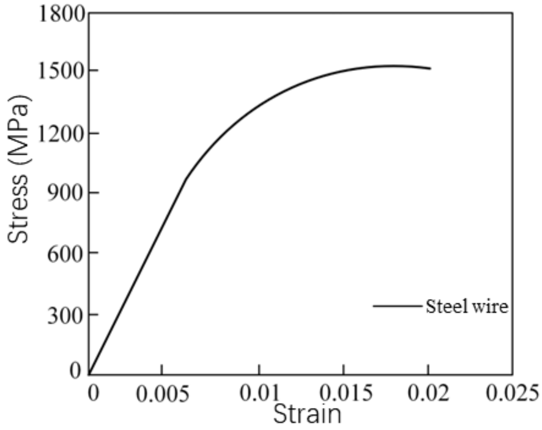

Fig. 10 – Steel-stranded wire axial tensile stress-strain curve

Properties and Parameters of PUC Material

In this study, the tensile intrinsic curve of PUC was obtained based on tests. According to the experimental results of PUC material, the modulus of elasticity of PUC material is taken as EPUC = 5500 MPA and Poisson's ratio is taken as v = 0.27. Figure 11 shows the measured axial tensile stress-strain curves for PUC materials. It is shown that in Figure 11, the ultimate tensile strain of PUC is 7000 με and the ultimate tensile stress of PUC is 35.6 MPa.

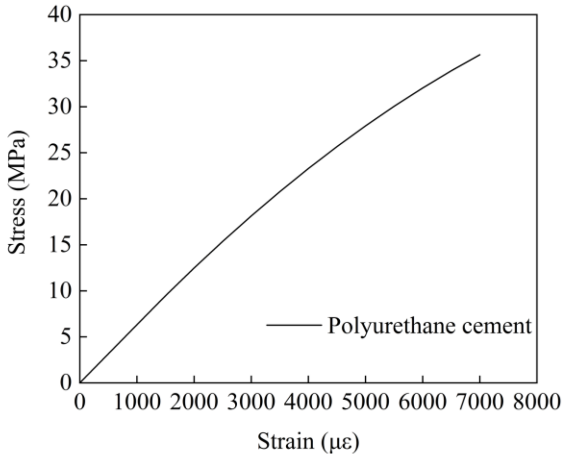

Fig. 11 – Measured axial tensile stress-strain curves of PUC materials

Finite Element Mechanism Analysis

Finite Element Modeling

The finite element units are selected as follows:

Solid units were selected for concrete, bearing pads and polyurethane cement; Selection of wire units for main reinforcement, hoop reinforcement and reinforcing strand mesh. See 3.1 for material parameter properties. In the model, the concrete and bearing pads are connected with a Tie, and the main reinforcement and rectangular hoop reinforcement in the concrete are embedded

DOI 10.14311/CEJ.2025.01.0006

in the Embedded region. The SWM is embedded in the polyurethane cement material using an Embedded region. Polyurethane cement material in contact with concrete select Tie. Constraints are added to the centerline of the pad by adding horizontal and vertical constraints at the supports to simulate simply supported beam boundary conditions.The mesh division size is 20mmx20mmx20mm and the model does not take into account the bond slip between the concrete and the reinforcement. A finite element model is established and the simulation results are compared and analyzed with the test results to verify the reliability of the simulation.

Deflection Analysis

Since the damage mode of the SWM-polymer mortar reinforced beams was peeling damage, the reinforcement and the SWM were not in full play and the results could not be analyzed accurately. Therefore, test beams B1 and B2 were not modeled. Unreinforced beams, beam B3, beam B4 and beam B5 were modeled and computationally analyzed to extract the deflections and ultimate deflections of the beams when the reinforcement yielded, respectively. The deflection clouds of beam CB, beam B3, beam B4 and beam B5 are shown in Figure 12.

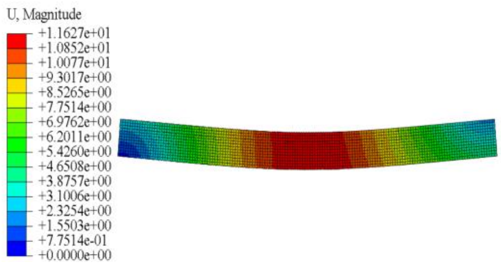

(a) – Deflection at yield of beam CB

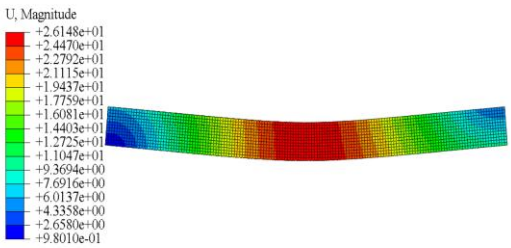

(b) – Deflection at limit state of beam CB

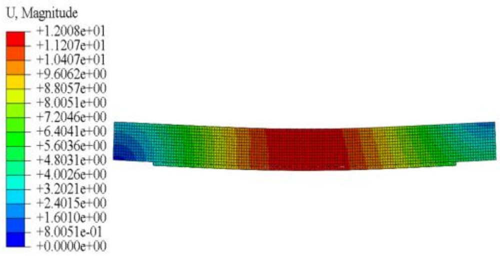

(c) – Deflection at yield of beam B3

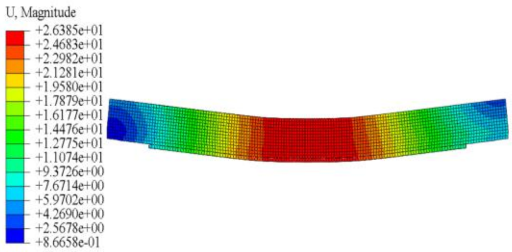

(d) – Deflection at limit state of beam B3

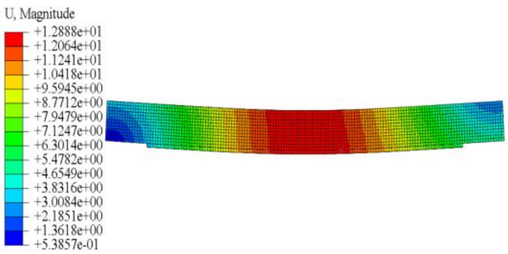

(e) – Deflection at yield of beam B4

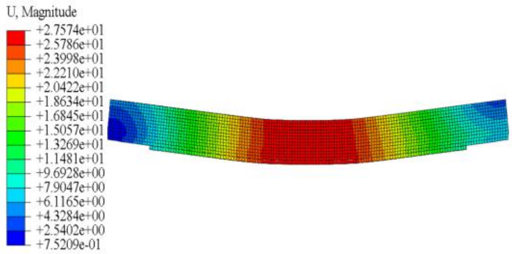

(f) – Deflection at limit state of beam B4

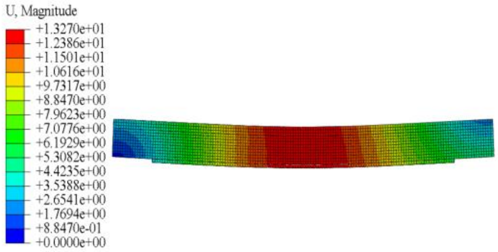

(g) – Deflection at yield of beam B5

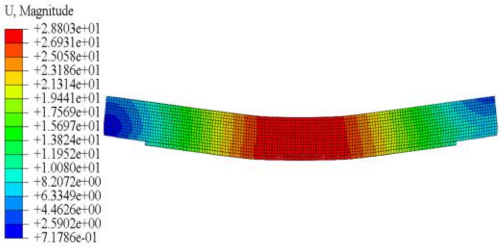

(h) – Deflection at limit state of beam B5

Fig.12 – Deflection clouds of beams CB, B3, B4 and B5

The unreinforced beam CB starts to yield its reinforcement when the load reaches 65 kN, at which point the deflection is 11.6 mm. Beam B3, which was strengthened using a combination of 5 longitudinal strands and 20mm thickness of PUC, entered the yield stage when the load reached 89.5 kN, at which point the deflection was 12 mm. The yield load was improved by 37.7% compared to the beam CB yield load. Beam B4, which was strengthened using a combination of 8 longitudinal strands and 20 mm thickness of PUC, had a load of 97 kN at the yield stage, at which point the deflection of the beam was 12.8 mm. The yield load is increased by 9% compared to beam B3. It shows that the yield load increases with the increase in reinforcement ratio for the same thickness of reinforcement. Beam B5, which was strengthened using a combination of 5 longitudinal strands and 30 mm thickness of PUC, had a load of 108 kN at the yield stage, at which point the deflection of the beam was 13.2 mm. The yield load is raised by 11.3% compared to beam B4. It shows that for the same thickness of reinforcement, the yield load increases with the increase in the thickness of reinforcement.

The ultimate load and ultimate deflection of beam CB are 78 kN and 26.1 mm respectively; The ultimate load and ultimate deflection of beam B3 are 117 kN and 26.4 mm respectively; The ultimate load and ultimate deflection of beam B4 are 130 kN and 27.6 mm respectively; The ultimate load and ultimate deflection of the B5 simulated beam were 144 kN and 28.8 mm respectively; Compared to beam CB, the ultimate loads of beams B3, B4, and B5 were enhanced by 50%, 67%, and 85%, respectively. Beam B4 with 8 longitudinal strands has an 11 % higher ultimate load compared to beam B3 with 5 longitudinal strands. It shows that the ultimate load increases gradually as the reinforcement ratio of the strand increases. Beam B5 with 30 mm thick PUC has a 10 % higher ultimate load compared to Beam B5 with 20 mm thick PUC. It can be seen that as the thickness of PUC increases, the ultimate load increases gradually.

Stress Analysis

(1) PUC stress

Through the post-processing module of ABAQUS finite element analysis software, the PUC stress clouds were extracted for each simulated beam reinforcement in the yield state and the limit state, as shown in Figure 13. The simulated beams for all three conditions went through yield and ultimate stages under load. Beam B3 strengthened with 5 longitudinal strands and 20 mm thick PUC had a stress of 11.9 MPa in the PUC at a load of 89.5 kN. At this point beam B3 enters the yield stage. The PUC stress is 31.4 MPa when the load reaches 117 kN. At this point the specimen reaches its limit state. Beam B4 strengthened with 8 longitudinal strands and 20 mm thick PUC had a stress of 12.3 MPa in the PUC at a load of 97 kN. At this point beam B3 enters the yield stage. The PUC stress is 32 MPa when the load reaches 130 kN. At this point the specimen reaches its limit state. Beam B5 strengthened with 5 longitudinal strands and 30 mm thickness of PUC had a stress of 13.4 MPa in the PUC at a load of 108 kN. At this point beam B3 enters the yield stage. At this point beam B3 enters the yield stage. The PUC stress is 32.4 MPa when the load reaches 144 kN. At this point the specimen reaches its limit state.

It is shown that the PUCs have all reached their ultimate stresses and fully utilized their strength. Moreover, as the reinforcement ratio of the SWM and the thickness of the PUC increase, the yield and ultimate loads gradually increase. The ultimate stresses of PUC in the simulated beams for all three conditions were much higher than the ultimate stresses of concrete. The PUC material proved to have good strength to meet the structural reinforcement needs.

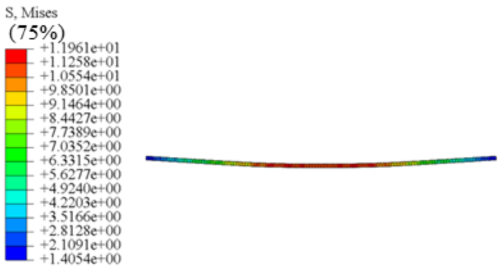

(a) – Stress in PUC at yield of beam B3

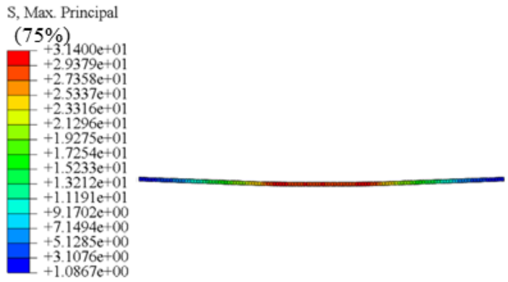

(b) – Limit state PUC stresses of the behavior of beam B3

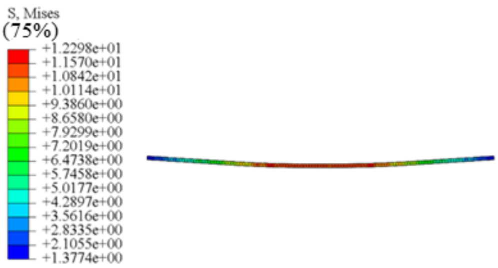

(c) – Stress in PUC at yield of beam B4

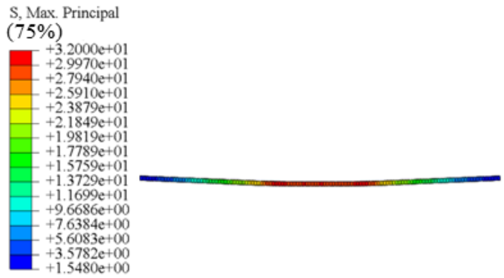

(d) – Limit state PUC stresses of the behavior of beam B4

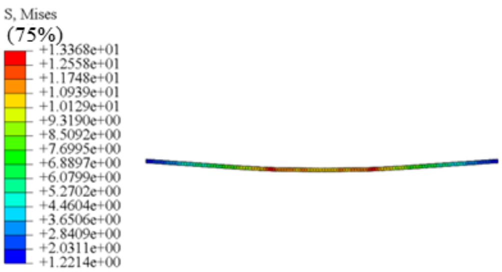

(e) – Stress in PUC at yield of beam B5

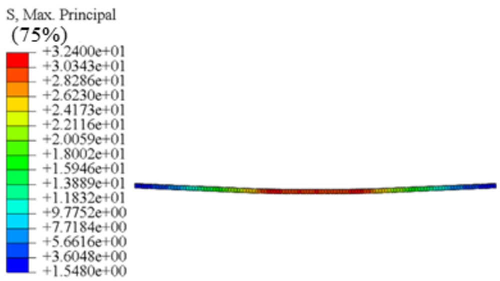

(f) – Limit state PUC stresses of the behavior of beam B5

Fig.13 – Stress clouds for PUC

(2) SWM stress

The strand stress clouds for beam B3, beam B4 and beam B5 are shown in Figure 14. Beam B3 begins to yield when the load reaches 89.5 kN, at which time the stress in the strand is 1140 MPa. Beam B4 strengthened with a composite of 8 longitudinal strands and 20 mm thickness PUC yielded its reinforcement at a load of 97 kN. The stress in the strand at this point is 1152 MPa. Beam B5 strengthened with a combination of 5 longitudinal strands and 30 mm thickness of PUC had a load of 108 kN at the yield stage. The stress in the strand at this point is 1160 MPa. This indicates that the strands in the reinforcement retained good strength when the specimen reached the yield state. In addition, the ultimate stresses of the strands in the reinforcement layers of beams B3, B4 and B5 all reached 1520 MPa, indicating that the form of damage of the beams was all bending damage in which the strands were pulled out.

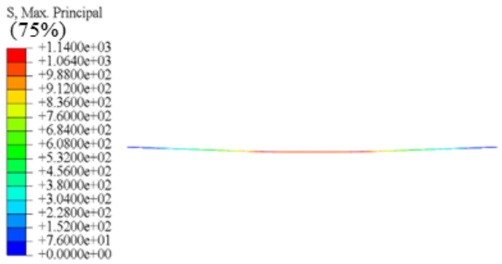

(a) – Strand stress at yield of beam B3

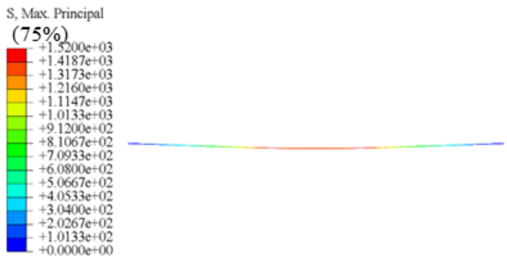

(b) – Strand stress of beam B3 at limit state

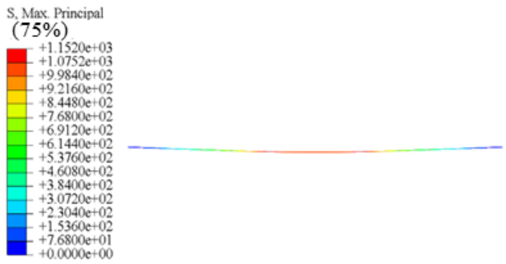

(c) – Strand stress at yield of beam B4

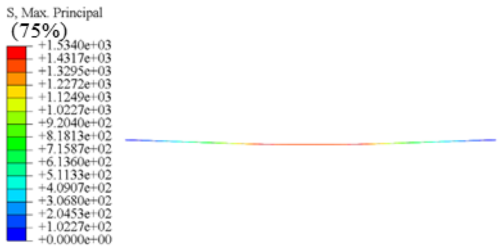

(d) – Strand stress of beam B4 at limit state

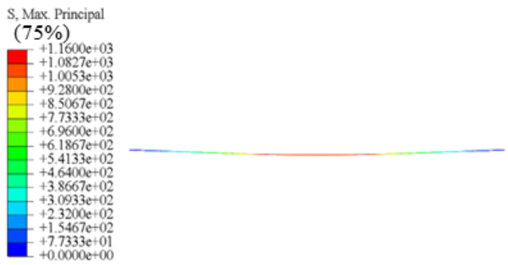

(e) – Strand stress at yield of beam B5

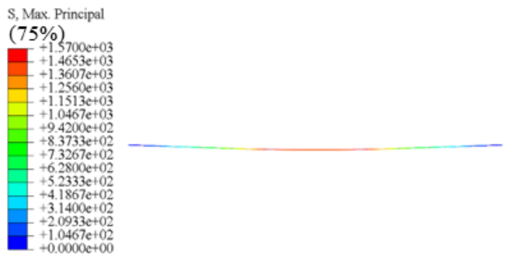

(f) – Strand stress of beam B5 at limit state

Fig.14 – Stress clouds of steel-stranded wires

(3) Reinforcement stress

The reinforcement stress clouds for beam CB, beam B3, beam B4 and beam B5 are shown in Figure 15. From Figure 15, it can be seen that the stresses in the rebars of the simulated specimens all exceeded 400 MPa, which reached the yield condition of the rebars. The stress is centered mainly at the underside of the reinforcement, indicating that the specimen has suffered bending damage. The ultimate stress of beam CB reinforcement is 440 MPa, beam B3 reinforcement is 500 MPa, beam B4 reinforcement is 521 MPa and beam B5 reinforcement is 555 MPa. Compared to beam CB, the tensile contribution of the reinforcement in beams B3, B4 and B5 was improved by 13.6%, 18% and 26%, respectively. It is shown that the composite reinforcement layer can appropriately increase the tensile contribution of the reinforcement. In addition, beam B4 with 8 longitudinal strands has 21 MPa more ultimate stress than the reinforcement of beam B3 with 5 longitudinal strands. It is shown that increasing the reinforcement ratio of the SWM can also increase the tensile contribution of the steel bars. Beam B5 with 30 mm thickness PUC had 55 MPa more ultimate stress in the reinforcement of beam B3 than that of beam B3 with 20 mm thick PUC. It is shown that an appropriate increase in the thickness of PUC can also improve the tensile contribution of the reinforcement.

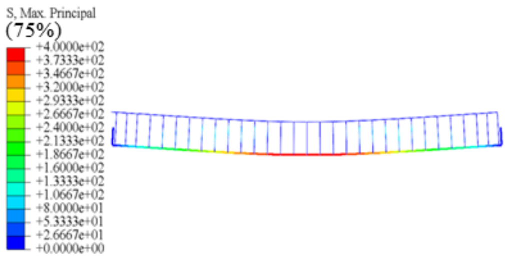

(a) – Reinforcement stress at yielding of beam CB

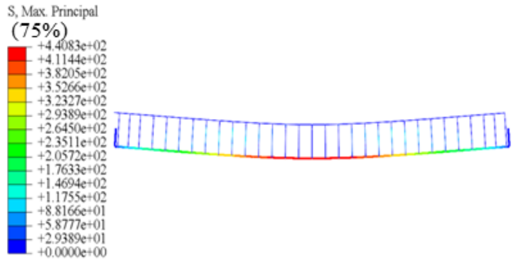

(b) – Steel reinforcement stresses of beam CB at limit state

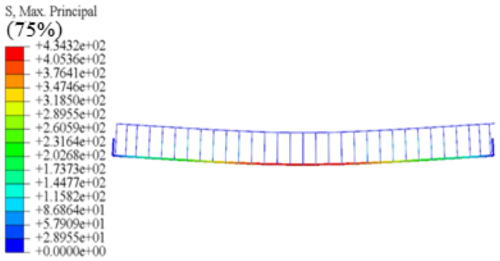

(c) – Reinforcement stress at yielding of beam B3

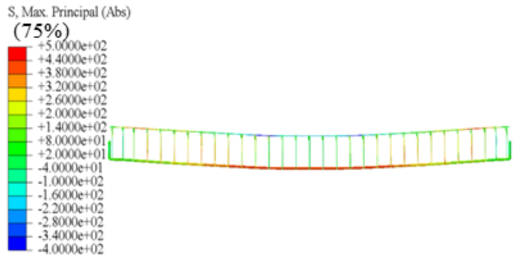

(d) – Steel reinforcement stresses of beam B3 at limit state

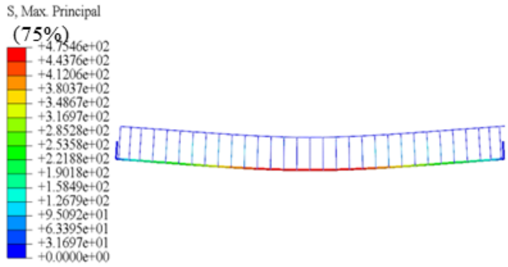

(e) – Reinforcement stress at yielding of beam B4

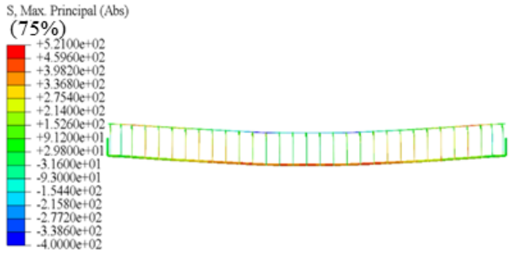

(f) – Steel reinforcement stresses of beam B4 at limit state

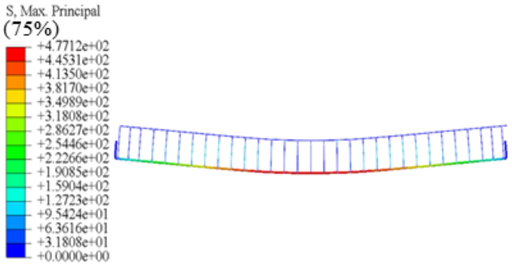

(g) – Reinforcement stress at yielding of beam B5

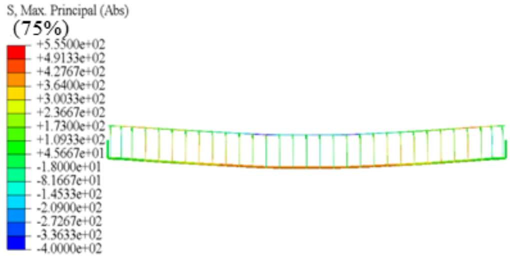

(h) – Steel reinforcement stresses of beam B5 at limit state

Fig.15 – Stress cloud of ordinary steel bar

Comparison of Load-Deflection Curves of Finite Element Model

After the finite element model analysis was completed, the finite element simulation results were compared with the test values as shown in Figure 16. From Figure 16, it is shown that the load-mid-span deflection curves of the finite element model have the same trend as the load-mid-span deflection curves of the test values, which are well-fitted.

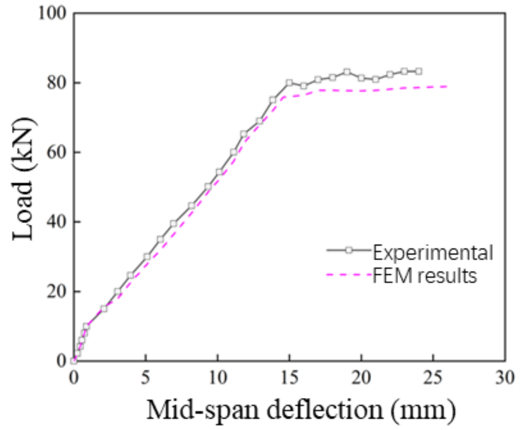

(a) – Beam CB

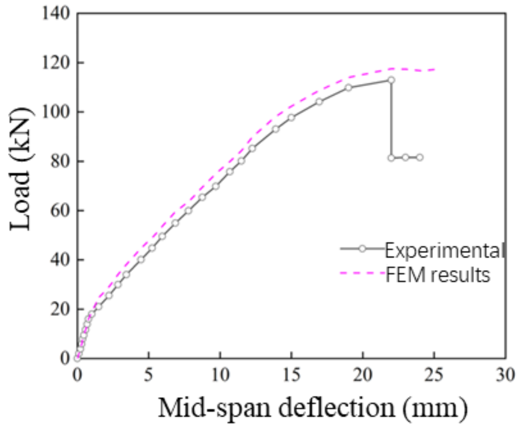

(b) – Beam B3

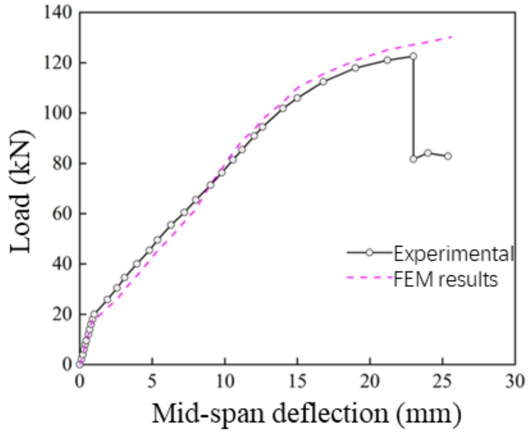

(c) – Beam B4

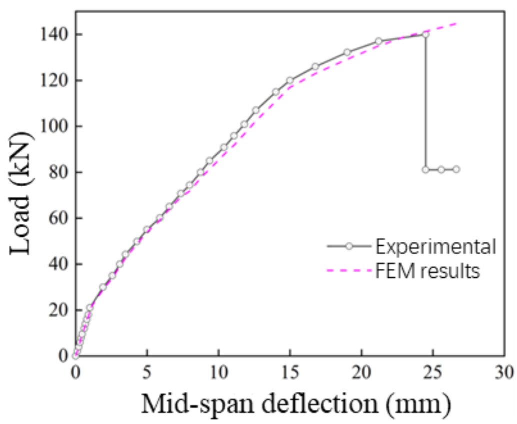

(d) – Beam B5

Fig. 16 – Load-deflection comparison curve of test value and finite element result

Analysis of Influencing Factors of Flexural Strengthened T-beams

Effect of Reinforcement Ratio of SWM on Reinforcement Performance

The SWM reinforcement ratio is defined as the ratio of the cross-sectional area of the longitudinal strands to the cross-sectional area of the upper unreinforced beams, which responds to the magnitude of the dosage of the SWM reinforcement ratio. The parameter settings for the simulated beams are shown in Table 3. All the parameters are the same except for the reinforcement ratio of the SWM. Eight longitudinal strands were used for each simulated beam, and the reinforcement ratio of the SWM was controlled by varying the diameter of the strands. The diameters of the longitudinal strands were 2.4 mm, 2.8 mm, 3.2 mm, 3.6 mm and 4 mm. The corresponding SWM reinforcement rates were 0.064%, 0.087%, 0.114%, 0.144% and 0.178%.

Tab.3 - Parameter setting

Beam	SWM reinforcement ratio	Longitudinal strand diameter/mm	Number of longitudinal strands/pc	Reinforcement layer thickness/mm	Tensile strength of SWM/MPa
WM-0.064	0.064%	2.4	8	20	1520
WM -0.087	0.087%	2.8	8	20	1520
WM -0.114	0.114%	3.2	8	20	1520
WM -0.144	0.144%	3.6	8	20	1520
WM -0178	0.178%	4	8	20	1520

The simulated beams with different SWM reinforcement rates were operated using finite element analysis software. The deflection values and load data were extracted respectively and the load-mid-span deflection curves were plotted. The load-deflection curves of the simulated beams with different SWM reinforcement ratios are shown in Figure 17. The trend of the load-deflection curves of the simulated beams with 5 different rates of SWM reinforcement was more or less the same, and all of them went through 3 phases, which were elastic, plastic, and destructive phases. The curve has a linear relationship between load and deflection in the first stage. As it becomes more loaded, the curve goes beyond the elastic phase and the curve slope decreases, at which point it enters the plastic phase. After exceeding the yield strength of the SWM, it enters the destruction phase. From Figure 17, it can be seen that the curve has a certain regularity. When the thickness of the reinforcement layer is constant, the rigid and bearing capacity of the simulated beam also increases with the increase of the reinforcement ratio of the SWM network.

The yield load values of the simulated beams with different SWM reinforcement rates are shown in Figure 18. The yield load of the simulated beam with a SWM reinforcement ratio of 0.064% is 92 kN; The yield load value of beam WM-0.087 is 104.6 kN, which is 13.7% higher than beam WM-0.064; The yield load value of beam WM-0.114 is 114.3 kN, which is 9.3% higher than the beam WM-0.087 yield load; The yield load value of beam WM-0.144 is 125 kN, which is 9.4% higher than the yield load of beam WM-0.114; The yield load value of beam WM-0.178 is 135 kN, which is 8% higher than the yield strength of beam WM-0.144. It is shown that the yield load increases gradually as the reinforcement ratio of the SWM increases. At a certain level of reinforcement, the increase in yield load decreases as the reinforcement rate increases.

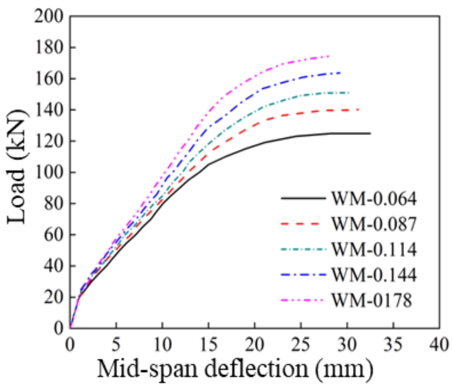

Fig.17 – Load-deflection curves of simulated beams of different SWM reinforcement ratios

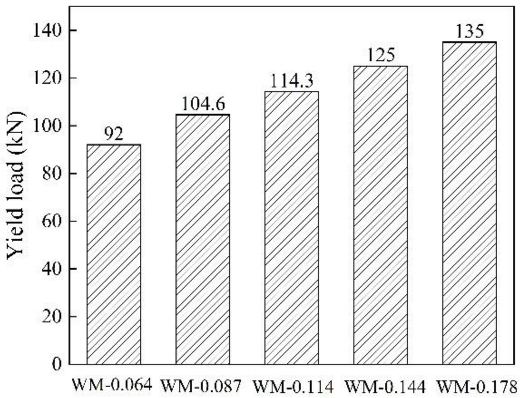

Fig.18 – Yield load values of simulated beams of different SWM reinforcement ratios

The ultimate load values of the simulated beams with different SWM reinforcement rates are shown in Figure 19. The ultimate loads of the SWM with 0.064%, 0.087%, 0.114%, 0.144% and 0.178% reinforcement were 122.6 kN, 139.5 kN, 152.5 kN, 166.7 kN and 180 kN. Compared to beam WM-0.064, with a 0.023% increase in the reinforcement ratio of the SWM, the ultimate load was increased by 13.8%; With a 0.05% increase in the reinforcement ratio of the SWM, the ultimate load was increased by 24.4%; With a 0.08% increase in the reinforcement ratio of the SWM, the ultimate load was increased by 36%; With a 0.114% increase in the reinforcement ratio of the SWM, the ultimate load was increased by 47%. It is shown that the ultimate load and the reinforcement ratio of the SWM are positively correlated.

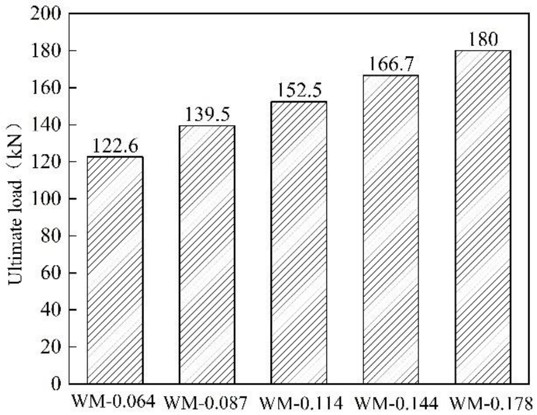

Fig.19 – Ultimate load values of simulated beams of different SWM reinforcement ratios

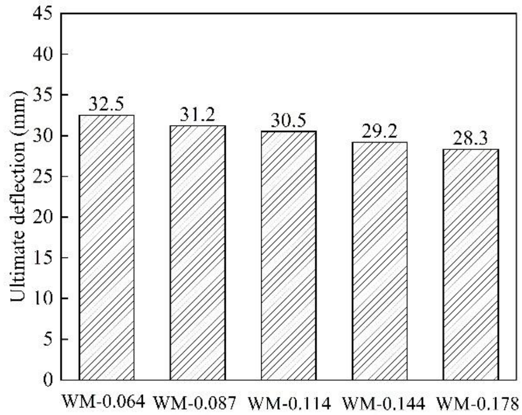

Fig.20 – Mid-span deflection values of the simulated beams while the strand is being pulled apart

After reinforcement with SWM-PUC composites. As the reinforcement ratio of the SWM increases, the deflection of the simulated beams decreases gradually under the same load. The mid-span deflection values of the simulated beams when the strand is pulled out are shown in Figure 20. The SWM reinforcement of 0.064%, 0.087%, 0.114%, 0.144% and 0.178% had deflections of 32.5 mm, 31.2 mm, 30.5 mm, 29.2 mm and 28.3 mm at the time of pull-off of the strand, respectively. Increasing the reinforcement ratio of the SWM decreases the flexural toughness of the beam. This is because increasing the reinforcement ratio will lead to an increase in the height of the compression zone of the cross-section and a decrease in the bending curvature, resulting in a decrease in the deformation capacity.

Effect of PUC Thickness on Reinforcement Performance

The PUC material was used as a composite reinforcement layer to increase the flexural load capacity of the specimen and firmly bonded to the concrete to avoid stripping damage. To verify the effect of PUC thickness on the flexural performance of reinforced beams in the positive section, simulated beams with different PUC thicknesses were established. The parameters are set as shown in Table 4. Parameters are the same except for PUC thickness. The PUC thicknesses were 20 mm, 25 mm, 30 mm, 35 mm and 40 mm.

Tab.4 - Parameter setting

Beam	PUC thickness/mm	Longitudinal strand diameter/mm	Number of longitudinal strands/pc	SWM reinforcement ratio	Tensile strength of SWM/MPa
PUC-20	20	2.4	5	0.064%	1520
PUC-25	25	2.4	5	0.064%	1520
PUC-30	30	2.4	5	0.064%	1520
PUC-35	35	2.4	5	0.064%	1520
PUC-40	40	2.4	5	0.064%	1520

The load-deflection curves of the simulated beams with different PUC thicknesses are shown in Figure 21. It is shown that the trend of the load-deflection curves of the simulated beams with different PUC thicknesses under all levels of loading is more or less the same, and all of them consist of elastic phase, plastic phase, and ultimate phase. The deflection in the span decreases as the thickness of PUC increases under the same load. In addition, the greater the thickness of PUC the greater the flexural capacity of the simulated beams. From Figure 21, it is shown that at a certain reinforcement rate of the SWM, the stiffness and load-carrying capacity of the simulated beams increased as the thickness of PUC increased.

The yield load values of the simulated beams with different PUC thicknesses are shown in Figure 22. The simulated beam reinforced with 20 mm thickness PUC enters the yielding stage when the load reaches 90.9 kN, at which point the deflection is 12.2 mm; The simulated beam with 25 mm thickness PUC enters the yielding stage when the load reaches 100.9 kN, at which point the deflection is 15.1 mm; The simulated beam with 30 mm thickness PUC enters the yielding stage when the load reaches 109.5 kN, at which point the deflection is 13 mm; The simulated beam with 35 mm thickness PUC enters the yielding stage when the load reaches 119.3 kN, at which point the deflection is 13.5 mm; The simulated beam with 40 mm thickness PUC enters the yielding stage when the load reaches 132 kN, at which point the deflection is 13.6 mm. The yield load is increased by 11% by adding 5 mm to the 20 mm thickness of PUC. The yield load is increased by 8.5% by adding 5 mm to the 25 mm thickness of PUC. The yield load is increased by 8.9% by adding 5 mm to the 30 mm thickness of PUC. The yield load is increased by 10.6 percent by adding 5 mm to the 35 mm thickness of PUC. It is shown that the yield load gradually increases as the thickness of PUC increases.

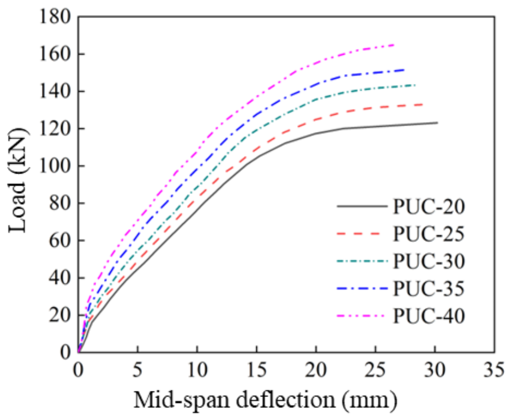

Fig.21 – Load-deflection curves of simulated beams of different PUC thicknesses

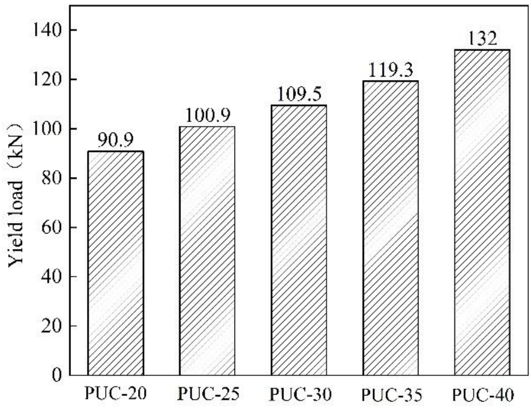

Fig.22 – Yield load values of simulated beams of different PUC thicknesses

The ultimate load values of the simulated beams with different PUC thicknesses are shown in Figure 23. The ultimate load of the PUC-20 simulated beam is 121.2 kN; The ultimate load of the PUC-25 simulated beam is 134.5 kN, which is 10.9% higher compared to the ultimate of the PUC-20 simulated beam; The ultimate load of the PUC-30 simulated beam is 146 kN, which is 8.5% higher compared to the ultimate load of the PUC-25 simulated beam; The ultimate load of the PUC-35 simulated beam is 159 kN, which is 8.9% higher compared to the ultimate load of the PUC-30 simulated beam; The ultimate load of the PUC-40 simulated beam is 176 kN, which is 10.7% higher compared to the ultimate load of the PUC-35 simulated beam. It can be seen that as the thickness of PUC increases, the ultimate load increases gradually. It is shown that PUC can be used not only as a bond anchoring material but also to reinforce the flexural properties of beams.

The mid-span deflection values of the simulated beams at PUC fracture are shown in Figure 24. The ultimate deflection of the simulated beam with PUC thickness of 20 mm is 30.2 mm; The ultimate deflection of the simulated beam with PUC thickness of 25 mm is 29.3 mm; The ultimate deflection of the simulated beam with PUC thickness of 30 mm is 28.6 mm; The ultimate deflection of the simulated beam with PUC thickness of 35 mm is 27.7 mm; The ultimate deflection of the simulated beam with PUC thickness of 40 mm is 26.5 mm. It is shown that as the thickness of PUC increases, the deflection of the simulated beams at failure gets smaller. The reason for this is that by increasing the thickness of PUC, the height of the compression zone in the cross-section of the reinforced beams under ultimate load increases. As the bending curvature becomes smaller, the deformation ability becomes worse, which leads to the reduction of toughness.

DOI 10.14311/CEJ.2025.01.0006

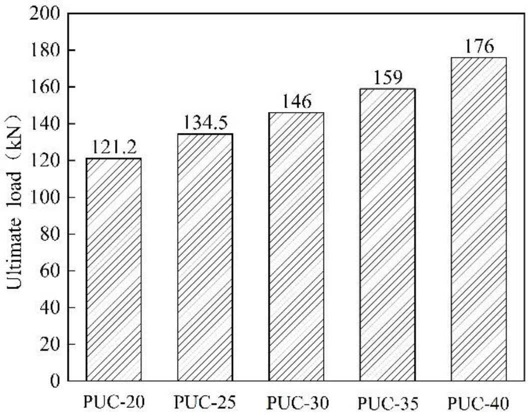

Fig.23 – Ultimate load values of simulated beams of different PUC thicknesses

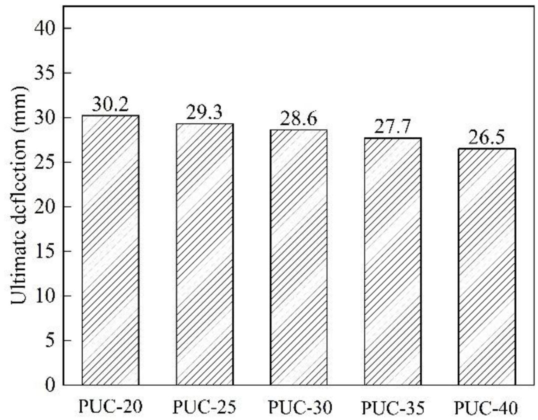

Fig.24 – Mid-span deflection values of the simulated beams at PUC fracture

From the results of the above analysis, it is concluded that the composite layer with PUC thickness of 40 mm and SWM reinforcement rate of 0.144% is the most effective reinforcement. The load-carrying capacity can be increased by up to 120 % compared to that of reinforced beams.

CONCLUSION

In this paper, the flexural performance of seven SWM-PUC composite strengthened beams was investigated experimentally. Based on the experimental study, the mechanical properties of strand mesh-polyurethane cement composite reinforced concrete beams were analyzed using finite element analysis software ABAQUS. The optimal strand mesh-polyurethane cement composite reinforcement layer configuration was explored. The following conclusions were drawn:

(1) A finite element model of a reinforced concrete T-beam with flexural reinforcement was developed using a simplified intrinsic relationship model of the material. The finite element results are in high agreement with the test results, indicating that the established SWM-PUC composite reinforcement beam model is reasonable.

(2) Computational analysis was carried out on reinforced concrete T-beam models with SWM reinforcement rates of 0.064%, 0.087%, 0.114%, 0.144%, and 0.178%. The results show a gradual increase in yield load as the reinforcement ratio of the SWM increases. However, at a certain level of reinforcement, the increase in yield load decreases as the reinforcement rate increases. With a 0.114% increase in the reinforcement rate of the SWM, the ultimate load was increased by 47% compared to the simulated beam with a 0.064% reinforcement rate of the SWM. It is shown that the ultimate load and the reinforcement ratio of the SWM are positively correlated.

(3) Computational analyses were carried out on reinforced concrete T-beam models with PUC thicknesses of 20 mm, 25 mm, 30 mm, 35 mm and 40 mm. It was concluded that for a certain reinforcement ratio of the SWM, the stiffness and load-carrying capacity of the beams increased as the thickness of PUC increased. Adding 10 mm to the 30 mm thickness of PUC increases the ultimate load by 20.5%. The optimum configuration of the SWM-PUC composite reinforcement layer was given by finite element analysis.

ACKNOWLEDGMENTS

The authors are grateful for the financial support of the Basic Research Projects of Liaoning Provincial Department of Education in 2024 (Project No. LJ212410153003), the Doctoral Start-up

Fund Projects of Liaoning Province (Project No. 2021-BS-168) and Shenyang Municipal Science and Technology Program Fund Project (23-407-3-19).

REFERENCES

[1] WANG, J., HE, X., et al. A real-time bridge crack detection method based on an improved inception-resnet-v2 structure. IEEE Access, 2021, 9, 93209–93223. DOI: 10.1109/ACCESS.2021.3093210.
[2] JIANG, H., FANG, Z., MA, Z. J., et al. Shear-friction behavior of groove interface in concrete bridge rehabilitation. *Journal of Bridge Engineering*, 2016, 21(11), 04016081. DOI: https://doi.org/10.1061/(ASCE)BE.1943-5592.0000953.
[3] ZHANG, S. S., YU, T., CHEN, G. M. Reinforced concrete beams strengthened in flexure with near surface mounted (NSM) CFRP strips: Current status and research needs. *Composites Part B: Engineering*, 2017, 131, 30-42. DOI: https://doi.org/10.1016/j.compositesb.2017.07.072.
[4] DE LORENZIS, L., TENG, J. G. Near-surface mounted FRP reinforcement: An emerging technique for strengthening structures. *Composites Part B: Engineering*, 2007, 38(2), 119-143. DOI: https://doi.org/10.1016/j.compositesb.2006.08.003.
[5] FANG, R., YANG, X. Cause and countermeasure of structure disease of bridge. In: *ICTIS 2013: Improving Multimodal Transportation Systems-Information, Safety, and Integration*. 2013, p. 470-475. DOI: https://doi.org/10.1061/9780784413036.064.
[6] LIU, Z. Q., GUO, Z. X., YE, Y. Flexural behaviour of RC beams strengthened with prestressed steel wire ropes polymer mortar composite. *Journal of Asian Architecture and Building Engineering*, 2022, 21(1), 48-65. DOI: https://doi.org/10.1080/13467581.2021.1928508.
[7] XING, G., WU, T., LIU, B. Experimental investigation of reinforced concrete T-beams strengthened with steel wire mesh embedded in polymer mortar overlay. *Advances in Structural Engineering*, 2010, 13(1), 69-79. DOI: http://dx.doi.org/10.1260/1369-4332.13.1.69.
[8] YUAN, F., CHEN, M., PAN, J. Flexural strengthening of reinforced concrete beams with high-strength steel wire and engineered cementitious composites. *Construction and Building Materials*, 2020, 254, 119284. DOI: https://doi.org/10.1016/j.conbuildmat.2020.119284.
[9] FISCHER, G., LI, V. C. Effect of fiber reinforcement on the response of structural members. *Engineering Fracture Mechanics*, 2007, 74(1-2), 258-272. DOI: https://doi.org/10.1016/j.engfracmech.2006.01.027.
[10] RANADE, R., LI, V. C., HEARD, W. F. Tensile rate effects in high strength-high ductility concrete. *Cement and Concrete Research*, 2015, 68, 94-104. cc DOI: https://doi.org/10.1016/j.cemconres.2014.11.005.
[11] WANG, X., YANG, G., QIAN, W. Tensile behavior of high-strength stainless steel wire rope (HSSSWR)-reinforced ECC. *International Journal of Concrete Structures and Materials*, 2021, 15(1), 1-15. DOI: https://doi.org/10.1186/s40069-021-00480-x.
[12] ZHENG, Y. Z., WANG, W. W., BRIGHAM, J. C. Flexural behaviour of reinforced concrete beams strengthened with a composite reinforcement layer: BFRP grid and ECC. *Construction and Building Materials*, 2016, 115, 424-437. DOI: https://doi.org/10.1016/j.conbuildmat.2016.04.038.
[13] ZHANG, K., QI, T., ZHU, Z., et al. Strengthening of a reinforced concrete bridge with a composite of prestressed steel wire ropes embedded in PUC. *Journal of Performance of Constructed Facilities*, 2021, 35(5), 04021063. DOI: https://doi.org/10.1061/(ASCE)CF.1943-5509.0001640.
[14] ZHANG, K., XUAN, J., SHEN, X., et al. Investigating the flexural properties of reinforced concrete T-beams strengthened with high-strength SWM-PUC. *Journal of Bridge Engineering*, 2024, 29(5), 04024023. DOI: https://doi.org/10.1061/JBENF2.BEENG-6524.
[15] LI, B., LIU, H., JIAN, J., et al. Static load test analysis of T-beam bridge shear strengthening by prestressed steel wire rope embedded in PUC (PSWR-PUC). *Sustainability*, 2023, 15(13), 10514. DOI: https://doi.org/10.3390/su151310514.
[16] ZHANG, K. Flexural simulation analysis of RC T-girders strengthed with PUC-prestressed steel wire ropes. *Stavební obzor - Civil Engineering Journal*, 2021, 30(4). DOI: https://doi.org/10.14311/CEJ.2021.04.0069.
[17] DHAKAL, R. P., MAEKAWA, K. Reinforcement stability and fracture of cover concrete in reinforced concrete members. *Journal of Structural Engineering*, 2002, 128(10), 1253–1262. DOI: https://doi.org/10.1061/(ASCE)0733-9445(2002)128:10(1253).

[18] SŁOWIK, M. The analysis of failure in concrete and reinforced concrete beams with different reinforcement ratio. *Archive of Applied Mechanics*, 2019, 89, 885–895. DOI: https://doi.org/10.1007/s00419-018-1476-5.

[19] NASER, M. Z., HAWILEH, R. A., ABDALLA, J. Modeling strategies of finite element simulation of reinforced concrete beams strengthened with FRP: A review. Jour*nal of Composites Science*, 2021, 5(1), 19. DOI: https://doi.org/10.3390/jcs5010019.

[20] FARON, A., ROMBACH, G. A. Simulation of crack growth in reinforced concrete beams using extended finite element method. *Engineering Failure Analysis*, 2020, 116, 104698. DOI: https://doi.org/10.1016/j.engfailanal.2020.104698.

[21] ALI, A. H., GOUDA, A., MOHAMED, H. M., et al. Nonlinear finite elements modeling and experiments of FRP-reinforced concrete piles under shear loads. In: *Structures*. Elsevier, 2020, 28, 106–119. DOI: https://doi.org/10.1016/j.istruc.2020.08.047.

CIVIL ENGINEERING JOURNAL

Article no. 7

THE CIVIL ENGINEERING JOURNAL 1-2025

ESG IMPLEMENTATION IN THE CONSTRUCTION INDUSTRY ACCORDING TO 2022-2024 SURVEYS

Vladimíra Nováková

Czech Technical University in Prague, Faculty of Civil Engineering, Department of Economics and Management in Construction, Thákurova 7, 166 29 Prague 6 -Dejvice, Czech Republic; vladimira.novakova@fsv.cvut.cz

Received: 16.01.2025

Received in revised form: 18.03.2025

Accepted: 23.03.2025

ABSTRACT

The transition to sustainability will gradually change the face of businesses in all sectors, not least construction. In terms of adopted EU legislation, it will have the greatest impact on their activities in less than 5 years. For companies, the adoption of sustainability principles means new business conditions, new market opportunities, the possibility of acquiring resources, but also new responsibilities. One of these is the obligation to report on ESG (information on the impact of their business on the environment, people and society). This article presents the results of ten sustainability surveys conducted between 2022 and 2024. All the data was collected using the questionnaire method. The aim of the article was to determine the willingness of companies operating in the Czech market to integrate sustainability aspects into their corporate strategies and to publish sustainability (ESG) reports based on the published results. The results show that there is currently a large gap in the level of ESG implementation not only between large and medium-sized construction companies, but also between Czech and foreign companies. The research confirms that ESG awareness or activity decreases with the size of the company. Many small and micro companies believe that ESG does not affect them. The sooner companies start reporting standardised sustainability data, the sooner and easier they will be able to access more favourable loans and financing from investors, and the sooner they will be able to contribute to the Sustainable Development Goals for Europe as a whole.

KEYWORDS

ESG, Non-financial reporting, Construction industry, Research

INTRODUCTION

The construction industry in general is one of the most important sectors in all developed economies around the world. Currently, construction companies have to cope with a number of challenges such as the shortage of skilled workers [1], the significant increase in the price of building materials [2] and energy [3] and the rise in interest rates [4]. Moreover, with the worsening impacts of climate change, they are forced to move towards a sustainable future. Like the global market, construction companies are facing new challenges in the area of non-financial reporting, which includes evaluation criteria in relation to environmental, social and corporate governance aspects, the so-called ESG. In addition to the traditional financial annual report, the European

Union has started to require selected companies to produce a sustainability report or ESG report according to European standards [5].

MATHERIALS AND METHODS

The research questions were selected based on the research area and topic [6]. The research area for the subsequent analysis focused on 'sustainability'. In this case, the research topic is "Implementation of environmental, social and governance (ESG) criteria in the construction industry based on survey data conducted between 2022 and 2024." The specific research objective and the main research question were then identified. The research objective was to analyse the results of surveys from publicly available sources provided by 10 Czech and foreign companies in the period 2022-2024 and, based on this, to answer the research question "What is the willingness of companies operating on the Czech market to include sustainability aspects in their corporate strategies and to publish sustainability (ESG) reports". The research methods included a qualitative content analysis of published results from surveys of Czech and foreign companies regarding the transition to sustainability and the obligation to report ESG data. According to [7], content analysis is a technique for extracting information and data from unstructured text. In this paper, its qualitative form was used due to the possibility of gaining deeper insights into the topic [6].

ESG - Three Key Factors for Assessing Corporate Social Responsibility

The ESG concept is the result of an effort to integrate environmental and social considerations together with responsible governance into the decision-making processes and investment strategies of companies. It serves as a measurement system for social responsibility and sustainability in three aspects: the environment (E for Environmental), the social environment (S for Social) and the way in which companies are governed and managed (G for Governance) [8]. The results of the measurement of these three aspects are then used to assess the company as a whole. ESG requires measurable targets, data collection and reporting. The outputs are quantitative data that are numerical and measurable. The advantages are their objectivity, ease of analysis and good comparability. Examples of quantitative data in ESG reporting could be the amount of greenhouse gas emissions (GHG emissions), the proportion of energy consumption from renewable sources, the number of workplace accidents, the amount of waste produced or the percentage of women in the company's management. An increasing part of the public is demanding information on sustainability, in addition to EU institutions, governmental and non-governmental organisations, such as investors, suppliers, customers and employees (stakeholders). Active involvement in socially beneficial activities can bring the company benefits in the form of greater support from these stakeholders and put it in a better position to deal with potential crisis situations [9]. The main motive behind the introduction of ESG is to increase transparency and to gain a more comprehensive view of companies' operations as well as to better compare them, which may ultimately encourage these companies to behave more responsibly [10]. A strong corporate focus on sustainability can not only attract and retain quality employees, but also increase existing productivity, satisfaction and motivation, and instil a sense of purpose and development [11]. Casey and Grenier [12] add that the market perceives companies that engage in responsible activities and reporting as less risky, which affects the financial performance of the company and the view of investors. ESG and non-financial reporting are therefore closely linked, with ESG as a sustainability measurement system providing key information that is then included in non-financial reporting.

Corporate Social Responsibility Versus ESG

The Sustainability Report (ESG) is based on the older concept of CSR. The main difference between CSR and ESG is that CSR is seen as an internal initiative to fulfil a corporate purpose. CSR initiatives are clearly stated and manifest in the organisation's culture and stated policies, whereas ESG reflects more the external impact of the company's activities. ESG is more about an external assessment of an organisation's impact on society and is generally easier to measure. In addition to CSR and ESG, the literature also refers to a similar concept called the 'triple bottom line', which characterises the three main areas of interest mentioned above and in which both concepts are involved [13]. The difference lies in the understanding of the economic sphere, which ESG calls governance. CSR focuses on investor relations, supplier-customer relations, customer relations, transparency and anti-corruption. ESG adds to this the independence of management, executive remuneration, shareholder rights, tax transparency or the regularity of internal and external audits [14]. CSR stands for Corporate Social Responsibility. It is defined as a voluntary commitment of companies to behave responsibly towards the environment and the society in which they operate. Compared to CSR, ESG focuses on a wider range of areas of concern and responsibility. The main added value of the ESG concept over CSR is the ability to assess and measure the extent of companies' efforts in this direction [15]. While CSR aims to make business responsible, ESG aims to measure this [16]. In recent years, CSR has become an important concern for many companies, regardless of their size or industry [17]. However, there are differences in the reporting and practice of CSR activities that can be specifically attributed to unique environmental conditions, locations, stakeholder expectations [18], industry norms and regulations, or firm interests [19]. Sustainability and ESG information tends to be similar across countries in that it focuses primarily or exclusively on the environment (E), particularly the carbon footprint, i.e. greenhouse gas emissions. Social issues (S) and risks associated with corporate governance (G) are mostly neglected [20]. Yet in the current climate where companies are fighting for every quality employee, the "S" is a particularly important indicator, as is the "G", because a company that does not manage risk or relationships with clients and suppliers will have little chance of success in the marketplace. According to [21], information related to Pillar S tends to be less reliable than for E and G, and in some regions, such as Europe, with strict privacy laws, it can be particularly difficult to measure and report this information. The implementation of CSR activities can be a source of competitive advantage [22]. According to [23], companies with strong social responsibility are more likely to be competitive and attract new customers. McKinsey regularly publishes reports and analyses on trends in the construction industry and their impact on sustainability and the ESG issues. According to McKinsey research (2019), more than 70% of consumers across industries such as construction, electronics and automotive are willing to pay up to 5% more for a green product if it meets the same performance standards as the same non-green alternative [11]. The World Business Council for Sustainable Development describes sustainability reporting as "public reports by companies that provide internal and external stakeholders with a picture of the company's position and activities in the economic, environmental and social dimensions" [24]. ESG reporting does not imply an obligation to meet specific standards, ESG reporting is simply reporting on how a company is doing in terms of sustainability. And as Zuo et al. mention, the purpose of sustainability reporting is to reveal the company's commitment and achievements towards all aspects of sustainability, from the perspective of internal and external stakeholders [25].

Corporate Sustainability Reporting Directive

In order to standardize the format of non-financial reporting and to elevate non-financial reporting to the level of financial reporting, the CSRD Corporate Sustainability Reporting Directive was adopted in 2021 [7]. The CSRD introduces stricter rules that require the inclusion of ESG criteria in reporting. It introduces an obligation for companies to report sustainability according to ESRS (European Sustainability Reporting Standards), in addition to a single electronic format. The aim is to ensure that the information reported is comparable, relevant and credible. The CSRD Directive sets out rules for sustainability disclosure for all companies that meet certain thresholds (see Figure 1). It also expands the reporting requirements for non-financial sustainability information compared to the requirements of the 2014 Non-Financial Reporting Directive (NFRD). The main reason is to increase transparency of companies and their value chains, to reduce greenwashing, to ensure sufficient data for transforming economies and decision making of financial institutions [26].

NFRD	CSRD			
2017	**2024**	**2025**	**2026**	**2028**
Companies traded on the stock exchange with more than **500 employees**	Large companies previosly covered by NFRD that meet at least two of the following requirements: - more than **500 employees** - more than **€50 million** net turnover - more than **€25 million** total assets	Large companies not previously covered that meet at least two of the following requirements: - more than **250 employees** - more than **€50 million** net turnover - more than **€25 million** total assets	Listed small and medium-sized enterprises, small and simple credit institutions and captive insurance companies.	Non-EU companies (companies with a net turnover of more than **€150 million** and at least one branch/subsidiary in the EU)

Fig. 1-Timetable for the start of ESG data reporting

Figure 1 illustrates the phased disclosure obligation for non-financial sustainability information under the EU-mandated CSRD. In the first phase, all companies that were already obliged to disclose information under the NFRD as of 2017 will have to report information for the 2024 financial year. In the second phase, the obligation to disclose ESG for the 2025 financial year will fall on all other large companies. Those that meet at least two of the following criteria at the balance sheet date: a) more than 250 employees, b) net turnover more than EUR 50 million, or c) assets more than EUR 25 million. In the third phase (for the 2026 financial year), listed small and medium-sized enterprises will have to report ESG (with a possible exemption until 2028). The last group to report non-financial information from 1 January 2028 will be non-European companies with significant activities in the EU. These are parent companies from outside the EU whose subsidiaries have a turnover exceeding EUR 150 million. The CSRD will affect more than 50,000 companies in the EU, compared to 12,000 companies reporting under the NFRD [27]. In the Czech Republic, the number of companies that have to disclose non-financial reporting will increase from 25 (e.g. CEZ, ŠKODA Auto, Česká spořitelna, etc.) to about 1,500 [28].

A number of national, EU and global surveys have been conducted to determine how prepared companies are for the obligation to implement and report on ESG (environmental, social and governance) criteria. The surveys focus on the readiness of companies to respond to increasing market and regulatory demands in the area of sustainability. These surveys help to identify trends, challenges and opportunities that are emerging in the implementation of green and sustainable practices, not only in the construction sector.

Sustainability - Survey Results

KPMG has been analysing sustainability reports since 1993 as part of its Survey of Sustainability Reporting [29]. It has data on 5,800 companies from 58 countries around the world. The Asia-Pacific region has the highest number of companies producing sustainability reports (89%), followed by Europe (82%), the Americas (74%) and the Middle East and Africa (56%).

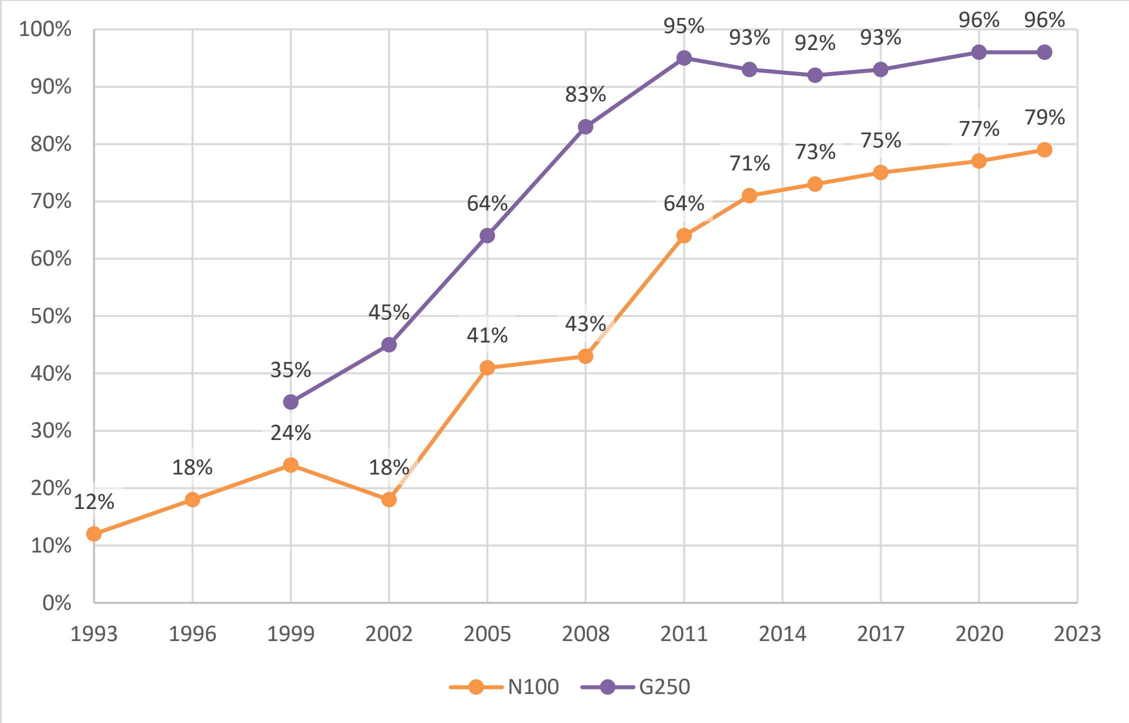

Fig.2 - Global Sustainability Reporting Rates

Figure 2 shows the percentage increase in sustainability reporting disclosure since 1993 for a group of the 100 most turnover-intensive companies from each country analysed (N100) and since 1999 for the 250 largest global companies (G250). As the chart confirms, an average of 18% of companies in the N100 group reported ESG data in 2002, while 20 years later, in 2022, the figure was 79%. The G250 shows a large percentage increase in ESG reporting, from 35% in 1999 to 95% in 2011. Since that year, the percentage has not changed much and is on average 94%. Thus, it can be seen that in the last 10 years, non-financial reporting is done by most of these major companies (94%). According to [20], in the Czech Republic the percentage is lower, namely 74%.

According to the KPMG "Global Construction Survey" [30] from 2023, an increasing proportion of companies fully perceive the benefits of ESG and consider sustainability an important element of their business strategies. Similarly, property owners are increasingly turning to renewable energy in an effort to reduce energy costs and greenhouse gas emissions. Research shows that construction companies are increasingly focusing on social (S) in ESG - employee relations, equal pay, diversity, inclusion, corruption prevention, etc., which brings new approaches to address long-standing challenges in projects [30]. It is (S) that is crucial for the construction industry in terms of working conditions on construction sites. Better occupational safety, health and trained employees can contribute significantly to increased labour productivity, reduced employee turnover, improved company reputation and most importantly reduced workplace deaths and injuries. According to [31], a decreasing trend of deaths and injuries can be observed in the Czech Republic in all sectors, including construction. In 2023, a historical low of 77 fatal occupational injuries was reported. Between 1993 and 2002, the number of fatal occupational injuries was 200-300 per year. Between 2003 and 2016, the number of deaths fell below 200. The categories of buildings, building structures and surfaces were the most frequent sources of fatal and serious occupational injuries [31]. In the environmental (E) domain, the following survey results are of interest [32]. Construction companies see the greatest potential for savings in insulation and reducing the energy consumption of buildings (42%) and in the use of renewable energy sources (30%). This is followed by heat recovery and heat management or recycling of materials and construction waste, which have been the focus of many construction companies in recent years.

The survey also shows that up to 17% of companies have experienced greenwashing by their suppliers or business partners in construction practice [32].

The following results came from a survey called "The ESG Imperative" [33]. The survey was conducted by BDO Belgium and Mercuri Urval in 13 countries: Austria, Belgium, Czech Republic, Denmark, Finland, France, Germany, Italy, the Netherlands, Norway, Spain, Sweden and Switzerland. The aim was to assess attitudes towards sustainability, barriers and main motivations for change. The research covered about 150 companies by questionnaire survey and online survey in November and December 2023. According to [33], a large majority of the companies surveyed (75%) already perceive ESG as a means of value creation, not as a mere fulfillment of requirements dictated by the state. Companies seem to be increasingly aware of the fact that sustainable behaviour can drive innovation and growth. Almost all companies (97%) expect sustainability to change their business model and operations, with 22% saying it will completely transform their company. According to 64% of respondents, the transition to sustainability will have the biggest impact on their operations in the next 5 years. Stakeholders (42% of respondents), new policy and legislation (30%), threats (reputational damage and financial losses) and opportunities (increased attractiveness, higher margins) (23%) and easier access to capital (1%) were cited as the main motives for moving to sustainability. Conversely, 26% cited cost and resource constraints as the main barriers to transforming to sustainability, 16% cited complex supply chains, 15% cited cultural and behavioural barriers, and 12% cited lack of awareness and understanding. According to the survey, 60% are reporting on ESG, 20% are preparing their first report and 18% are planning to do so in the next 1-2 years. 28% of unlisted large companies and 38% of SMEs have not yet translated their ESG strategy into operational objectives. The stakeholders that are most pushing companies to be more sustainable are customers (67%), public authorities/governments (50%) and existing or potential employees (51%). 78% of companies have already received specific questions on sustainability from their customers, 58% from employees and future talent and 55% from public authorities/governments. It can thus be concluded that sustainability is more than just a fashion trend. It is a necessary transformation that is gradually changing the behaviour of businesses in all sectors.

At the end of 2023, a survey called "ESG Rating" [34] was conducted in the Czech Republic. It was created in cooperation with the Association of Social Responsibility and CEMS - The Global Alliance in Management Education at the University of Economics in Prague and Forbes Czech Republic.The "ESG Rating" survey confirmed that there is a fairly significant difference in the experience of large and small and medium-sized companies when it comes to reporting non-financial indicators. Out of the surveyed sample of 135 Czech companies with a total turnover of CZK 1.2 trillion in 2022 (17.2% of domestic GDP), 61% of large companies disclose ESG reports, while only 22% of smaller companies do. The survey also confirmed that company size has a direct impact on the quality and depth of reporting. Smaller businesses cannot afford to employ or hire an ESG expert and lack a deeper understanding of sustainability information. Conversely, it is these businesses that score points against large social enterprises (S), often paying increased attention to their employees and local communities. Based on the results of the research, the top ten large and top five small and medium-sized companies were published [35]. The top-ranked company in the SME category was Konsit, a civil engineering company, with its decarbonisation strategy developed based on its carbon footprint data. It received points in area G for business etiquette (publicly available code of ethics, trained employees, anti-corruption programme, etc.) [34].

Other findings were reported in the "PwC CEO Survey 2024" [36]. PwC is a global network of professional services firms employing more than 360,000 people in 151 countries. PwC regularly conducts surveys that focus on environmental, social and governance (ESG) factors. These surveys cover all industries, including construction. As the construction industry is one of the most carbon-intensive sectors, there is increasing pressure for emissions reductions and energy efficiency improvements. Data was collected from 19 November to 10 December 2023. 4,290 respondents, including 188 companies, participated in the global survey. The "PwC CEO Survey

2024" produced the following findings. The main motives for making changes to reduce carbon footprint, besides self-beliefs (32%), are the increase in demand for products and services with lower carbon footprint from customers (17%), the obligation to handle non-financial reporting (13%), pressure to reduce carbon footprint in the supply chain from customers (10%), and investor demands to reduce carbon footprint (9%). Only 4% of CEOs surveyed said that carbon footprint reduction is required by the financing bank. Availability of subsidies was mentioned by 2% of respondents. 13% are not motivated to make changes to reduce their carbon footprint. There is an increase in the number of companies that have implemented specific measures to reduce their carbon footprint (50%) or have already developed a strategy to reduce their carbon footprint (34%). There is also a noticeable increase in companies that measure their carbon footprint.

Further sustainability results have been published by CEEC Research. This company has compiled data in the second quarterly analysis of the Czech construction industry in 2023. Data from CEEC Research [32] shows that ESG is playing an increasingly important role in investment decisions for new construction projects. Whereas previously it was mainly financial criteria and project performance that determined the decision, today more and more investors and developers are focusing on long-term sustainability and social responsibility. Almost 2/5 of the construction companies surveyed (38%) think that ESG criteria are very important. The data confirms that construction companies are implementing a range of measures to reduce their carbon footprint and limit negative environmental impacts. The most common measures include saving energy (71%), reducing the amount of mixed waste generated (57%), using recycled building materials (56%) and extending the life of machinery and equipment (56%). There is also a growing effort to shorten the supply chain and reduce traffic.

Another survey carried out in the Czech Republic is called the "Carbon Tracker 2023". 36 companies (23%) of the 155 largest Czech companies (by turnover in 2022) participated in the survey. The results of the "Carbon Tracker 2023" survey [37] show that almost every second company in the Czech Republic does not yet calculate its carbon footprint or refuses to disclose it for various reasons (51%). However, companies are beginning to address the issue of carbon footprint. Only 2 out of 155 companies surveyed do not intend to address this area in the next two years. The most frequent motives for calculating the carbon footprint are requirements coming from a business partner, a parent company or due to a legal obligation. A total of 38 companies (25%) have set decarbonisation targets, most of them at group level, focusing mainly on reducing Scope 1 and Scope 2 (emissions from own operations). Another interesting finding is that the companies do not yet have a defined position for an ESG specialist. Only 5 companies out of 155 (1.3%) have a sustainability manager or director.

According to the "Survey of Sustainability Reporting" [29], a study of the 100 largest Czech companies in terms of turnover (as of 2022), 48 domestic companies (almost 50%) list reducing their carbon footprint among their ESG goals. 20 companies (20%) want to achieve this goal by reducing their own emissions. The rest, i.e. the majority of companies, count on purchasing emission allowances or other offset instruments. These are mainly companies in sectors that are difficult to decarbonise (cement, lime, glass, etc.) or companies that postpone emission reductions until later [30].

Further findings are presented in EY's "EY EU Taxonomy Barometer 2023" [38]. In the EU Taxonomy Barometer, the company analysed and reported on the reporting practices of 320 companies in 17 EU countries across 12 sectors. The companies are listed on the main stock exchanges of the selected countries and represent approximately 92% of the EU's gross domestic product. 96% of non-financial companies (265 out of 277) disclosed their taxonomy data in their report, 89% (236 out of 277) disclosed at least one of the three key indicators (Turnover KPI, CapEx KPI, OpEx KPI). 25% of companies are able to report their turnover eligibility with taxonomy, more than a third are not able to report activities that would support sustainable goals. This is often due to lack of data or inability to deliver data.

In the autumn of 2023, the Chamber of Commerce of the Czech Republic conducted a survey entitled "Chamber Barometer". 444 micro, small, medium and large companies from various sectors of the economy and from all regions of the Czech Republic participated in the survey. 62

companies represented the construction sector (27 micro, 17 small, 18 medium and 3 large construction companies). The Chamber Barometer [39] shows that sustainability is currently being addressed mainly by large companies. 78% of them are actively engaged in ESG and a further 14% are planning to do so. 37% of small companies and 28% of micro companies are already engaged in sustainability. 23% of micro companies (less than 10 employees) have no idea what the term ESG means. There is a big difference between companies that are part of large companies' supply chains (51% are actively engaged in ESG) and those that are not (29%). The results also show that the construction industry lags behind the manufacturing sector in terms of ESG. Almost all companies cite cost savings, the need to comply with new legislation (medium 45%, large 61%) and the company's public image (medium 24%, large 41%) as the main reasons for their interest in sustainability. For very small companies, where ESG is not required, the most common motive is the company's own interests and values (21%). Increased competitiveness in the market was cited by almost a quarter of medium and large companies. Large companies also cited corporate policy of parent companies and pressure from customers and business partners as motives. For a third of small companies, the motive is to reduce labor costs or solve the lack of qualified workers. Looking at the sector, it appears that the long-term lack of qualified labor (29%) is the main motive in the construction industry. On the contrary, the factors that most demotivate companies to apply ESG in their strategies include unclear and complex legislation, lack of information, time, finance and human resources for the implementation of new rules. For small and medium-sized companies, it is also a fear of losing competitiveness due to higher costs or product prices. 41% of large companies are also worried about this, especially those from countries outside the EU, which are mostly not covered by similar regulations. For 31% of large companies, lengthy approval processes that make it difficult to implement projects are also a demotivating factor. The survey also shows that half of the companies surveyed have a concrete idea of how much money they will invest in sustainability activities over the next three years. A quarter of companies do not know and the last quarter do not plan to invest at all. Large companies are most likely to invest in ESG projects, with almost three quarters of them planning to invest millions of CZK, some even tens to hundreds of millions. When small and micro companies (especially self-employed) consider investing (32%), it is for amounts up to CZK 100,000 (3 954 euros) or in the lower hundreds of thousands. In particular, construction companies intend to focus on more transparent payment of employees, renewable energy sources and the circular economy, which should ensure greater self-sufficiency in the sector and better access to raw materials. The survey shows that large companies are aware of the new rules and are preparing for them. 12% of large companies say they are ready for the new legislation and a further 30% are in the process of implementing it. On the contrary, a quarter of large companies are still in the early stages of adapting to non-financial reporting and are unsure of their next steps. There are 6% of large companies that are not preparing at all for the change in the rules and have no plans to do so. Even if SMEs are not directly affected by the new rules, if they are part of the supply chain of large companies, they can expect new obligations to appear in their commercial contracts. The survey shows that small and medium-sized enterprises are not aware of this. 83% of micro companies (67% of small companies and 35% of medium-sized companies) are convinced that ESG does not concern them, but 74% of them (59% of small companies, 28% of medium-sized companies) are part of the supply chain of companies that will have to report on ESG. They are therefore likely to be affected by the new rules.

Companies in the Czech Republic have realised that data collection and analysis will be a necessity as early as 2022, according to the results of a survey conducted by the Confederation of Industry and Transport of the Czech Republic [40]. Survey period: 5/5 - 8/6/2022, Number of respondents: 100 industrial companies in the Czech Republic. The survey found that 87% of companies actively promote sustainability and 60 per cent believe it's essential to compete. 29% of companies are not aware of their obligations under the ESD Directive. The most common barriers to implementing sustainability were identified by business representatives as lack of competent staff, lack of funding, lack of transparency in legislation, lack of knowledge and lack of technology to actually implement EGS.

RESULTS

This article examines the implementation of environmental, social and governance (ESG) criteria in the construction industry, based on data from surveys conducted in 2022-2024. The findings reveal a significant disparity in ESG readiness and implementation between companies of different sizes and geographies. The research confirms that ESG awareness or activity declines with company size. Larger companies, particularly in regions with established ESG legislation (such as Europe and Asia Pacific), show higher levels of ESG reporting and integration into business strategies. These companies have significant resources and expertise to enable effective implementation of ESG standards, including measuring carbon footprints, reducing emissions and improving the social aspects of business.

On the contrary, smaller and medium-sized companies, particularly in the Czech Republic, face more significant challenges. Low awareness of ESG principles and regulatory requirements, limited human capacity and financial resources are the main barriers to effective implementation. Many companies in this category do not know how to apply ESG principles in practice and lack the knowledge to develop sustainable strategies and reporting. The article also points to a lack of transparency, with smaller companies having less incentive to disclose their ESG data, despite growing pressure from investors and regulators. Many small and micro companies believe that ESG does not apply to them. They are unaware that they could be sanctioned in the future for failing to disclose the required information. In addition, by ignoring sustainability reporting, they risk financing problems and a loss of competitiveness.

CONCLUSION

The article highlights the growing pressure for ESG compliance, driven by investor demands, regulatory requirements (such as the CSRD Directive) and increasing public awareness of sustainability issues. While larger companies are generally more advanced in their ESG journey, integrating sustainable practices into their operations and reporting, smaller companies often face significant challenges in terms of resources, expertise and understanding. This gap requires targeted support and leadership to ensure equal participation across the industry. Future research can focus on developing practical strategies and tools to help smaller firms overcome these barriers and encourage wider adoption of sustainable practices across the construction industry. Addressing these challenges is essential to building a more sustainable and responsible construction industry worldwide.

REFERENCES

[1] Přikryl J., Fibiger J., Karásek J. et al., 2023. National analysis of the current state of the Czech Republic. Also available from: https://database.craftedu.eu/storage/app/media/DoubleDecker/cs/DELIVERABLE%20D2.3%20%C4%8CR_V6.pdf. (written in Czech)

[2] Monitoring the evolution of prices of construction materials [online]. 2024 [cit. 2024-11-13]. Available from: https://www.urs.cz/software-a-data/sledovani-vyvoje-cen-materialu. (written in Czech)

[3] Electricity and gas prices stabilise in 2023. Eurostat [online]. 2023 [cit. 2024-11-13]. Available from: https://ec.europa.eu/eurostat/web/products-eurostat-news/w/ddn-20231026-1

[4] How has the CNB's two-week repo rate developed? Czech National Bank [online]. 5/3/2024 [cit. 2024-11-13]. Available from: https://www.cnb.cz/cs/casto-kladene-dotazy/Jak-se-vyvijela-dvoutydenni-reposazba-CNB. (written in Czech)

[5] Directive (EU) 2022/2464 of the European Parliament and of the Council of 14 December 2022 amending Regulation (EU) No 537/2014, Directive 2004/109/EC, Directive 2006/43/EC and Directive 2013/34/EC on corporate sustainability reporting. In: Official Journal of the European Union. 2022. Also available from: https://eur-lex.europa.eu/legal-content/CS/TXT/?uri=CELEX:32022L2464

[6] Saunders M., Lewis P., Thornhill A., 2019. Research methods for business students. Eight edition. Harlow: Pearson. ISBN 9781292016627

[7] Berelson B., 1954. Content analysis. Handbook of social psychology.

[8] Zhang N., Yang Ch., Wang S. Research progress and prospect of environmental, social and governance: A systematic literature review and bibliometric analysis. Journal of Cleaner Production [online]. 2024, 447, 141-489 [cit. 2024-11-13]. ISSN 0959-6526. Available from: doi: 10.1016/j.jclepro.2024.141489

[9] Lorencová L., 2023. Research shows: CSR brings economic benefits to companies. Donio [online]. 2023. [cit. 2024-11-13]. Available from: https://www.donio.cz/blog/vyzkum-ukazuje-csr-prinasi-firmam-nejen-spolecenskou-odpovednost-ale-i-ekonomicke-vyhody

[10] Tschopp D., Heufner R.J. Comparing the Evolution of CSR Reporting to that of Financial Reporting. Journal of Business Ethics [online]. 2015, 127(3), 565–577 [cit. 2024-11-13]. ISSN 0167-4544, 1573-0697. Available from: doi:10.1007/s10551-014-2054-6

[11] Koller T., Nuttall R., Henisz W. 2019. Five Ways that ESG Creates Value. The McKinsey Quarterly, ProQuest Central. [online]. ISSN 00475394. Available from: https://www.proquest.com/docview/2371931251?fromopenview=true&pq-origsite=gscholar

[12] Casey R. J., Grenier J. H., 2015. Understanding and Contributing to the Enigma of Corporate Social Responsibility (CSR) Assurance in the United States. AUDITING: A Journal of Practice & Theory. [online]. roč. 34, č. 1, s. 97-130. ISSN 1558-7991. Available from: https://doi.org/10.2308/ajpt-50736

[13] Annual Reports For A Company In Poland, 2022. Thompson&Stein [online]. 2022 [cit. 2024-11-13]. Dostupné z: https://www.thompsonstein.com/en/services/accounting-services/accounting-in-poland/annual-reports-for-the-company-in-poland/

[14] O'Neill S., 2024. What is the difference between CSR and ESG? Corporate Governance Institute [online]. 2024 [cit. 2024-11-13]. Available from: https://www.thecorporategovernanceinstitute.com/insights/lexicon/what-is-the-difference-between-csr-and-e

[15] Britz T., Meier A., 2022. On the current context of ESG in the context of the European Union and the Czech Republic. In: Vpravo.cz [online]. Praha: Rödl & Partner, 22.12.2022 [cit. 2024-11-13]. Available from: https://www.epravo.cz/top/clanky/kaktualnim-souvislostem-esg-vkontextu-evropske-unie-a-ceske-republiky115700.html

[16] Kaźmierczak M. A literature review on the difference between CSR and ESG. SPSUTOM [online]. 2022, 2022(162), 275-289 [cit. 2024-11-13]. ISSN 1641-3466. Available from: doi:10.29119/1641-3466.2022.162.16

[17] Nuttall R., Browne J., 2013. Beyond corporate social responsibility: Integrated external engagement. McKinsey & Company. [cit. 2024-11-13]. Available from: https://www.mckinsey.com/capabilities/strategy-and-corporate-finance/our-insights/beyond-corporate-social-responsibility-integrated-externalengagement

[18] Du S., Vieira E. T., 2012. Striving for Legitimacy Through Corporate Social Responsibility: Insights from Oil Companies. Online. Journal of Business Ethics. [online]. roč. 110, č. 4, s. 413-427. ISSN 0167-4544. Available from: https://doi.org/10.1007/s10551-012-1490- 4

[19] Athanasopoulou A., Selsky J. W., 2015. The Social Context of Corporate Social Responsibility: Enriching Research with Multiple Perspectives and Multiple Levels. Business & Society. [online]. 54, 322-364. Available from: https://doi.org/10.1177/0007650312449260

[20] Prokešová M., 2023. A quarter of the Czech Republic's leading companies do not report on ESG. KPMG. [online]. [cit. 2024-11-13]. Available from: https://kpmg.com/cz/cs/home/pro-media/tiskovezpravy/2023/02/ctvrtina-prednich-ceskych-firem-neinformuje-oesg.html. (written in Czech)

[21] Quinn J., 2022. ESG and Its Critics, New Thinking. [online]. 2022 [cit. 2024-11-13]. Available from: https://www.newthinking.com/business/esg-and-its-critics

[22] Skýpalová R., Kučerová R., Blašková V., 2016. Development of the Corporate Social Responsibility Concept in Small and Medium-Sized Enterprises. Prague Economic Papers. Praha: Vysoká škola ekonomická. [online]. roč. 25, č. 3, s. 287-303. ISSN 12100455. Available from: https://doi.org/10.18267/j.pep.558

[23] Kašparová K., Kunz V., 2013. Modern approaches to corporate social responsibility and CSR reporting. Grada Publishing. ISBN 978-80-247-4480-3. (written in Czech)

[24] Jones T., Shan Y., Goodrum P. An investigation of corporate approaches to sustainability in the US engineering and construction industry, Construction Management and Economics, 2010, 28, 971-983

[25] Zuo J., Zillante G., Wilson L., Davidson C., Pullen S. Sustainability policy of construction contractors: A review. Renewable and Sustainable Energy Reviews, 2012, 16, 3910– 3916

[26] Sustainability as a key topic not only of the European agenda, p. 4, AG-3-web.indd (kacr.cz)

[27] Segal M. EFRAG. Releases Proposed EU Sustainability Reporting Standards for Small Companies. ESGtoday [online]. 2024 [cit. 2024-11-13]. Available from: https://www.esgtoday.com/efrag-releases-proposed-eu-sustainability-reporting-standards-for-smallcompanies

[28] Machová A. Non-financial reporting will affect around 1,500 companies in the Czech Republic. EY [online]. 2022 [cit. 2024-11-13]. Available from: ttps://www.ey.com/cs_cz/sustainability/alice-machova-nefinancnireporting-se-v-cesku-dotkne-zhruba-1500. (written in Czech)

[29] Mccalla-Leacy J., Shulman J., Threlfall R. KPMG International. Big shifts, small steps: Survey of Sustainability Reporting 2022 [online]. 2022 [cit. 2024-11-13]. Available from: https://assets.kpmg.com/content/dam/kpmg/xx/pdf/2022/10/ssr-smallsteps-big-shifts.pdf

[30] Armstrong G., Gilge C., Max K., Vora S. Familiar challenges— new approaches: 2023 Global Construction Survey. KPMG [online]. 2023, 40 [cit. 2024-11-13]. Available from: https://assets.kpmg.com/content/dam/kpmg/nl/pdf/2023/sectoren/2023-globalconstruction-survey.pdf

[31] Annex to the report on accidents at work in the Czech Republic in 2023 [online]. Research Institute for Occupational Safety, 2024 [cit. 2024-11-13]. Available from: https:// zsbozp.vubp.cz/priloha-ke-zprave-o-pracovni-urazovosti-v-ceske-republice-v-roce-2023-rozsirujici-a-doplnujici-analyticka-studie

[32] Interest in sustainability opens up opportunities for construction companies [press release]. 13/07/2023. CEEC Research. Prague. Also available from: https://ceec.eu/media/?rok=2023. (written in Czech)

[33] The ESG Imperative: Business Trends Among European Companies. 6.5.2024. Available from: https: //www.bdo.cz/cs-cz/temata/advisory-cs/esg/jak-prorusta-udrzitelnost-do-strategie-a-hodnot-spolecnosti, //www.bdo.cz/getmedia/d778aa80-ce09-4043-b48d-1c6f75588473/The-ESG-Imperative-Business-Trends-Among-European-Companies_PROOF4.pdf

[34] Krajíčková Z., Sattler R. Do you do business fairly? ESG Rating again assesses the responsibility of Czech companies. Forbes [online]. 2023 [cit. 2024-11-13]. Available from: https://forbes.cz/podnikate-ferove-esg-rating-znovu-hodnotil-zodpovednost-ceskych-firem. (written in Czech)

[35] ESG rating: Which companies are in the top ten for sustainability and ESG? [online]. 2023 [cit. 2024-11-13]. Available from: http://www.spolecenskaodpovednost.cz/esg-rating-ktere-firmy-se-umistily-mezi-nejlepsimi-na-zaklade-udrzitelnosti-a-esg/.(written in Czech)

[36] PwC CEO Survey 2024: Is the time of revival coming? [online]. In: PwC, 2024 [cit. 2024-11-13]. Available from: https://www.pwc.com/cz/cs/ceo-agenda/assets/2024/CEO-Survey-2024-brozura.pdf. (written in Czech)

[37] Carbon Tracker 2023 [online]. PwC Czech Republic. 2023 [cit. 2024-11-13]. Available from: https://carbontracker.cz/cz/vysledky. (written in Czech)

[38] EY EU Taxonomy Barometer 2023 [online]. EY Building a better working world, 2023 [cit. 2024-11-13]. Available from: https://assets.ey.com/content/dam/ey-sites/eycom/en_gl/topics/assurance/assurance-pdfs/ey-eu-taxonomy-barometer-2023-final.pdf.

[39] Chamber Barometer: Business Sustainability [online]. Chamber of Commerce of the Czech Republic. 2023 [cit. 2024-11-13]. Available from: http:// www.komora.cz/app/uploads/2024/05/esg.pdf. (written in Czech)

[40] Sustainability - SP CR Survey. Available from: http://www.spcr.cz/images/Pruzkum_SPCR_udrzitelnost_vysledky_25072022.pdf (written in Czech)

FLEXURAL ANALYSIS OF STEEL MESH REINFORCED POLYURETHANE CONCRETE MATERIAL

Dandan Hu[1], Liangxiang Guo[2] and Baozhen Yan[3]

1. *School of Civil and Architectural Engineering, Harbin University, No.109 Zhongxing Road, Harbin, Heilongjiang Province, China; Hardandan@163.com*
2. *Construction Department, Guangzhou Highway Engineering Group Co. LTD, No. 6 Suiyin Erheng Road, Guanzhou, Guangdong Province, China*
3. *Design Department, Heilongjiang Province Highway Bridge Survey Design Co. Ltd., No. 90 Qingbin Road, Harbin, Heilongjiang Province, China*

Received: 07.10.2024

Received in revised form: 16.12.2024

Accepted: 15.01.2025

ABSTRACT

In this paper, a new method of steel mesh reinforced polyurethane concrete (SMPC) material for bridge reinforcement is proposed because of the peeling failure of the reinforced layer of steel mesh reinforced polymer mortar (SMPM) material. Using the excellent anti-corrosion and tensile properties of high-strength steel mesh, as well as the advantages of strong adhesion and fast curing speed of polyurethane concrete, the two materials are combined together. In order to verify the feasibility of this strengthening method, the mechanical properties of SMPC material are investigated by bending test of SMPC material sheet. The main factors affecting the tensile properties of the composites are analyzed by considering the test variables such as specimen width, specimen thickness, glue-powder ratio and curing time. Based on the simplified tension model of high strength steel wires and the stress-strain relationship between tension and compression of polyurethane concrete, the calculation method of flexural bearing capacity of composite materials is obtained. The test results show that the flexural strength of the composite can be improved by increasing the width of the specimen, and the deflection can be reduced by increasing the reinforcement ratio, while the influence of the glue-powder ratio on the deflection is small.

KEYWORDS

Steel mesh reinforced polyurethane concrete (SMPC) material, Steel mesh reinforced polymer mortar (SMPM) material, Flexural performance test, Analysis of influence factors

INTRODUCTION

With the increase of bridge operation time and vehicle load, the structural diseases of bridge are increasing. For bridges with structural diseases, their bearing capacity and structural durability may not meet the requirements of the current code. There are big security risks, demolition and reconstruction is not economical and unreasonable. The existing old bridges are tested and evaluated, and reinforced and reformed according to the actual situation of the bridges [1-3]. This can not only increase the life of the old bridge in service, but also save a lot of costs, bring huge economic benefits to the society, and reduce the occurrence of bridge accidents [4-6].

The steel mesh has the characteristics of light weight and high strength, and composite mortar is often used as the bonding and anchoring material. The composite mortar and steel mesh is used to strengthen the bridge structure. Xing [7] conducted an experimental study on the flexural performance of reinforced concrete beams reinforced by steel mesh reinforced polymer mortar (SMPM) material, and the results showed that the reinforcement of reinforced concrete beams by PM-SWM was an effective means of flexural reinforcement. Compared with the contrast beam, the bearing capacity and stiffness of the reinforced beam are significantly improved, and the calculation method of the flexural bearing capacity of the reinforced beam is proposed. Wang [8] conducted a test study on the shear resistance of reinforced concrete (RC) beams reinforced by high-strength steel mesh and polymer mortar. The damage mode, load-deflection curve, strength, stiffness and ductility of the beam are studied and analyzed. The mechanical properties of the reinforced beams are improved, and the shear resistance is increased by 38.47% ~ 71.37%. Finally, according to the specification, the prediction model of the shear capacity of the test beam is established. However, due to the poor tensile property and bonding property of the composite mortar, the SMPM reinforcement layer will be stripped and damaged, and the utilization rate of the steel stranding network will be reduced [9-13].

Polyurethane concrete (PC) material not only has fast setting speed and high early strength, but also shows the advantages of light weight, high strength and high toughness after curing. The material itself has good bonding strength and acid and alkali corrosion resistance [14-17]. Polyurethane concrete (PC) composite material is gradually applied in the field of bridge reinforcement. PC material is a new type of composite material with polyurethane as matrix and cement as reinforcement, which has the advantages of corrosion resistance, light weight and high strength. Zhang [18] conducted an experimental study on reinforced concrete T-beams reinforced by SMPC material. Factors such as the rate of wire mesh placement and the type of material the wire mesh is embedded in are considered. The test results show that SMPC reinforced beams exhibit greater yield load, ultimate load and stiffness than PM-SWM reinforced beams, and SMPC material reinforced beams can effectively inhibit crack propagation. Zhang [19] conducted a study on the flexural performance of reinforced concrete T-beams reinforced by SMPC material, and the test results showed that SMPC materials could significantly improve the flexural bearing capacity of the reinforced beams. Compared with the beams reinforced by PM-SWM, the beams reinforced by SMPC materials did not have peeling damage, and it can inhibit the generation and development of cracks.

In order to further apply SMPC material to practical engineering, it is necessary to further study the flexural properties of the composites. The four-point flexural test of thin plate specimens is carried out, and the failure mode and characteristics of thin plate specimens under load are investigated. Based on the simplified tensile model of steel mesh and the PC stress-strain relationship, the calculation method of flexural bearing capacity of composites is obtained, which provides a basis for material design and engineering application of urethane cement-steel mesh composites.

TESTING PROGRAM

Specimen design and preparation

The four-point bending test of SMPC material plate with length of 400 mm was carried out. The thickness of the thin-plate specimens is 25 mm. The wire mesh is welded by high-strength steel wire with a diameter of 1mm, and the square hole size of the wire mesh is 15 mm×15 mm.

The variables considered in the four-point bending test are the thickness of the specimen and the ratio of polyurethane to cement powder. Specimen widths are 120 mm, 100 mm, 80 mm and 60 mm, respectively. The weight of rubber powder in polyurethane concrete is 0.5, 1.0 and 1.5, respectively. A total of 3 specimen sets and 12 specimen groups (3 specimens in each group) were designed and produced, with a total of 36 thin-plate specimens. The F-a specimen set consists of 4 specimen groups, including F-a1, F-a2, F-a3 and F-a4. Each specimen group has a different width to explore the influence of specimen width on the bending properties of thin-plate specimens. The F-b set is similar to the F-a set, each containing four test sets, and only the PU cement mix ratio is changed to explore the influence of PU cement powder ratio on the bending properties of the composite. F-c sets were used as variables for 4 groups of steel mesh with different layers, and the influence of steel mesh reinforcement ratio on the bending performance of the sheet was investigated. Detailed design parameters of thin plate specimens are shown in Table 1.

Tab. 1 - Design parameters of thin plate specimens

Specimen set	Specimen group	Steel mesh layers	PC mix ratio	Specimen width/mm	Longitudinal wire spacing/mm
F-a	F-a 1	4	0.5	120	45
	F-a 2	4	0.5	100	35
	F-a 3	4	0.5	80	25
	F-a 4	4	0.5	60	15
F-b	F-b 1	4	1.0	120	45
	F-b 2	4	1.0	100	35
	F-b 3	4	1.0	80	25
	F-b 4	4	1.0	60	15
F-c	F-c 1	4	1.5	120	45
	F-c 2	3	1.5	120	45
	F-c 3	2	1.5	120	45
	F-c 4	1	1.5	120	45

The production process of thin plate specimen is shown in Figure 2. The specific production process is as follows:

(1) Make a wood template, and reserve holes in the board for passing through the steel mesh.
(2) Pass the steel strand through the hole reserved for the template, first through the longitudinal steel strand, and then through the horizontal steel strand, so that the vertical steel wires and the horizontal steel wires constitute the steel mesh.
(3) Anchor both ends of the steel mesh to the side of the template with a lock.
(4) Use a cross buckle to fix the wire mesh, and apply impermeable glue at the opening of the template extending out of the wire to prevent cement from flowing out.
(5) Cut excess steel wire with steel wire pliers.
(6) Prepare release agent with silica gel and talc powder, and brush release agent on the inner wall of the template to facilitate later release.
(7) Take appropriate amount of polyisocyanate and polyol into the beaker and put it in 150° oven for 30 minutes. Polyurethane concrete is prepared according to the mix ratio and fully stirred to pour polyurethane concrete.
(8) After the test piece was poured, the exposed cement surface is covered with plastic wrap. The formwork is removed 24 h later, and the test block was put into the standard curing room for curing. After the curing, the test piece is taken out of the standard curing room (temperature 20±2℃) for testing.

Experimental process

The loading of the bending test is shown in Figure 1. Switch the universal testing machine from tension mode to pressure mode, and install the support and loading head on the testing machine. Three displacement meters are arranged longitudinally at the mid-span of the thin plate specimen and under the loading head to measure the vertical deformation of the specimen. The displacement meter is arranged at the straddle and loading points respectively. The thin plate specimen is placed on the support, the upper and lower surfaces of the specimen are cleaned with alcohol, and the compressive strain and tensile strain are measured on the upper and lower surfaces as auxiliary test results. The load is measured in real time by a pressure sensor above the loading head. The test load is controlled by displacement, and the loading rate is constant at 0.5 mm/min. The test load and displacement meter data can be displayed on the computer in real time.

The test is carried out by four-point loading method. The distance between the two supports is 300 mm, the distance between the loading point and the support is 100 mm, and the distance between the loading point and the loading point is 100 mm.

After the test began, the traction loading head of the universal testing machine moved downward. When the loading head is in contact with the thin plate specimen, the load value and displacement value increase uniformly. As the test continued, the thin plate specimen gradually deformed, accompanied by the crisp fracture sound, a long crack appeared in the middle of the specimen, and the polyurethane cement was damaged. In the event of failure, the fracture of the steel strand and the cracking of the polyurethane cement occur almost simultaneously. At this time, the thin-plate specimen also reached the ultimate load and maximum deflection.

Fig. 1 - Four-point bending test

ANALYSIS OF FOUR POINT BENDING TEST RESULTS

Based on the pressure sensor and displacement meter, the load-mid-span displacement curve of the thin plate shaped SMPC specimen under the F-a specimen set is obtained, as shown in Figure 2. F-a1, F-a2, F-a3 and F-a4 have different specimen widths. The F-a1 specimen group with the smallest width but the largest reinforcement ratio has the largest average ultimate load of 13.85 kN. The F-a 4 specimen group with the largest width but the smallest reinforcement ratio has the smallest average ultimate load, which is 5.64 kN. With the increase of load, the mid-span displacement growth rate of F-a1 specimen group is significantly lower than that of the other three groups, which indicates that a higher width of specimen can significantly inhibit the expansion of mid-span displacement, but the width of specimen has almost no effect on the displacement growth.

DOI 10.14311/CEJ.2025.01.0008

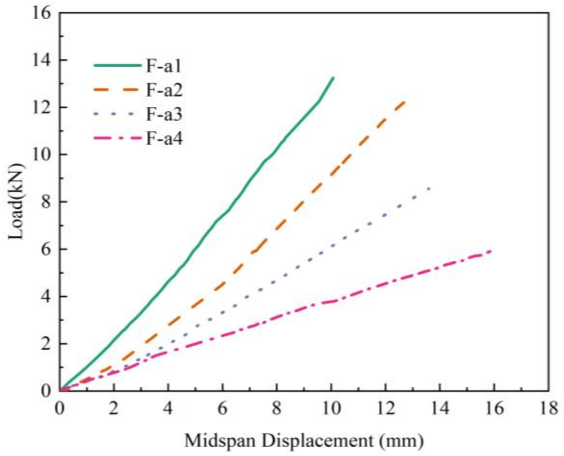

Fig. 2 - Load-displacement curve of F-a set

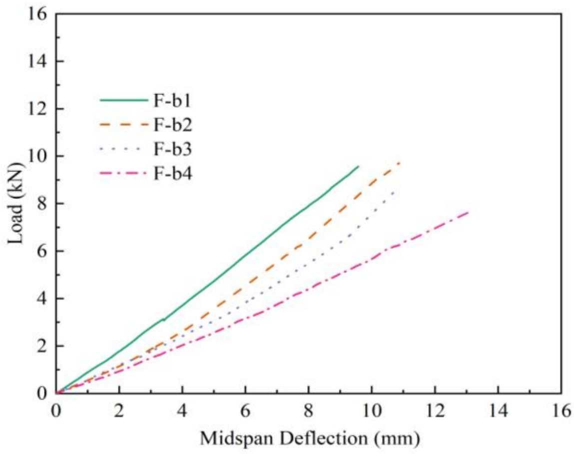

Fig. 3 - Load-displacement curve of F-b set

The load-displacement curve of the SMPC thin plate specimen of F-b specimen set is shown in Figure 3. Compared with the F-a set, the F-b set is made of polyurethane concrete with a rubber to powder ratio of 1. The F-b1 group with the largest width has the largest growth rate. The average limit load of group F-b1 can reach 9.72 kN, which is 29% larger than the 7.53 kN of group F-b4 respectively. In terms of mid-span displacement, F-b4 group has a maximum average mid-span displacement of 12.99 mm, which is 42 % higher than that of F-b1 group, which is 9.60 mm. In general, the ultimate load and the maximum mid-span displacement of each group in F-b set are lower than those in F-a set with rubber powder ratio of 1.5.

The load-displacement curve of the SMPC thin plate specimen of F-c specimen set is shown in Figure 4. F-c sets have steel mesh with different layers to explore the influence of reinforcement ratio on the bending properties of composites. In general, the ultimate load is positively correlated with the ratio of reinforcement, and the mid-span displacement is positively correlated with the ratio of reinforcement. According to the trend of the curve, the load-displacement curve of F-c1 group with the highest reinforcement ratio increases the fastest. When the ultimate load is reached, the average mid-span displacement of F-c1 group is 8.85 mm. F-c4 group has the slowest load growth among the four groups. When the load is 5.32 kN, the specimen breaks and fails. The F-c4 group with the smallest reinforcement ratio also has the largest mid-span displacement in this sample set, which is 11.66 mm.

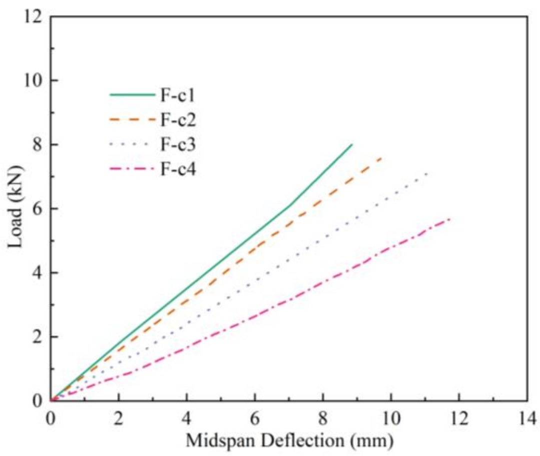

Fig. 4 - Load-displacement curve of F-c set

ANALYSIS OF INFLUENCE FACTORS

The width of the specimen significantly affects the maximum deflection and ultimate load of the SMPC specimen. F-a1, F-a2, F-a3 and F-a4 thin plate specimens have different widths, and the ultimate load values along the span direction of the specimens are shown in Figure 5. With the increase of the width of the specimen, the maximum deflection of the SMPC specimens also increases. The average maximum deflection of F-a4 specimen group is 15.85 mm, and the average maximum deflection is 1/20 of the span. The width of F-a1 specimen group is 120 mm, and the maximum bearing capacity is 13.85 kN. Compared with F-a2, F-a3 and F-a4 groups, the ultimate load of F-a1 is increased by 11%, 38% and 59%, respectively. This also shows that the increase of the width of the specimen increases the bending bearing capacity of the steel mesh reinforced polyurethane concrete (SMPC) material.

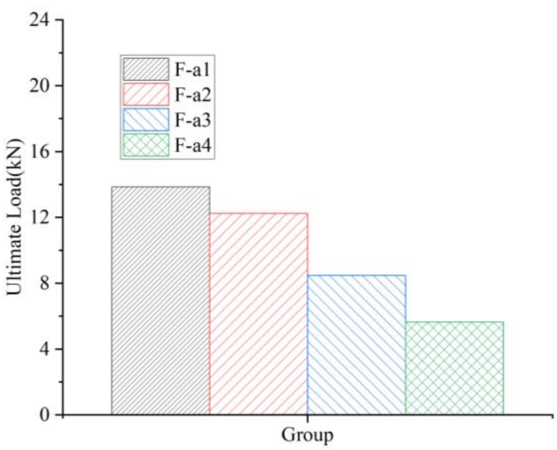

Fig. 5 - The influence of specimen width on the bending performance of composite materials

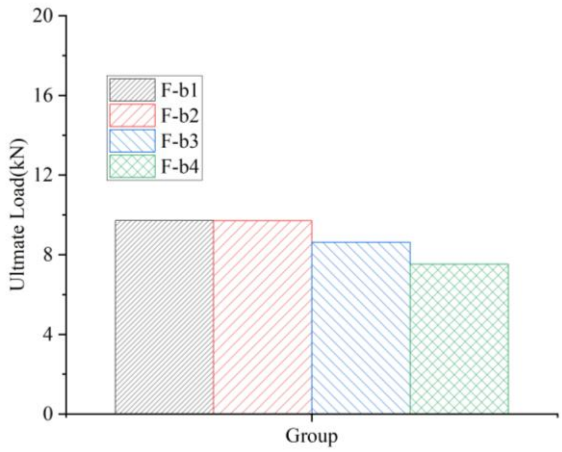

Fig. 6 - The influence of rubber powder ratio on the bending performance of composite materials

The ratio of glue to powder has a significant effect on the ultimate load of polyurethane concrete-steel mesh specimen, but has little effect on the maximum deflection. The relationship between the ultimate loads of thin plate specimens with different glue-powder ratios is shown in Figure 6. The maximum deflection of thin plate does not change significantly with the difference of PC mix ratio. The maximum deflection of F-a1, F-b1 and F-c1 specimens is 10.07 mm, 9.60 mm and 8.85 mm, respectively, with the maximum difference not exceeding 8%. The mix ratio of PC will affect the ultimate bending load. The F-a1 specimen with a glue-powder ratio of 1.5 is subjected to the maximum ultimate load, which is 30% and 42% higher than that of F-b1 specimen with a glue-powder ratio of 1.0 and F-c1 specimen with a glue-powder ratio of 0.5, respectively.

DOI 10.14311/CEJ.2025.01.0008

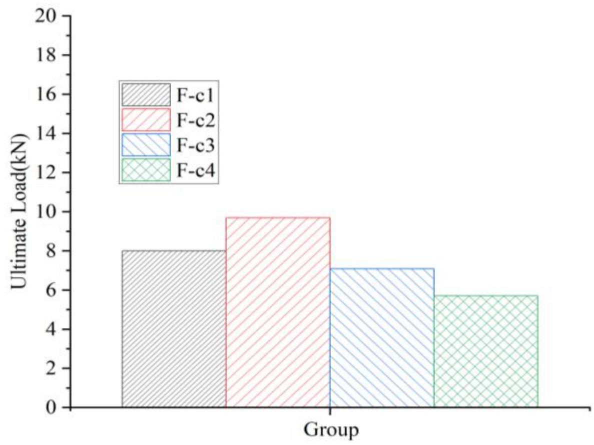

Fig. 7 - The influence of reinforcement ratio on the bending performance of composite materials

The reinforcement ratio can significantly affect the ultimate load and deflection of SMPC specimen. The relationship between reinforcement ratio of steel mesh and ultimate load at failure is shown in Figure 7. The ratio of reinforcement is negatively correlated with mid-span deflection. The average deflection of F-c1 specimen group with the largest reinforcement ratio is the smallest (8.85 mm). The mid-span deflection increases gradually with the decrease of steel mesh layers. The average deflection of F-c4 specimen group with the smallest reinforcement ratio is the largest, which is 11.66 mm. The ratio of reinforcement is positively correlated with the ultimate load. The ultimate load of F-c1 group with the highest reinforcement ratio is 8.0 kN, 17% lower than that of F-c2 group with a slightly smaller reinforcement ratio of 9.69 kN, 13% and 40% higher than that of F-c3 group and F-c4 group, respectively.

THEORETICAL ANALYSIS OF FOUR-POINT BENDING TEST

Calculation model of flexural capacity

(1) Tension model of high-strength steel mesh

The simplified stress-strain relationship of high-strength steel mesh is based on the double broken line model, as shown in Figure 8. The model simplifies the tension constitutive relation of steel strand into two stages. Its expression is shown in formula (1).

DOI 10.14311/CEJ.2025.01.0008

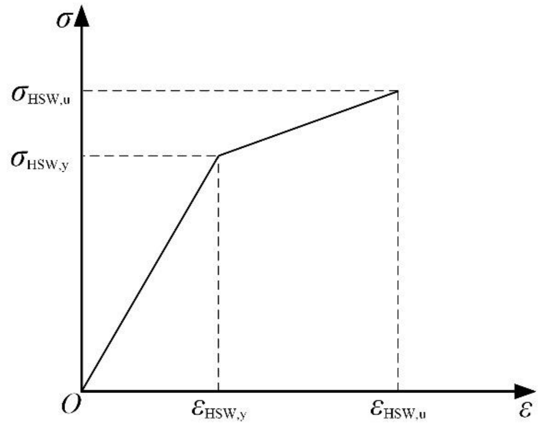

Fig. 8 - Simplified stress-strain relationship of tensile SM

$$\sigma_{\mathrm{SM}}=\begin{cases} E_1\varepsilon_{\mathrm{SM}} & \left(0\le\varepsilon_{\mathrm{SM}}\le\varepsilon_{\mathrm{SM,y}}\right) \\ \sigma_{\mathrm{SM,y}}+E_2\left(\varepsilon_{\mathrm{SM}}-\varepsilon_{\mathrm{SM,y}}\right) & \left(\varepsilon_{\mathrm{SM,y}}\le\varepsilon_{\mathrm{SM}}\le\varepsilon_{\mathrm{SM,u}}\right) \end{cases} \tag{1}$$

Where E1 and E2 are the elastic modulus of the mesh in the first and second stages respectively. The elastic modulus varies according to the diameter of the steel mesh, as shown in Table 2. $\sigma_{SM,y}$ is the tensile stress at the end of the first stage of the tensile process of the strand, and its value is about 80% of the ultimate tensile stress of the strand $\sigma_{SM,u}$. $\sigma_{SM,y}$ is the tensile strain at the end of the first stage in the tensile process of the steel mesh, and its value is about 45% of the ultimate tensile strain $\sigma_{SM,u}$.

Tab. 2 - Value of elastic modulus of F-c

Steel mesh layers	First stage elastic modulus E1 (GPa)	Second stage elastic modulus E2 (GPa)
1	135	32.0
2	130	31.5
3	108	22.5
4	97	21.3

(2) PC tensile model

The stress-strain simplified relationship of polyurethane concrete is shown in Figure 9. The constitutive relation of PC is simplified from quadratic function to linear relation. The simplified stress-strain curve is shown in Figure 10. $\sigma_{PC,tu}$ and $\varepsilon_{PC,tu}$ are the ultimate tensile stress and ultimate tensile strain of polyurethane concrete, respectively. The expression is shown in formula (2).

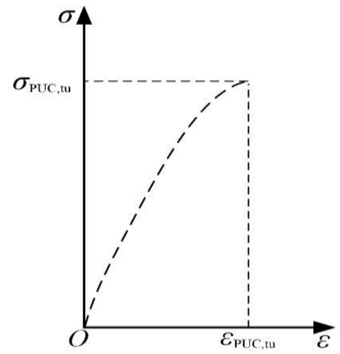

(a) *Tensile constitutive relationship of PC*

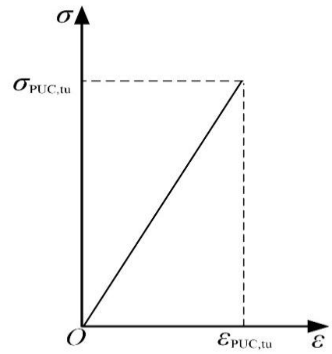

(b) *Simplified tensile constitutive relationship of PC*

Fig. 9 - Stress-strain relationship of tensile PC

$$\sigma_{\mathrm{PC,t}} = E_{\mathrm{PC,t}}\varepsilon_{\mathrm{PC,t}} \tag{2}$$

Where $\sigma_{PC,t}$ and $\varepsilon_{PC,t}$ are tensile stresses and strains of polyurethane concrete, respectively. $E_{PC,t}$ is the simplified tensile elastic modulus of polyurethane concrete, which is 4.5GPa.

(3) PC compression model

The compressive constitutive relationship of PC is shown in Figure 11. The nonlinear compression model is adopted. The model is similar to the stress-strain relationship in ECC, which is divided into ascending and flattening sections. In order to facilitate calculation, the compression model is also simplified, and the quadratic function relationship in the ascending section is simplified to a linear relationship. The simplified expression is shown in formula (3).

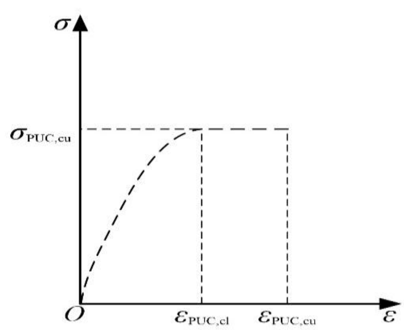

(a) *Compressed constitutive relationship of PC*

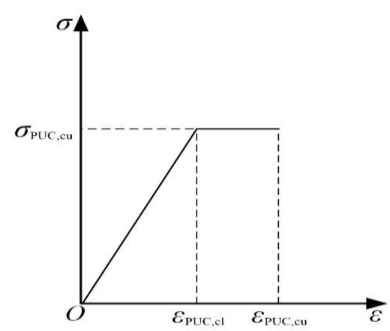

(b) *Simplified compressed constitutive relationship of PC*

Fig. 10 - Stress-strain relationship of compressed PC

$$\sigma_{\mathrm{PC,c}}=\begin{cases}\dfrac{\varepsilon_{\mathrm{PC,c}}}{\varepsilon_{\mathrm{PC,cl}}}\sigma_{\mathrm{PC,cl}} & \left(0\le\varepsilon_{\mathrm{PC,c}}\le\varepsilon_{\mathrm{PC,cl}}\right)\\ \sigma_{\mathrm{PC,cu}} & \left(\varepsilon_{\mathrm{PC,cl}}\le\ \varepsilon_{\mathrm{PC,cu}}\right)\end{cases} \tag{3}$$

Where: $\sigma_{PC,c}$ is the compressive stress of polyurethane concrete, $\varepsilon_{PC,c1}$ is the compressive strain corresponding to the ultimate compressive strength of polyurethane concrete, $\varepsilon_{pc,c1}$ is the ultimate compressive strain at the top of the plate when the thin plate specimen is broken by bending, the ultimate compressive strain $\varepsilon_{PC,cu}$ is 0.02.

(4) Calculation formula of flexural bearing capacity

In the calculation of flexural strength of SMPC material, the working condition of SMPC material in tension area is considered. The stress-strain distribution of the section of thin plate specimen is shown in Figure 11. *h* and *b* represent the height and width of the specimen respectively. h_0 is the effective height of the section. a_s is the thickness of the protective layer of the steel mesh. x_0 is the height of compressive zone of PC. $\sigma_{hsw,t}$ and $\varepsilon_{hsw,t}$ are the stress and strain of high-strength steel mesh. $\sigma_{PC,t}$ and $\varepsilon_{PC,t}$ are tensile stresses and ultimate tensile stresses of PC, respectively. $\varepsilon_{PC,c}$ and $\varepsilon_{PC,u}$ are compressive strain and ultimate compressive strain of PC respectively. $\sigma_{PC,cu}$ is the ultimate compressive stress of polyurethane concrete. ψ is the tensile stress parameter of PC.

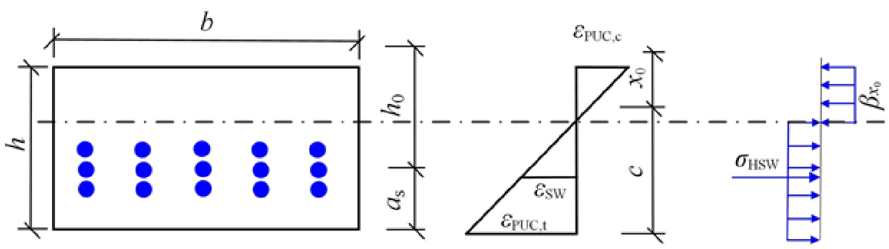

Fig. 11 - Stress and strain distribution of SMPC material during bending

According to the stress-strain distribution of the cross section of the composite material during bending, formula (4) is derived through the balance equation of force and bending moment:

$$\mathrm{M}=\sigma_{\mathrm{SM}}A_{\mathrm{SM}}\left(h-a_{\mathrm{s}}-\frac{1}{2}\beta\mathrm{x}_0\right)+\frac{1}{2}\sigma_{\mathrm{PC,t}}b\left(h\text{-}x_0\right)\left[h+\left(1-\beta\right)x_0\right] \tag{4}$$

Under the limit failure state of thin plate specimen, the strain and stress of high-strength steel mesh:

Where, b is the section width; h is the section height. For thin-plate specimens in this test, h is 25mm. σ_{SM} is the stress of steel mesh. a_{SM} is the height of the wire. For the thin plate specimen with the strand vertically centered, a_{SM} is 12.5mm. a_{SM} is the cross-sectional area of the longitudinal wire. The value is based on the diameter of the wire.

CONCLUSIONS

This paper presents a new material of steel mesh reinforced polyurethane concrete (SMPC). In order to verify the feasibility of this strengthening method, the mechanical properties of SMPC material are investigated by bending test of SMPC material sheet. The research conclusions are as follows:

(1) Increasing the width of thin plate specimens can improve the bending bearing capacity of steel mesh reinforced polyurethane concrete (SMPC) material. The width of the thin plate specimen

is 120 mm, and its maximum bearing capacity is 13.85 kN, and its ultimate load is 11%, 38% and 59% higher than that of the F-a2 (100 mm), F-a3 (80 mm) and F-a4 (60 mm) specimens, respectively. Maximum deflection reduced by 37%.

(2) The ratio of glue to powder has a significant effect on the ultimate load of SMPC specimen, but has little effect on the maximum deflection. The glue-powder ratio of F-a1 specimen group is 1.5 and the ultimate load is 13.85 kN, which is 42% and 73% higher than that of F-b1 specimen group with glue-powder ratio of 1.0 and F-c1 specimen group with glue-powder ratio of 0.5 respectively.

(3) The ultimate load of thin plate specimens increases with the increase of reinforcement ratio. The F-c1 specimen group exhibited the smallest mean deflection, only 8.85 mm, due to its highest reinforcement ratio. The ultimate load of F-c1 group with the highest reinforcement ratio reached 8.0 kN, which was 5.8% higher than that of F-c2 group with a slightly lower reinforcement ratio of 7.56 kN.

REFERENCES

[1] Jiang Y., Yang G., Li H., 2023. Knowledge Driven Approach for Smart Bridge Mmaintenance Using Big Data Mining. Automation in Construction, vol. 146, pp. 104673. ISSN 0926-5805, https://doi.org/10.1016/j.autcon.2022.104673

[2] Yanev B., RichardsI G. A. C., 2013. Designing Bridge Maintenance on the Network and Project Levels. Structure and Infrastructure Engineering, vol. 9, no. 4, pp. 349-363. ISSN 1573-2479, Designing Bridge Maintenance on the Network and Project Levels

[3] Orcesi A. D., Frangopol D. M., Kim S., 2010. Optimization of Bridge Maintenance Strategies Based on Multiple Limit States and Monitoring. Engineering Structures, vol. 32, no. 3, pp. 627-640. ISSN 0141-02, https://doi.org/10.1016/j.engstruct.2009.11.009

[4] Mahdi I M., Khalil A. H., Mahdi H. A., 2022. Decision Support System for Optimal Bridge’ Maintenance. International Journal of Construction Management, vol. 22, no. 3, pp. 342-356. ISSN 1562-3599, https://doi.org/10.1080/15623599.2019.1623991

[5] Ren G., Ding R., Li H., 2019. Building An Ontological Knowledgebase for Bridge Maintenance. Advances in Engineering Software, vol. 130, pp. 24-40. ISSN 0965-9978, https://doi.org/10.1016/j.advengsoft.2019.02.001

[6] Furuta H., Kameda T., Nakahara K., 2006. Optimal Bridge Maintenance Planning Using Improved Multi-Objective Genetic Algorithm. Structure and Infrastructure Engineering, vol. 2, no. 1, pp. 33-41. ISSN 1573-2479, https://doi.org/10.1080/15732470500031040

[7] Xing G., Wu T., LIiu B., 2010. Experimental investigation of Reinforced Concrete T-beams Strengthened with Steel Mesh Embedded in Polymer Mortar Overlay. Advances in structural Engineering, vol. 13, no. 1, pp. 69-79. ISSN 1369-4332, https://doi.org/10.1080/15732470500031040

[8] Wang T., He M., Wu H., 2024. Experimental Study on RC Beams Shear-strengthened with Composite Polymer Mortar and Steel Strands Wire Mesh. Structural Concrete, vol. 25, no. 4, pp. 2660-2676. ISSN 1464-4177, https://doi.org/10.1002/suco.202300630

[9] Siwowski T., Piatek B., Siwowska P., 2020. Development and Implementation of CFRP Post-tensioning System for Bridge Strengthening. Engineering Structures, vol. 207, pp. 110266. ISSN 0141-0296, https://doi.org/10.1016/j.engstruct.2020.110266

[10] Sun L. P., Liu Z., Liu Y. Z., 2014. Analysis the Flexural Properties of RC Beams Strengthened by High Strength Steel Mesh and Polymer Mortar Using the Finite Element. Applied Mechanics and Materials, vol. 444, pp. 1067-1071. ISSN 1022-6680, https://doi.org/10.4028/www.scientific.net/AMM.444-445.1067

[11] Li Y., Zhao S., Yao Z., 2023. Flexural Behavior of Reinforced Concrete Beams Strengthened Using Recycled Industrial Steel-wire Mesh High-performance Mortar. Case Studies in Construction Materials, vol. 19, pp. 02472. ISSN 2214-5095, https://doi.org/10.1016/j.cscm.2023.e02472

[12] Liao W., Wang H., Li M., 2019. Large Scale Experimental Study on Bond Behavior Between Polymer Modified Cement Mortar Layer and Concrete. Construction and Building Materials, vol. 228, pp. 116751. ISSN 0950-0618, https://doi.org/10.1016/j.conbuildmat.2019.116751

[13] Zhong S., He M., Ding, Y., 2023. Study on the Effect of Pre-stressed Level on the Force Performance of Wedge Steel Plate Jacket and Steel Mesh-PCM Strengthened RC Beams. Structures, vol. 57, pp. 105283. ISSN 2352-0124, https://doi.org/10.1016/j.istruc.2023.105283

[14] Kexin Z., Qunsheng S. Strengthening of a Reinforced Concrete Bridge with Polyurethane-cement Composite (PUC). The Open Civil Engineering Journal, vol. 10, no. 1. ISSN 2164-3164, https://doi.org/10.1061/(ASCE)CF.1943-5509.0001640

[15] Hou N., Li J., Li X., 2022. Study on Toughening and Temperature Sensitivity of Polyurethane Concrete (PUC). Materials, vol. 15, no. 12, pp. 4318. ISSN 1996-1944, https://doi.org/10.3390/ma15124318

[16] Zhang K., Zhu X., Cao Y., 2023. Experimental Study on Mechanical Properties of Polyurethane Concrete Composite (PUC) under Various Temperatures. Materiale Plastice, vol. 60, no. 2. ISSN 0025-5289, https://doi.org/10.37358/Mat.Plast.1964

[17] Li C., Zhang W., Sun G., 2023. Research on Damping Properties and Microscopic Mechanism of Polyurethane Concrete-based Composites. Construction and Building Materials, vol. 365, pp. 130137. ISSN 0950-0618, https://doi.org/10.1016/j.conbuildmat.2022.130137

[18] Zhang K., Sun Q., 2018. The Use of Wire Mesh-polyurethane Vement (WM-PUC) Composite to Strengthen RC T-beams Under Flexure. Journal of Building Engineering, vol. 15, pp. 122-136. ISSN 2352-7102, https://doi.org/10.1016/j.jobe.2017.11.008

[19] Zhang K., Xuan J., Shen X., 2024. Investigating the Flexural Properties of Reinforced Concrete T-beams Strengthened with High-strength Steel Mesh and Polyurethane Concrete. Journal of Bridge Engineering,vol. 29, no. 5, pp. 04024023. ISSN 1084-0702, https://doi.org/10.1061/JBENF2.BEENG-6524

Article no. 9

THE CIVIL ENGINEERING JOURNAL 1-2025

TESTING OF AVAILABLE MEASUREMENT METHODS FOR CUBATURE CALCULATIONS

Ondřej Váňa

Czech Technical University in Prague, Faculty of Civil Engineering, Department of Geomatics, Thákurova 7, Praha 6, Czech Republic; ondrej.vana@fsv.cvut.cz

Received: *10.12.2024*

Received in revised form: *15.02.2025*

Accepted: *28.03.2025*

ABSTRACT

This article focuses on efficient methods for measuring volume, especially cubature control in landfill inspections. Several technologies were tested involving GNSS, UAV photogrammetry, UAV laser scanning, and videogrammetry to find a technology that enables fast and accurate data collection. The research was focused as a help for the Czech Environmental Inspectorate. These methods were compared using processed point clouds and volume calculations in 3Dsurvey software, evaluating their accuracy, cost, and technical requirements. Results show that UAV photogrammetry and videogrammetry allow quick data collection with minimal effort and price, while GNSS provides precise georeferencing but has limitations in surface modelling. Laser scanning with UAV is precise, but expensive for typical users. The processed point clouds were analysed for volume estimation accuracy, confirming their suitability for landfill monitoring. This article helps optimize geodetic methods for environmental inspections, highlighting the strengths and weaknesses of each approach. The findings provide valuable guidance for selecting the most suitable technologies in geodetic and environmental applications.

KEYWORDS

GNSS, Emlid, 3Dsurvey, UAV photogrammetry, videogrammetry, volumes, L1 lidar, point cloud

INTRODUCTION

Geodesy covers a wide range of methods and has applications in many areas of human activity. One of them is volume computing using geodetic methods, which incorporates a range of advanced technologies and techniques designed to accurately measure and analyse three-dimensional data for various applications in geodesy, engineering, environmental monitoring, and natural resource management. Central to this process is the use of Geographic Information Systems (GIS), which integrates spatial data with computational tools to analyse topography, elevation, and terrain. GIS allows for the visualization and manipulation of geographic data in 2D and more recently in 3D formats, providing a platform for the creation of digital elevation models (DEMs) or digital surface models (DSMs) that form the foundation for volume calculations.

Remote sensing technologies such as LiDAR (Light Detection and Ranging) and photogrammetry have revolutionized volume computation. LiDAR, which uses laser pulses to measure distances to the Earth's surface, generates highly accurate 3D point clouds that capture detailed topographic features, even in dense vegetation or difficult terrain. Photogrammetry, which involves the use of overlapping aerial or satellite imagery, is another powerful tool for deriving 3D models of the landscape. These remote sensing methods, when combined with GIS, allow for precise volume calculations of natural and man-made features, such as mountains, rivers, reservoirs, excavation sites, and construction projects.

Additionally, Global Navigation Satellite Systems (GNSS) play a critical role in volume computing. GNSS provides highly accurate georeferencing and positioning data that is essential for precise surveying and mapping. Surveying equipment, such as total stations and digital levels, can complement GNSS by collecting high-precision elevation data, which is then used in volume computation for smaller-scale projects or areas where satellite-based data may not be sufficient. The integration of these technologies allows for the efficient and accurate computation of volumes, whether for land reclamation, flood modelling, mining, or construction, offering significant advantages in terms of speed, cost-effectiveness, and accuracy. Furthermore, the use of software platforms that can process large datasets, such as AutoCAD, ArcGIS, and specialized volume calculation tools, enables professionals to automate and optimize the volume estimation process. How it was written, determination of cubature is one of the disciplines that geodesy is dedicated to. Its determination can be done in several ways and by several methods.

Cubature can be calculated classically by geodetical measuring ways using total stations, formerly with theodolites and measuring tapes [1], or by other geodetically methods like photogrammetry. New modern method of digital photogrammetry and laser scanning give us better solution which is more precise and easier to use.

Aerial analogue photogrammetry has been used for a long time, for example, to monitor opencast mining activities, especially in brown coal mining areas. Terrestrial analogue photogrammetry then for computing cubature in quarries or sand pits. In nineties of 20th century modern digital photogrammetry began to be used based on scanned analogue images. After new Millenium automated digital photogrammetry based on SfM (Structure from Motion) and MVS (Multi View Stereo) has become very popular [2].

This includes terrestrial photogrammetry methods, but also the very popular drone technology. Much of the research has been focused on determining the cubature of forest stands. Pavelka et al. dealt with the topic of volume calculation, but they were more interested in comparing the RPAS method with other geodetic methods [3]. The use of digital aerial photogrammetry is mentioned e.g. by Kovanič et al. [4]. Tomljanović, et al discuss problems and using of drones in forestry [5].

Other technology used is laser scanning in terrestrial aerial or mobile applications. Mobile mapping especially as personal handheld technology seems to be very useful and popular in recent years. Běloch et al. analyses using and precision of mobile laser scanning [6], Štroner et al use drones with lidar sensor for volume calculations. Integration of DJI Zenmuse L1 LiDAR with Photogrammetry Software for Enhanced Data Acquisition, explored the integration of the DJI Zenmuse L1 LiDAR system for improved data acquisition and processing. The findings demonstrated the system's effectiveness in capturing detailed terrain information and generating precise digital models [7].

Another method common in surveying is the use of GNSS. For example, Emlid's Reach RS3 technology was tested by Oniga et al to verify whether it makes sense to use ground control points (GCP) in drone photogramnmetry for building model [8]. Using GNSS for monitoring or collecting geographical data is typical in technical or geographical practice [9], [10].

Lian et al explore a new non-contact targeting technology, namely videogrammetry. They discuss the principles, processes, and typical examples of its application. It is also one of the most significant sources for understanding the functioning of videogrammetry [11]. The videogrammetry method, which can be considered one of the most accessible and inexpensive, has been used in computer vision calculations in forest exploration, where it has played a major role in collecting date [12].

It is necessary to mention the data collecting with UAV in general. Drone cameras, such as the P1 photogrammetric camera from DJI, give a large possibility of using in urban planning for example. Its quality was investigated at HafenCity University Hamburg, where it was flown over the test area and compared, among other things, with the LiDAR L1, also from DJI [13].

The research highlighted the system's capability to produce high-quality digital terrain models and its suitability for various surveying tasks. Next article compared different UAV-LiDAR systems, including the DJI Zenmuse L1, for environmental monitoring purposes. The study emphasized the importance of selecting appropriate processing software, such as 3Dsurvey, to achieve accurate results [14], [15]. The result of the calculations is then a digital terrain model that is then compared. Reportedly, 3Dsurvey uses the same method of model calculation as described by Guo et al, , who described it as a regular pyramid hierarchy [16].

In the Czech Republic, there is a precise digital relief model (DMR 5G) of the entire country, which can be used by people for free. But it has a limited resolution (1-2 points on sqr. meter in open landscape) and accuracy (the reported mean squared height error is 0.18 m in exposed terrain and 0.30 m in wooded terrain), and it is more than 12 years old. The inspection people were also interested in comparing it with this model, because they often get into situations where they discover a black dump and need to compare the surface before and after contamination. DMR 5G is the subject of an article that discusses its use for other state mapping work [17]. All the methods described above show, among other things, how surveying is moving into completely different dimensions than it was ten to fifteen years ago. The problem of effectively educating the modern surveyor is addressed in [18]. This article may also point out that what was previously done only by a surveyor can now be done by another worker after training. In this research the 3Dsurvey software was used for computing of cubature calculations [19].

METHODS

A total of four measurement methods were used, which included the terrestrial and aerial variants. The methods were chosen to be the least demanding for the surveyor, field measurements and greater knowledge.

Test area

A test site was used to investigate the usability of the technologies and to compare their financial performance. The test site selected was city the Radim landfill in the Central Bohemian Region.

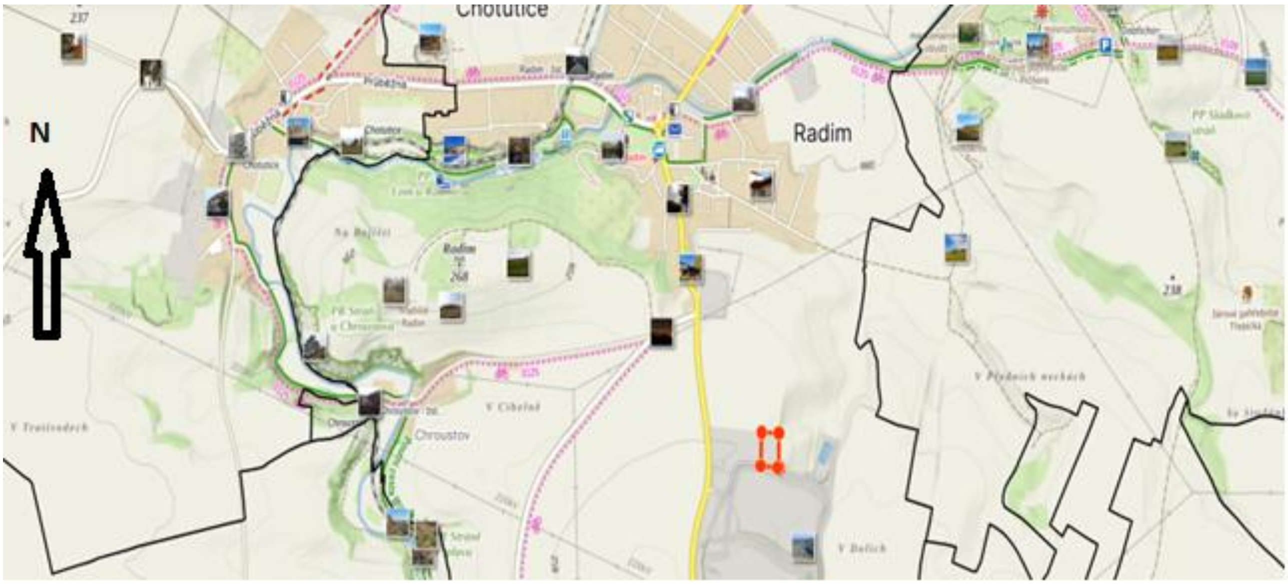

Fig.1 - Map of tested area, Radim, screenshot from https://mapy.cz, [50°03'49.7"N 15°01'01.4"E]

Fig.2 - Preparation by DJI M300, Emlid RS3 base station and 3gon Positioning worker, photo by O.Váňa

Used technology

GNSS

GNSS technology Emlid Reach RS3 was used. It was chosen because it is easier to operate for the general user. Anyone can download the app to their mobile phone. In RTK mode, the technology measures H: 7 mm + 1 ppm and V: 14 mm + 1 ppm. At the same time, it can measure with a tilt angle of maximal 60°, making the worker's job easier by not having to hold the spirit level [20].

Fig.3 - GNSS Emlid RS3, photo by O. Váňa

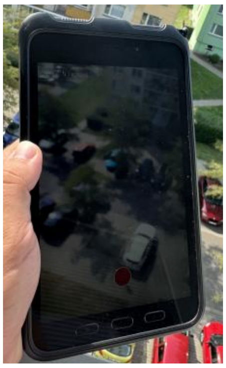

Fig.4 - Samsung Galaxy TAB 3, photo by O. Váňa

UAV - Photogrammetry

Photogrammetry was used twice. From DJI compan, the Zenmuse P1 and Mavic 3 Enterprise sensors were used. The DJI P1 sensor has a pixel size of 4.4 μm, 45MPix, 3-axis stabilization system and an aperture range of f/2.8-f/16. The carrier drone was the DJI Matrice 300 RTK. The DJI P1 was connected to an Emlid base station - for the purpose of collecting correction data [21].

Fig.5 - DJI P1, Heliguy.com

Fig.6 - DJI M3E, DJI.com

Fig.7-DJI L1, Heliguy.com

Mavic 3 Enterprise (M3E) incorporates a 4/3 CMOS sensor with 20MPix and with aperture range f/2.8-f/16. This drone was flown on an RTK correction connection through private provider TopNET [22].

UAV - LiDAR

DJI Zenmuse L1 sensor was used as the technology with LiDAR data collection. As in the case of M3E, it was also subject to corrections from the TopNET provider. The DJI L1 has an accuracy of around 3cm in point position at 100 m, 240,000 points per second, ideally from the altitude 50 m above the ground. It uses an RGB camera to colour the point cloud. Its disadvantage is that it must be computed in DJI's software, namely TERRA. This is not the case for photogrammetry [20].

Videogrammetry

The video record was done with a Samsung Galaxy TAB 3 tablet, which was installed with 3Dsurvey software and Emlid Flow application, which turns the GNSS RS3 into a mock location. The software on the tablet then records the video and telemetry data. The result is then a video with the camera location data at a specific time. Accuracy is determined by the quality of the captured video and the lens in the tablet.

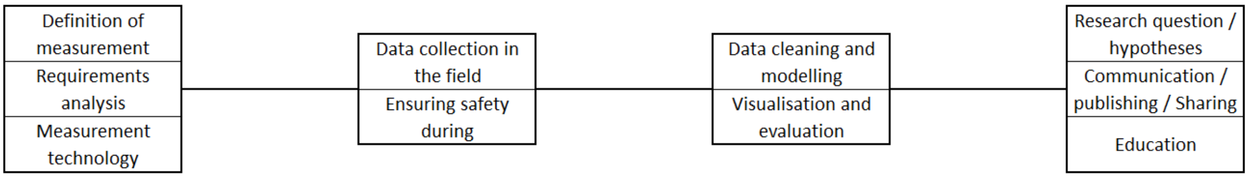

Fig.8 - Processing flow chart

DATA COLLECTION

To ensure accurate volume calculations, multiple geodetic measurement techniques were employed, as detailed in the previous section. A crucial aspect of data collection was the meticulous planning of aerial surveys, optimization of image overlap, and strategic placement of photogrammetric control points.

Planning of Aerial Missions

The aerial missions were carefully designed considering the characteristics of the surveyed area, the required resolution, and the available technological capabilities. For UAV-based

DOI 10.14311/CEJ.2025.01.0009

photogrammetry, an optimal flight altitude of 50 meters was determined to achieve the desired Ground Sampling Distance (GSD). The flight trajectories were structured to ensure uniform coverage of the target area while maintaining adequate image overlap, as detailed below.

Image Acquisition and Resolution

A total of 250 images were captured with UAV DJI M3E, and 184 images with the DJI P1, providing a sufficient density of points for subsequent processing in 3Dsurvey software.

In addition to standard photogrammetry, videogrammetry was employed using a high-frame-rate recording device. Although videogrammetry generally exhibits lower data fidelity compared to conventional snapshot-based photogrammetry, its precision remains adequate for volumetric computations.

Flight time for DJI M3E was 12 minutes, for DJI P1 with Matrice 300 RTK carrier 15 minutes and for L1 LiDAR 14 minutes. Flight altitude was typically 50 metres.

Image Overlap Optimization

To enhance reconstruction accuracy, UAV photogrammetry adopted 80% lateral overlap and 70% longitudinal overlap between images. These parameters were selected based on established theoretical knowledge to maximize data redundancy and ensure precise point triangulation for 3D modelling. It was used by both photogrammetrical systems.

Control Points for Accuracy Enhancement

Control points were systematically distributed across the surveyed terrain, with a higher concentration in regions exhibiting pronounced topographic variations. A total of six GCPs were employed, measured using GNSS technology with a 2–3 cm spatial precision. The measurements were conducted using EMLID GNSS receivers in RTK mode, leveraging internet-based corrections.

Fig.9 - Placement of Ground Control Points, by O. Váňa

Article no. 9

THE CIVIL ENGINEERING JOURNAL 1-2025

RESULTS

Processing of all data was done in 3Dsurvey software. Both photogrammetry and videogrammetry data processing were made and then calculation of terrain model and subsequent calculation of cubature.

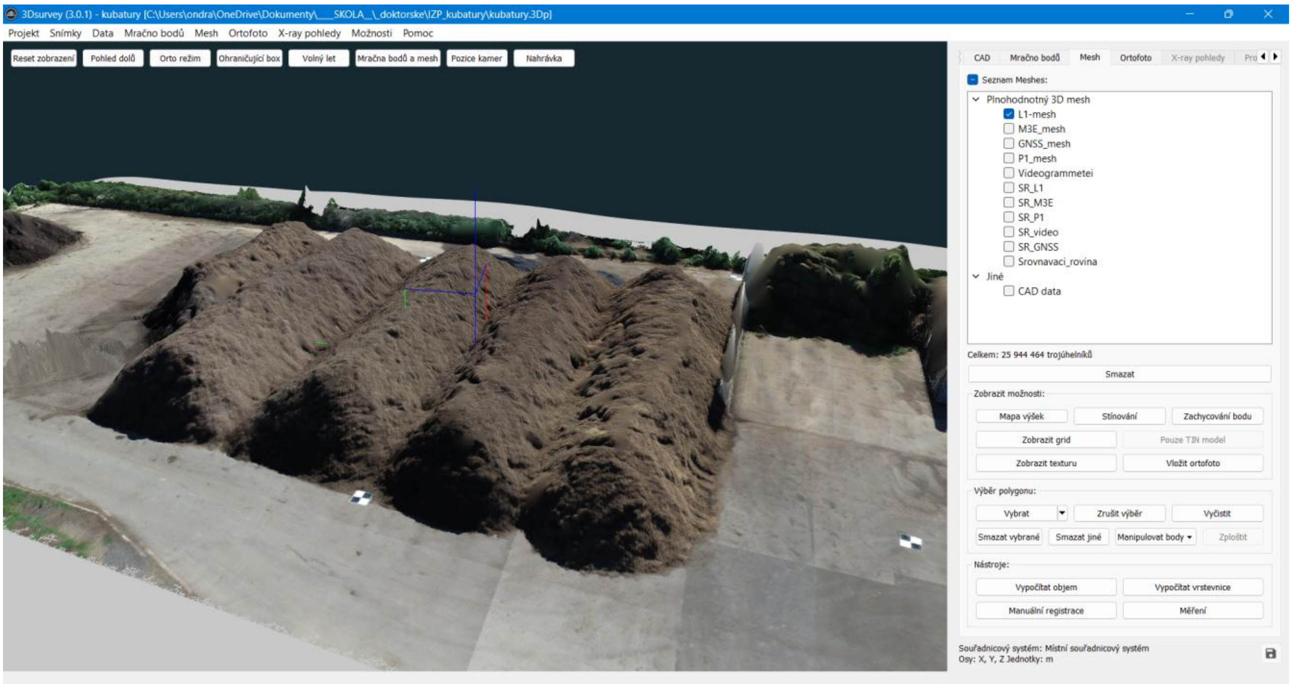

Fig.10 - 3Dsurvey, DJI L1 technologies, DSM reduction model - 25,944,464 triangles, by O. Váňa

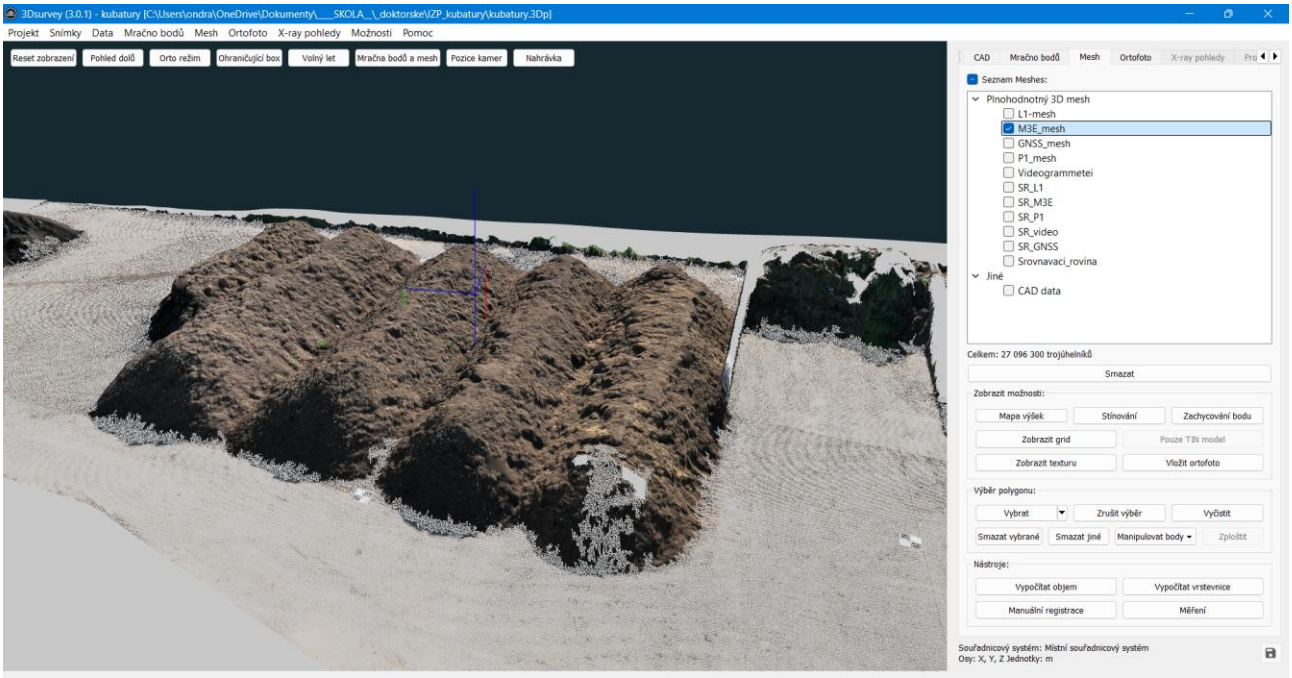

Fig.11 - 3Dsurvey, DJI M3E technologies, DSM reduction model - 27,096,300 triangles, by O. Váňa

CIVIL ENGINEERING JOURNAL

Article no. 9

THE CIVIL ENGINEERING JOURNAL 1-2025

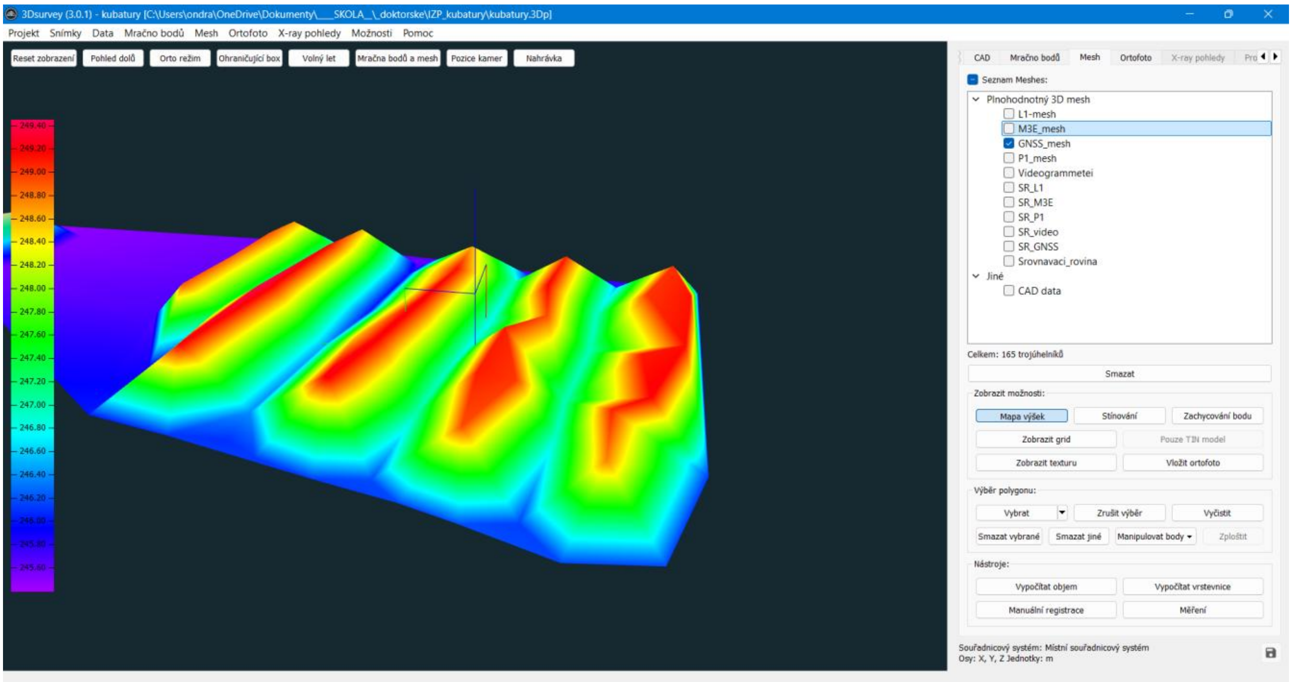

Fig.12 - 3Dsurvey, GNSS technologies, DSM reduction model - 165 triangles, by O. Váňa

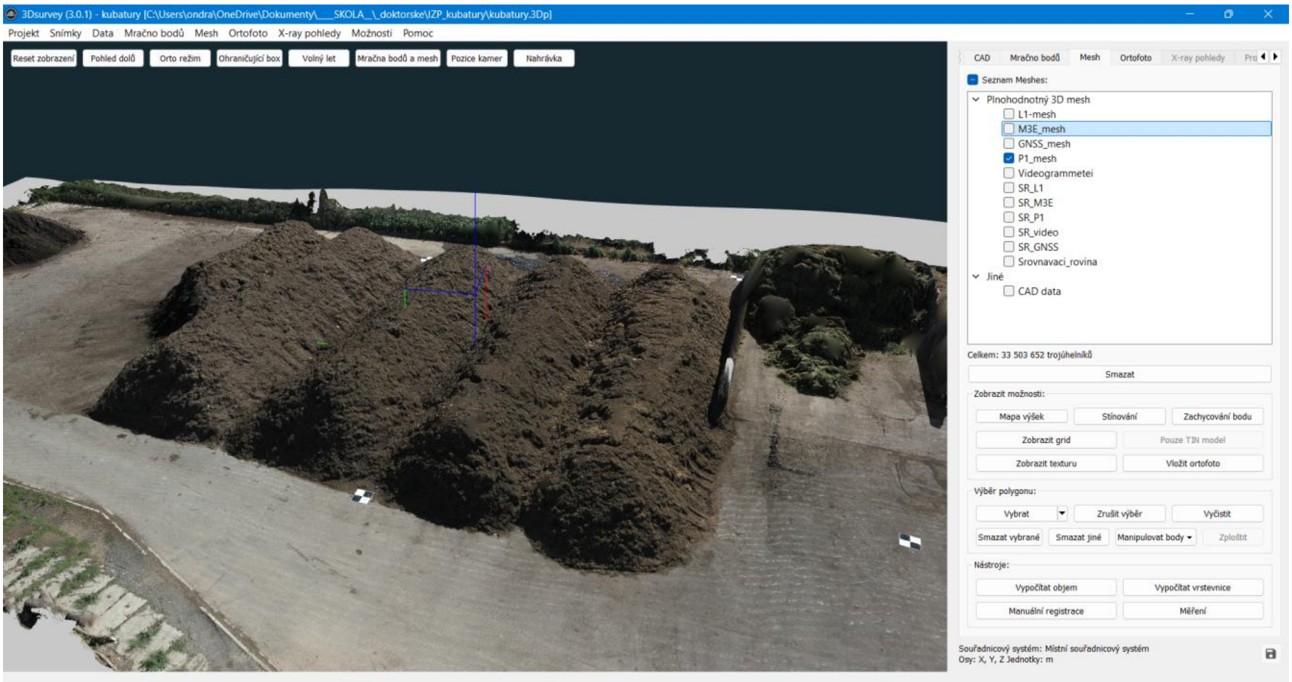

Fig.13 - 3Dsurvey, DJI P1 technologies, DSM reduction model - 33,503,652 triangles, by O.Váňa

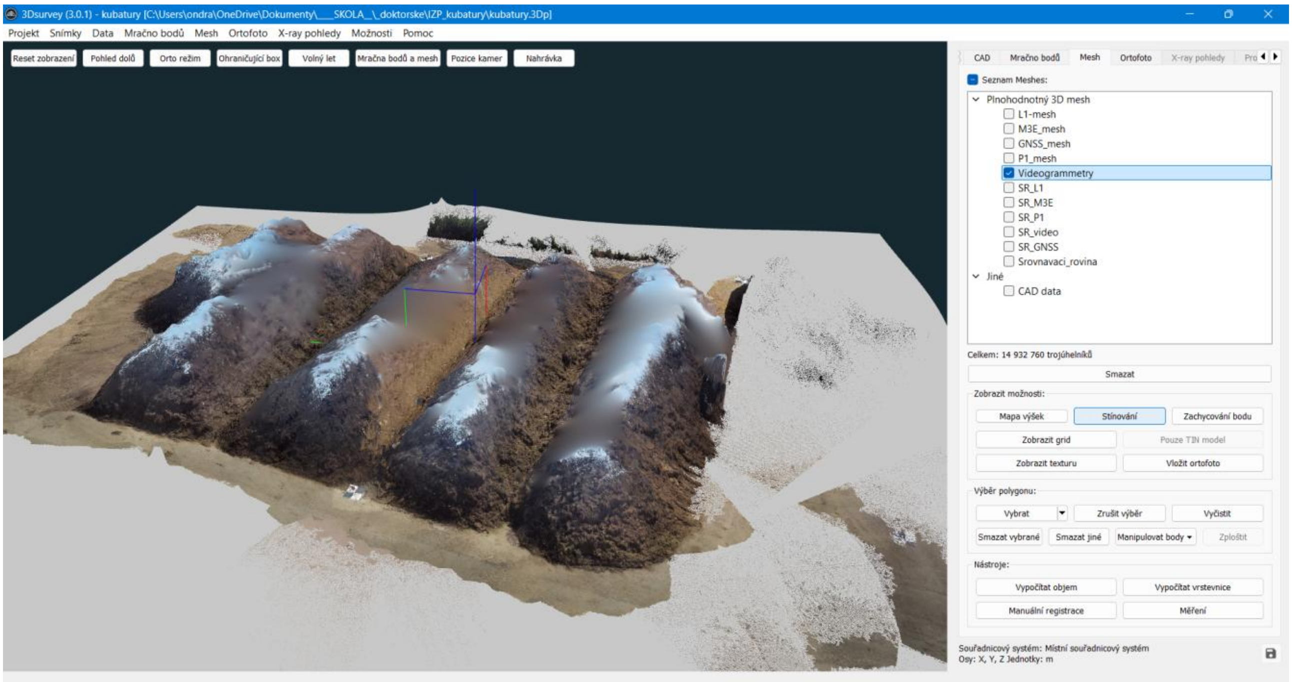

Fig.14 - 3Dsurvey, Videogrammetry technologies, DSM reduction model - 14,932,760 triangles, by O.Váňa

This software is a robust software where photogrammetry, videogrammetry, processed LiDAR data and a list of coordinates from GNSS measurements were calculated. The software can also calculate a terrain model from these measurements so that everything can be compared. All measurement methods were in the Czech Mandatory Coordinate System S-JTSK and altitude Bpv. The main comparison pile was the middle part. The comparison plane here was the height of the concrete surface for each measurement separately and the data taken from the DMR 5G. The first testing was to check the DMR 5G heights against the GNSS Emlid RS3 and M3E measurements, which are sufficient for verification, as the remaining P1, L1 and videogrammetry methods are based on GNSS Emlid RS3 measurements. This testing is very important for the environmental inspectorate, because many times they must look for the original condition before the material was buried and therefore must calculate the change of the original terrain.

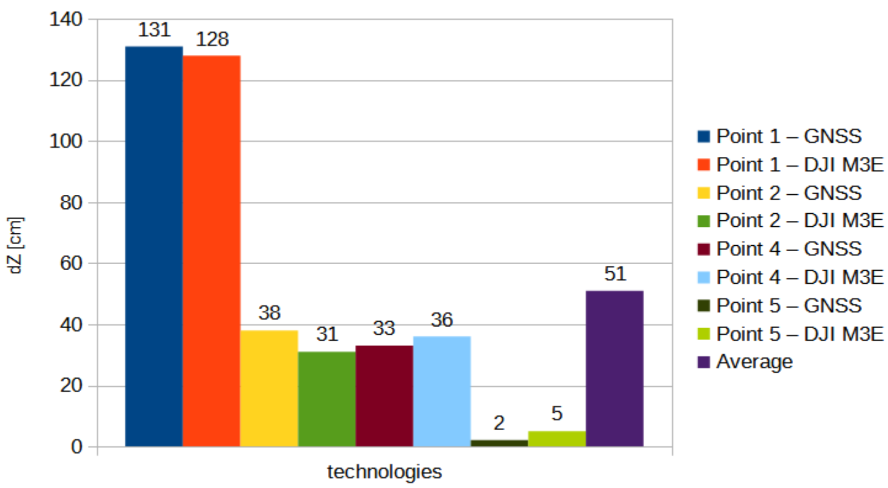

Fig.15– Graph comparing the height of a selected point in the area surrounding the landfill, always using two independent technologies with DMR 5G.

The inspection, which verifies the accuracy of landfill volumes, uses DMR5G as a reference from the time when the landfill did not exist, i.e., the original terrain. For smaller landfills, the accuracy of the original terrain is essential for accurately deriving the landfill volume. In this case, a total of 5 points were surveyed in the area around the landfill using various technologies (see Figure 15) to verify the accuracy and reliability of DMR5G locally. The points were selected at random, and 5 points is not a large number and depends on their selection. Nevertheless, the data show that in this case, the state digital terrain model 5G (DMR) always shows an average vertical error of 51 cm when comparing two independent technologies (ground measurements and aerial measurements), as can be seen in Figure15. This comparison was carried out as an additional independent verification of the data, and the Czech inspection authority relies primarily on this data when imposing any penalties. This means that a certain margin of error must be allowed for small landfills.

According to the Czech Office of Surveying and Cadastre, the reported mean squared error in open countryside is approximately 18 cm, suggesting that elevation accuracy varies significantly depending on the measurement method and environmental conditions. This discrepancy underscores the need for careful calibration and validation of remote sensing data when used for precise geospatial applications [23].

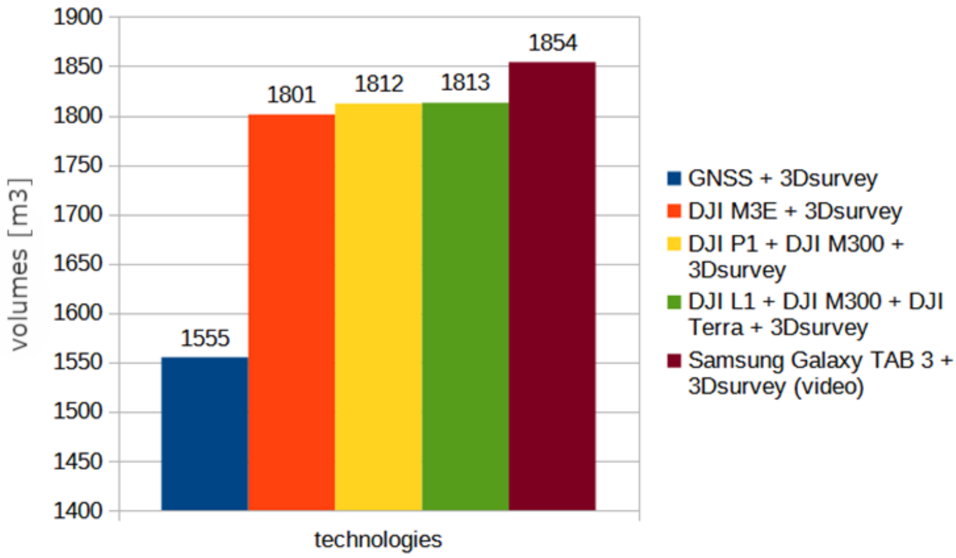

Fig.16 - Comparison of volumes from different technologies

Here it is a very active area, so some surface treatment may have been carried out shortly before the day of the measurement. Another comparison is the results of the volumes calculated by different technologies. The comparison of elevation measurements using GNSS technology and the more precise laser scanning method shows differences in the range of a few centimetres, but for peak measurement points, the deviations can exceed 10 cm. A detailed analysis can be found in the profiles of individual measurement points at the peaks of the surveyed volume (see Figures 17,18).

A key conclusion of this study is that while GNSS technology has certain inaccuracies in determining point positions, especially when tilt-based measurements are used, the primary factor affecting measurement accuracy was not the technology itself but rather the insufficient distribution of measurement points for volume assessment. The author of this study considers the density and placement of points to be the main reason for the observed differences compared to other methods. Moreover, GNSS technology focuses less effectively on volumetric objects than other methods due to its selective nature. Measurement points are chosen directly in the field, which can lead to distortions in the terrain model. For example, when measuring volumetric objects, attention is usually given only to the bottom and top boundaries, which affects data interpretation, as illustrated below.

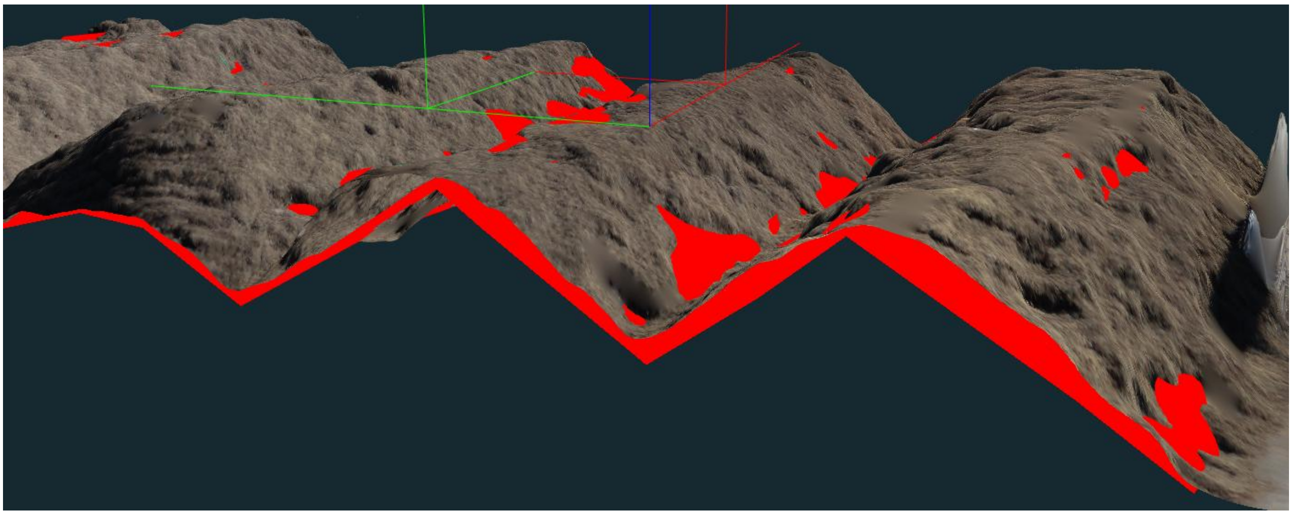

Fig.17-GNSS (red colour) and L1 data comparison, by O. Váňa

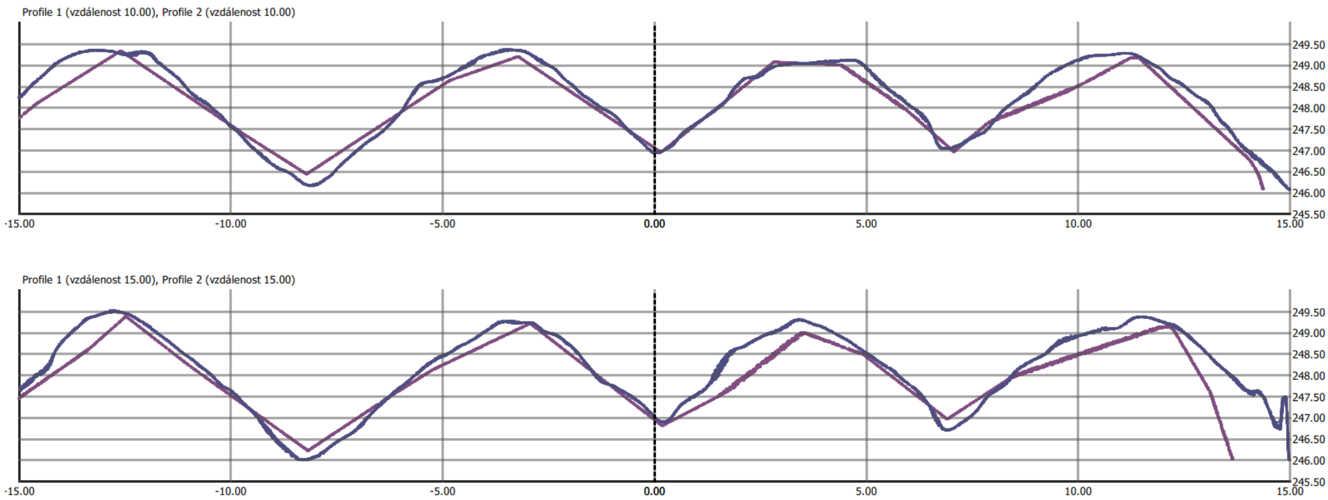

Fig.18 – Cross-sections of the point cloud measured by GNSS (pink colour) and L1 (blue colour) for elevation difference comparison, by O. Váňa

When performing local measurements with GNSS, it is essential to select the points that define the shape of the landfill. If they are selected correctly, the shape and the resulting volume can be used. However, it is not always possible to measure the landfill with such precision.

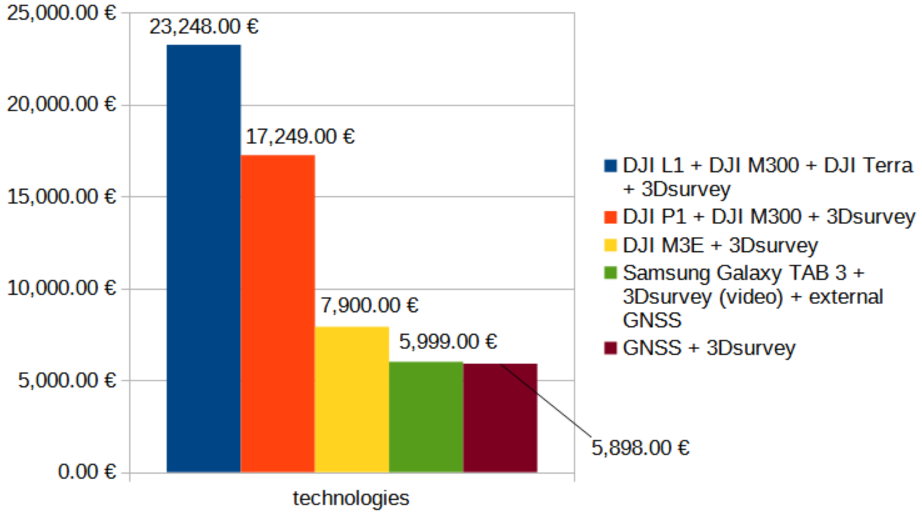

Fig.19 – Comparison of price for used technologies

CONCLUSION

A comparative analysis of GNSS, UAV photogrammetry, UAV laser scanning, and videogrammetry methods was successfully conducted. Additionally, a check measurement was performed to determine if DMR5G could be utilized at this site or if it indicated any terrain alterations. However, the average resulting value of 51 cm suggests that the measured location is an active landfill, which may have been temporarily landscaped on the day of the DMR5G measurement. Despite this, the comparison of the volumes themselves was surprisingly successful.

GNSS measurements stand out significantly. One major drawback of GNSS is the manual data selection. In the field, the surveyor must manually choose measurement points, which can greatly distort the site's perception unless considerable time is spent measuring and selecting points. Despite this, the technology is quite affordable; for instance, the Emlid RS3 is priced at around €3,000 and does not require any additional software to produce outputs in a binding geodetic coordinate system.

Videogrammetry might be the most advantageous method. It is relatively inexpensive as it can be implemented with any Android device paired with an external GNSS receiver, such as the Reach RS3. Although this method yields better results, it still requires manual traversal of the entire measurement area. Additionally, software must be purchased to process the video data.

Drones, such as DJI L1, P1, or M3E, have proven to be highly accurate. However, the main disadvantage is the need for permission to fly over the area. Without permission, other technologies mentioned earlier must be used. The most precise method is likely DJI L1 LiDAR data acquisition, which does not require point cloud calculations based on photographs, unlike the DJI P1 and M3E. However, acquiring the DJI L1 necessitates purchasing a carrier like the Matrice 300/350, DJI Terra for data processing, and software for cubature processing. For the DJI P1, while DJI Terra is not strictly necessary, it still requires additional software for optimal results.

If we have permission to fly in the area and we are looking for the easiest solution for volume mapping without requiring results in the mandatory Czech geodetic system, the most suitable choice including software is the DJI M3E + 3Dsurvey for €7,900. If flying is not an option, the most suitable method is videogrammetry using an Android phone with an external GNSS receiver and 3Dsurvey, totalling €5,999.

A new feature in this field is mapping using LiDAR on iOS Pro and Pro MAX versions, which unfortunately were not available for this measurement. Their advantage lies in the collection of point clouds and, thanks to GNSS, direct output in the binding geodetic system. The future of this study aims to test this technology on a large scale, starting with a comparison of LiDAR data.

ACKNOWLEDGEMENTS

I would like to thank the company 3gon positioning, who provided me with the measurement technology for this article. Furthermore, the representative of the Czech Environmental Inspectorate, who arranged the permit and access to the landfill for measurement purposes. I also thank F. Mužík, who manages university internal grant SGS 2025, SGS25/047/OHK1/1T/11.

REFERENCES

[1] Hauf et al.: Book (in Czech) Geodesy, Terrestrial Photogrammetry, Geodézie – technický průvodce. SNTL – nakladatelství technické literatury, Praha 1982. 544s.

[2] Morita, M. M., Loaiza Carvajal, D. A., González Bagur, I. L., Bilmes, G. M., 2024. A Combined Approach of SFM-MVS Photogrammetry and Reflectance Transformation Imaging to Enhance 3D Reconstructions. J. Cult. Herit. 2024, 68, 38–46. https://doi.org/10.1016/j.culher.2024.05.008.

[3] Pavelka, K.., Matoušková, E. Pavelka, K., Jr., 2023. Remarks on Geomatics Measurement Methods Focused on Forestry Inventory. Sensors 2023, 23, 7376. https://doi.org/10.3390/s23177376

[4] Kovanič, Ľ., Blistan, P., Zelizňaková, V.,Palková, J., 2017. Surveying of Open Pit Mine Using Low-Cost Aerial Photogrammetry. 10.1007/978-3-319-45123-7_9.

[5] Tomljanović, K., Kolar, A.,Đuka, A., Franjević, M., Jurjević,L., Matak, I., Ugarković, D., Balenović, I., 2022. Application of UAS for Monitoring of Forest Ecosystems – A Review of Experience and Knowledge, Croat. j. for. eng. 43(2022)2 487, https://doi.org/10.5552/crojfe.2022.1727

[6] Běloch, L., Pavelka, K., 2024. Optimizing Mobile Laser Scanning Accuracy for Urban Applications: A Comparison by Strategy of Different Measured Ground Points. Appl. Sci. 2024, 14, 3387. https://doi.org/10.3390/app14083387

[7] Štroner, M., Urban, R. Křemen, T. Braun, J., 2023. UAV DTM acquisition in a forested area – comparison of low-cost photogrammetry (DJI Zenmuse P1) and LiDAR solutions (DJI Zenmuse L1). European Journal of Remote Sensing, 56, 2023. https://doi.org/10.1080/22797254.2023.2179942

[8] Oniga, E., Boroianu, B., Morelli, L., Remondino, F., Macovei, M., 2024. Beyond ground control points: cost- effective 3D building reconstruction through GNSS-integrated photogrammetry. The International Archives of the Photogrammetry, Remote Sensing and Spatial Information Sciences, XLVIII-2/W4-2024, 2024, p. 333–339. https://doi.org/10.5194/isprs-archives-XLVIII-2-W4-2024-333-2024

[9] Richter, C., Teichert, B., Pavelka, K. 2021. Astronomical Investigation to Verify the Calendar Theory of the Nasca Lines. Appl. Sci. 2021, 11, 1637. https://doi.org/10.3390/app11041637

[10] Zahradník, D., Vynikal, J., Pavelka, K. 2023. Investigation of Inner Lining Loss and Correlation with Steel Structure Ovality in Rotary Kilns. Appl. Sci. 2023, 13, 12811. https://doi.org/10.3390/app132312811

[11] Lian, Y., Feng, Z., Huai, Y., Lu, H., Chen, S., Li, N. 2021. Terrestrial Videogrammetry for Deriving Key Forest Inventory Data: A Case Study in Plantation. Remote Sens. 2021, 13, 3138. https://doi.org/10.3390/rs13163138

[12] Musicco, A., Rossi, N, Verdoscia, C.,2023. Accuracy evaluation of smartphone-based videogrammetry for cultural heritage documentation process. The International Archives of the Photogrammetry, Remote Sensing and Spatial Information Sciences, XLVIII-M-2–2023, 2023, p. 1119–1126. https://doi.org/10.5194/isprs-archives-XLVIII-M-2-2023-1119-2023

[13] Kersten, T., Wolf, J., Lindstaedt, M., 2022. Investigations into the accuracy of the uav system DJI MATRICE 300 RTK with the sensors ZENMUSE P1 and L1 in the Hamburgtest field. The International Archives of the Photogrammetry Remote Sensing and Spatial Information Sciences XLIII-B1-2022:339-346, 2022. https://doi.org/10.5194/isprs-archives-XLIII-B1-2022-339-2022

[14] Smith, J., Brown, L., Adams, R., 2024. Development and Performance Evaluation of a Very Low-Cost UAV-Lidar System for Forestry Applications. ResearchGate.

[15] Doe, J., Smith, A., Johnson, R., 2024. A Comparative Analysis of Point Clouds Acquired from UAV Photogrammetry and UAV-based LiDAR in Built Environment.

[16] Guo, H., Li, W., Dong, J., Duan, Y. 2024. A method for hierarchical weighted fitting of regular grid DSM with discrete points. ISPRS Annals of the Photogrammetry, Remote Sensing and Spatial Information Sciences, X-1–2024, 2024, p. 91–98.

[17] Dušánek, P. ZABAGED® - Altimetry - DMR 5G. Digital Relief Model of the Czech Republic 5th Generation on S-JTS (in Czech); K, Bpv, www.cuzk.cz (accessed on 25 September 2024).
[18] Young, G., Murphy, R., Smith, M.2010. Investigating how education is shaping the modern Surveyor/Geomatic Engineer. FIG Congress 2010, Facing the Challenges – Building the Capacity, Sydney,Australia, https://www.fig.net/resources/proceedings/fig_proceedings/fig2010/papers/ts08g/ts08g_young_murphy_et_al_4062.pdf
[19] Volume calculation, technical manual from developer 3Dsurvey, (reached on 3.10.2024)
[20] Reach RS3 RTK GNSS Receiver, www.emlid.com, (reached on 1.10.2024)
[21] Zenmuse P1 - Full-frame Aerial Surveying, www.dji.com, (reached on 1.10.2024)
[22] Specs - DJI Mavic 3 Enterprise - DJI Enterprise, www.dji.com, (reached on 2.10.2024)
[23] Brázdil,K., Pressová, J., Šíma, J.2020. Realized refinements of the position of selected objects Basic geographic data base, (in Czech) Realizovaná zpřesnění polohy vybraných objektů Základní báze geografických dat (ZABAGED). GAKO, 2020, 2020/ 8.

CIVIL ENGINEERING JOURNAL

Article no. 10

THE CIVIL ENGINEERING JOURNAL 1-2025

STATIC PERFORMANCE ANALYSIS OF PRESTRESSED Π-TYPE BEAM CABLE-STAYED BRIDGE CABLE DAMAGE

Dandan Hu

School of Civil and Architectural Engineering, Harbin University, No.109 Zhongxing Road, Harbin, Heilongjiang Province, China; Hardandan@163.com

Received: 11.04.2024
Received in revised form: 05.12.2024
Accepted: 17.01.2025

ABSTRACT

With the increasing span of cable-stayed bridges, the self-weight of the structure accounts for a large proportion. The π-type beam, due to its small cross-sectional area, can significantly reduce the self-weight and cost. It is suitable for double-cable surface system cable-stayed bridges and has therefore experienced rapid development. This paper takes a prestressed π-type beam cable-stayed bridge in China as an engineering example, and focuses on the overall and local parameter sensitivity of the structure, as well as the force characteristics under cable damage. The main factors causing cable damage in prestressed π-type beam cable-stayed bridges are analyzed, and the selection of elastic modulus as the damage variable is determined. Based on the finite element model analysis of the actual bridge, different cable damage simulations are selected to analyze the static variations of the main beam and cables caused by single-side, symmetrical, and asymmetrical cable damage, as well as the dynamic variations of the overall bridge. It significantly affects the vertical displacement of the short main span main beam. When the short cable is damaged 100%, the maximum deflection of the main beam can reach up to 5.29 mm. when the medium cable is damaged 100%, the maximum deflection of the main beam can reach up to 17.87 mm. This analysis provides a reference for the mechanical performance analysis of prestressed π-type beam cable-stayed bridges under similar cable damage conditions in the future.

KEYWORDS

Cable-stayed bridge, π-shaped beam, Finite element analysis, Static performance

INTRODUCTION

A cable-stayed bridge is a large-span statically indeterminate structural system composed of towers, beams, and cables. Currently, both domestic and foreign cable-stayed bridges often adopt a cable-dense system [1-3]. Due to the excellent lateral force performance and large flexural rigidity of the closed box section main beam, it is widely used in various forms of cable-stayed bridges. In order to enhance the wind resistance, inclined webs are often used, which also increase the construction difficulty. Due to practical needs and the maturity of construction techniques, the span of cable-stayed bridges continues to increase, resulting in an increasing proportion of the structure's self-weight to the applied load. In response to this, bridge designers have proposed the use of a π-shaped main beam section to reduce the self-weight of the main beam [4-6].

Currently, research on prestressed π-type beam cable-stayed bridges has mainly focused on the optimization of cable forces, both domestically and internationally, while studies on the effects of parameters on the operational stage of prestressed π-type beam cable-stayed bridges are relatively scarce [7]. The overall structural parameters have a significant impact on cable-stayed bridges, where auxiliary piers, located between the bridge piers and towers, play a supportive role in significantly improving the overall stiffness of cable-stayed bridges and reducing the vertical displacement of the main beam [8-11]. Under live loads, the use of auxiliary piers can effectively reduce the internal forces and limit the vertical displacement of the main beam, while also reducing the negative reactions at the auxiliary piers. This makes it more convenient to provide counterweights for short main spans in cable-stayed bridges with π-shaped beam sections, which is advantageous for the overall structure [12]. Additionally, certain local structural parameters also have a significant impact on cable-stayed bridges. As cable-stayed bridges are large-span statically indeterminate structures, factors such as temperature changes cannot be ignored in their performance analysis [13]. Therefore, conducting in-depth research on the effects of overall and local parameter variations on the structural performance of π-type beam cable-stayed bridges is of great importance for their development [14].

As a critical component of the entire system, the stay cables bear the majority of the load acting on the main beam. However, during daily operation, various factors such as sheath damage, wire corrosion, and vibration fatigue can cause damage to the stay cables to varying degrees. The damage to the stay cables leads to a redistribution of cable forces across the entire bridge and can induce varying levels of deflection in the main beam, directly affecting the service life of the bridge [15-16]. Currently, research on cable damage mainly focuses on integral box girder and other main beam forms of cable-stayed bridges, and there is limited research on the effects of cable damage on π-shaped beam cable-stayed bridges. With the continuous improvement of inspection methods, a series of protective measures have been developed for cable damage. However, these measures cannot guarantee the safe operation of cable-stayed bridges entirely. If the impact of cable damage on the structural performance of π-shaped beam cable-stayed bridges can be studied, it can provide theoretical support for daily maintenance projects of π-shaped beam cable-stayed bridges.

ENGINEERING BACKGROUND

The engineering background of this study is a single-tower cable-stayed bridge with pre-stressed π-shaped beams in Jilin Province, China. The total length of the bridge is 617.06 m, and the span combination is 39.9 m+89.1 m+151 m, with the second span being the main bridge section under investigation. The main bridge adopts an "H" shaped single-tower double-plane cable-stayed bridge with precast concrete (PC) beams. The span combination of the main bridge is 39.9 m + 89.1 m + 151 m. The main bridge structure is a fixed system, with a 2.0 % bidirectional cross slope in the transverse direction, and designed for City-Class A loading. The main tower has a total of 18 pairs of spatial cables arranged in a fan shape. The inclined cables are arranged at a distance of 0.8 m from the edge of the main beam. The layout of the pre-stressed π-shaped beam cable-stayed bridge is shown in Figure 1.

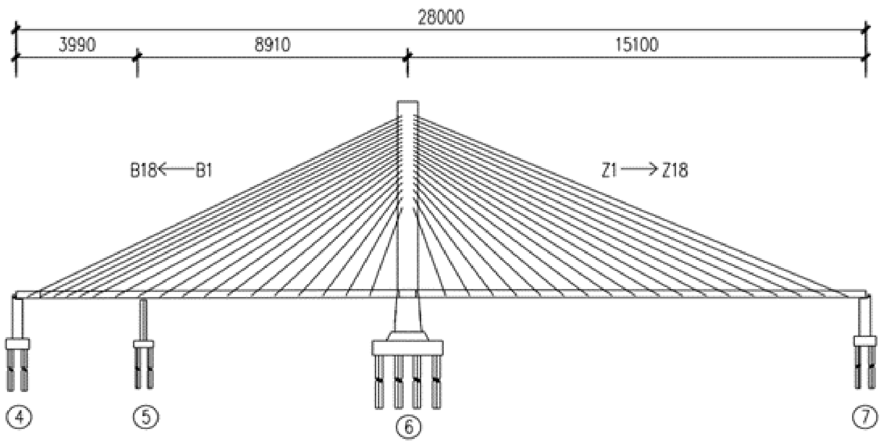

Fig. 1 – Layout diagram of the main bridge

(1) Main beam structure

The main beam adopts a pre-stressed concrete "π" shaped cross-section. The width of the main beam section is 26.5 m, and the height is 2.3 m. It is designed with a bidirectional 2% cross slope. The basic spacing of the transverse beams is 3.9 m, 3.65 m, and 4.25 m. The transverse beams are all equipped with pre-stressed steel hinge lines. The main beam is connected to the main tower using a fixed system, and both the main beam and the transverse beams are made of C55 concrete.

(2) Main tower

The main tower of the cable-stayed bridge adopts an H-shaped main tower. The height of the main tower is 117.318 m. The cross-section of the tower column is a hollow rectangular shape, with a full width of 6.8 m in the middle and upper tower columns longitudinally, and a width of 4.0 m in the transverse bridge direction. The upper part of the lower tower column gradually increases from a width of 6.8 m to a full width of 8.8 m longitudinally, and the width in the transverse bridge direction gradually increases to 7.5 m.

The cross-section of the transverse beam is a hollow rectangular shape. The upper transverse beam has a rectangular cross-section of 6.2 m × 4 m, while the lower transverse beam has a width of 6.4 m and a height ranging from 6 m to 6.27 m. A tower pedestal with a height of 3 m is provided at the top of the main tower's bearing platform. Except for the lower transverse beam, which is made of C55 concrete, the rest of the main tower structures are made of C50 concrete.

(3) Stay cable

The main tower is equipped with a total of 72 stay cables, with each cable spaced at a designed interval of 7.8 m. The cable spacing changes to 7.8 m, 7.3 m, and 4.25 m corresponding to the length variations of the main span's cast-in-place segments. The stay cables are positioned 0.8 m away from the edge of the main beam cross-section. The stay cables are all made of Φ s 15.2 steel strand with a standard strength of 1860 MPa. The stay cable numbering is shown in Figure 1.

FINITE ELEMENT ANALYSIS MODEL

The finite element model of this prestressed π-type girder cable-stayed bridge is established and analyzed using the specialized bridge analysis software, Midas Civil. The main beam and main tower are simulated using 2D beam elements, with section dimensions set to match the actual conditions. The overall finite element model of the prestressed π-type girder cable-stayed bridge consists of 483 nodes and 399 elements, with 327 beam elements, including 235 main beam elements and 92 main tower elements. There are 72 truss (stay cable) elements that only experience tension. The complete bridge finite element model is shown in Figure 2.

The main beam and main tower are simulated in the cable-stayed bridge using the shared node approach to model the fixed support system. The auxiliary piers and main beam are rigidly connected, and the connection between the stay cable anchorage points, main beam, and main tower is simulated using rigid connections as well. The transverse beams on the main beam and main tower are made of C55 concrete. The lower transverse beam of the main tower, upper tower columns, middle tower columns, lower tower columns, and tower base are made of C50 concrete. The 5# auxiliary pier is made of C40 concrete.

Both longitudinal and transverse prestressing tendons are made of high-strength low-relaxation prestressing strand with a single strand diameter of Φ s 15.2 mm. The standard strength of the strand is 1860 MPa, with an elastic modulus of 1.95×10^5 MPa, and a cross-sectional area of 140 mm^2.

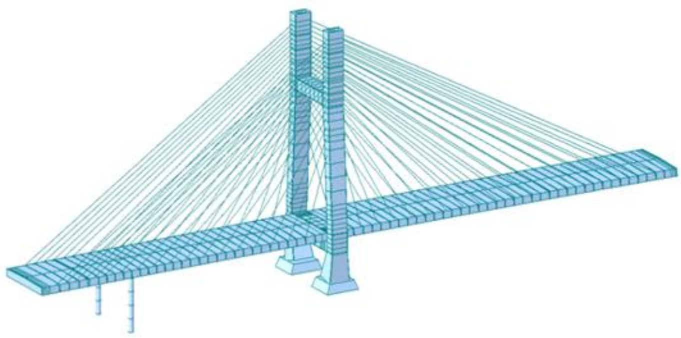

Fig. 2 – The finite element model of the main bridge

STATIC PERFORMANCE ANALYSIS OF THE PRESTRESSED Π-TYPE GIRDER CABLE-STAYED BRIDGE UNDER IDENTICAL DAMAGE CONDITIONS OF STAY CABLES

In order to analyze the influence of stay cable damage on the static performance of the structure, the most deviated stay cable at the furthest point from the main tower is selected from the long, medium, and short cables as a representative stay cable for damage simulation and analysis.

Analysis of the Influence of Static Performance under the Same Level of Damage for Single-side Stay Cables

This section primarily focuses on the analysis of the influence of single-side stay cable damage at the same level of 60% on the static characteristics of the prestressed π-type girder cable-stayed bridge. The load combinations are shown in Table 1.

Tab. 1 - Damage load combination table

Operating conditions	Cable damage	Cable identification
Operating conditions 1	Secondary span and short main span cable damage	B6
Operating conditions 2	Secondary span and short main span mid-cable damage	B12
Operating conditions 3	Secondary span and short main span long-cable damage	B18
Operating conditions 4	Long main span short-cable damage	Z6
Operating conditions 5	Long main span mid-cable damage	Z12
Operating conditions 6	Long main span long-cable damage	Z18

Using the Midas Civil software, the six working conditions mentioned above can be simulated by changing the elastic modulus of the inclined cables. The analysis will provide the internal force variation of each cable and the vertical displacement variation of the main beam under each working condition, as shown in Figure 3 and Figure 4. The maximum displacement variation values can be found in Table 2. In the cable force variation graph, negative values represent the inclined cable condition without any damage.

In comparison with the cable forces, for this working condition, the cable force of the inclined cable is reduced. A positive value represents the internal force of the inclined cable in comparison with the undamaged cable condition, and for this working condition, the cable forces of the inclined cable are increased. In the vertical displacement variation graph of the main beam, a positive value indicates that the point on the main beam moves upward after cable damage, while a negative value indicates that the point moves downward compared to the situation before cable damage.

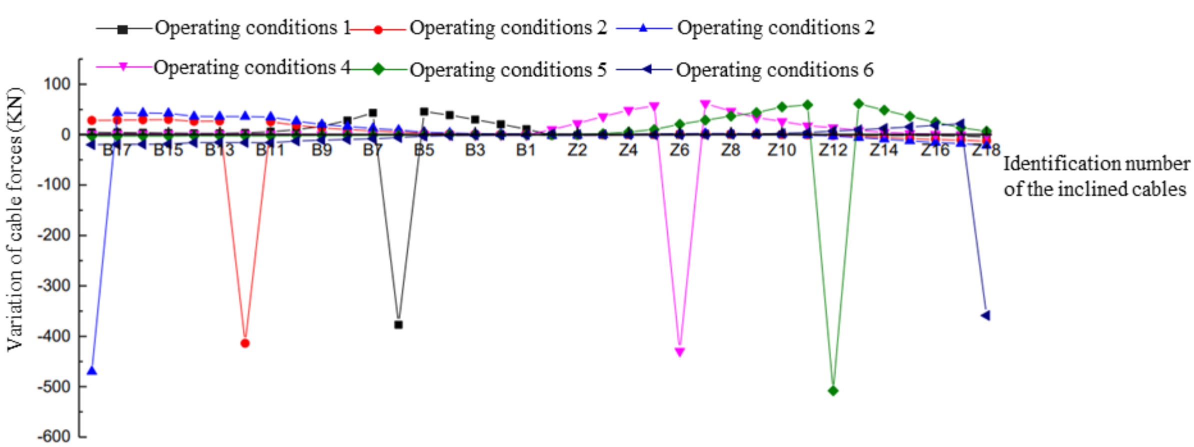

Fig. 3 – Graph of cable force variation for damaged inclined cables

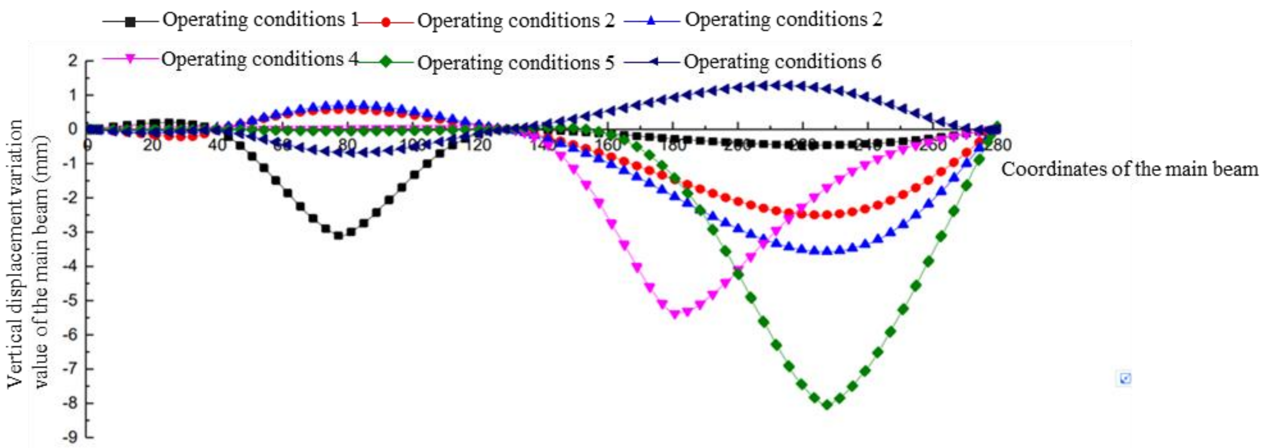

Fig. 4 – Graph of vertical displacement variation of the main beam with damaged inclined cables

From Figure 3, it can be observed that for 60% damage to the inclined cables on auxiliary and short main spans, the decrease in cable force variation value around the damaged cable decreases gradually with increasing distance. However, in the case of damage to the short and medium cables, the aforementioned decrease trend is more prominent, indicating that the excessive tensile force after damage to the long cable is not evenly distributed to the surrounding inclined cables. In the case of 60% damage to the inclined cable on the long main span, the damage to the long cable has minimal impact on other inclined cables, and the excessive tensile force after damage is distributed to the surrounding inclined cables to a similar extent when damage occurs to the short and medium cables.

Overall, the damage to the inclined cables has limited impact on the surrounding cables, with only a significant effect on approximately 24 nearby cables. The influence on distant cables is relatively small. When the inclined cables are damaged, there is a change in cable force for the damaged cables.

The decrease in value is most pronounced, and the cable forces on both sides of the damaged inclined cables will increase to varying degrees. The magnitude of the increase in cable force will gradually decrease with increasing distance from the damaged inclined cables, but there will be a certain degree of decrease in the cable forces on the opposite side inclined cables.

From Figure 4 and Table 2, it can be concluded that for the auxiliary span, the impact on the vertical displacement can be considered negligible due to its small span and the occurrence of cable damage throughout the bridge. For the short main span, there is only a noticeable deflection in scenarios 1 and 6 compared to the undamaged condition, with a maximum deflection of 3.11 mm observed in scenario 1. However, in scenarios 5 and 6, an upward deflection is observed at various points compared to the undamaged condition, with a similar level of impact on the short main span in both scenarios. For the long main span, scenario 5 shows a significant impact on the vertical displacement, with a peak value of up to 8.05 mm.

Generally speaking, the closer the damaged inclined cable is to the location of maximum bending moment on the main beam, the greater the impact on the vertical displacement of the main span.

Tab. 2 - Table of maximum displacement changes

Operating conditions	Operating conditions 1	Operating conditions 2	Operating conditions 3	Operating conditions 4	Operating conditions 5	Operating conditions 6
Maximum positive displacement (mm)	0.2	0.58	0.7	0.03	0.11	1.28
Maximum negative displacement (mm)	3.11	2.5	3.57	5.38	8.05	0.68

Analysis of the Influence of Symmetric Inclined Cables with the Same Level of Damage on Static Performance

The main study focuses on the analysis of the influence of symmetric inclined cables with the same level of damage (60%) on the static characteristics of prestressed π-type girder cable-stayed bridges. The combination of working conditions is shown in Table 3.

Tab. 3 - Table of damage condition combinations

Operating conditions	Cable damage combinations	Slant cable numbering
Operating conditions 7	Damage to four short cables on the left and right sides of the main tower	B6+ Z6
Operating conditions 8	Damage to four intermediate cables on the left and right sides of the main tower	B12+ Z12
Operating conditions 9	Damage to four long cables on the left and right sides of the main tower	B18+ Z18

Using the Midas Civil software, the three scenarios mentioned above were simulated for cable damage by modifying the elastic modulus of the slant cables. The analysis results include the variation of internal forces in each cable and the vertical displacement of the main beam as shown in Figure 5 and Figure 6. The maximum displacement variations are listed in Table 4. In the cable force variation graphs, negative values represent a decrease in cable force compared to the intact condition of the cables, indicating a decrease in cable force for that scenario. Positive values represent an increase in cable force compared to the intact condition of the cables, indicating an increase in cable force for that scenario. In the vertical displacement variation graph of the main beam, positive values indicate an upward movement of the corresponding point of the main beam after cable damage, while negative values indicate a downward movement compared to the pre-damage condition of the cable.

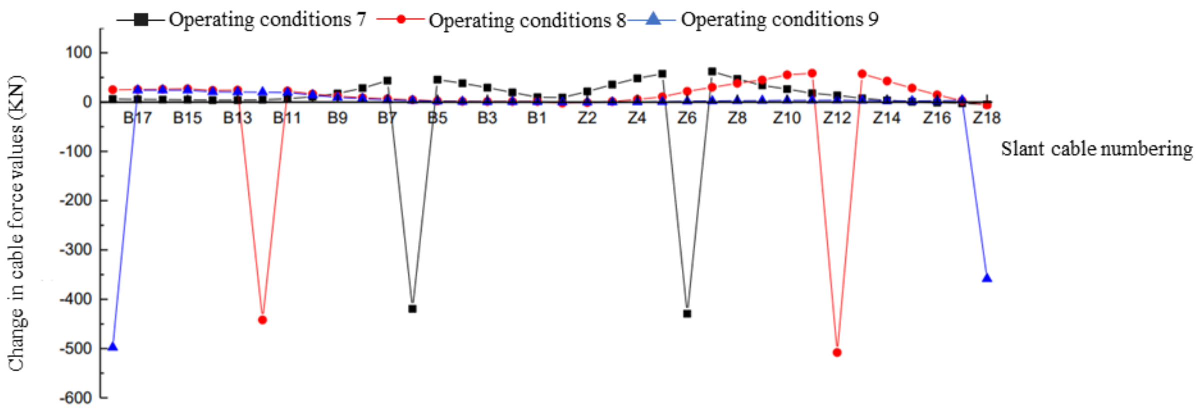

Fig. 5 – Symmetric cable force variation diagram for damaged inclined cables

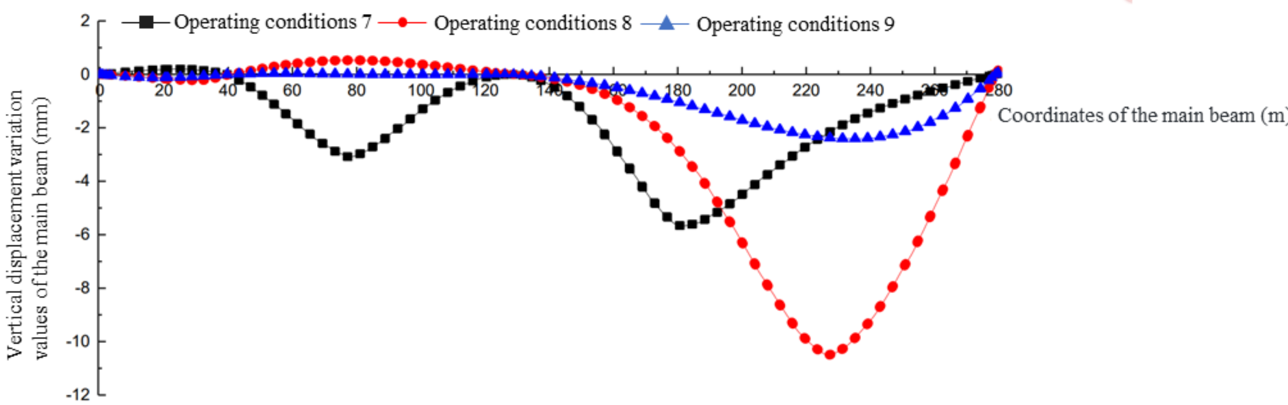

Fig. 6 – Symmetric inclined cable damaged main beam vertical displacement variation diagram

According to Figure 5, it can be concluded that the largest variation in cable force occurs when damage is present in the diagonal cables of auxiliary spans and short main spans, with a decrease of 497 kN and a variation range of 6.87%. Similarly, for the diagonal cables in long main spans, the cable force variation is most significant, with a decrease of 508 kN and a variation range of 12.9%.

According to Figure 6 and Table 4, it can be concluded that for the auxiliary spans, the influence of symmetric cable damage on the vertical displacement of the main beam can be negligible. For the short main spans, the vertical displacement is most significantly affected by symmetric short cable damage, with a maximum variation range of 3.08 mm. Similarly, for the long main spans, the symmetric middle cable damage has the most significant impact, with a maximum variation range of 10.50 mm. Moreover, the peak variation in displacement is close to the location of the damaged cable in the long main span.

Tab. 4 - Damage load combination table

Operating conditions	Maximum positive displacement (mm)	Maximum negative displacement (mm)
Operating conditions 7	0.20	5.66
Operating conditions 8	0.53	10.50
Operating conditions 9	0.07	2.41

Analysis of the Influence of Static Performance under the Same Degree of Damage for Asymmetrical Inclined Cables

The main study focuses on the analysis of the effects of asymmetric inclined cables with pre-stressed π-type beam cable-stayed bridge on the static characteristics of the cable-stayed bridge under the same damage level of 60%. The combinations of damage conditions are listed in Table 5.

Tab. 5 - Combination of damage conditions

Operating conditions	Cable damage	Diagonal cable number
Operating conditions 10	Damage to the left short cable and right middle cable on the main tower	B6+ Z12
Operating conditions 11	Damage to the short cable on the left side and the long cable on the right side of the main tower	B6+ Z18
Operating conditions 12	Damage to the middle cable on the left side and the short cable on the right side of the main tower	B12+ Z6
Operating conditions 13	Damage to the middle cable on the left side and the long cable on the right side of the main tower	B12+ Z18
Operating conditions 14	Damage to the long cable on the left side and the short cable on the right side of the main tower	B18+ Z6
Operating conditions 15	Damage to the long cable on the left side and the middle cable on the right side of the main tower	B18+ Z1

Using the Midas Civil software, the damage simulation of the 6 working conditions through changing the elastic modulus of the inclined cables is conducted. The variations in cable forces and vertical displacements of the main beam under each working condition are shown in Figure 8 and Figure 8. The maximum displacement change values are listed in Table 6. In the cable force variation graph, negative values indicate a decrease in cable force compared to the intact condition, while positive values indicate an increase in cable force. In the vertical displacement variation graph of the main beam, positive values indicate an upward movement of the point after cable damage, while negative values indicate a downward movement compared to the pre-damage state.

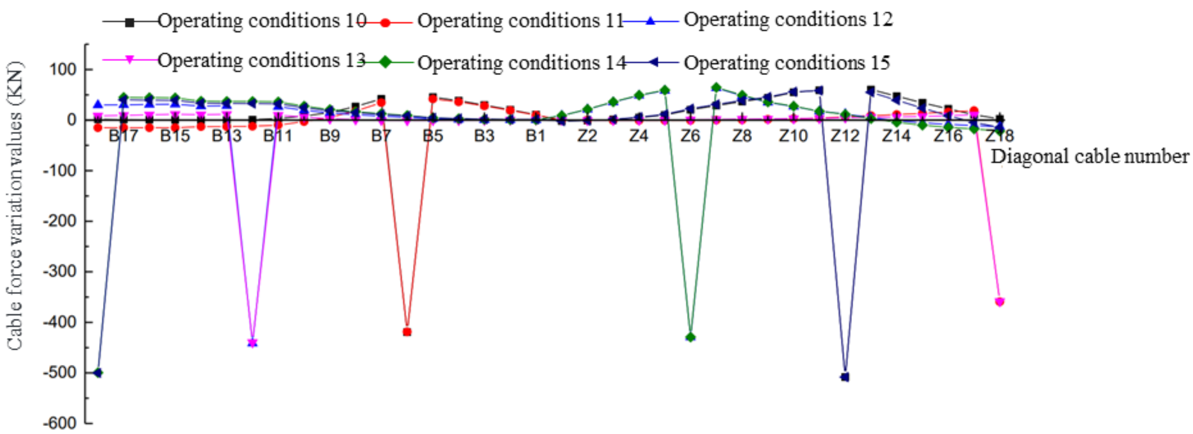

Fig. 7 – Asymmetric inclined cable damage cable force variation graph

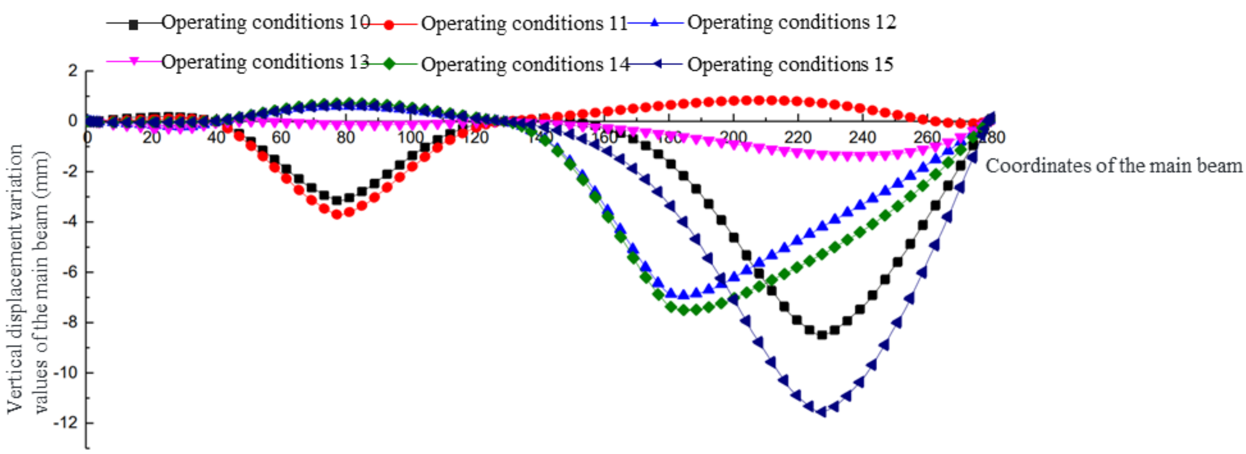

Fig. 8 – Graph showing the variation of vertical displacement of the main beam due to asymmetric inclined cable damage

From Figure 7, it can be concluded that when asymmetric damage occurs in the inclined cables of the entire bridge, the increase in cable force will not be affected by the damage to the cables on the other side of the main tower. It is essentially equivalent to a combination of cable force increment values under the condition of damage to a single side of the cables.

From Figure 8 and Table 6, it can be concluded that for the auxiliary span, regardless of the combination of asymmetric damage in the bridge cables, the impact on its main beam vertical displacement can be negligible. However, for the short main span, load case 11 has the most significant influence on its main beam vertical displacement, with a variation value of 3.71 mm. Similarly, for the long main span, load case 15 has the most significant influence on its main beam vertical displacement, with a variation value of 11.55 mm.

STATIC PERFORMANCE ANALYSIS OF PRESTRESSED Π-SHAPED BEAM CABLE-STAYED BRIDGES UNDER DIFFERENT STAY CABLE DAMAGE CONDITIONS

Considering the selection of stay cables corresponding to load cases 7, 8, and 9, the impact of different levels of symmetric stay cable damage on cable-stayed bridges is studied. The damage levels of the stay cables are set at 20%, 40%, 60%, 80%, and 100%, respectively, and compared with the intact condition for comparative analysis. The load case numbers corresponding to the damage levels are indicated in Table 6.

Tab. 6 - Damage condition combination table

Operating conditions	Stay Cable Damage Combination	Stay Cable Identification Number
Operating conditions 16	Symmetrical Short Cable Damage 20%	B6+ Z6
Operating conditions 17	Symmetrical Short Cable Damage 40%	B6+ Z6
Operating conditions 18	Symmetrical Short Cable Damage 60%	B6+ Z6
Operating conditions 19	Symmetrical Short Cable Damage 80%	B6+ Z6
Operating conditions 20	Symmetrical Short Cable Damage 100%	B6+ Z6
Operating conditions 21	Symmetrical Middle Cable Damage 20%	B12+ Z12
Operating conditions 22	Symmetrical Middle Cable Damage 40%	B12+ Z12
Operating conditions 23	Symmetrical Middle Cable Damage 60%	B12+ Z12
Operating conditions 24	Symmetrical Middle Cable Damage 80%	B12+ Z12
Operating conditions 25	Symmetrical Middle Cable Damage 100%	B12+ Z12
Operating conditions 26	Symmetrical Long Cable Damage 20%	B18+ Z18
Operating conditions 27	Symmetrical Long Cable Damage 40%	B18+ Z18
Operating conditions 28	Symmetrical Long Cable Damage 60%	B18+ Z18
Operating conditions 29	Symmetrical Long Cable Damage 80%	B18+ Z18
Operating conditions 30	Symmetrical Long Cable Damage 100%	B18+ Z18

Using the Midas Civil software, a simulation of stay cable damage was conducted for the aforementioned 15 load cases by varying the elastic modulus of the stay cables. The analysis provides the variation of internal forces in each cable and the vertical displacement of the main beam for each load case, as shown in Figure 9 - Figure 14. In the cable force variation plot, negative values indicate a decrease in cable force compared to the undamaged condition, while positive values indicate an increase in cable force compared to the undamaged condition. In the main beam vertical displacement plot, positive values represent an upward movement of the main beam at that point after cable damage, while negative values represent a downward movement compared to the pre-damage condition of the cables.

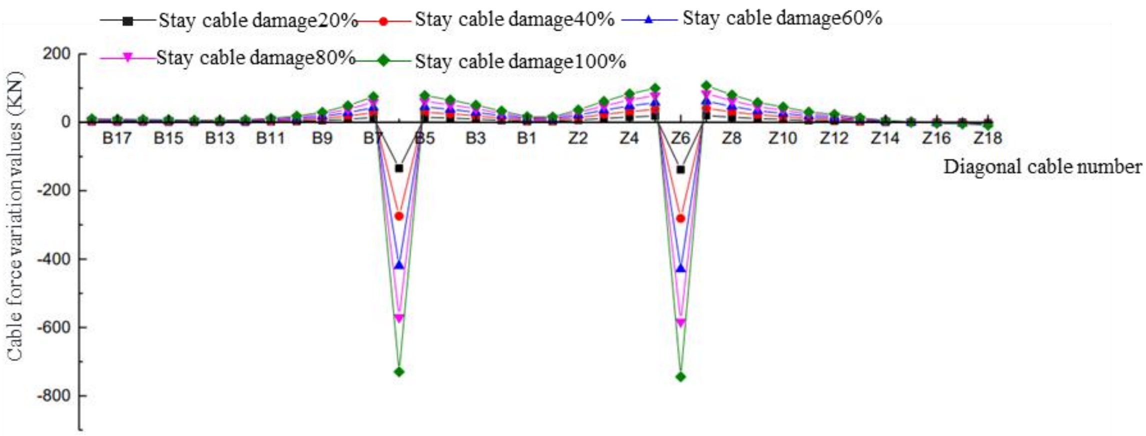

Fig. 9 – Symmetrical short cable damage - cable force variation plot

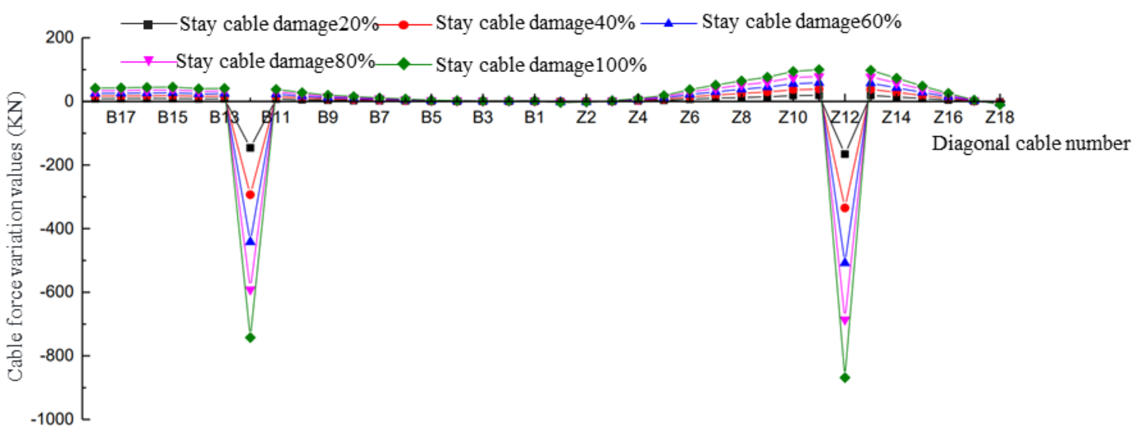

Fig. 10 – Symmetrical medium cable damage - cable force variation plot

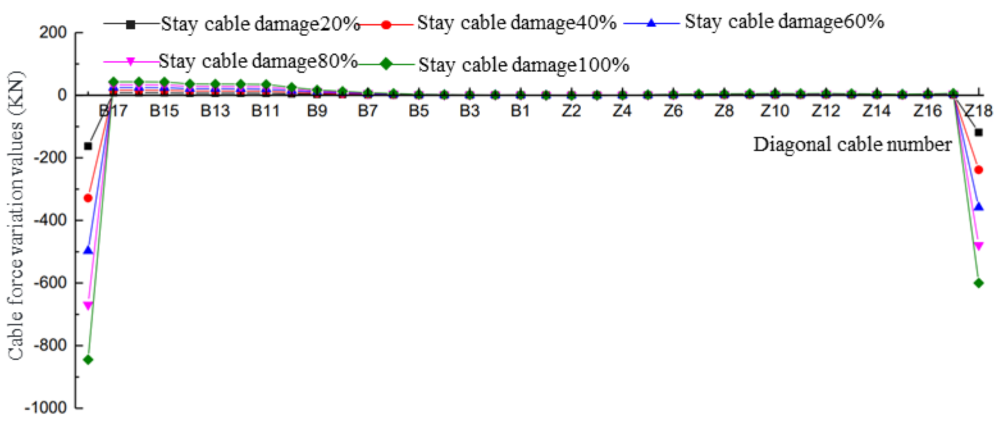

Fig. 11 – Symmetrical long cable damage - cable force variation plot

From Figure 10 - Figure 12, it can be concluded that as the degree of damage to the same cable location increases, the reduction in internal force of the damaged cable becomes more significant. At the same time, the different levels of damage to the cables have a similar trend in redistributing the internal forces of the π-type cable-stayed bridge. Cables closer to the damaged cable experience larger changes in internal forces, whereas cables farther away from the damaged cable generally do not exhibit significant changes.

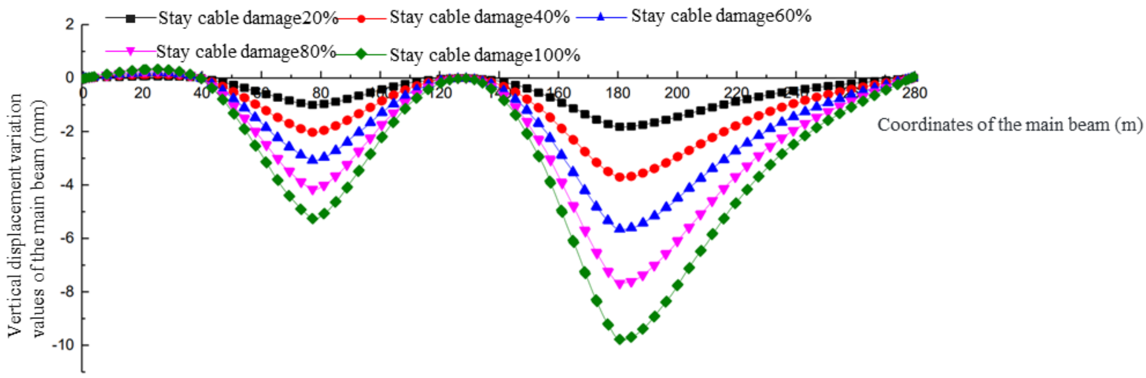

Fig. 12 – Symmetrical short cable damage - vertical displacement variation plot of the main beam

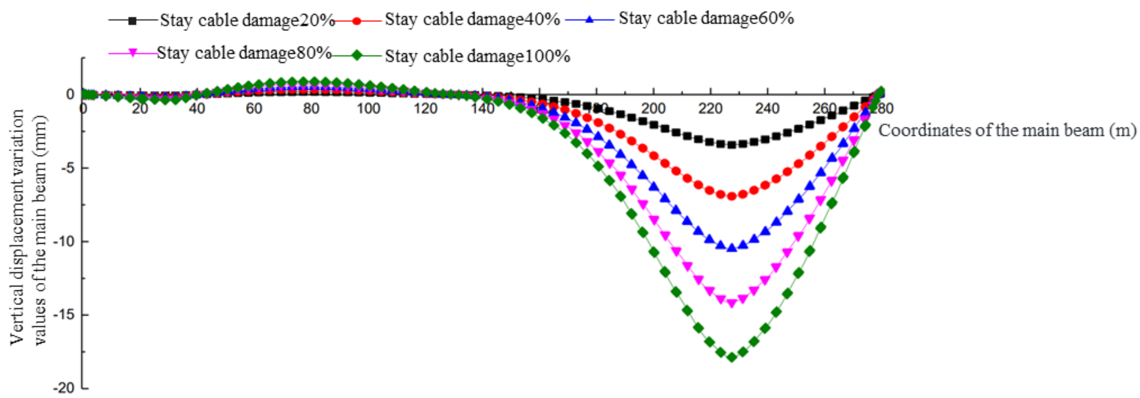

Fig. 13 – Symmetrical medium cable damage - vertical displacement variation plot of the main beam

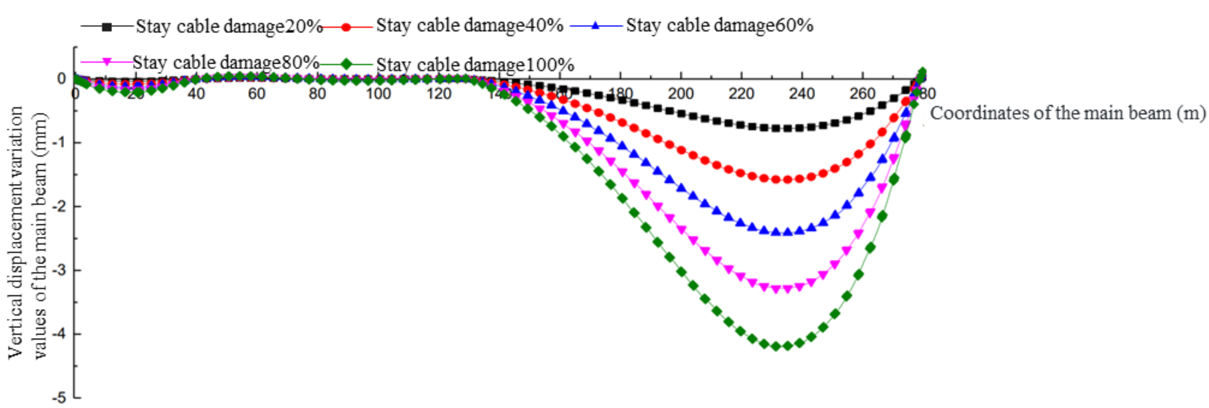

Fig. 14 – Symmetrical long cable damage - vertical displacement variation plot of the main beam

DOI 10.14311/CEJ.2025.01.0010

Based on Figure 12 - Figure 14, it can be observed that for symmetrical cable damage at any level, it has minimal impact on the vertical displacement of the auxiliary span main beam. However, in the case of symmetrical short cable damage, it significantly affects the vertical displacement of the short main span main beam. When the short cable is damaged 100%, the maximum deflection of the main beam can reach up to 5.29 mm. Symmetrical cable damage leads to deflections at various points along the long main span main beam, especially when the medium cable is damaged 100%, the maximum deflection of the main beam can reach up to 17.87 mm. In general, for damage to the same cable location, the greater the extent of cable damage, the greater the impact on the vertical displacement of the main beam. However, the trend of vertical displacement remains the same. The maximum deformation of the main beam occurs at the location of the damaged cable. The vertical displacement of the main beam is greater closer to the damaged cable and smaller farther away from it.

CONCLUSION

This paper takes a prestressed π-type beam cable-stayed bridge in China as an engineering example, and focuses on the overall and local parameter sensitivity of the structure, as well as the force characteristics under cable damage. The main factors causing cable damage in prestressed π-type beam cable-stayed bridges are analyzed, and the selection of elastic modulus as the damage variable is determined. Conclusions are as follows:

(1) After damage occurs to symmetric or asymmetric cable-stays, the peak impact on cable forces is observed at the location of the damaged cable itself. The force value of the damaged cable decreases significantly, while the surrounding cable forces increase and exhibit a decreasing trend towards both sides. However, when damage occurs to a single-side cable-stay, the cable force on the other side of the main tower may decrease to some extent, but the level of impact can be considered negligible.

(2) For the same level of damage, the trend and extent of the influence on cable forces for symmetric cable-stays and single-side cable-stays are generally similar. It significantly affects the vertical displacement of the short main span main beam. When the short cable is damaged 100%, the maximum deflection of the main beam can reach up to 5.29 mm. when the medium cable is damaged 100%, the maximum deflection of the main beam can reach up to 17.87 mm.

(3) Due to the presence of the auxiliary pier, whether symmetric or asymmetric cable damage occurs, the impact on the linearity of the main span girder is much greater than the impact on the linearity of the auxiliary span and short main span. When damage occurs to the long cables of the auxiliary span, short main span, or the medium cable of the main span, it has the most adverse effect on the vertical displacement of the main beam and requires careful observation during the operation of the bridge. The closer the damaged cable is to the mid-span of the respective span, the greater its influence on the vertical displacement of that span. Within the elastic working range, different levels of damage.

REFERENCES

[1] Bai H, Li R, Xu G, et al. Aerodynamic performance of Π-shaped composite deck cable-stayed bridges including VIV mitigation measures[J]. Journal of Wind Engineering and Industrial Aerodynamics, 2021, 208: 104451.

[2] Zhang K, Li D, Xue X. Process monitoring and terminal verification of π–section girder cable-stayed bridge[J]. International Journal of Building Pathology and Adaptation, 2023.

[3] Mandić R, Hadži-Niković G, Ćosić S. Investigation of the behavior of the cable-stayed bridge under test load[J]. Geofizika, 2011, 28(1): 145-160.
[4] Cho S, Yim J, Shin S W, et al. Comparative field study of cable tension measurement for a cable-stayed bridge[J]. Journal of Bridge Engineering, 2013, 18(8): 748-757.
[5] Soneji B B, Jangid R S. Influence of soil–structure interaction on the response of seismically isolated cable-stayed bridge[J]. Soil Dynamics and Earthquake Engineering, 2008, 28(4): 245-257.
[6] El Ouni M H, Kahla N B, Preumont A. Numerical and experimental dynamic analysis and control of a cable stayed bridge under parametric excitation[J]. Engineering Structures, 2012, 45: 244-256.
[7] Wen J, Han Q, Xie Y, et al. Performance-based seismic design and optimization of damper devices for cable-stayed bridge[J]. Engineering Structures, 2021, 237: 112043.
[8] Li C, Li H N, Hao H, et al. Seismic fragility analyses of sea-crossing cable-stayed bridges subjected to multi-support ground motions on offshore sites[J]. Engineering Structures, 2018, 165: 441-456.
[9] Soneji B B, Jangid R S. Passive hybrid systems for earthquake protection of cable-stayed bridge[J]. Engineering structures, 2007, 29(1): 57-70.
[10] Liu Z, He F, Yan A, et al. Mechanism and Aerodynamic Countermeasures of Vortex-Induced Vibration of a Cable-Stayed Bridge with Narrow Π-Shaped Girder Sections[J]. Journal of Bridge Engineering, 2023, 28(12): 04023090.
[11] Hou N, Sun L, Chen L. Cable reliability assessments for cable-stayed bridges using identified tension forces and monitored loads[J]. Journal of Bridge Engineering, 2020, 25(7): 05020003.
[12] Kang H, Su X, Pi Z. Planar nonlinear dynamic analysis of cable-stayed bridge considering support stiffness[J]. Nonlinear Dynamics, 2022, 107(2): 1545-1568.
[13] Ma C, Duan Q, Liao H. Experimental investigation on aerodynamic behavior of a long span cable-stayed bridge under construction[J]. KSCE Journal of Civil Engineering, 2018, 22: 2492-2501.
[14] Wang R, Xu Y, Li J. Transverse seismic behavior studies of a medium span cable-stayed bridge model with two concrete towers[J]. Journal of Earthquake Engineering, 2017, 21(1): 151-168.
[15] Larsen A, Larose G L. Dynamic wind effects on suspension and cable-stayed bridges[J]. Journal of Sound and Vibration, 2015, 334: 2-28.
[16] Cong Y, Kang H. Planar nonlinear dynamic behavior of a cable-stayed bridge under excitation of tower motion[J]. European Journal of Mechanics-A/Solids, 2019, 76: 91-107.